Non-perturbative investigation of current correlators in twisted mass lattice QCD

D i s s e r t a t i o n

zur Erlangung des akademischen Grades

d o c t o r r e r u m n a t u r a l i u m
(Dr. rer. nat.)

im Fach Physik

eingereicht an der

Mathematisch-Naturwissenschaftlichen Fakultät I

der Humboldt-Universität zu Berlin

von

Diplom-Physiker Marcus Petschlies

Präsident der Humboldt-Universität zu Berlin
Prof. Dr. Jan-Hendrik Olbertz

Dekan der Mathematisch-Naturwissenschaftlichen Fakultät I
Prof. Dr. Stefan Hecht

Gutachter/innen:
1. Prof. Dr. Michael Müller-Preußker
2. Prof. Dr. Elisabetta Pallante
3. Prof. Dr. Friedrich Jegerlehner

Tag der mündlichen Prüfung: 25. März 2013

To my father,
Frank Petschlies,
Who so bravely fought, what he could not defeat.

Abstract

We present the results of an investigation of hadronic current-current correlators based on the first principles of Quantum Chromodynamics. Specifically we apply the non-perturbative methods of lattice QCD in the twisted mass formulation with dynamical up and down quark and take advantage of its automatic $O(a)$ improvement of physical observables.

As a special application we discuss an ab-initio calculation of the hadronic contribution to the corrections of leading order in the electromagnetic coupling to the muon anomalous magnetic moment a_μ^{hlo}. The muon anomaly is regarded as one of the promising quantities for the search for new physics beyond the standard model. The origin of the strong interest in the muon anomaly lies in the persistent discrepancy between its theoretical estimate from standard model physics on the one hand and its experimental measurement on the other. In the theoretical determination the hadronic leading order part is currently afflicted with the largest uncertainty amongst the contributions from all standard model sectors and a dedicated lattice investigation of the former can be of strong impact on future theoretical estimates.

We discuss in detail our comprehensive study of all systematic uncertainties involved in the lattice calculation, including three spatial lattice volumes, two lattice spacings, pion masses ranging from 650 MeV down to 290 MeV and the quark-disconnected contribution. Given the pion masses accessible in lattice simulations at the time, bridging the gap with a_μ^{hlo} to the physical point poses a particular problem. We present a new method for the extrapolation to the physical point that softens the dependence of a_μ^{hlo} on the pion mass. This method allows for a linear extrapolation in the latter with small statistical uncertainty at the physical point. As a result we determine the contribution of up and down quark as $a_\mu^{\mathrm{hlo}}(N_f = 2) = 5.69\,(15)\,10^{-8}$.

The methods used for the muon are extended to all three standard model leptons. In particular for the electron and tau we find $a_e^{\mathrm{hlo}}(N_f = 2) = 1.512\,(43)\,10^{-12}$ and $a_\tau^{\mathrm{hlo}}(N_f = 2) = 2.635\,(54)\,10^{-6}$.

A conservative estimate of the systematic uncertainties irrespective of statistical significance leads to $\Delta_\mu = 0.42 \cdot 10^{-8}$, $\Delta_e = 0.125 \cdot 10^{-12}$ and $\Delta_\tau = 0.092 \cdot 10^{-6}$.

Finally, we estimate the charm contribution to a_μ^{hlo} in so-called partially quenched twisted mass lattice QCD, which besides dynamical up and down quarks in the sea includes the charm quark in the valence sector of the theory. As a result we find $a_\mu^{\mathrm{hlo}}(\mathrm{charm}) = 1.447\,(24)\,(30)\,10^{-9}$ in very good agreement with a dispersion-relation based result using experimental data for the hadronic $R-$ratio.

Zusammenfassung

Mit dieser Arbeit stellen wir die Resultate einer Untersuchung von Strom-Strom-Korrelatoren beruhend auf den Grundprinzipien der Quantenchromodynamik vor. Wir benutzen die nicht-perturbativen Methoden der sogenannten twisted mass Gitter-QCD mit dynamischem up- und down-Quark und nutzen dabei das automatische $O\left(a^2\right)$-Skalierungsverhalten physikalischer Observablen im Kontinuumlimes aus.

Als spezielle Anwendung diskutieren wir die nicht-perturbative Berechnung des hadronischen Beitrags zur Korrektur in führender Ordnung in der elektromagnetischen Kopplung zum anomalen magnetischen Moment des Myons a_μ^{hlo}. Die Myon-Anomalie gilt allgemein als eine sehr geeignete Größe für die aktuelle Suche nach neuer Physik jenseits des Standardmodells. Die Ursache für das gesteigerte Interesse an der Myon-Anomalie liegt in der anhaltenden Diskrepanz zwischen dem aus dem Standardmodell berechneten Wert einerseits und dem experimentell gemessenen andererseits. Innerhalb der theoretischen Bestimmung ist der hadronische Anteil führender Ordnung unter den Beiträgen aus allen Sektoren des Standardmodells mit der größten Unsicherheit behaftet und genießt derzeit somit naturgemäß Priorität.

Wir beschreiben im Detail unsere Datenanalyse und umfassende Studie aller systematischen Unsicherheiten, die mit der Gitterrechnung einhergehen, auf der Grundlage von drei räumlichen Gittervolumina, zwei Gitterabständen, Pionmassen im Bereich von 650 MeV bis hinunter zu 290 MeV und den Quark-unverbundenen Beiträgen. Für die Extrapolation zum physikalischen Punkt stellen wir eine neue Methode vor, welche die andernfalls eine stark gekrümmte Extrapolationskurve erfordernde Abhängigkeit von der Pionmasse hinreichend abschwächt. Sie ermöglicht so eine lineare Extrapolation in der Pionmasse zum physikalischen Punkt mit vergleichsweise sehr geringer statistischer Unsicherheit. Im Ergebnis bestimmen wir den Beitrag von up- und down-Quark zu $a_\mu^{\mathrm{hlo}}(N_f = 2) = 5.69\,(15)\,10^{-8}$.

Die für den Fall des Myons dargelegten Methoden werden anschließend auf alle drei Leptonen des Standardmodells erweitert. Insbesondere erhalten wir für das Elektron- und das Tau-Lepton $a_e^{\mathrm{hlo}}(N_f = 2) = 1.512\,(43)\,10^{-12}$ und $a_\tau^{\mathrm{hlo}}(N_f = 2) = 2.635\,(54)\,10^{-6}$.

Mit einer konservativen Abschätzung der systematischen Fehler ungeachtet ihrer statistischen Signifikanz erhalten wir $\Delta_\mu = 0.42 \cdot 10^{-8}$, $\Delta_e = 0.125 \cdot 10^{-12}$ und $\Delta_\tau = 0.092 \cdot 10^{-6}$.

Abschließend schätzen wir den Beitrag des charm-Quarks zu a_μ^{hlo} in der sogenannten Partially Quenched tmLQCD, in der das charm-Quark nur im Valenzsektor der Theorie auftritt. Als Resultat erhalten wir $a_\mu^{\mathrm{hlo}}(\mathrm{charm}) = 1.447\,(24)\,(30)\,10^{-9}$. Dieses Ergebnis stimmt mit der Vorhersage über die Dispersionsrelation unter Hinzunahme experimenteller Daten für das hadronische $R-$Verhältnis überein.

Contents

1 Introduction

This work is concerned with the study of quark current correlators in Quantum Chromodynamics (QCD), our theory of the strong interactions. These current correlators are basic objects in QCD and can provide very important information about the structure of QCD. As an essential element, they encode the mass spectrum of the bound states and the corresponding decay constants which can be extracted via the transfer matrix formalism. However, the current correlators carry a lot more information such as the size of the hadronic leading order contribution to the muon anomalous magnetic moment a_μ^{had}, the strength of the strong coupling constant α_s or the values of the quark masses m_q. It is precisely the goal of this thesis to extract this information by a suitable analysis of current correlators using the non-perturbative tool of lattice QCD. As we will see, it will indeed be possible to extract accurate values for a_μ^{had} with controlled systematic errors. Although the extraction of the strong coupling and quark mass has been carried out in the same spirit with results presented at the annual international symposium on lattice field theory [107, 78], a detailed discussion of the analysis is not covered by this thesis.

Before entering a more focused discussion on the just mentioned quantities, it is worth to address the rapidly evolving scenery of lattice QCD. Many collaborations world-wide, including the European Twisted Mass Collaboration (ETMC) whose physics program incorporates this thesis, have made use of recent substantial progress of the simulation algorithms, the advent of new supercomputer architectures reaching now the multi petaflop regime and significant conceptual developments of lattice fermion formulations. This led then to a situation where simulations today are carried out very close to or even at the physical pion mass, small values of the lattice spacing and large volumes. Thus, these are exciting times for numerical simulations employing lattice techniques for models of high-energy physics. Because of the remarkable improvements just mentioned, the calculations have reached a new level of precision and we are now capable of controlling the systematic uncertainties of lattice computations. As a consequence, lattice field theory is now considered as a most important tool to test the standard model and, moreover, to find the anticipated frontier of physics beyond it.

As examples where this just mentioned leap forward has led to a substantial progress, we will discuss in detail in this thesis the magnetic moments of the standard model leptons, and in particular their anomalous contribution. In addition, we have addressed the strong coupling constant and the charm quark mass which are most important fundamental parameters of QCD. To be more specific, we will concentrate on the analysis of the 2-point correlators to extract these quantities. That with the presently available gauge field configurations such a challenging goal of obtaining precise results for the hadronic leading order anomalous magnetic moments of the standard model leptons

can be reached is highly encouraging.

The relevance for achieving accurate results for these quantities lies in the fact that also the corresponding experimental precision is very high. Hence, theoretical lattice calculations have to aim at matching this precision. On the experimental side it is basically the process of electron-positron annihilation to hadronic final states via a virtual photon state which provide data that can be analyzed with theoretical tools from QCD or that can be confronted to standard model predictions. The strength and incentive of lattice calculations is that here results can be obtained in a way that is truly independent from any experimental data and which follow from the QCD Lagrangian alone. In this sense, lattice QCD calculations allow to test a theoretical model from first principles without relying on further assumptions or additional modeling. The thesis will then establish an example how such a first principle computation is carried through by describing the steps for an evaluation of a_μ^{had}.

Let us in the following describe in more detail the relevance of the lepton anomalous magnetic moments.

The electron and muon anomalous magnetic moments are often called gold-plated observables for the standard model. The reason is that firstly the anomalous magnetic moment of the electron serves as the basis for an extremely precise determination of the coupling constant in Quantum Electrodynamics, reaching a relative uncertainty of 0.37 parts per billion [68], which makes it one of the most accurate measurements of a physical quantity ever carried out. The muon anomalous magnetic moment on the other hand is a highly suitable quantity for probing basically all fundamental forces of the standard model since in its theoretical calculation electromagnetic, weak and hadronic contributions enter. Also in this case, due continuous theoretical and experimental efforts it is one of the most precisely calculated and measured quantities in physics and with an impressive agreement between standard model calculations and experiment to 5 digits. Yet there is a persistent discrepancy at the level of approximately three standard deviations between the theoretical and experimental determination. This has led to intense research over the past five decades to resolve this difference.

The strong motivation for the already performed, ongoing and planned immense research activity is the exciting possibility that this $3\,\sigma$ discrepancy is a sign of new physics beyond the standard model. This singles out the muon magnetic moment as a prime candidate observable to detect such new physics. Since contributions from beyond standard model particles or processes at a characteristic energy scale M_{new} are expected to enter the muon anomaly in the form m_μ^2/M_{new}^2, the muon is for instance by a factor of $m_\mu^2/m_e^2 \sim 4\times 10^4$ more sensitive to new physics than the electron anomalous magnetic moment, which more than compensates for the lower precision in the muon experiments. From that point of view the τ lepton would even be 300 times more sensitive than the muon, but so far experimentation with τ leptons is significantly more complicated due to the τ's very short lifetime.

One important ingredient in the computation of the muon magnetic moment is the hadronic contribution to leading and next-to-leading order in the electromagnetic coupling and it is exactly here where lattice computations are required. For brevity we will

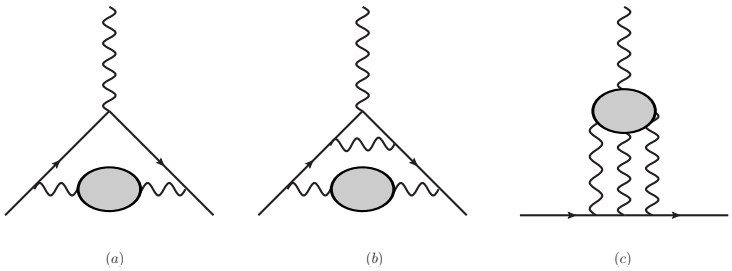

Figure 1.1: Diagrams for leading order (a) and next-to-leading order (b) hadronic vacuum polarization and next-to-leading order light-by-light scattering (c) contributions to leptonic anomalous magnetic moments

leave out the reference to the coupling when the meaning is unambiguous in context. In figure 1.1 (a)-(c) we show the prototype diagrams for those contributions. Diagram (a) denotes the leading order hadronic vacuum polarization contribution which we will focus on in this thesis. Subfigures (b) and (c) show diagrams entering at next-to-leading order; (b) is again a hadronic vacuum polarization type contribution, whereas (c) is a new kind of diagram of light-by-light scattering type, whose lattice investigation is still in its beginnings. In all cases the shaded ellipse represents the full QCD interaction. The leading order hadronic contribution accounts for the by far largest uncertainty and its thorough investigation and a precise computation of this contribution with our specific lattice methods is one of the main topics of this work.

The situation is much more difficult for the next largest hadronic uncertainty originating from the light-by-light scattering which appears at order α^3_{QED}. In that case a direct calculation using experimental data is not possible and current evaluations of the corresponding diagrams have to make rather strong use of model assumptions thereby introducing additional systematic uncertainties, cf. references [108, 103, 64, 24] for a collection of recent results.

For lattice calculations it is also a very difficult task since it involves a 4-point function, cf. [110, 20] for early reports from approaches in lattice QCD. So far the estimates of the absolute size of this contribution have been well below the precision reachable for the hadronic leading order piece and therefore did not have a strong impact on resolving the existing discrepancy. However, newly planned experiments will lead to a substantial increase of the accuracy of the muon magnetic moment which necessitates to also take the light-by-light contribution theoretically into account and compute to a precision as required by the experiments. This issue has been discussed at a dedicated workshop focusing solely on the light-by-light piece organized by the Institute of Nuclear Theory at the University of Washington [21].

The muon anomalous magnetic moment has been studied experimentally over many years, most recently during the E821 experiment of the Muon g-2 Collaboration at Brookhaven National Laboratory with data taking at their muon storage ring facility from 1997 to 2001. The precision reached with these results for the muon anomaly were the basis for the presently observed discrepancy and for the detailed results we refer

to their final report [9] and the references therein. From the theoretical side, it became clear over the years that the hadronic leading order contribution a_μ^{had} is a most important ingredient in the standard model analysis. Since a_μ^{had} is in principle a non-perturbative quantity, this triggered calculations in lattice QCD as pioneered in [19]. Subsequent work [63, 5] extended and refined the lattice computations of a_μ^{had}. However, all these early attempts suffered from the –at that time– inability to control the systematic effects of the lattice calculation. The investigation in [5] made an important step forward in using dynamical up, down and strange quarks but was not able to quantify discretization effects since the data was restricted to only one lattice spacing. They also neglected the influence of so-called quark-disconnected (singlet) contributions. Thus the calculations from lattice QCD were not as precise as required by the experiments and it was doubtful whether and when lattice QCD results for a_μ^{had} would be available that enter directly the standard model analysis of $g_\mu - 2$.

When we will report in this thesis about the substantial progress in computing a_μ^{had}, it is interesting to start with a note about the time this project needed for a successful completion. The work, embedded in the ETMC, started in 2007 and a first proceedings contribution to the 2008 Lattice conference in Williamsburg (Virginia, USA) was published in [112]. At that time the ETM collaboration was in the process of generating gauge field ensembles for two dynamical light quark flavors, three lattice spacings, up to three different spatial lattice volumes and a range of up to five different light sea quark masses. The collaboration had also started to compute quark-disconnected (singlet) diagrams and had developed special techniques that helped to calculate these contributions more accurately than standard methods. With another intermittent report at the 2010 Lattice conference in Italy [113] it then took still four years to publish a paper [52] where a final and precise value for the leading order part of a_μ^{had} was presented. In this paper, based on which we will give a detailed description in this thesis, the major systematic effects inherent to the lattice computations were quantified. In addition, a new method to compute a_μ^{had} was introduced which lead to a substantially reduced error of the final result as compared to earlier works, [48, 111].

Besides ETMC, now a number of other collaborations have started to compute a_μ^{had}, e.g. a group at the Mainz University using improved Wilson fermions [38] and the group at the University of Edinburgh using the domain wall fermion discretization [25]. Having a number of groups with different lattice discretizations of QCD will in the end lead to an extremely valuable crosscheck of the result for a_μ^{had} from lattice QCD simulations.

The increased precision of a_μ^{had} from lattice QCD comes at a time, where plans of the installation of two new experiments materialize. The first experiment is the one at the Fermi National Accelerator Laboratory [28] which will be largely based on the finished BNL experiment both conceptually and technically. The second experiment is a new high-precision measurement of the muon anomalous magnetic moment and electric dipole moment at the Japan Proton Accelerator Research Complex J-PARC [123, 73]. The FNAL experiment aims for a final uncertainty for $g_\mu - 2$ of 0.14 parts per million and can thus further substantially reduce the uncertainty of the muon anomalous magnetic

moment. Matching such an accuracy with lattice QCD simulations is very challenging but also exciting: if indeed in the end a discrepancy between experimental results and standard model calculations at the 5σ level is found, then this would be generally accepted as a manifestation of the breakdown of the standard model and clearly opens the way to a new and so far undiscovered model of elementary particle interactions.

The determination of the fundamental standard model parameters strong coupling and charm quark mass has been an essential part of this project and though we do not discuss the details in this work we would like to comment on its relevance as well. The strong coupling constant enters virtually any perturbative calculation of QCD matrix elements at small distances. Knowledge about its precise value is thus an important requirement to calculate cross sections involving QCD processes. The relevance of knowing the charm quark mass precisely is given by its –somewhat indirect– role in today's rather active search for physics beyond the standard model. The charm quark mass enters in particular the determinations of the elements of the Cabibbo-Kobayashi-Maskawa matrix (CKM matrix) as it appears in flavor physics. Sometimes the elements of the CKM matrix are over-constraint by measurements which offers –in combination with precise data available– an enhanced sensitivity to new physics and allows for a test of predictions from models extending the standard model [36, 3]. The inclusive, semi-leptonic B meson decays $\bar{B} \to X_c\, l\, \bar{\nu}$ with charmed final states denoted by X_c are one example for providing a possibility to determine the CKM matrix element V_{cb}. The transition amplitude for such a process involves a hadronic part, namely the correlation of two weak charm-bottom current operators; the short distance QCD effects of the latter are separated from the long distance ones (operator product or short distance expansion) and calculated in perturbation theory as functions of $m_{\text{charm}}/m_{\text{bottom}}$. Further examples are the rare B and K meson decays of the types $B \to X_{s,d}\,\gamma$ (inclusive, radiative B decay) and $K \to \pi\, \nu\, \bar{\nu}$. In those cases the decay channels including internal charm quark loops give a substantial contribution to the amplitudes and again a precise value of m_{charm} is necessary to give discriminating power to the corresponding data fits.

The authors of reference [2] proposed a new lattice-based determination of α_s and m_{charm} using a combination of lattice data and perturbative QCD results, which has since become known as the current correlator method. With obvious modifications it can be extended to extract the bottom quark mass [97] as well as non-perturbative renormalization factors for heavy-light currents in non-relativistic QCD [91].

The success of the current correlator method is based on the availability of the necessary results for the perturbative expansions of the polarization functions to which the lattice results are matched. In particular, the achievement of reaching the four loop order in the perturbative series has greatly added to the accuracy of the extraction of the quark mass and the reduction of the scale dependence appearing in the perturbative series.

One strong point of this method lies in the variety of types of polarization functions for which lattice QCD can provide data and perturbation theory an expansion in strong coupling and quark mass. It thus overcomes the restrictions of the experimental data based dispersive approach using the vector correlator.

As part of our project we investigate the current correlator method using gauge field

configurations of the ETM collaboration and – relying on an alternative lattice model and analysis method – aim for an independent check on the statistical uncertainties and systematic effects claimed in the existing literature. We note that within the ETMC other and different methods have already been applied in studying both the light and heavy quark masses (cf. ref. [13], [17], [16], [42]) as well as the strong coupling (cf. ref. [18, 79]).

It is important to note that in this work we are performing calculations with only up and down quarks as sea quarks, which is a severe difference to the situation found in Nature and can have a significant influence on the quantities studied here. However, it is still perfectly possible to compare to experimental data when they are translated to our situation in a suitable way. In addition, neglecting the strange and charm degrees of freedom is often still a very good approximation to the real physical world. Nevertheless, with the ongoing physics program of the ETMC, implementing the much more realistic simulation of four dynamical fermion flavors, there is the opportunity to continue this work including the complete first two quark generations. We believe that the work in this thesis provides a most valuable and important basis for such a more realistic computation.

We organized this work as follows: in chapter 2 we will review the theoretical background and standard tools for the discussion to follow and recall some fundamental QCD concepts. In a second part we will detail the theoretical setup of lattice QCD for our practical calculations and outline how the data we analyze is obtained. Chapter 3 will be devoted to the study and interpretation of current correlators as fundamental objects in twisted mass lattice QCD. We will review the data acquisition techniques and discuss different methods to arrive at the central ingredient for a_μ^{hlo}, the polarization function in momentum space. After recalling the phenomenological background of the muon anomaly as well as the situation of current experimental and theoretical determinations in chapter 4, we proceed to the final analysis to extract the leptonic anomalous magnetic moments as well as a detailed discussion of the error budget in chapter 5 The final chapter 6 will contain a summary of our results, our conclusions and an outlook upon the plethora of projects, running and planned, possibilities and challenges this field of lattice QCD offers in the future to the inquisitive lattice physicist.

2 The Standard Model, QCD and the lattice method

To appreciate both the foundations as well as the potential implications of this work we need to at least partly unfold the compacted notion of "$N_f = 2$ tmLQCD", what it stands for and why it is the method of choice. One aspect must be to pin down the place in the full and complex theory of the standard model of elementary particle physics we find ourselves in using the above mentioned method. Another one of equal importance is to lay out the assumptions we make and practical methods we use for our work, which will lead closer to a meaningful interpretation of the results and in how far they allow us to infer information on standard model properties.

In this chapter we shall thus recapitulate the more formal framework of the discussion to follow by briefly touching the key words such as the standard model, QCD in particular, Euclidean field theory to the specialized tools of lattice gauge theory that we employ in our work.

2.1 The Standard Model and Quantum Chromodynamics

2.1.1 Overview of the Standard Model

The theoretical framework that lies beneath our calculation is the Standard Model of elementary particle physics. It is the established theoretical model describing the interactions of the most fundamental matter fields observed in Nature, the quarks and leptons, and the gauge bosons that mediate the strong and electroweak interaction. Moreover, experimental evidence is now being gathered at the LHC [1, 29] on the existence of a boson consistent with the field content of the predicted Higgs sector of the standard model.

At present there are quark fields of six known distinct flavors called up (u), down (d), charm (c), strange (s), top (t) and bottom (b) as well as three types of lepton fields, electron (e), muon (μ) and tau (τ) with their corresponding neutrino fields ν_e, ν_μ and ν_τ. These quark and lepton fields are usually grouped into three pairs called families or generations as depicted in table {2.1}. The gauge boson degrees of freedom comprise the photon field γ and the W and Z vector fields of the electroweak interaction and the gluon fields A mediating the strong interaction. The structure of the weak interaction further entails the introduction of chirality of the fermion fields, assigning particle fields the property of being either right- or left-handed. The complete organizational scheme is shown in table {2.1}.

	Fermionic matter fields			Bosonic gauge fields	Higgs field
quarks	$\begin{pmatrix} u \\ d \end{pmatrix}_L$	$\begin{pmatrix} c \\ s \end{pmatrix}_L$	$\begin{pmatrix} t \\ b \end{pmatrix}_L$	$\gamma, W^{\pm}, Z, A$	H
	u_R, d_R	c_R, s_R	t_R, b_R		
leptons	$\begin{pmatrix} e \\ \nu_e \end{pmatrix}_L$	$\begin{pmatrix} \mu \\ \nu_\mu \end{pmatrix}_L$	$\begin{pmatrix} \tau \\ \nu_\tau \end{pmatrix}_L$		
	e_R, ν_{eR}	$\mu_R, \nu_{\mu R}$	$\tau_R, \nu_{\tau R}$		

Table 2.1: Field content of the Standard Model. The subscripts L and R refer to the two types of chirality of these fields that can occur in the SM, left-handed (L) and right-handed (R).

The standard model lagrangian is constructed such that the structure of the fields entering it and the way they are coupled to form a scalar-valued functional make it invariant with respect to the action of the gauge symmetry group given in equation (2.1).

$$SU(3)_{\text{color}} \times SU(2)_{\text{weak}} \times U(1)_{\text{Y}} \xrightarrow[\text{symmetry breaking}]{\text{electroweak}} SU(3)_{\text{color}} \times U(1)_{\text{em}} \,. \tag{2.1}$$

It displays the decomposition into subgroups associated with color, weak and hypercharge (Y). It is spontaneously broken by electroweak symmetry breaking modeled by virtue of the Higgs mechanism that plays a fundamental role in explaining the generation of masses of the matter fields and the massive electroweak gauge bosons W and Z. With their corresponding gauge symmetry left intact, the gluon and photon fields remain in a massless state. Along with each factor of the gauge group or equivalently with each interaction comes a coupling, which we just name and associate with the corresponding group factor.

$$\alpha_s = \frac{g_s^2}{4\pi} \leftrightarrow SU(3)_{\text{color}} \tag{2.2}$$

$$g \leftrightarrow SU(2)_{\text{weak}} \tag{2.3}$$

$$g' \leftrightarrow U(1)_{\text{Y}} \,. \tag{2.4}$$

Note that in the electroweak sector the Higgs mechanism implies a mixing of couplings g and g' to produce the known electromagnetic coupling constant $\alpha_{\text{QED}} = e^2/(4\pi)$ with $e = g\sin(\theta_W)$ and $\tan(\theta_W) = g'/g$ defines the weak mixing angle.

On the level of the lagrangian the factorization of the gauge group in equation (2.1) translates into a separation of the full lagrangian into individual summands,

$$\mathcal{L}_{SM} = \mathcal{L}^{kin} + \mathcal{L}^{int}_{QED} + \mathcal{L}^{int}_{weak} + \mathcal{L}^{int}_{QCD} + \mathcal{L}^{int}_{Higgs} \,, \tag{2.5}$$

where $\mathcal{L}_{kin}$ gathers the kinetic terms of all the matter and gauge fields and the remaining

four addends contain the interaction terms for the corresponding theory sector. As outlined before, the lattice calculation will be entirely focused on the non-perturbative treatment of a modified version of the quark and gluon contribution to $\mathcal{L}^{kin}$ and the mutual and self interaction structures contained in $\mathcal{L}^{int}_{QCD}$.

$$\mathcal{L}_{QCD} = \mathcal{L}^{kin}\left(\mathrm{q} = \mathrm{u,d,c,s,t,b;\ A}\right) + \mathcal{L}^{int}_{QCD}\,. \tag{2.6}$$

The explicit form will be given below. Besides the full QCD contribution, considering the muon anomaly will require us to take $\mathcal{L}^{int}_{QED}$ into account to next-to-leading order in QED perturbation theory.

This restriction of the standard model to the full treatment of only the QCD sector of the theory represented by going from equation (2.5) to (2.6) is a necessary step in view of our present conceptual knowledge and computational capabilities concerning the non-perturbative handling of gauge theories. Moreover, using the $N_f = 2$ tmLQCD formulation for our lattice calculation will entail another constraint concerning the number of quark flavors summed over in equation (2.6), which we will limit to up and down. Meeting these technical demands results in systematic and unavoidable differences between the model calculations and those involving experimental data. Of course these systematics do not only start by using a 2-flavor model of QCD, but to a certain, yet much smaller degree, by neglecting the dynamics of the remaining sectors of the standard model. This is a predominant concern with electromagnetic interactions, a subject that has recently come under more focused studies. The investigation of the strange and charm flavor dynamics has by now reached a more mature status with an ETMC four flavor calculation in full swing.

Still with present numerical results these limitations need to be kept in mind and taken into account when aspiring a comparison to experiment.

2.1.2 Quantum Chromodynamics

Within the gauge theory of Quantum Chromodynamics the quark fields $q = u,\ d,\ c,\ s,\ t,\ b$ transform with respect to a spin-1/2 representation of the Lorentz-group and the fundamental representation of the gauge group $SU(3)_{\text{color}}$, whereas the gluon vector fields A transform under the adjoint representation of the latter. The complete QCD lagrangian in Minkowski space is given in equation (2.7).

$$\mathcal{L}_{QCD} = -\frac{1}{2}\mathrm{Tr}\left(G_{\mu\nu}\,G^{\mu\nu}\right) + \sum_q \left\{\bar{q}\left(i\not{\partial} - m_q\right)q + g_s\bar{q}\not{A}q\right\}\,, \tag{2.7}$$

where

$$G_{\mu\nu} = \partial_\mu A_\nu - \partial_\nu A_\mu + g_s\left[A_\mu\,,\,A_\nu\right] \tag{2.8}$$

is the gluon field strength tensor, the sum extends over the quark flavors q and m_q and g_s denote the bare quark mass for quark flavor q and the bare strong coupling constant,

respectively. We have suppressed all spinor, color and spacetime indices, which when fully expanded would read $q = q_{\alpha\, i}(x)$ and $A_\mu = A^a_\mu(x)\,(T^a)_{ij}$, where $\alpha = 0,\ldots,3$ for the $2^{[D/2]}-$dimensional spinor representation in $D = 4-$dimensional spacetime, $i, j = 0, 1, 2$ for the $N_c = 3-$dimensional fundamental color representation and $a = 1,\ldots,8$ for the $(N_c^2 - 1) = 8-$dimensional adjoint color representation. The matrices T^a are the generators of the Lie-algebra $su(3)_{\text{color}}$ with permutation relations $\left[T^a\,,\,T^b\right] = f^{abc}\,T^c$ defining the set of structure constants $\{f^{abc} \,:\, a,b,c = 1,\ldots,N_c^2 - 1\}$. They are typically represented by the Gell-Mann matrices.

A complete setup for a perturbative treatment of QCD will require the definition of a gauge fixing condition. This leads to the introduction of another auxiliary anticommuting field, the ghost field denoted by c, via the Faddeev-Popov-method [49] and two additional terms in the QCD Lagrangian

$$\mathcal{L}_{gf} = -\frac{1}{2\xi}\,(\partial \cdot A^a)^2 \tag{2.9}$$

$$\mathcal{L}_{ghost} = \bar{c}\,\partial \cdot D\,c \tag{2.10}$$

$$\left(D_\mu c\right)^c = \left(\partial_\mu\,\delta^{cb} + g_s f^{cab} A^a_\mu\right) c^b$$

We emphasize that these two amendments are indispensable for perturbative calculations. In our lattice calculation we will solely consider gauge invariant observables and their continuum counterparts, i.e. correlation functions of operators that transform trivially with respect to gauge transformations. The perturbative expressions for the latter are independent of any choice of a gauge fixing condition up to and including the order of the perturbative expansion considered.

The given kinetic and interaction terms determine the Feynman rules for QCD as the basis for the perturbative calculation of correlation functions of the elementary fields. Though we do not intend to perform perturbative calculations in this work we will at times use the diagram technique for the purpose of illustrating physical contexts.

QCD at low energy

Although the field content, couplings and masses and the interaction structure stated above fully define QCD up to renormalization conditions, its structure at energy scales of order of $\Lambda_{\text{QCD}} \lesssim O\,(1\,\text{GeV})$ necessitates a change of language in the phenomenological description: the relevant degrees of freedom are the color-neutral bound states of mesons (quark-antiquark states) and baryons (3-quark-states). Replacing quark masses and strong coupling, their masses and decay constants amongst others lend themselves to a natural description of phenomena in the low-energy region of QCD, thus precisely in the realm of lattice QCD.

From the (lattice) field theoretical point of view, this is the regularization and renormalization scheme we will follow in our lattice QCD calculation: the theory will be regularized by an ultraviolet cutoff given by the inverse lattice spacing, $\Lambda_{\text{UV}} \sim 1/a$, and an infrared cutoff, the inverse size $\Lambda_{\text{IR}} \sim 1/L$, dictated by the requirement of keeping

a finite volume. In principle, instead of considering renormalized coupling and quark masses the theory is renormalized by shifting the lattice spacing and a suitable set of dimensionful hadronic observables. The physical point is approached by taking the lattice spacing to zero and the observables to their physical values. Although not considered explicitly this will set the renormalized lattice coupling and the renormalized quark masses on the lattice. Explicit translations between the two schemes are given by the β function relating lattice spacing and coupling and e.g. lattice chiral perturbation theory relating the light pseudoscalar meson masses to the light quark mass parameter. Beyond that, individual correlation functions will repuire further additive or multiplicative renormalization.

In the course of our work we will discuss phenomena and quantities that generally involve quarks from the first two families only, that is up, down and charm. Among those we consider up and down collectively as light and the charm as a heavy quark. Moreover, we always consider up and down as mass degenerate in the continuum target theory. The precise meaning of light and heavy will be explained in the context of the specific applications we discuss in this work.

The hadrons that will play an eminent role are the pion states as the light pseudo-Goldstone bosons with quantum numbers $J^P = 0^-$ for total angular momentum J and parity P, whose emergence is a result of the breaking of the chiral symmetry group for two quark flavors:

$$SU(2)_L \times SU(2)_R \xrightarrow[\text{breaking}]{\text{chiral symmetry}} SU(2)_V \,.$$

In lattice hadron phenomenology the mass of the light pseudoscalar state as well as its decay constant are quantities that can be extracted from a simulation with comparatively high precision and whose extrapolation to the continuum theory have the advantage of being controllable by low energy effective field theory. Hence they are preferential observables to set the energy or length scale in the otherwise dimensionless lattice model.

Moving along the meson spectrum the light vector mesons ρ, ω and ϕ come into focus. Owing to the vector meson dominance hypothesis the ρ meson as the lightest vector meson ($J^P = 1^-$) is at the heart of our data analysis for the anomalous leptonic moments. These states are resonances that would normally decay preferably to 2- or 3-pion states or kaons. The situation is more involved for the lattice regularization and has recently been studied extensively for tmLQCD in [53]. Later on one of our focal points will be a controlled handling of the vector meson correlator and showing that the calculation of the lepton anomalies in lattice QCD is tied to understanding the effects of the light vector mesons. We will come back to this issue when discussing the lepton anomalous magnetic moments in detail.

Here we singled out some prominent examples of the QCD spectrum that we will repeatedly use in an isolated manner. The observables we calculate on the lattice, first and foremost the hadronic vacuum polarization, are, however, inclusive quantities: the lattice method allows for the correlation functions they are derived from to incorporate

the effects of the complete hadron spectrum from the infrared up to energies or momenta determined by the ultraviolet lattice cutoff. This includes for instance effects from baryons and excited states for the mesons mentioned above, and though there may be no explicit reference to these individual contributions, they form an integral part of e.g. the lattice estimates of the lepton anomalies.

2.2 Euclidean Field Theory and Lattice QCD

2.2.1 Euclidean Field Theory

In general the calculation of correlation functions in QCD leads to infinite expressions, which may show up in terms of divergent functions of a potential energy-momentum cut-off Λ or in terms of poles $1/(4-D)^n$ in a dimensionally regularized theory.

The lattice discretization of QCD provides a specific gauge invariant regularization of QCD: the theory is considered on a 4-dimensional, discrete spacetime hypercube of finite temporal and spatial extent, T, L. As mentioned before this entails the natural introduction of both an infrared ($\propto 1/L$) and ultraviolet ($\propto 1/a$) energy-momentum cut-off leading to finite sums in position and momentum space. Divergences will consequently appear as singularities in the limit $a \to 0$ or $L \to \infty$. The major power of the lattice model, however, surfaces when the Wick rotation to Euclidean space $\mathbb{R}^4$ is applied. In the path integral formulation this implies a modification

$$\begin{aligned}\int \mathcal{D}[A]\,\mathcal{D}[q\,\bar{q}]\,\exp(i\mathcal{S}_{\mathrm{M}}[A,q,\bar{q}]) \\ \longrightarrow \int \prod_{x,\mu} \mathcal{D}U_\mu(x) \prod_{x,\alpha,c} \mathcal{D}q(x)_{\alpha c}\mathcal{D}\bar{q}(x)_{\alpha c}\,\exp(-\mathcal{S}_E[U,q,\bar{q}])\end{aligned}$$

where $\mathcal{S}_{\mathrm{M}}$ is the QCD action in Minkowski space and $\mathcal{S}_{\mathrm{E}}$ is the Wick rotated action in Euclidean space. The $SU(3)$-valued gauge fields U are the discretized replacements for the continuum $su(3)$-valued gauge field A and will be given below. The important point is that now we have an integral over a countable number of quark and gluonic degrees of freedom with a weight given by $\exp(-\mathcal{S}_{\mathrm{E}})$ with an action that is bounded from below. The path integral formulation of QCD can thus be reinterpreted as the description of a statistical system of the fermionic matter and gauge boson fields with the probability distribution for field configurations given by $p(U,q,\bar{q}) \propto \exp\left(-\mathcal{S}_{\mathrm{E}}[U,q,\bar{q}]\right)$. Going further and adding the non-zero lattice spacing and finite volume of the lattice model leads to a finite number of quark and gluonic degrees of freedom, which can be treated analytically in case of the quark fields due to the Grassmann integration formalism. $\mathcal{D}U_\mu(x)$ denotes the so-called Haar-measure according to which the gauge fields can in principle be integrated analytically as well. However, due to the enormously high dimensionality of the resulting integral such an approach is unfeasible and the gauge field integration is thus tackled using numerical methods: the integral is estimated by virtue of a simulation of the statistical system on a finite lattice in Euclidean space.

The migration of QCD between Minkowski and Euclidean space and also its propagation to the lattice formulation have been the subject of a number of fundamental theoretical work. It is due to the work of Osterwalder and Schrader [104] that the preconditions for Euclidean Green functions to allow for the construction of the target field theory have been laid out. Moreover, Osterwalder and Seiler [105] showed that Lattice models as we use one meet these preconditions and are well defined. Lüscher [92] proved the positivity of the Wilson fermion action and hence put its treatment as a statistical system on firm ground. This thread of works was completed by the authors of [60] giving proof that this property holds true under additional chiral improvement of the Wilson model. This constitutive groundwork puts us in the comfortable position of having in hand a theoretically well-established lattice model that we can readily use as a tool for our purposes.

2.2.2 tmLQCD

The twisted mass lattice QCD formulation has first been proposed and subsequently described in a series of works by Frezzotti et al. [59, 60, 57, 50, 58]. It is a special lattice regularization of the fermionic degrees of freedom of QCD with two flavors of dynamical light, mass degenerate sea quarks, up and down. The characteristics of this lattice model have been thoroughly investigated and its practical handling continuously developed further in numerous works by many collaborators within the European Twisted Mass Collaboration [120, 23, 8]. In [117] Shindler gives a comprehensive review of tmLQCD and in [74] the computer code used in this work for the production of fermion propagators has been made publicly available and its technical details have been discussed. Despite all the covering literature we will devote some space to a brief review of tmLQCD and its most important aspects, for one to set the notation and also to highlight features that are of importance for our later discussion.

To do so we naturally start with the tmLQCD action for a lattice $\mathbb{L} = \{0, \ldots, (N_t - 1)a\} \times \{0, \ldots, (N_s - 1)a\}^3$ as given in equations (2.11), (2.12)

$$\begin{aligned}
\mathcal{S}^{tmLQCD} &= \mathcal{S}_{\text{gauge}} + \mathcal{S}^{tmLQCD}_{\text{ferm}} \\
\mathcal{S}_{\text{gauge}} &= \beta \left(b_0 \sum_{\text{plaquettes } P} \text{Tr}\left(1 - \frac{1}{3} P\right) + b_1 \sum_{\text{rectangles } R} \text{Tr}\left(1 - \frac{1}{3} R\right) \right) \qquad (2.11) \\
\mathcal{S}^{tmLQCD}_{\text{ferm}} &= a^4 \sum_{x \in \mathbb{L}} \bar{\chi}(x) \left(\left[D_W + m_0 + i\mu_0 \gamma_5 \tau^3 \right] \chi \right)(x) \\
&= a^4 \sum_{x \in \mathbb{L}} \bar{\chi}(x) \Big(\Big[\frac{1}{2} \gamma_\mu (\nabla^f_\mu + \nabla^b_\mu) - \left(\frac{ar}{2} \nabla^b_\mu \nabla^f_\mu - m_{\text{crit}} \right) \\
&\quad + (m_0 - m_{\text{crit}}) + i\mu_0 \gamma_5 \tau^3 \Big] \chi \Big)(x) \,. \qquad (2.12)
\end{aligned}$$

The coefficients b_0, b_1 in the gauge action are chosen so as to fulfill the conditions of tree-level Symanzik improvement in the gauge sector, i.e. $b_0 + 8b_1 = 1$ (normalization)

and $b_1 = -1/12$ (improvement condition) [124, 125, 118, 119, 95]. With these choices the gauge action is accurate to $O\left(a^2\right)$ towards the continuum limit. m_{crit} is the critical bare quark mass: for a fixed value of bare coupling it determines the point where the light current quark mass becomes zero up to effects of order of the lattice spacing [22].

The twisted mass formulation is usually given the attribute Wilson-like. This is due to its being identical to Wilson's originally proposed fermion lattice action [126] up to the twisted mass term $i\gamma_5\tau^3$. In a more general notion of Wilson fermions the Wilson parameter r, which is the same for both fermion flavors in equation (2.12), can have a different chiral phase for up and down quark. tmLQCD is a special case of this general scenario with opposite phases for up and down quark. Before specifying the details of equations (2.11) and (2.12) we would like to illustrate the twisting procedure. In the continuum theory one can consider the fermion action amended by a twisted mass term just as well. In that case this term appears as the result of a physically irrelevant change of integration variables in the path-integral formalism, meaning one changes a fermion doublet $\psi = (u,\, d)$ according to

$$\psi \to \chi = \mathrm{e}^{-i\frac{\omega}{2}\gamma_5\tau^3}\psi\,; \quad \bar{\psi} \to \bar{\chi} = \bar{\psi}\mathrm{e}^{-i\frac{\omega}{2}\gamma_5\tau^3}\,. \tag{2.13}$$

with bare twist angle ω defined by $\tan(\omega) = \mu_0/m_0$. The twist is a non-anomalous axial flavor rotation imposed upon the quark fields. The covariant derivative part of the continuum action is invariant due to its spin-flavor structure $D \sim \gamma_\mu \otimes \mathbb{1}_2$, $\mathrm{e}^{i\frac{\omega}{2}\gamma_5\tau^3}\not{D} = \not{D}\mathrm{e}^{-i\frac{\omega}{2}\gamma_5\tau^3}$ and hence

$$\bar{\psi}(x)\not{D}\psi(x) = \bar{\chi}(x)\not{D}\chi(x)\,. \tag{2.14}$$

A mass term on the other hand with general mass matrix $M = \mathrm{diag}(m_u,\, m_d)$, which is a product of the spin unit matrix and a linear combination of $\mathbb{1}$ and τ^3, will transform as follows

$$\begin{aligned}\bar{\psi}(x)M\psi(x) &= \bar{\chi}(x)\mathrm{e}^{i\frac{\omega}{2}\gamma_5\tau^3}M\mathrm{e}^{i\frac{\omega}{2}\gamma_5\tau^3}\chi(x) = \bar{\chi}(x)\,M\mathrm{e}^{i\omega\gamma_5\tau^3}\chi(x) \\ &= \cos(\omega)\,\bar{\chi}(x)M\chi(x) + i\sin(\omega)\,\bar{\chi}(x)\gamma_5 M\tau^3\chi(x)\,.\end{aligned} \tag{2.15}$$

Hence the mass term will be rotated in flavor space and for a generic twist angle ω and in case of mass degenerate light quarks $m_u = m_d = m_0$ the massive Dirac operator assumes the form form

$$\not{D} + \cos(\omega)m_0 + i\sin(\omega)m_0\gamma_5\tau^3 \tag{2.16}$$

in terms of the fields $\chi, \bar{\chi}$. Adhering to standard notation we shall call the quark field basis in which the quark mass matrix is diagonal with real and non-negative entries the physical basis (ψ, $\bar{\psi}$ in the above equations); the alternative one is conventionally termed the twisted basis (χ, $\bar{\chi}$ above).

The twisted mass lattice formulation uses the standard definitions of the $SU(3)$ valued

gauge fields U consisting of discretized parallel transporters $U = \left\{U_\mu(x) \,|\, x \in \mathbb{L}\right\}$ with

$$U_\mu(x) = \mathcal{P} \exp\left(a \int_x^{x+a\hat{\mu}} dy^\nu \, A_\nu^b \, T^b(y) \right) \tag{2.17}$$

as well as covariant forward and backward derivative

$$\begin{aligned} \left(\nabla_\mu^f \psi\right)(x) &= \frac{1}{a}\left(U_\mu(x)\psi(x+a\hat{\mu}) - \psi(x)\right) \\ \left(\nabla_\mu^b \psi\right)(x) &= \frac{1}{a}\left(\psi(x) - U_\mu(x-a\hat{\mu})^\dagger \psi(x-a\hat{\mu})\right). \end{aligned} \tag{2.18}$$

The lattice action in the now defined physical basis is given by

$$\begin{aligned} \mathcal{S}^{tmLQCD}\left[\bar{\psi}, \psi, U\right] = a^4 \sum_{x\in\mathbb{L}} \bar{\psi}(x) \Big(\Big[\frac{1}{2}\gamma_\mu \left(\nabla^f + \nabla_\mu^b\right) \\ - i\gamma_5 \tau^3 \left(\frac{ar}{2} \nabla_\mu^f \nabla_\mu^b - m_{\text{crit}} \right) + M \Big] \psi \Big)(x) \end{aligned} \tag{2.19}$$

with bare polar quark mass $M = \sqrt{(m_0 - m_{\text{crit}})^2 + \mu_0^2}$ and explicitly showing the subtracted Wilson term.

One of the great advantages of the twisted mass formulation of lattice QCD is the automatic cancellation of $O(a)$ lattice artifacts in the continuum limit of multilocal, multiplicatively renormalizable, parity even correlation functions [57] at so-called maximal twist. For that to happen apart from the improvement of the gauge action and the chiral rotation of the fermion mass matrix just described no further operator dependent improvement is needed. This makes the $O(a)$ improvement program much more feasible when compared to the clover-improved fermion action while at the same time avoiding issues of non-locality as they would appear for the staggered fermion discretization.

The definition of maximal twist (formally twist angle $\omega = \pi/2$) is unique up to lattice artifacts [57, 4] and this is the setup we will be considering throughout this work. The procedure of tuning to maximal twist has been described in references [75, 23]; the untwisted bare quark mass m_0 (or equally well the Wilson hopping parameter $\kappa = 1/(2am_0 + 8r)$) is adjusted to its critical value $m_0 \to m_{\text{crit}}$ by observing the PCAC quark mass extracted from the ratio

$$m^{\text{PCAC}}(m_0) = \frac{1}{2} \frac{\sum_{\vec{x}} \langle \nabla_0^b A_0^a(t,\vec{x}) \, P^a(y) \rangle}{\sum_{\vec{x}} \langle P^a(t,\vec{x}) \, P^a(y) \rangle}, \quad t \text{ large}, \, a = 1, 2 \tag{2.20}$$

The axial vector current and pseudoscalar interpolating field appearing on the right-

hand side of equation (2.20) are given by

$$A_0^a(x) = \bar{\chi}(x)\,\gamma_5\gamma_0\,\tau^a\,\chi(x)$$
$$P^a(x) = \bar{\chi}(x)\,\gamma_5\,\tau^a\,\chi(x)\,.$$

On practical terms maximal twist is reached if the current quark mass satisfies the condition

$$m^{\mathrm{PCAC}}(m_{\mathrm{crit}},\,\mu_0) \leq \delta\mu_0\,, \quad \delta \approx 0.1\,. \tag{2.21}$$

A key feature of the twisted mass lattice formulation are the symmetry breaking patterns entailed by the introduction of the twisted mass term. Already the subtracted Wilson term explicitly breaks the symmetry of the lattice fermion action under $SU(2)_A$ transformations and hence reduces the flavor symmetry group according to $SU(2)_A \times SU(2)_V \to SU(2)_V$. The twisted mass term transforms non-trivial under vector flavor rotations generated by τ^1, τ^2 and hence further reduces the symmetry group $SU(2)_V \to U(1)_3$, the vector subgroup generated by τ^3. For the present context this will result in the removal of the degeneracy of spectroscopic quantities of isospin triplet operators. Examples relevant for us are e.g. $f_{\pi^\pm} \leftrightarrow f_{\pi^0}$, $m_{\pi^\pm} \leftrightarrow m_{\pi^0}$ or $f_{V^\pm} \leftrightarrow f_{V^0}$, $m_{V^\pm} \leftrightarrow m_{V^0}$, the pseudoscalar and vector meson decay constant and mass. The splittings are of course rooted in $O\left(a^2\right)$ lattice artifacts and the general empirical perception is that they are not harmful to the extraction of lattice quantities, i.e. the coefficient of the a^2 is sufficiently small — except for the case of the pion mass splitting [56] (cf. also reference [41] for a theoretical interpretation). Nevertheless this issue plays a principle role when it comes to the then necessary choice of interpolating operators for the generation or annihilation of states in the calculation of matrix elements and we will come back to that question later on.

The second major issue is the explicit breaking of the (continuum-like) parity symmetry, since the twisted mass term in the fermion action changes sign under the parity transformation. The implication of the reduced symmetry is the introduction of mixing patterns of contributions from states of different parity to renormalized matrix elements. Yet again, these modifications will be lattice artifacts that will alter the path along which we reach the continuum limit, but the target continuum theory is known to be preserved.

2.2.3 Estimation and interpretation of correlation functions

The lattice QCD method is inherently tied to the interpretation of the lattice model as a statistical system and hence to the application of the path integral formalism. The statistical weight is given by the exponential of the Euclidean lattice action in equations (2.12) (or (2.19)) and (2.11). By standard procedures the path integration of the gauge fields is then approximated by ensemble averages over gauge configuration ensembles that are the result of Markov-Chain-Monte-Carlo simulations with importance sampling. These simulations were carried out within the European Twisted Mass Collaboration over a period of several years. Since in all our analyses we start out from the already

thermalized and calibrated gauge configuration ensembles and including the necessary background to illuminate the details of their production would lead us too far away from our subject, we refer to the extensive literature on the simulation procedure in general [43, 115, 69] and the techniques and modifications for the twisted mass approach in particular [50, 51, 121, 23].

Due to the mathematical properties of anticommuting variables the path integration of fermion fields is carried out analytically as in the continuum field theory. This leads to the effective lattice gauge action which is actually used in the molecular dynamics step of the hybrid-Monte-Carlo algorithm. Since it will be the generic case for us we will illustrate the statements given above by giving the steps for the estimation of the vacuum expectation value of a multilocal operator $O(y_1, \ldots, y_n)$, which is in general a sum of products of components of quark and gauge fields with specific numerical constants. For brevity we will use the notation

$$O[\ldots](\ldots) = O[U,\, \psi,\, \bar{\psi}](y_1,\, y_2,\, \ldots, y_n)$$

$$\begin{aligned}
&\langle O(y_1, \ldots, y_n)\rangle = \\
&= \frac{1}{\mathcal{Z}} \int \prod_{x,\mu} \mathcal{D}U_\mu(x) \prod_{x,f,\alpha,c} \mathcal{D}\psi^f_{\alpha,c}(x)\mathcal{D}\bar{\psi}^f_{\alpha,c}(x)\, O[\ldots](\ldots)\, \mathrm{e}^{-\mathcal{S}_{\text{gauge}}[U] - \mathcal{S}^{\text{tmLQCD}}_{\text{ferm}}[U,\psi,\bar{\psi}]} \\
&= \frac{1}{\mathcal{Z}} \int \prod_{x,\mu} \mathcal{D}U_\mu(x) \frac{\prod_{x,f,\alpha,c} \mathcal{D}\psi^f_{\alpha,c}(x)\mathcal{D}\bar{\psi}^f_{\alpha,c}(x)\, O[\ldots](\ldots)\, \mathrm{e}^{-\mathcal{S}^{\text{tmLQCD}}_{\text{ferm}}[U,\psi,\bar{\psi}]}}{\prod_{z,f,\alpha,c} \mathcal{D}\psi^f_{\alpha,c}(z)\mathcal{D}\bar{\psi}^f_{\alpha,c}(z)\, \mathrm{e}^{-\mathcal{S}^{\text{tmLQCD}}_{\text{ferm}}[U,\psi,\bar{\psi}]}} \times \\
&\qquad \prod_{z,f,\alpha,c} \mathcal{D}\psi^f_{\alpha,c}(z)\mathcal{D}\bar{\psi}^f_{\alpha,c}(z)\, \mathrm{e}^{-\mathcal{S}^{\text{tmLQCD}}_{\text{ferm}}[U,\psi,\bar{\psi}] - \mathcal{S}_{\text{gauge}}[U]} \\
&= \frac{1}{\mathcal{Z}} \int \prod_{x,\mu} \mathcal{D}U_\mu(x)\, \tilde{O}[U](\ldots),\, \mathrm{e}^{-\mathcal{S}_{\text{gauge}}[U] - \log(\det(\mathcal{M}[U]))} \qquad (2.22) \\
&\sim \frac{1}{N_{\text{config}}} \sum_{i=1,\ldots,N_{\text{config}}} \tilde{O}[U^{(i)}](y_1, \ldots, y_n)\,. \qquad (2.23)
\end{aligned}$$

In writing down equation (2.22) we use the quark-bilinearity of the fermion action, i.e. conceiving the spinor fields as complex valued $12 \times$ volume dimensional vectors, we can write $\mathcal{S}^{\text{tmLQCD}}_{\text{ferm}} = \bar{\psi}\mathcal{M}\psi$. $\tilde{O}[U]$ is the purely gauge field dependent operator that results from the operator $O[U, \psi, \bar{\psi}]$ upon performing the Wick contractions. $\mathcal{Z}$ is the partition function, the path integral with the unit operator inserted. Passing from equation (2.22) to (2.23) is the step that requires the sample gauge fields to be generated by importance

Figure 2.1: Low-energy interpretation of 2-point current correlators: quark flow diagram (left) and meson propagator (right).

sampling with probability distribution

$$p(U^{(i)}) \propto \exp\left(-\mathcal{S}^{\text{eff}}_{\text{gauge}}\left[U^{(i)}\right]\right) \tag{2.24}$$
$$\mathcal{S}^{\text{eff}}_{\text{gauge}}\left[U^{(i)}\right] = \mathcal{S}_{\text{gauge}}\left[U^{(i)}\right] + \log\left(\det\left(\mathcal{M}\right)\left[U^{(i)}\right]\right).$$

In the course of this work we will consider operators O that are a product of two local or one-point-split bilinear quark current operators, schematically $\bar{\psi}(x)\,\Gamma\,\psi(y)$ with $y = x,\ x \pm a\hat{\mu}$); the precise definitions will be given elsewhere. Hence the interpretation of the resulting 2-point functions is that of meson propagators. The contributions to the correlation functions from meson states follow from the quantum number of the current operators, which serve as the interpolating fields for the meson states and contain their creation and annihilation operators, together with the symmetry properties of the lattice model. To illustrate this point we again consider the case of the 2-point function built from the product of two current operators with spin-flavor structure given by Γ as used above. The left-hand side of figure [2.1] shows the perturbative interpretation including the detailed quark flow and (exemplary) gluon exchange. In the low-energy description these degrees are traded for the effective description in terms of hadronic degrees of freedom denoted by the intermediate hadronic states $\left|\,\Gamma\,(p)\,\right\rangle$ with momentum p and quantum numbers encoded by Γ this 2-point function will represent. Our computational treatment of the 2-point functions will be according to standard methods and we will come back to the concrete extraction of numerical information from the correlation functions during the discussion of the analyses for the different quantities we are interested in.

2.3 Partially Quenched tmLQCD

In the course of our work we will consider correlation functions of charm quark currents. They enter the lattice model as quenched degrees of freedom [116]. Since the field content of our lattice model is then a mixture of full QCD in the light sector and quenched quark flavors in the charm sector, we speak of a partially quenched lattice QCD calculation (PQQCD). On a field theoretical level this amounts to considering an enlarged theory with the previously introduced two flavors of sea quarks up and down amended by a doublet of heavy quarks χ_h^+, χ_h^- with the superscript sign referring to the sign of the heavy quark twisted mass term in the lagrangian and a corresponding doublet of heavy bosonic fields with spin 1/2, i.e. pseudofermions $\tilde{\chi}_h^+$, $\tilde{\chi}_h^-$ [100], with bare

mass parameters identical to those of the heavy fermion doublet. In a diagrammatic expansion of any matrix element calculated in such a model the inner loop contributions of the heavy doublet and the pseudofermions will then cancel due to identical parameters but opposed statistic and only the (unquenched) sea quark contributions remain. This method has been discussed by Münster et al. for the special framework of tmLQCD chiral perturbation theory in [101].

Practically, the heavy fermion doublet enters only at the level of the calculation of current correlation functions. Their propagators are produced using the existing ETMC 2-flavor gauge field ensembles by inverting a Wilson twisted mass Dirac operator identical to that of the dynamical light quark sector except for a change in the bare twisted quark mass which is then chosen larger so as to excite meson states with masses in the region of those of the D meson, the η_c or J/ψ. In this procedure it is particularly appealing that apart from the quark mass no further tuning of lattice parameters is necessary to guarantee the automatic $O(a)$ improvement of the twisted mass formalism also in the heavy quark valence sector. In particular the critical bare mass in the charm sector is the same as in the light sector.

We would like to illustrate the effect of quenching from a diagrammatic point of view with figure [2.2]. It shows contributions to the quark current 2-point function (filled diagram on the left-hand side) up to 3-loop order ($O\left(\alpha_s^2\right)$) with single solid lines representing light fermions and double lines the quenched heavy fermion species. At 1- and 2-loop order (right-hand side of the first line) only internal gluon loops can appear. Starting at the 3-loop level secondary quark production sets in as corrections to internal gluon propagators. In our lattice calculation we would neglect the first two diagrams of the third line but include the following two with analogous patterns at higher loop orders, where correspondingly many more diagrams are excluded. Some perturbative expansions in the literature keep track of the origin of the contributions to diagrams by providing results separated by group structure and as functions of the number of light (massless in that case) and heavy fermion flavors, $N_f = N_l + N_h$. In such cases we can retain consistency at this level and actually specify to the case realized in our lattice model, i.e. $N_l = 2$ (though a priori not massless, since we will extrapolate to the physical point, not the chiral limit) and $N_h = 0$. Since these differences start at second order in α_s one might fall for the perception that these differences between full and partially quenched theory will be small. Yet this argument is far from rigorous, since it is a perturbative one and cannot account for inherently non-perturbative effects. Still we shall find that for the questions we pose the answer derived from light flavor dynamics alone gives a good approximation of the full result.

Another issue arises when it comes to the scale setting and tuning of bare parameters in the lattice calculation to arrive in the physical target theory. As we just mentioned, from the perturbative point of view it is possible to disentangle contributions from different (numbers of) flavors in a loop-wise consideration. In the non-perturbative lattice data we do not have such direct discriminating means. The most direct and probably reliable way to see the significance of the dynamical strange and charm contributions in the whole analysis will be to actually include strange and/or charm quark flavors in the

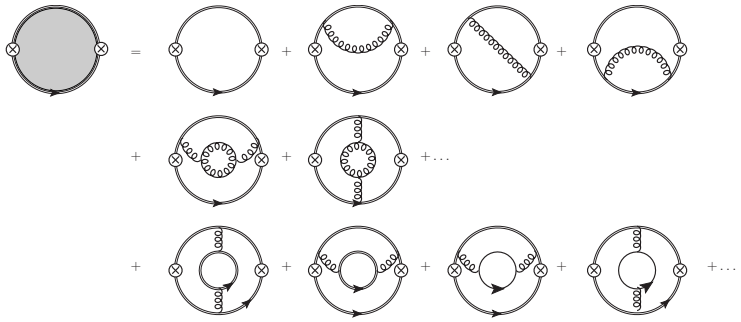

Figure 2.2: Types of Feynman diagrams up to order $O\left(\alpha_s^2\right)$ contributing to the charm current-current correlator (graph with ghost loop omitted)

simulation and redo the analysis, which is something that is presently being pursued [54].

Practically, we usually normalize the lattice parameters by imposing the matching of a dimensionful quantity to equal its experimental counterpart in units of the lattice spacing to define the energy or length scale (lattice spacing a) and to tune dimensionless ratios of quark mass dependent quantities to the physical value. This procedure would be completely valid if the target theory aimed for in the lattice continuum extrapolation would be the same as the one underlying the experimental situation. However, in the case of two light dynamical flavors amended by a valence charm quark this does not hold. We would e.g. equal the masses of two π or J/ψ excitations that reside in theories with different flavor content. So we change the renormalization scheme as compared to the full theory and shift bare coupling and quark masses to values that for quantities we use (f_π, m_π/f_π, $m_{J/\psi}/f_\pi$ would be a typical triplet) will compensate the effects of the missing quark flavors. As noted before, in principle this concerns the effects of all sectors of the standard model that we do not include in our simulation. But it is known that the corrections arising from Quantum Electrodynamics and the weak interaction are small for the quantities we look at when compared to the statistical and systematic uncertainties we can estimate with data at hand. For the time being we can thus neglect such inconsistencies. Note however, that with current developments of lattice calculations this notion will soon start to loose its justification in case of the QED corrections which continuously gain in significance.

To round up this survey we add that the renormalization pattern for the correlation functions with valence quarks will go through as before. In the field theoretic sense any divergence arising from a charm loop will be exactly canceled by its bosonic ghost-counterpart. Moreover, the scheme is mass independent and hence the 2-flavor renormalization factors determined in the light quark sector will be the appropriate ones also for the charm current operators.

We close this discussion by mentioning that lattice calculations with a partially quenched charm quark have already been frequently performed within the ETM Collaboration (cf. e.g. [12, 14, 16, 15, 17]). For the quantities investigated there the quenching

effects did not cause severe artifacts and the results obtained were compatible with experiment. Based on these observations we too expect a manageable impact on our analysis.

We have now marked the main concepts that form the basis of our lattice investigation and mentioned the major tools that have been deployed by our predecessors and the European Twisted Mass Collaboration to arrive in a position where we started our project. We will now proceed with a detailed account of the data accumulation and analysis that has been performed to obtain the results for the muon anomaly.

3 Current correlators and vacuum polarization in tmLQCD

3.1 Introduction and nomenclature

The objects we are primarily interested in are the polarization functions defined by 2-point quark-bilinear current correlators. As a motivation we start with the well known continuum formulation and then translate to lattice quantities,

$$\begin{aligned}\Pi^{\delta}_{\mu\nu}(q) &= -i \int d^4x \, \langle J^{\delta}_{\mu}(x) \, J^{\delta}_{\nu}(0) \rangle \, \mathrm{e}^{iqx} = \left(q_\mu \, q_\nu - \delta_{\mu\nu} \, q^2 \right) \Pi^{\delta}(q^2) + q_\mu \, q_\nu \, \Pi^{\delta}_{L}(q^2) \\ q^2 \, \Pi^{\kappa}(q) &= -i \int d^4x \, \langle J^{\kappa}(x) \, J^{\kappa}(0) \rangle \, \mathrm{e}^{iqx} \, . \end{aligned} \tag{3.1}$$

The superscripts $\delta = v, a$ and $\kappa = s, p$ denote the Lorentz structure of the currents and polarization functions: v - vector, a - axial vector, s scalar and p - pseudoscalar. The corresponding currents have the usual form

$$\begin{aligned} J^{v}_{\mu} &= \bar{\psi} \, \gamma_\mu \, \tau \, \psi \\ J^{a}_{\mu} &= \bar{\psi} \, \gamma_\mu \, \gamma_5 \, \tau \, \psi \\ J^{s} &= \bar{\psi} \, \tau \, \psi \\ J^{p} &= \bar{\psi} \, \gamma_5 \, \tau \, \psi \, . \end{aligned} \tag{3.2}$$

The τ matrix denotes the flavor structure of the current. In case of QCD with two massless quarks, it is a linear combination of $\tau^0 = \mathbb{1}_2$ and the Pauli matrices.

The polarization functions are normalized by a subtraction at zero momentum, we thus write

$$\Pi^{\delta,\kappa}_{R}(q^2) = \Pi^{\delta,\kappa}(q^2) - \Pi^{\delta,\kappa}(0) \, . \tag{3.3}$$

The vector and axial vector polarization functions are split into two contributions: the transverse part Π^{δ} and the longitudinal part Π^{δ}_{L}, both preceded by corresponding projectors in equation (3.1). As follows directly the longitudinal part is related to the current divergence

$$q^\mu \, \Pi^{\delta}_{\mu\nu}(q) = \int d^4x \, \langle \nabla_\mu J^{\delta}_{\mu}(x) \, J^{\delta}_{\nu}(0) \rangle \, \mathrm{e}^{iqx} = q_\nu \, q^2 \, \Pi^{\delta}_{L}(q^2) \, . \tag{3.4}$$

For the electromagnetic hadronic current

$$J_\mu^{\mathrm{em}}(x) = \bar{\psi}(x)\, Q^{\mathrm{em}}\, \gamma_\mu\, \psi(x) \qquad (3.5)$$
$$Q^{\mathrm{em}} = \mathrm{diag}(Q_u,\, Q_d,\, \ldots)$$

exact current conservation implies that the longitudinal part is identically zero, $\Pi_L^v \equiv 0$. In case of the 2-flavor axial vector vacuum polarization, the partial conservation relation connects Π_L^a and Π^p

$$q^2\, \Pi_L^a(q^2) = (4m_q^2) \left(\Pi^p(q^2) - q^2\ \partial\, \Pi / \partial q^2 \big|_{q^2=0} \right). \qquad (3.6)$$

The analytic properties of the polarization functions have been discussed at length in the literature (cf. e.g. [106, 88, 96, 7] and references therein) Let us take the electromagnetic current as an example. For brevity we will for the time being omit a superscript from the polarization tensor and function. The central equation is a form of Cauchy's Integral Theorem derived from the causality of the theory.

$$\Pi(q^2) - \Pi(0) = \frac{q^2}{\pi} \int\limits_{4m_\pi^2}^{\infty} \frac{ds}{s}\, \frac{\mathrm{Im}\,(\Pi(s))}{s - q^2 - i\epsilon}\,. \qquad (3.7)$$

The integral is taken along the branch cut in the complex q^2 plane starting at the 2-hadron production threshold $s = 4m_\pi^2$, where the polarization function is discontinuous across the real axis with a discontinuity proportional to the imaginary part. Below the threshold, in particular around the origin and for spacelike momenta, $Q^2 = -q^2 > 0$, Π is an analytic function of Q^2.

We are specifically interested in two applications of these properties. We only state them here as a motivation, the details will be given at a later stage. For the vacuum polarization caused by pair production of massive quarks $q\bar{q}$, analyticity in a neighborhood of the origin allows a Taylor expansion of the polarization function in the form

$$\Pi_{q\bar{q}} = \sum_{k=0}^{\infty} C_k \left(\frac{q^2}{4m_q^2} \right)^k \qquad (3.8)$$

If the polarization functions are understood as renormalized in some specific scheme, their derivatives at zero momentum are proportional to powers of the renormalized quark mass with coefficients $C_k = C_k(\alpha_s,\, m_q)$ that can be calculated in perturbation theory.

Secondly, the analytic function $\Pi(Q^2 = -q^2)$ can be estimated in lattice QCD for a discrete set of lattice momenta and forms the basis for the calculation of the leading order hadronic contribution a_l^{hlo} to the lepton anomalous magnetic moments in lattice QCD. The latter follow from an integral of Π_R with a known weight function arising from the leading order QED-perturbative correction to the lepton-photon vertex.

3.2 Currents in tmLQCD

In terms of elementary fields the lattice currents are built analogously to the continuum counterparts as color-neutral quark bilinears with a suitably chosen flavor and Lorentz structure. Due to the non-zero lattice spacing there is, however, an ambiguity: additionally to the local lattice currents formally equivalent to the continuum ones we can define non-local lattice currents with quark fields separated by any fixed number of lattice sites subject to gauge invariance and recovering the continuum currents in the limit $a \to 0$. In twisted mass lattice QCD at non-zero twist angle we must distinguish the operators in the physical and twisted basis (cf. 2.2.2). The currents in the physical basis (formulated in terms of the physical quark fields ψ), once properly renormalized, are directly linked to their continuum counterparts in the continuum limit $a \to 0$. For a generic twist angle, the renormalized currents in the twisted basis are linear combinations of the currents in the physical basis with renormalization factors as part of the coefficients. Thus for instance in the general frame work the renormalized non-singlet vector current $V^{\pm}$ and axial vector current $A^{\pm}$ in the twisted basis will fulfill the relation

$$\begin{pmatrix} V_\mu^\pm(x) \\ A_\mu^\pm(x) \end{pmatrix}_R = \begin{pmatrix} Z_\mathcal{V}\,\cos(\omega_R) & Z_\mathcal{A}\,\sin(\omega_R) \\ -Z_\mathcal{V}\,\sin(\omega_R) & Z_\mathcal{A}\,\cos(\omega_R) \end{pmatrix} \begin{pmatrix} \mathcal{V}_\mu^\pm(x) \\ \mathcal{A}_\mu^\pm(x) \end{pmatrix}. \tag{3.9}$$

We use the notation ω_R for the twist angle to indicate that it is defined from the renormalized quark masses $\tan(\omega_R) = \mu_R/m_R$. Reference [57] lists the complete set of relations for the quark bilinears. We focus on the case of maximal twist where we set $\omega_R = \pi/2 + O(a)$. Then relations like (3.9) are decoupled and the relation of twisted and physical currents assumes a simplified form. The definition of the renormalized local currents is given in equation (3.10).

$$\begin{aligned}
\left[V_\mu^\pm\right]_R &= Z_V^{NS}\,\bar\chi\,\gamma_\mu\,\tau^\pm\,\chi && = Z_V^{NS}\,i\,\bar\psi\,\gamma_\mu\,\gamma_5\,\tau^\pm\,\psi \\
\left[V_\mu^3\right]_R &= Z_V^{NS}\,\bar\chi\,\gamma_\mu\,\tau^3\,\chi && = Z_V^{NS}\,\bar\psi\,\gamma_\mu\,\tau^3\,\psi \\
\left[V_\mu^0\right]_R &= Z_V^{S}\,\bar\chi\,\gamma_\mu\,\chi && = Z_V^{S}\,\bar\psi\,\gamma_\mu\,\psi \\
\left[A_\mu^\pm\right]_R &= Z_A^{NS}\,\bar\chi\,\gamma_\mu\,\gamma_5\,\tau^\pm\,\chi && = Z_A^{NS}\,i\,\bar\psi\,\gamma_\mu\,\tau^\pm\,\psi \\
\left[A_\mu^3\right]_R &= Z_A^{NS}\,\bar\chi\,\gamma_\mu\,\gamma_5\,\tau^3\,\chi && = Z_A^{NS}\,\bar\psi\,\gamma_\mu\,\gamma_5\,\tau^3\,\psi \\
\left[A_\mu^0\right]_R &= Z_A^{S}\,\bar\chi\,\gamma_\mu\,\gamma_5\,\chi && = Z_A^{S}\,\bar\psi\,\gamma_\mu\,\gamma_5\,\psi
\end{aligned}$$

$$
\begin{aligned}
[S^{\pm}]_R &= Z_S^{NS}\,\bar{\chi}\,\tau^{\pm}\,\chi &&= Z_S^{NS}\,\bar{\psi}\,\tau^{\pm}\,\psi \\
\left[S^3\right]_R &= Z_S^{NS}\,\bar{\chi}\,\tau^3\,\chi &&= Z_S^{NS}\,i\,\bar{\psi}\,\gamma_5\,\psi \\
\left[S^0\right]_R &= Z_S^{S}\,\bar{\chi}\,\chi &&= Z_S^{S}\,i\,\bar{\psi}\,\gamma_5\,\tau^3\,\psi \\
[P^{\pm}]_R &= Z_P^{NS}\,\bar{\chi}\,\gamma_5\,\tau^{\pm}\,\chi &&= Z_P^{NS}\,\bar{\psi}\,\gamma_5\,\tau^{\pm}\,\psi \\
\left[P^3\right]_R &= Z_P^{NS}\,\bar{\chi}\,\gamma_5\,\tau^3\,\chi &&= Z_P^{NS}\,i\,\left[\bar{\psi}\,\psi\right]_{sub} \\
\left[P^0\right]_R &= Z_P^{S}\,\bar{\chi}\,\gamma_5\,\chi &&= Z_P^{S}\,i\,\bar{\psi}\,\tau^3\,\psi
\end{aligned}
\tag{3.10}
$$

We adhere to the convention in [32] of labeling the renormalization factors according to the fields they renormalize in the twisted basis. The superscripts NS, S are to distinguish the renormalization factors for the non-singlet and singlet currents.

In addition to the local vector current we will use the 1-point-split electromagnetic current

$$
\begin{aligned}
J_\mu^{\mathrm{em}}(x) = \frac{1}{2}\Big[&\bar{\chi}(x)\,(\gamma_\mu - 1)\,U_\mu(x)\,Q^{\mathrm{em}}\,\chi(x+a\hat{\mu}) \\
&+ \bar{\chi}(x+a\hat{\mu})\,(\gamma_\mu + 1)\,U_\mu(x)^\dagger\,Q^{\mathrm{em}}\,\chi(x)\Big]
\end{aligned}
\tag{3.11}
$$

In flavor space the twisted mass Dirac operator is a linear combination of $\mathbb{1}_2$ and τ^3. But so is the electromagnetic charge matrix for up and down quark

$$
Q^{\mathrm{em}} = \begin{pmatrix} +2/3 & 0 \\ 0 & -1/3 \end{pmatrix} = \frac{1}{6}\,\mathbb{1} + \frac{1}{2}\,\tau^3
$$

So the twisted mass fermion action is invariant under transformations generated by Q^{em}

$$
\begin{aligned}
\chi(x) &\to \chi'(x) = \chi(x) + i\alpha(x)\,Q^{\mathrm{em}}\,\chi(x) \\
\bar{\chi}(x) &\to \bar{\chi}'(x) = \bar{\chi}(x) - i\alpha(x)\,\bar{\chi}(x)\,Q^{\mathrm{em}}\,.
\end{aligned}
\tag{3.12}
$$

J^{em} is the associated Noether current and exactly conserved at non-zero lattice spacing, which is expressed in the divergence relations or Ward-Takahashi identities

$$
\langle \nabla_\mu^b\, J_\mu^{\mathrm{em}}(x) \rangle = 0 \tag{3.13}
$$

$$
\langle \nabla_\mu^b\, J_\mu^{\mathrm{em}}(x)\, O(y_1,\ldots,y_n) \rangle = \sum_{k=0}^{n} \langle \frac{\delta\, O(y_1,\ldots,y_n)}{\delta\alpha(y_k)}\,\delta(y_k - x) \rangle\,, \tag{3.14}
$$

where O is a multilocal operator made of sums of products of quark and gauge fields. The most important application of equation (3.14) for us is the case $O = J_\nu^{\mathrm{em}}$, such that

the identity reads

$$\langle \nabla^b_\mu J^{\mathrm{em}}_\mu(x)\, J^{\mathrm{em}}_\nu(y)\rangle = a\,\nabla^b_\mu\,\delta(x-y)\,\delta_{\mu\nu}\,\langle S_\nu(y)\rangle \tag{3.15}$$

$$S_\nu(y) = \frac{1}{2}\Big(\bar\chi(y)\,(\gamma_\nu - r)\,U_\nu(y)\,(Q^{\mathrm{em}})^2\,\chi(y+\hat\nu) - \bar\chi(y+\hat\nu)\,(\gamma_\nu + r)\,U_\nu(y)^\dagger\,(Q^{\mathrm{em}})^2\,\chi(y)\Big). \tag{3.16}$$

Equations (3.13) and (3.14) are rather important for the practical realization of the lattice calculation. As opposed to the definitions in equation (3.10) the Noether current is protected against any further multiplicative renormalization. The divergence relations of J^{em}_μ put restrictions on possible lattice artifacts, especially anisotropy effects. Moreover, the identities hold already on the level of individual gauge fields if the quark propagators are calculated exactly. We can see this easily by the usual way of taking the expectation value defined by the path integral as a two-step procedure $\langle\ \ \rangle = \langle\langle\ \ \rangle_f\rangle_{U_{eff}}$ with $\langle\ \ \rangle_f$ denoting the analytic Grassmann integration over fermion fields and $\langle\ \ \rangle_{U_{eff}}$ the expectation value of the resulting purely gauge field dependent quantities with respect to the effective gauge action. The effective gauge action, consisting of the original plaquette an rectangle loop gauge action plus the determinant of the fermion matrix, is invariant under the vector flavor rotations. The derivation of the Ward-Takahashi-identity thus goes through as before with only the fermionic part of the action and partition function. In the appendix 2 we added a more practical way to see the gauge-field-wise identities. On practical grounds the requirement that the Ward identity must be fulfilled for every individual gauge field is a valuable tool to check the correctness of the implementation of the electromagnetic current correlator.

The non-perturbative renormalization of the local currents has been thoroughly described in [32], resulting in the calculation of the scale-invariant Z-factors Z_V^{NS}, Z_A^{NS} and Z_P^{NS}/Z_S^{NS}. The same Z-factors will be used to renormalize products the lattice currents. This poses no particular problem unless we include products at the same space time point. Such contact terms, if they arise, deserve special attention.

3.3 2-point current correlators

On the way to estimating the polarization functions we build renormalized 2-point correlators of the above defined currents. For the local currents this proceeds in analogy to equation (3.1), where we replace the continuous Fourier integral with the discrete Fourier transform.

To determine spectral quantities and matrix elements we use the usual mixed $(t, \vec{p})$

Meson	Operator	
	physical	twisted
$\pi^{\pm}$	$\bar{u}\gamma_5 d$, $\bar{d}\gamma_5 u$	$\bar{\chi}_u\gamma_5\chi_d$, $\bar{\chi}_d\gamma_5\chi_u$
π^0	$\bar{u}\gamma_5 u - \bar{d}\gamma_5 d$	$\bar{\chi}_u\chi_u + \bar{\chi}_d\chi_d$
ρ^0	$\bar{u}\gamma_i u - \bar{d}\gamma_i d$	$\bar{\chi}_u\gamma_i\chi_u - \bar{\chi}_d\gamma_i\chi_d$
η_c	$\bar{c}\gamma_5 c$	$\bar{\chi}_c^+\chi_c^+$, $\bar{\chi}_c^+\gamma_5\chi_c^-$
J/ψ	$\bar{c}\gamma_i c$	$\bar{\chi}_c^+\gamma_i\bar{\chi}^+$, $\bar{\chi}_c^+\gamma_i\gamma_5\chi_c^-$
$D^{\pm}$	$\bar{c}\gamma_5 d$, $\bar{d}\gamma_5 c$	$\bar{\chi}_c^+\gamma_5\chi_d$, $\bar{\chi}_d\gamma_5\chi_c^+$
D^0	$\bar{c}\gamma_5 u$, $\bar{u}\gamma_5 c$	$\bar{\chi}_c^+\gamma_5\chi_u$, $\bar{\chi}_u\gamma_5\chi_c^+$

Table 3.1: Meson fields and interpolating operators in the physical and twisted basis.

representation at large Euclidean time.

$$\begin{aligned} C_{JJ}(t_x - t_y, \vec{p}) &= \sum_{\vec{x}} \langle J(t_x, \vec{x})\, J(t_y, \vec{y})\rangle\, \mathrm{e}^{i\vec{p}(\vec{x}-\vec{y}} \\ &= \sum_{\text{states}\ n} \sum_{\alpha} \left|\langle 0 \,|\, J(0) \,|\, n, \vec{p}, \alpha\rangle\right|^2\, \mathrm{e}^{-E_n(\vec{p},\alpha)(t_x - t_y)}\,, \end{aligned} \tag{3.17}$$

where we denote a generic state with total 3-momentum $\vec{p}$ and other quantum numbers α by $|n, \vec{p}, \alpha\rangle$.

In the standard case of zero spatial momentum we extract the mass and decay constant of the lightest meson state generated by current J in question. In table {3.1} we list the mesons and associated interpolating operators we use. The details about their analysis will be given elsewhere. The contraction formula for the 2-point correlators of these operators is listed in the appendix 3.3 for completeness. Though not written there the final correlation functions will include the appropriate renormalization factors.

For the polarization functions we complete the Fourier transform in the time direction and obtain the correlators in momentum space at the discrete lattice momenta $q = 2\pi(n_0/T, \vec{n}/L)$, where $n_0 = 0, \ldots, T/a - 1$, and $n_i = 0, \ldots, L/a - 1$. A slight variation of this procedure is used for the conserved vector current. Apart from that the case of the conserved vector current is at the center of our work, so we will elaborate on the vector case as a detailed example.

3.4 A detailed study of the vector case

For the 2-point correlator of the conserved vector current we can exploit the identity (3.14) further to define the polarization tensor in momentum space. We define the

tensors $\Pi_{\mu\nu}(x,y)$ and $\tilde{\Pi}_{\mu\nu}(q)$ as follows

$$\Pi_{\mu\nu}(x,y) = \langle J^{\text{em}}_{\mu}(x)\, J^{\text{em}}_{\nu}(y)\rangle - a\,\delta(x-y)\,\langle S_{\nu}(y)\rangle \tag{3.18}$$

$$\tilde{\Pi}_{\mu\nu}(q) = \sum_{x\in\mathbb{L}} \mathrm{e}^{iq(x+a\hat{\mu}/2-y-a\hat{\nu}/2)}\,\Pi_{\mu\nu}(x,y) \tag{3.19}$$

The so defined polarization tensor $\tilde{\Pi}_{\mu\nu}$ fulfills a corresponding homogeneous Ward identity in momentum space

$$\hat{Q}_{\mu}\,\tilde{\Pi}_{\mu\nu}(q) = 0\;\forall\, q \tag{3.20}$$

$$\hat{Q}_{\mu} = \hat{Q}_{\mu}(q) = \frac{2}{a}\sin\left(\frac{aq_{\mu}}{2}\right); \qquad q_{\mu} = 2\pi\frac{n_{\mu}}{L_{\mu}},$$

where L_{μ} is the box length of the lattice in direction μ ($L_0 = T$, $L_i = L$, $i = 1,2,3$) and $n = (n_0,\ldots,n_3)$ is an integer vector with $0 \le n_{\mu} < L_{\mu}/a$. The Ward identity in momentum space is completely equivalent to the corresponding relation in position space and thus again holds independently of the chosen gauge configuration. Note that in our definition the source location y is fixed and the Fourier transform is only carried out with respect to x. Consequently the Ward identity will not be fulfilled for the index ν on a gauge field-wise level, but only upon the restoration of translational invariance by the gauge field average.

3.4.1 Space time symmetry and the definition of $\Pi(\hat{Q}^2)$

In continuum Euclidean field theory the definition in equation (3.19) together with the Ward identity (3.15) and the Euclidean space time symmetry group, the orthogonal group $O(4)$, would be sufficient to conclude that in fact the vacuum polarization tensor can be written as

$$\tilde{\Pi}_{\mu\nu}(q)\big|_{\text{cont.Eucl.FT}} = \left(q_{\mu}q_{\nu} - \delta_{\mu\nu}\,q^2\right)\Pi(q^2)$$

for all momenta q with a unique scalar function $\Pi(q^2)$. On the lattice with non-zero lattice spacing $a > 0$ and finite box length L the space time symmetry group is reduced to the hyper-cubic group $H(4) \subsetneq O(4)$. With our lattice setup this reduction is taken even further due to the difference in the space and time extension of the lattice $T = 2L$ and the violation of parity symmetry by the twisted mass term. It follows that the polarization tensor can be written in the continuum like form as above, that is dictated by Euclidean symmetry, but the right-hand side has to be supplemented by lattice artifacts that parametrize the symmetry violations on the lattice

$$\tilde{\Pi}_{\mu\nu}(q) = \left(\hat{Q}_{\mu}\hat{Q}_{\nu} - \delta_{\mu\nu}\,\hat{Q}^2\right)\Pi(q^2) + a\,R_{\mu\nu}(q)\,. \tag{3.21}$$

$R_{\mu\nu}$ are the residual contributions that cannot be written like the first term. Note that we must still have $\hat{Q}_{\mu}\,R_{\mu\nu} = 0$ for all $\hat{Q}$. Since for $a \to 0$ we can expand $\hat{Q}_{\mu} = q_{\mu} + a^2\,q_{\mu}^3/24 + O\left(a^5\right)$, equation (3.21) defines a correctly normalized polarization function in

the continuum limit. The components of the polarization tensor $\tilde{\Pi}_{\mu\nu}$ do not in general benefit from the automatic $O(a)$ improvement of the twisted mass formalism, which only holds for such combinations of correlation functions that fulfill the premises of the proof [117]. We thus formally write equation (3.21) with $O(a)$ lattice artifacts.

We can write down the definition of Π as in equation (3.21) but in practice we do not have access to it. Instead we must define an estimator which approximates it as good as possible. We can understand equation (3.21) as a vector relation with composite index $\lambda = 4\mu + \nu = 0, \ldots, 15$ and define the projector matrix $P_{\mu\nu}(q)$ by

$$\begin{aligned} P_{\mu\nu}(q) &= \left(\hat{Q}_\mu \hat{Q}_\nu - \delta_{\mu\nu}\, \hat{Q}^2\right) \\ P_{\mu\rho}(q)\, P_{\rho\nu}(q) &= -\hat{Q}^2\, P_{\mu\nu}(q) \\ P_{\mu\mu}(q) &= -3\hat{Q}^2\,. \end{aligned} \tag{3.22}$$

We thus use the following projection (with summation over repeated indices μ, ν):

$$\Pi(q) = \sum_{q' \in [q]_{\mathbb{L}}} \mathrm{Re}\left(\tilde{\Pi}_{\mu\nu}(q')\right) P_{\mu\nu}(q') \left(\sum_{q' \in [q]_{\mathbb{L}}} P_{\mu\nu}(q') P_{\mu\nu}(q') \right)^{-1} . \tag{3.23}$$

The set $[q]_{\mathbb{L}}$ is given by all lattice momenta q' that are related to q by a Euclidean lattice space time symmetry transformation. In the twisted mass formulation at non-zero lattice spacing and finite volume not all these transformations are realized as symmetry transformations of the theory. As detailed in the report by Shindler [117] (1) parity and (2) time reversal are not symmetries when applied in the continuum form, but only if combined with a discrete flavor transformation ($\mu_0 \to -\mu_0$). Moreover, due to the relation $T = 2L$ there is no natural (3) permutation of the 0- and (1,2,3)-components of the 4-momenta. The set $[q]_{\mathbb{L}}$ includes the identifications (1)-(3) and is thus larger than an orbit of the actual lattice symmetry group would be.

Note that with $P_{\mu\nu}(q) P_{\mu\nu}(q) = 3(\hat{Q}^2)^2$ and the Ward identity the definition in equation (3.23) is equivalent to

$$\Pi(q) = -\frac{1}{3\hat{Q}^2} \frac{1}{\#[q]_{\mathbb{L}}} \sum_{q' \in [q]_{\mathbb{L}}} \mathrm{Re}\left(\tilde{\Pi}_{\mu\mu}(q')\right) . \tag{3.24}$$

Here $\#[q]$ denotes the number of elements of the class $[q]$. The definition in equation (3.23) is most convenient for us for several reasons. Firstly, averaging over non-equivalent classes of lattice momenta is not a problem of principle, since this non-equivalence must be attributed to finite-size effects and effects of non-zero lattice spacing. Both of these will vanish once the corresponding limits are taken. In particular equation (3.23) guarantees the correct infinite volume and continuum limit. Secondly, with regard to automatic $O(a)$ improvement we are actually required to consider a parity-even correlation function and thus the averaging over momenta that are related by a permutation of spatial components plus the transformation $-\mathbb{1}_3$ is mandatory. Thirdly,

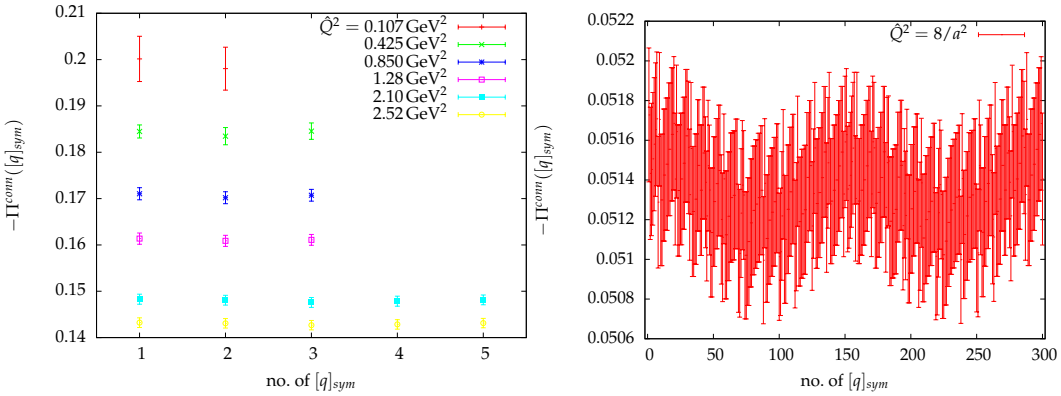

Figure 3.1: Left: non-equivalent classes of momenta in the low-momentum region ($\hat{Q}^2 \lesssim 2.5\,\mathrm{GeV}^2$) with corresponding values of Π for ensemble $B2$; right: case of maximal multiplicity for $a^2\hat{Q}^2 = 8$.

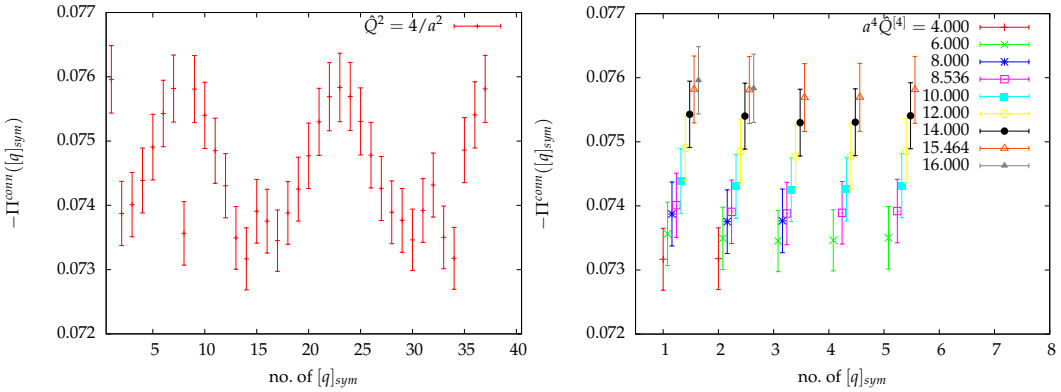

Figure 3.2: Left: larger splittings in medium momentum region $a^2\hat{Q}^2 = 4$; right: $\hat{Q}^{[4]}$ dependence of the Π for different momentum classes $[q]_{\mathbb{L}}$.

as we will discuss below, the important momentum region for our fits of the polarization function contains, depending on the lattice volume, typically the lowest 6 to 20 values of $\hat{Q}^2$. For those momenta at the lower end of the spectrum there are hardly any multiplicities that are not related to the points (1), (2) or (3) above. In particular all these momentum classes still have identical $\hat{Q}^{[2]}$, $\hat{Q}^{[4]}$, $\hat{Q}^{[6]}$, $\hat{Q}^{[8]}$. Moreover, our ability to resolve these non-degeneracies inflicted on $\Pi(q)$ at all is limited by the available statistics. We would like to illustrate this point with an example. We will give the details and parameters of the individual gauge field ensembles below, but let us just use the lattice data for $\Pi(q)$ from the ensemble B_2 (cf. table {3.4} below for ensemble details): it has a moderately small pion mass $m_\pi \approx 420\,\mathrm{MeV}$ and a medium lattice size $L \approx 1.9\,\mathrm{fm}$. It is one of the ensembles for which we have the largest amount of statistic available and thus it is a preferred choice for the question at hand. In figures [3.1] and [3.2] we show the quark-connected contribution for the vacuum polarization function

$\hat{Q}^2\,[\mathrm{GeV}^2]$	1	2	3	4	5
0.107	$[(1,0,0,0)]$	$[(-1,0,0,0)]$			
0.425	$[(0,0,0,1)]$	$[(2,0,0,0)]$	$[(-2,0,0,0)]$		
0.850	$[(0,0,1,1)]$	$[(2,1,0,0)]$	$[(-2,1,0,0)]$		
1.28	$[(0,1,1,1)]$	$[(2,1,1,0)]$	$[(-2,1,1,0)]$		
2.10	$[(0,2,1,0)]$	$[(2,2,0,0)]$	$[(4,1,0,0)]$	$[(-4,1,0,0)]$	$[(-2,2,0,0)]$
2.52	$[(0,2,1,1)]$	$[(2,2,1,0)]$	$[(4,1,1,0)]$	$[(-4,1,1,0)]$	$[(-2,2,1,0)]$

Table 3.2: Representatives of momentum classes for the left panel of figure [3.1].

Π^u built from the up-quark conserved vector current (cf. equation (3.11) with Q^{em} substituted by $\mathrm{diag}(1,0)$ and the definition in (3.4.2) below) with only those averages performed which are based on lattice symmetries (in particular not (1)-(3) above). We call these sets $[q]_{sym} \subsetneq [q]_{\mathbb{L}}$. The left panel of figure [3.1] is most relevant for our calculation. The renormalized vacuum polarization function requires the subtraction of $\Pi(\hat{Q}^2 = 0)$ which is drawn from a fit with major support in the lowest-momentum region, typically $\hat{Q}^2 \lesssim 2\,\mathrm{GeV}^2$. The multiplicity of momenta is small (5 being the extreme case up to $2.5\,\mathrm{GeV}^2$) and all the realizations are related via points (1)-(3) above with the corresponding $\Pi(q)$ in very good agreement. As an example we list the different classes of momenta $[q]_{sym}$ labeled by a representative in each case in table {3.2}. The momenta in physical units follow from using $a = 0.079\,\mathrm{fm}$ for the lattice spacing [8].

The situation changes slightly in the intermediate momentum region, which we roughly take to be in the interval $3\,\mathrm{GeV}^2 \leq \hat{Q}^2 \leq 5\,\mathrm{GeV}^2$. Here multiplicities are enhanced and so is the feathering of $\Pi(q)$ with stronger discrepancies between different classes of momenta realizing one and the same $\hat{Q}^2$: the left panel of figure [3.2] shows how the splitting reaches the level of 4 standard deviations between minimum and maximum at $\hat{Q}^2 = 4/a^2$ with errors added in quadrature. However, comparing the data for closely neighbored momenta - also such with low multiplicity - we find a spreading of approximately equal magnitude.

The right panel of figure [3.1] shows another extreme case: for the momentum $\hat{Q}^2 = 8/a^2$ the multiplicity reaches a maximum, yet different realizations all agree within 1.5 standard deviations. Towards the high momentum region multiplicities decrease again and the agreement of different realizations $[q]_{sym}$ improves.

From the arguments above and a look at the available data we thus conclude that in the relevant small momentum region we cannot significantly discriminate different classes of momenta and our advocated procedure of averaging over the complete set $[q]_{\mathbb{L}}$ is a safe way to proceed. If we fit $\Pi(\hat{Q}^2)$ data at larger momenta where distinct classes $[q]_{\mathbb{L}} \cap [q']_{\mathbb{L}} = \emptyset$ with $\hat{Q}(q)^2 = \hat{Q}(q')^2$ exist, we leave them side-by-side in the fit. Despite that ambiguity we will refer to the polarization function as a unique $\Pi(\hat{Q}^2)$. In some cases we will go further and average over all realizations q with same $\hat{Q}^2$ and thus produce a truly single valued $\Pi(\hat{Q}^2)$. Since from our experience results do not significantly depend on this choice we will not mention it any further.

Another comment is in order concerning the explicit selection of the real part of Π in

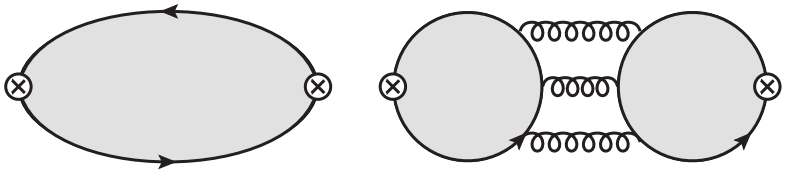

Figure 3.3: Quark-connected (left) and disconnected diagram (right); the shaded filling represents the full QCD interaction; the right-hand side shows an exemplary three-gluon exchange between the quark loops

equation (3.23). This prescription is linked to the flavor symmetry pattern of the twisted mass formalism. In the following we will use the notation for the 1-point-split valence quark currents J^q_μ for $q = u, d$ and a bar on the flavor index is meant as the alternate flavor, i.e. $J^{\bar{u}}_\mu = J^d_\mu$. As detailed in the appendix 3.4 we then have the relation

$$\langle J^{q_1}_\mu(x)\, J^{q_2}_\nu(y)\rangle^*_f = \langle J^{\bar{q}_1}_\mu(x)\, J^{\bar{q}_2}_\nu(y)\rangle_f \,.$$

Carrying the flavor notation over to the vacuum polarization tensor in momentum space we thus have

$$\tilde{\Pi}^{q_1 q_2}_{\mu\nu}(q) = \left(\tilde{\Pi}^{\bar{q}_1 \bar{q}_2}_{\mu\nu}(-q)\right)^* \,. \tag{3.25}$$

In particular for the flavor diagonal cases the polarization functions $\Pi^u = \Pi^{uu}$ and $\Pi^d = \Pi^{dd}$ fulfill

$$\Pi^u(\hat{Q}^2) = \left(\Pi^d(\hat{Q}^2)\right)^* \,. \tag{3.26}$$

In other words, due to the non-degeneracy of up and down quark the polarization function can have an imaginary part. This is an unphysical, pure lattice artifact and hence most likely an $O(a)$ effect. The real part on the other hand has a non-zero continuum limit and with the parity average included in the prescription (3.23) it fulfills the requirements of the twisted mass formalism to be automatically accurate to $O\left(a^2\right)$.

3.4.2 Lattice calculation of the electromagnetic current-current correlator

The structure of the correlator will allow for two kinds of contributions: quark-connected and quark-disconnected ones,

$$\Pi_{\mu\nu}(x, y) = C_{\mu\nu}(x, y) + D_{\mu\nu} \,.$$

Diagrammatically, the quark-connected contributions are those with a closed valence fermion loop connecting both vector vertices; the quark-disconnected diagrams have the main feature of two closed valence quark loops, one at each vertex. We depict the situation in figure [3.3]. We will use different methods to estimate the connected and disconnected piece numerically, each optimized for the different structure of the contribution.

Having equation (3.18), the defining relation for the vacuum polarization tensor in

position space, at hand we can proceed with its representation in terms of lattice degrees of freedom, quark propagators and gauge fields. To do that we introduce some notation to simplify the following formulas.

$$\begin{aligned} H_\mu^-(x) &= -\frac{1}{2}(r-\gamma_\mu)U_\mu(x) \\ H_\mu^+(x) &= -\frac{1}{2}(r+\gamma_\mu)U_\mu(x-a\hat{\mu})^\dagger \\ J_\mu^{\mathrm{em}} &= \bar{\chi}(x)H_\mu^-(x)\,Q^{\mathrm{em}}\chi(x+a\hat{\mu}) - \bar{\chi}(x+a\hat{\mu})\,H_\mu^+(x+a\hat{\mu})\,Q^{\mathrm{em}}\chi(x)\,. \end{aligned} \tag{3.27}$$

The definition of the spin-color matrices $H_\mu^\pm$ has been chosen such that the hopping matrix H, of the twisted mass Dirac operator can be written as

$$H(x,y) = \sum_\mu \Big(H_\mu^-(x)\delta(x+a\hat{\mu}-y) + H_\mu^+(x)\delta(x-a\hat{\mu}-y)\Big)$$

(cf. also the definition in appendix 2).

Using the definitions above we can write down the gauge field dependent quark-connected part $C_{\mu\nu}$ of the current-current correlator as follows

$$\begin{aligned} C_{\mu\nu}(x,y) &= \langle J_\mu^{\mathrm{em}}(x)\,J_\nu^{\mathrm{em}}(y)\rangle_f^{conn} \\ &= -\mathrm{Tr}\Big(H_\nu^-(y)\,Q^{\mathrm{em}}\,S(y+a\hat{\nu},x)\,H_\mu^-(x)\,Q^{\mathrm{em}}\,S(x+a\hat{\mu},y)\Big) \\ &\quad + \mathrm{Tr}\Big(H_\nu^+(y+a\hat{\nu})\,Q^{\mathrm{em}}\,S(y,x)\,H_\mu^-(x)\,Q^{\mathrm{em}}\,S(x+a\hat{\mu},y+a\hat{\nu})\Big) \\ &\quad + \mathrm{Tr}\Big(H_\nu^-(y)\,Q^{\mathrm{em}}\,S(y+a\hat{\nu},x+a\hat{\mu})\,H_\mu^+(x+a\hat{\mu})\,Q^{\mathrm{em}}\,S(x,y)\Big) \\ &\quad - \mathrm{Tr}\Big(H_\nu^+(y+a\hat{\nu})\,Q^{\mathrm{em}}\,S(y,x+a\hat{\mu})\,H_\mu^+(x+a\hat{\mu})\,Q^{\mathrm{em}}\,S(x,y+a\hat{\nu})\Big)\,. \end{aligned} \tag{3.28}$$

The trace operation is in spinor, color and flavor space.

In our implementation of the lattice calculation of the connected contribution we use point-to-all propagators for the up- and down-quark. These are the result of solving the equations

$$D_{\mathrm{W}}^{\mathrm{tm\,u/d}}\phi_{u/d}(y,\,\alpha,\,a) = \eta(y,\,\alpha,\,a)\,,$$

with indices $\alpha = 0,\ldots,3$, $a = 0,1,2$ and the source location $y \in \mathbb{L}$. Here the spinor field η is a point source with elements

$$\eta(y,\,\alpha,\,a)_{z,\beta,b} = \delta(z-y)\,\delta_{\alpha\beta}\,\delta_{ab} \tag{3.29}$$

such that the field $\phi_{u/d}(y,\,\alpha,\,a)$ holds one column of the complete propagator matrix

$$\phi_{u/d}(y,\,\alpha,\,a)_{z,\beta,b} = D_{\mathrm{W}}^{\mathrm{tm\,u/d}}{}_{\beta\alpha,\,ba}(z,y)\,.$$

To suppress correlation effects the components of the source location are chosen randomly.

With the point-to-all method only the calculation of propagator elements $S(x, y)$ for any x but fixed source location y is feasible. Hence we use γ_5-Hermiticity of the twisted mass Dirac operator

$$\begin{aligned} D_{\mathrm{W}}^{\mathrm{tm\,d/u}} &= \gamma_5\, D_{\mathrm{W}}^{\mathrm{tm\,u/d}\dagger}\, \gamma_5 \\ S_{u/d}(y, x) &= \gamma_5\, S_{d/u}(x, y)^\dagger\, \gamma_5 \end{aligned} \tag{3.30}$$

to switch the space time arguments.

The price to pay is the implied change of flavor (sign change of the twisted quark mass in $D_{\mathrm{W}}^{\mathrm{tm}}$ or the propagator) that mixes up and down flavors in the connected contractions. This in turn implies that not only the up-type propagators but also the down-type ones need to be calculated. We thus use a total of $2\,(u,\, d) \times 5\,(\text{source locations}) \times 4\,(\text{spin}) \times 3\,(\text{color}) = 120$ inversions for each gauge configuration. The contractions performed in practice in terms of the propagator fields ϕ are listed in the appendix 3.1 (cf. equation (19)). Note that using the conserved current means a factor of 5 more inversions to produce the quark-connected part of the polarization tensor than compared to a calculation using the local vector current or a combination of conserved and local current with the local current at the source y. Moreover, due to the introduction of the gauge field in the current operator the correlators are noisier in comparison to the local-local variant. However, due to the lattice regularization the local current does not satisfy an exact Ward identity and it requires multiplicative renormalization. We thus think that the advantages of using the conserved current correlator outweigh the increased numerical cost.

Since the complete quark propagator of the light doublet is diagonal in flavor space, $S = D_{\mathrm{W}}^{\mathrm{tm}\,-1} = \mathrm{diag}(S_u,\, S_d)$ we can simplify the result in equation (3.28) by using the flavor specific contributions C^q to the connected part of the current correlator. We thus have

$$C_{\mu\nu}(x, y) = (Q_u^{\mathrm{em}})^2\, C_{\mu\nu}^u(x, y) + (Q_d^{\mathrm{em}})^2\, C_{\mu\nu}^d(x, y)\,. \tag{3.31}$$

A similar pattern holds for the contact term (3.16): it contains the electromagnetic charge matrix squared and all factors are flavor diagonal. We can thus carry over the flavor decomposition to the complete connected part of the vacuum polarization tensor in position space and hence also to momentum space

$$\tilde{\Pi}_{\mu\nu}^{conn}(q) = \left(\frac{2}{3}\right)^2 \tilde{\Pi}_{\mu\nu}^{conn\,u}(q) + \left(-\frac{1}{3}\right)^2 \Pi_{\mu\nu}^{conn\,d}(q)\,, \tag{3.32}$$

with the explicit charge factors inserted. We have shown earlier that indeed the relation $\tilde{\Pi}_{\mu\nu}^{conn\,u}(q) = \left(\tilde{\Pi}_{\mu\nu}^{conn\,d}(-q)\right)^*$ holds and in taking the real part in the definition of Π as given in equation (3.23) we explicitly remove any flavor symmetry breaking in the

valence sector. We thus calculate in practice

$$\mathrm{Re}\left(\tilde{\Pi}^{conn}_{\mu\nu}\right)(q) = \frac{5}{9}\,\mathrm{Re}\left(\tilde{\Pi}^{conn\,u}_{\mu\nu}\right)(q)\,. \tag{3.33}$$

In position space this translates into

$$\begin{aligned}
&\mathrm{Re}\left(\tilde{\Pi}^{conn\,u}_{\mu\nu}\right)(q) \\
&\quad= \sum_{x\in\mathbb{L}} \mathrm{e}^{iq(x+a\hat{\mu}/2-y-a\hat{\nu}/2)}\,\frac{1}{2}\left(\Pi^{conn\,u}_{\mu\nu}(x,y) + \left(\Pi^{conn\,u}_{\mu\nu}(-x-a\hat{\mu},-y-a\hat{\nu})\right)^*\right) \\
&\quad= \sum_{x\in\mathbb{L}} \mathrm{e}^{iq(x+a\hat{\mu}/2-y-a\hat{\nu}/2)}\,\frac{1}{2}\left(\Pi^{conn\,u}_{\mu\nu}(x,y) + \left(T_F^1\times P_F^1\left(\Pi^{conn\,u}_{\mu\nu}\right)(x,y)\right)^*\right)
\end{aligned} \tag{3.34}$$

on the level of individual gauge configurations. T_F^1 and P_F^1 are the twisted time reversal and twisted parity operations [117] and exact symmetries of the lattice action. The calculation can thus be reduced to

$$\mathrm{Re}\left(\tilde{\Pi}^{conn\,u}_{\mu\nu}\right)(q) = \sum_{x\in\mathbb{L}} \mathrm{e}^{iq(x+a\hat{\mu}/2-y-a\hat{\nu}/2)}\,\mathrm{Re}\left(\Pi^{conn\,u}_{\mu\nu}(x,y)\right). \tag{3.35}$$

The contracted quark-disconnected contributions $D_{\mu\nu}$ read:

$$\begin{aligned}
L_\mu(x) &= \langle J^{\mathrm{em}}_\mu(x)\rangle_f \\
&= -\mathrm{Tr}\left(H^-_\mu(x)\,Q^{\mathrm{em}}\,S(x+a\hat{\mu},x) - H^+_\mu(x+a\hat{\mu})\,Q^{\mathrm{em}}\,S(x,x+a\hat{\mu})\right) \\
D_{\mu\nu}(x,y) &= \langle J^{\mathrm{em}}_\mu(x)\rangle_f\,\langle J^{\mathrm{em}}_\nu(y)\rangle_f = L_\mu(x)\,L_\nu(y)\,.
\end{aligned} \tag{3.36}$$

We further define the following flavor and isospin-specific quantities

$$\begin{aligned}
L^{q\,-}_\mu(x) &= \mathrm{Tr}\left(H^-_\mu(x)\,S_q(x+a\hat{\mu},x)\right) \\
L^{q\,+}_\mu(x) &= \mathrm{Tr}\left(H^+_\mu(x+a\hat{\mu})\,S_q(x,x+a\hat{\mu})\right) \\
L^0_\mu(x) &= \left(L^{u\,-}_\mu(x) + L^{d\,-}_\mu(x)\right) - \left(L^{u\,+}_\mu(x) + L^{d\,+}_\mu(x)\right) \\
L^1_\mu(x) &= \left(L^{u\,-}_\mu(x) - L^{d\,-}_\mu(x)\right) - \left(L^{u\,+}_\mu(x) - L^{d\,+}_\mu(x)\right) \\
L_\mu(x) &= \frac{2}{3}(L^{u\,+}_\mu(x) - L^{u\,-}_\mu(x)) - \frac{1}{3}(L^{d\,+}_\mu(x) - L^{d\,-}_\mu(x)) = \frac{1}{6}\,L^0_\mu(x) + \frac{1}{2}\,L^1_\mu(x)\,.
\end{aligned} \tag{3.37}$$

Using again the γ_5-Hermiticity relation tells us that

$$\begin{aligned}
L^{u\,-}_\mu(x) &= \left(L^{d\,+}_\mu(x)\right)^* \\
L^{u\,+}_\mu(x) &= \left(L^{d\,-}_\mu(x)\right)^*
\end{aligned} \tag{3.38}$$

and vice versa, which implies that L^0_μ is purely imaginary, while L^1_μ is purely real. From

this we deduce that

$$D_{\mu\nu}(x,y) = \Big(\frac{1}{6}\,L^0_\mu(x) + \frac{1}{2}\,L^1_\mu(x)\Big) \times \Big(\frac{1}{6}\,L^0_\nu(y) + \frac{1}{2}\,L^1_\nu(y)\Big)$$
$$\mathrm{Re}\Big(D_{\mu\nu}(x,y)\Big) = \Big(\frac{1}{6}\Big)^2\,L^0_\mu(x)\,L^0_\nu(y) + \Big(\frac{1}{2}\Big)^2\,L^1_\mu(x)\,L^1_\nu(y)\,. \tag{3.39}$$

Inspecting equation (3.36) we see that for the Fourier transform in x we require the propagators from $x \to x + a\hat{\mu}$ for all $x \in \mathbb{L}$. As mentioned earlier, due to the computational cost the point-to-all method is unfeasible to produce them. Instead we apply the method of stochastic volume sources which lead to so-called all-to-all propagators. They result from solving the same equation as before

$$D^{\mathrm{tm}}_{\mathrm{W}\,u/d}\,\phi^r_{u/d} = \eta^r\,, \tag{3.40}$$

albeit now with stochastic volume sources as the right-hand side. The label r denotes different independent source fields. The $24(L/a)^3(T/a)$ real elements of η^r are independent and identically distributed random variables subject to the Gaussian distribution with zero mean and unit variance. In terms of the probability distribution:

$$p(\mathrm{Re}\left(\eta^r_{x,\alpha,a}\right) = \xi) = \frac{1}{\sqrt{2\pi}}\,\mathrm{e}^{-\frac{\xi^2}{2}} \tag{3.41}$$

independently for all triples (x,α,a) of lattice site, spinor and color index and equally for the imaginary part of η^r. Denoting the expectation value by $\mathrm{E}[\quad]$ we thus have the standard calculus

$$\mathrm{E}\Big[\mathrm{Re}\left(\eta^r_{x,\alpha,a}\right)\Big] = 0 = \mathrm{E}\Big[\mathrm{Im}\left(\eta^r_{x,\alpha,a}\right)\Big]$$
$$\mathrm{E}\Big[\eta^r_{x,\alpha,a}\,{\eta^s_{y,\beta,b}}^*\Big] = 2\delta^{rs}\,\delta(x-y)\,\delta_{\alpha\beta}\,\delta_{ab}$$
$$\mathrm{E}\Big[\phi^r_{u/d}(x)\,\eta^r(y)^\dagger\Big] = 2\delta^{rs}\,D^{\mathrm{tm}}_{\mathrm{W}\,u/d}(x,y)\,. \tag{3.42}$$

The last line of equations (3.42) means with the pair $(\eta^r,\,\phi^r)$ one can estimate any element of the complete quark propagator. Deferring the detailed contraction formulas to the appendix 3.2 we use the fact that with the all-to-all method we implicitly estimate the quark-disconnected contribution to the vacuum polarization tensor in position space $\Pi^{disc}_{\mu\nu}(x,y)$ for all (x,y) (in contrast to the connected piece, where the source location y was fixed). The Fourier transform can thus be carried out in both arguments leading to

$$\tilde{\Pi}^{disc}_{\mu\nu}(q) = \sum_{x,y\in\mathbb{L}} \mathrm{e}^{iq(x+a\hat{\mu}/2-y-a\hat{\mu}/2)}\,\Pi^{disc}_{\mu\nu}(x,y) \tag{3.43}$$
$$= \sum_{x\in\mathbb{L}} \mathrm{e}^{iq(x+a\hat{\mu}/2)}\,L_\mu(x) \times \sum_{x\in\mathbb{L}} \mathrm{e}^{-iq(y+a\hat{\nu}/2)}\,L_\nu(y)$$
$$= \tilde{L}_\mu(q)\,\tilde{L}_\nu(-q)\,. \tag{3.44}$$

Since we must use independent pairs of source and propagator for both factors of $\tilde{L}$ in equation (3.44) the estimator assumes the form

$$\tilde{\Pi}^{disc}_{\mu\nu}(q) = \frac{1}{N_s(N_s-1)} \sum_{1\le r<s\le N_s} \left(\tilde{L}^r_\mu(q)\, \tilde{L}^s_\nu(-q) + \tilde{L}^s_\mu(q)\, \tilde{L}^r_\nu(-q) \right). \tag{3.45}$$

Here N_s denotes the number of source-propagator-pairs available for the estimation.

We make use of the noise reduction method advocated in [76, 23] to modify the estimators for L^0 and L^1. The short derivation of the formulas is included in the appendix 3.2 and the final estimators read

$$\begin{aligned} L^r_\mu(x) = {} & \frac{2i}{3} \operatorname{Im}\left(\phi^r(x)^\dagger\, \gamma_5\, H^-_\mu(x)\, \gamma_5\, [D_W\, \phi^r]\,(x+a\hat{\mu}) \right) \\ & + 2\mu_0 \operatorname{Im}\left(\phi^r_u(x)^\dagger\, \gamma_5\, H^-_\mu(x)\, \phi^r_u(x+a\hat{\mu}) \right). \end{aligned} \tag{3.46}$$

The advantage of writing the estimators in the way shown in equation (3.46) was outlined in [23]: both summands contain an implicit sum over the space time index of the source fields. This amounts to a factor of the lattice volume $V = L^3T$ in the signal-to-noise ratio, changing the latter from $O\left(1/\sqrt{V^2}\right)$ to $O(1)$ due to the implied averaging. Note that the conversion of the L^1 estimator based on the first line of (20) constitutes a special case of the non-singlet vector Ward identity in the twisted basis and again holds on the level of individual gauge fields

$$\delta^V_\alpha := \begin{cases} \chi(x) & \to \chi'(x) = \chi + i\alpha(x)\tau^1\, \chi(x) \\ \bar{\chi}(x) & \to \bar{\chi}'(x) = \bar{\chi} - i\alpha(x)\bar{\chi}(x)\, \tau^1 . \end{cases} \tag{3.47}$$

$$\nabla^b_\mu \langle J^1_\mu(x)\, J^2_\nu(y)\rangle_f = ia^{-4} \langle J^3_\nu(y)\rangle_f \left(\delta(x-y) + \delta(x-y-a\hat{\nu})\right) - 2\mu_0 \langle P^2(x)\, J^2_\nu(y)\rangle_f . \tag{3.48}$$

with $\langle J^3_\nu(y)\rangle_f = L^1_\nu(y)$. Upon summation over the space time index x the transformation follows. This corresponds to an axial Ward identity in the physical basis and shows that L_1 can in fact be strongly suppressed by an explicit factor of the bare quark mass[1]. Bearing in mind that we can start from the real part of $\Pi^{disc}_{\mu\nu}$, which would be given by $L^0L^0 + L^1L^1$ this modification significantly weakens the impact of the latter term compared to the first and the estimates are not changed significantly if the L_1 term is left out.

Finally, the projection to extract the polarization function $\Pi^{disc}(q)$ is equivalent to that for the connected piece. Note that with the stochastic volume source method the quark propagators are not obtained exactly but estimated (as opposed to the point-to-all method), such that in contrast to the connected polarization tensor the Ward identity is also not fulfilled exactly (meaning to machine precision) but only stochastically and e.g. equations (3.23) and (3.24) will lead to different results for any finite N_s. The prescription (3.23) contains a factor of 4 more stochastic observables that are averaged and is thus preferable over the alternate (3.24).

[1] In tmLQCD the product $\mu_0\, P^2$ is a renormalized operator

The quark-disconnected contribution to the vacuum polarization tensor have not been considered in previous applications of the latter, e.g. in lattice estimates of the leading order hadronic muon anomaly. The main reasons for neglecting them against the connected piece are mainly twofold: the disconnected contribution requires stochastic methods and is notoriously harder to estimate than the connected piece (with e.g. the rather clean point source method). Moreover, their contribution to the polarization function is expected to be much smaller than the connected one. Several reasons have been put forward in favor of this argument.

First, if we were to deploy a QCD model with two degenerate quark flavors then up and down propagator will also be identical and the only source of distinction of quark flavors will come from the charge matrix. The vacuum polarization tensor in position space can then be written as

$$\begin{aligned}\Pi_{\mu\nu}(x,y) &= \left(Q_u^{\mathrm{em}2} + Q_d^{\mathrm{em}2}\right) C_{\mu\nu}(x,y) + \left(Q_u^{\mathrm{em}} + Q_d^{\mathrm{em}}\right)^2 D_{\mu\nu}(x,y) \\ &= \frac{5}{9}\, C_{\mu\nu}(x,y) + \frac{1}{9}\, D_{\mu\nu}(x,y)\,,\end{aligned}$$

where $C_{\mu\nu}$ and $D_{\mu\nu}$ are now the corresponding expressions for the connected and disconnected contribution for one quark flavor. Thus from the charge matrix in the case of two quark flavors, the disconnected contribution is suppressed by a factor 5 relative to the connected one. If we went further to a calculation with mass-degenerate up, down and strange quark, the disconnected contributions would cancel completely. However, in the physical situation with the strange quark mass larger than the up and down quark mass this cancellation ceases to be exact. Even with mass-non-degenerate quarks the cancellation will occur in perturbative momentum regions, where $q^2 \gg m_q^2$ and the contributions of individual quarks approach each other: quark mass effects become suppressed by powers of m_q^2/q^2. In that sense perturbative QCD oftentimes considers the $N_f = N_l + 1$ case with N_l massless quarks and one heavy quark (charm or bottom) such that quark-disconnected contributions only start with the heaviest quarks in the valence sector.

Secondly, in perturbation theory it is known that the quark-disconnected diagrams (or singlet diagrams in the pQCD community) only start contributing at $O\left(\alpha_s^3\right)$. This is a consequence of Furry's Theorem [62] applied to QCD. The expansion of the vacuum polarization function in perturbative QCD is available to 3-loop order with mass corrections [30] [2] and 4-loop order in the massless case [7]. So from the pQCD point of view we expect a priori that in the high momentum region, where pQCD results are applicable with small running strong coupling, the singlet piece will be suppressed. Nevertheless such a perturbative argument does not necessarily apply in the low energy domain, which is of primary interest to us and the impact of the quark-disconnected diagrams on e.g. the error budget for the estimate of $\Pi(0)$ should be checked explicitly.

Thirdly, an effective field theory investigation has been carried out by the authors of [87, 37] using partially quenched chiral perturbation theory coupled to photons. Within

[2] Some derivatives of the heavy quark vacuum polarization have been calculated to four-loop order.

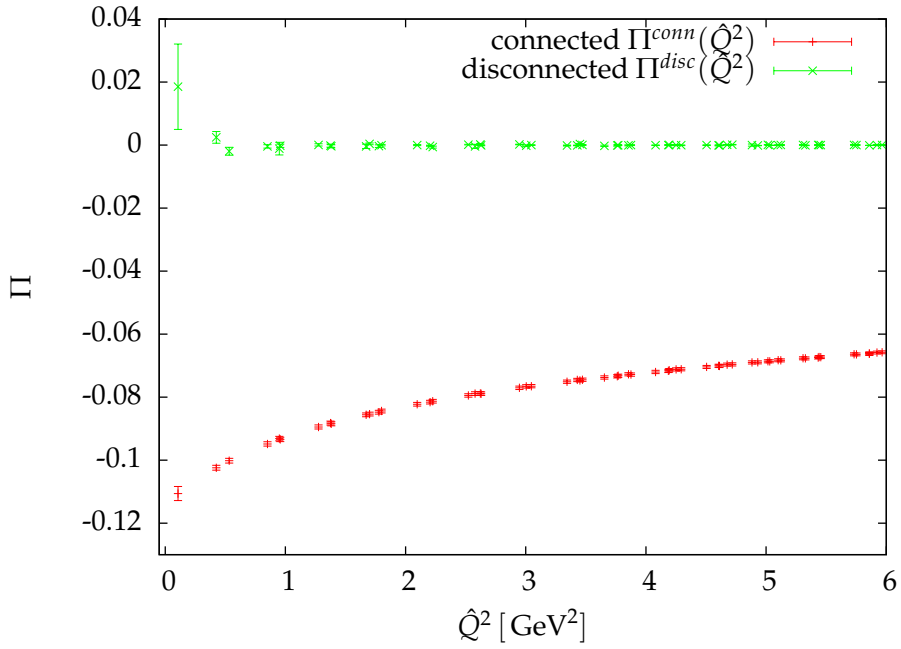

Figure 3.4: Example of unsubtracted vacuum polarization data, separated into connected (lower line) and disconnected part (upper line). The data is taken from ensemble B_2.

this framework the authors derived the relation

$$\frac{\Pi_R^{disc}(q^2)}{\Pi_R^{conn}(q^2)} = -\frac{1}{10} \qquad (\text{NLOPQ}\chi\text{PT})\,. \tag{3.49}$$

for the ratio of the subtracted disconnected to connected vacuum polarization function at next-to-leading order in chiral perturbation theory. As was discussed in the same work, this result is an approximation that may hold at small quark masses and small momenta and does not include the coupling to the vector resonances. It is thus a priori unclear how far such a result might be applicable in current lattice calculations given the accessible pion masses and lattice momenta. Yet, in the sense of the current discussion, this result assesses the quark-disconnected contribution as a 10% correction to the connected one in the region of applicability.

Notwithstanding the availability of these arguments we are convinced that a dedicated investigation of the quark-disconnected contribution, in particular with reference to the hadronic leading order muon anomaly, is worthwhile. Even if its magnitude is small as expected it would put us in a position to reliably estimate its impact on the (systematic) error budget of the lattice estimates.

We close the introduction to the calculational procedure by showing an exemplary data set taken from the ensemble B_2 (cf. table {3.4} for the details). The upper (lower) curve represents the unsubtracted disconnected (connected) contribution to the vac-

uum polarization $\Pi(\hat{Q}^2)$. The data will be discussed in more detail later on, but at this point we can observe the general quality of the data. We find that the connected contribution comes out as a smooth and rather accurate curve from the lattice calculation. On the other hand the estimate of the quark-disconnected contribution turns out to be consistent with zero beyond the smallest three lattice momenta. For the lowest three lattice momenta the values are still compatible with zero within errors, but the latter are sizeable compared to the ones of the connected vacuum polarization. Thus we anticipate for the summed, complete vacuum polarization data analysis that the disconnected contribution will not cause significant alterations over the connected contribution concerning the absolute values. But at the mentioned lowest momenta it does have an impact on the uncertainty and hence a careful analysis of the combined data in that regime has to be carried out in order to estimate the error budget of $\Pi(0)$ and the subtracted $\Pi(\hat{Q}^2) - \Pi(0)$.

3.4.3 Comparison to perturbative QCD

As a valuable cross check we can compare our lattice data for the renormalized vacuum polarization function with the prediction from perturbative QCD. Further on there are two other motivations for such a comparison: firstly, in application to the muon anomaly it was shown in reference [5] that the perturbative polarization function can be used in the integral definition of the leading order hadronic contribution for the integration of the high momentum tail. But only if a smooth transition from lattice data to the perturbative curve can be established. With regard to the second application we note that the comparison and matching of pQCD and lattice results for the polarization function is one source to extract the coupling and quark masses.

It is thus highly interesting to see what a comparison of LQCD and pQCD yields in the range of our available space like lattice momenta. To that end we use the results for the 3-loop and 4-loop vacuum polarization provided in [30, 7] and the 4-loop QCD β-function as given in [122, 31].

In figure [3.5] we show a comparison between lattice data for the vacuum polarization with 1-, 2-, 3- and 4-loop perturbation theory. We start from the large q^2 expansion of $\Pi(q^2)$ with $N_f = N_l + 1$ quark flavors comprising N_l massless quarks and one heavy quark flavor. The perturbative expansion then has the form

$$\begin{aligned} \Pi(q^2;\, \bar{\mu}) &= \sum_{l=0}^{L} \left(\frac{\alpha_s(\bar{\mu};\, \Lambda^{(2)}_{\overline{\text{MS}}})}{\pi} \right)^l \Pi^{(l)}(q^2;\, \bar{\mu}) \\ \Pi^{(l)}(q^2;\, \bar{\mu}) &= C^{(l)}_{m \leq n}(-q^2/\bar{\mu}^2)\, \log(-4z)^m \, \frac{1}{z^n} \,. \end{aligned} \tag{3.50}$$

The residual momentum dependence of the C-coefficients is via powers of the logarithmic term $\log(-q^2/\bar{\mu}^2)$. We use the standard notation $z = q^2/(4\bar{m}(\bar{\mu})^2)$, where $\bar{\mu}$ is the $\overline{\text{MS}}$ renormalization scale and $\bar{m}(\bar{\mu})$ is the heavy quark mass renormalized in the $\overline{\text{MS}}$ scheme. Quark mass corrections appear with negative integer powers of z. With the

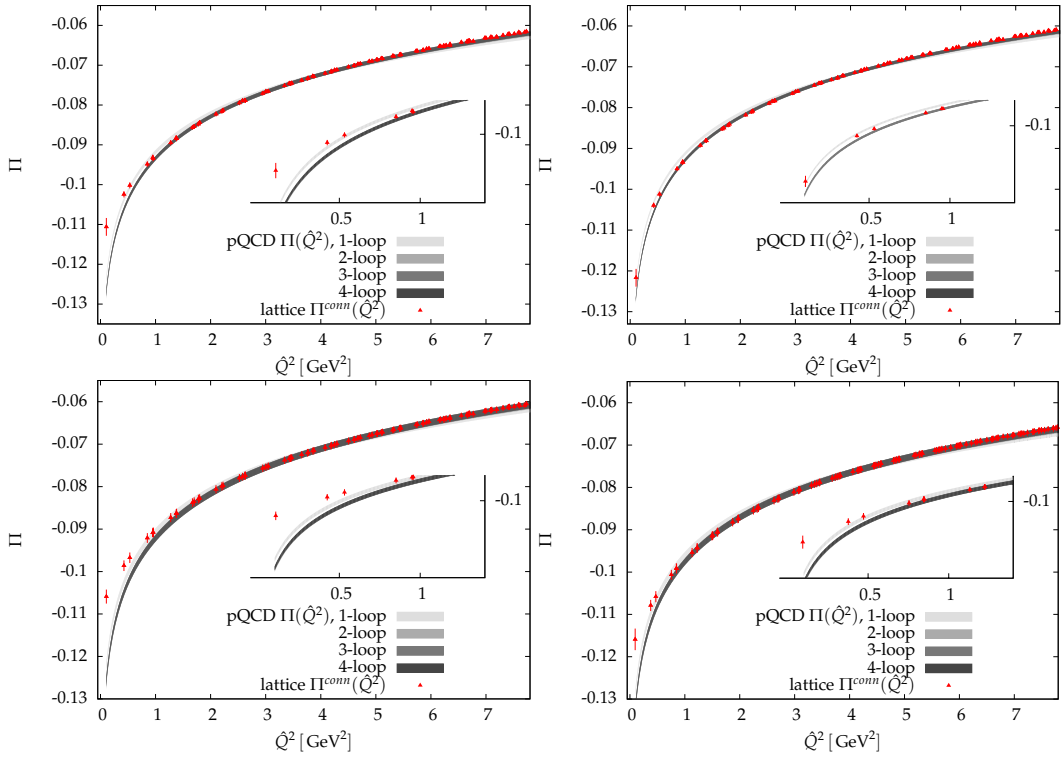

Figure 3.5: Exemplary comparison of lattice vacuum polarization data with 1-, 2-, 3- and 4-loop $\overline{\text{MS}}$ perturbation theory at $\bar{\mu} = 2\,\text{GeV}$. The lattice data originate from ensemble B_2 (upper left), B_1 (upper right), B_5 (lower left) and C_2; pQCD results from [7] are shifted by an ensemble dependent constant. The difference between 2-, 3- and 4-loop pQCD is unresolvable.

quark masses from table {3.4} we deduce that even for the largest quark mass we have $m_q^2/Q^2 \lesssim 0.01$ at $Q^2 = 1\,\mathrm{GeV}^2$ and we check that all such contributions are negligible. Since this is an expansion valid for $\bar{m}^2/Q^2 \ll 1$ we can use this approximation in the well-defined limit $\bar{m} \to 0$ in which only the $C_{00}^{(l)}$ coefficient survives and the remaining momentum dependence is given by the logarithms $\log(-q^2/\bar{\mu}^2)$. The $\overline{\mathrm{MS}}$ strong coupling constant α_s at renormalization scale $\bar{\mu}$ is calculated from the 4-loop β-function [30]. We use the iterative solution of the β-function correct up to terms of $O\left(1/\log(\bar{\mu}^2/\Lambda^2_{\overline{\mathrm{MS}}})^5\right)$ as given in reference [31]. The value of $\Lambda^{(2)}_{\overline{\mathrm{MS}}}$ for 2-flavor QCD has been calculated in [40][3]. Both the lattice and perturbative result for Π have to be additively renormalized, $\Pi_R(\hat{Q}^2) = \Pi(\hat{Q}^2) - \Pi(0)$, by removing the divergent value at zero momentum. Note that with the above notation $\hat{Q}^2 = -q^2$. $\Pi(0)$ cannot be obtained from the perturbative calculation, so we implicitly use the value obtained from the lattice calculation: we determine an additive shift δ between the lattice and perturbative data by finding the optimum shift that minimizes the difference between them in the momentum interval $3.5\,\mathrm{GeV}^2 \leq \hat{Q}^2 \leq 4.5\,\mathrm{GeV}^2$.

$$\begin{aligned} \Pi_{\mathrm{pQCD}}(\hat{Q}^2) &= \Pi_{\mathrm{lQCD}}(\hat{Q}^2) + \delta \\ \Pi_{\mathrm{R,\,pQCD}}(\hat{Q}^2) &= \Pi_{\mathrm{pQCD}}(\hat{Q}^2) - \Pi_{\mathrm{lQCD}}(0) - \delta\,. \end{aligned} \tag{3.51}$$

Looking at the upper left panel of figure [3.5] we remark that with such a choice of an optimized δ the agreement around $\hat{Q}^2 = 4\,\mathrm{GeV}^2$ is implied, yet the agreement towards higher and lower momentum is significant. It represents the data for ensemble B_2 but the observation of good agreement of perturbative and non-perturbative results in the range $1\,\mathrm{GeV}^2 \leq \hat{Q}^2 \leq 6\,\mathrm{GeV}^2$ is valid for all ensembles. The uncertainty of the perturbative curves stem from the variation of $\Lambda^{(2)}_{\overline{\mathrm{MS}}} = 0.245\,(23)\,\mathrm{GeV}$. The renormalization scale has been chosen as $\bar{\mu} = 2\,\mathrm{GeV}$, which will lead to small logarithmic contributions in the matching region. At even smaller momenta the divergent perturbative $\log(\hat{Q}^2/\bar{\mu}^2)$ terms cause the steeper slope of the pQCD result. At the opposite end, $\hat{Q}^2 \gtrsim 6\,\mathrm{GeV}^2$ lattice artifacts have an increasingly significant impact and cause the growing disagreement at larger $\hat{Q}^2$. The momentum range, where agreement of the perturbative and non-perturbative polarization function prevails, is in principle dependent on the quark mass μ_0, the lattice spacing a and the lattice size L. Since we compare to pQCD with massless quarks, the agreement towards lower momenta will be the better, the smaller the quark mass in the lattice calculation, provided the lattice volume remains sufficiently large such that finite volume effects do not take over. We find this notion confirmed in the upper right and lower left panel of figure [3.5]: we display the analogous comparison for the ensembles B_1 and B_5 which have the smallest and largest available quark mass for the lattice spacing $a = 0.079\,\mathrm{fm}$ and lattice size $L = 1.9\,\mathrm{fm}$, respectively. The B_1 data virtually agrees with the 4-loop formula (modulo the additive shift) even below

[3] Meanwhile an updated value has been presented in [61]: $\Lambda^{(2)}_{\overline{\mathrm{MS}}} = 0.310\,(20)\,\mathrm{GeV}$. For our purpose of illustration we stick with the previous version at this point.

momenta of $\hat{Q}^2 = 1\,\mathrm{GeV}^2$, whereas the B_5 data shows a discrepancy of about one standard deviation already around this point. At large momentum a smaller lattice spacing should cause weaker lattice artifacts and thus the coincidence should prevail to higher momenta. We can check for this behavior with the help of the lower right panel of figure [3.5], where we plot another comparison using the C_2 ensemble data. The assessment is slightly hampered by the larger statistical error of the data. Yet we find full agreement of the central values with the perturbative results also beyond $\hat{Q}^2 = 7\,\mathrm{GeV}^2$.

In conclusion we find good agreement of lattice data and massless $N_f = 2$ perturbation theory for momentum values starting surprisingly low at $\hat{Q}^2 \gtrsim 1.5\,\mathrm{GeV}^2$. Moreover, we observe that we cannot significantly discriminate the 3- and 4-loop pQCD vacuum polarization result in the region of interest displayed in figure [3.5]. Yet only the full 4-loop result will contain the lowest order quark-disconnected contribution. This corroborates our conception of a non-significant change of the absolute value of the vacuum polarization data when including the disconnected piece at least for $\hat{Q}^2 \gtrsim 1.5\,\mathrm{GeV}^2$. The modifications at lowest momenta in a combined analysis remain to be investigated.

3.5 Temporal moments of the polarization function

Up to now we described how we estimate a polarization function for a set of discrete lattice momenta. One constraint in this kind of calculation is that the momentum cannot be zero, because to extract the polarization function itself we need to divide by a power of the square of the 4-momentum. There are situations where the derivatives of the polarization functions are required. The Adler function is one example: it is the logarithmic derivative of $\Pi^v(q^2)$ and would require to know the derivative at all momenta. Another example is the heavy quark vacuum polarization Π_h. As mentioned earlier, in pQCD it can be expanded in a neighborhood of the origin in a series in $z = q^2/(4\bar{m}_h^2)$. Thus derivatives of Π_h at the origin are proportional to powers of the renormalized heavy quark mass. Determining the derivatives from taking discrete derivatives of the lattice vacuum polarization data suffers from the low density of momenta in the region of low momenta. There the gaps between neighboring lattice momenta and to the origin are $O\left((2\pi/L)^2\right)$. This amounts to $0.4\,\mathrm{GeV}^2$ for a typical lattice of size $L = 2\,\mathrm{fm}$. Another common possibility would be to fit $\Pi(q^2)$, extrapolate it to zero momentum and take the derivative from the fit function. This introduces systematic dependencies on the choice of a fit function, fit ranges, the goodness of the fit, etc..

An economic way to estimate derivatives of the polarization functions at zero momentum has been put forward in reference [2]. This method relies on the fact that via

the Fourier transform and at zero spatial momentum we have the correspondence

$$\left(\frac{d}{dq^2}\right)^n\Bigg|_{q^2=0} = \left(\frac{1}{2q_0}\frac{d}{dq_0}\right)^n\Bigg|_{\vec{q}=0,\, q_0=0}$$

$$\frac{d^m \tilde{f}}{d\, q_0^m}(q_0=0) \leftrightarrow \int_{-\infty}^{\infty} t^m f(t)\, dt\,. \tag{3.52}$$

Note that if in particular we have a function $\tilde{f}(q_0^2)$ we can write

$$\frac{d\,\tilde{f}}{d\,q_0^2}\bigg|_{q_0=0} = \frac{1}{2}\frac{d^2\,\tilde{f}}{d\,q_0^2}\bigg|_{q_0=0}\,.$$

This is the case for our applications. Due to its form the right-hand side of equation (3.52) has been termed temporal moment of $f(t)$.

On the lattice we define analogous lattice moments starting from the current correlators at zero spatial momentum:

$$G_n^{\delta,\kappa} = a^6 \sum_{t/a=-(T/(2a)-1)}^{T/(2a)-1} (t/a)^n \langle J^{\delta,\kappa} J^{\delta,\kappa}(t,\, \vec{q}=0)\rangle\,. \tag{3.53}$$

We use the multiplicatively renormalized currents in equation (3.53) (cf. table (3.10)). Since the contribution from $t = 0$ has zero weight, the contribution from coinciding spacetime points is excluded and we have correctly renormalized moments G_n. The factors of the lattice spacing are to make the lattice moments dimensionless. By periodicity we can average the current correlators at t and $-t \sim T - t$. Odd moments will vanish since the correlators are even with respect to time reversal, whereas an odd power of t changes sign. For the even moments we get

$$G_{2n}^{\delta,\kappa} = 2\,a^6 \sum_{t/a=1}^{T/(2a)-1} (t/a)^{2n} \langle J^{\delta,\kappa} J^{\delta,\kappa}(t,\, \vec{q}=0)\rangle^{av} \tag{3.54}$$

$$\langle J^{\delta,\kappa} J^{\delta,\kappa}(t,\, \vec{q}=0)\rangle^{av} = \frac{1}{2}\left(\langle J^{\delta,\kappa} J^{\delta,\kappa}(t,\, \vec{q}=0)\rangle + \langle J^{\delta,\kappa} J^{\delta,\kappa}(T-t,\, \vec{q}=0)\rangle\right)\,. \tag{3.55}$$

The correspondence of taking derivatives with respect to q_0 and integrating with powers of t is only exact in the continuum. As usual the lattice definition (3.53) will be affected by the discretization of the integral (non-zero lattice spacing) and the finite volume and time extent. The impact of changing spatial volume and lattice spacing must be checked by comparing results from different lattice simulations. Another question that immediately comes to mind is whether the G_n are well defined when it comes to the cut-off in the t-summation. To sketch the situation we can assume that the current correlator is replaced by a series of exponentials with ascending energies. The integrand

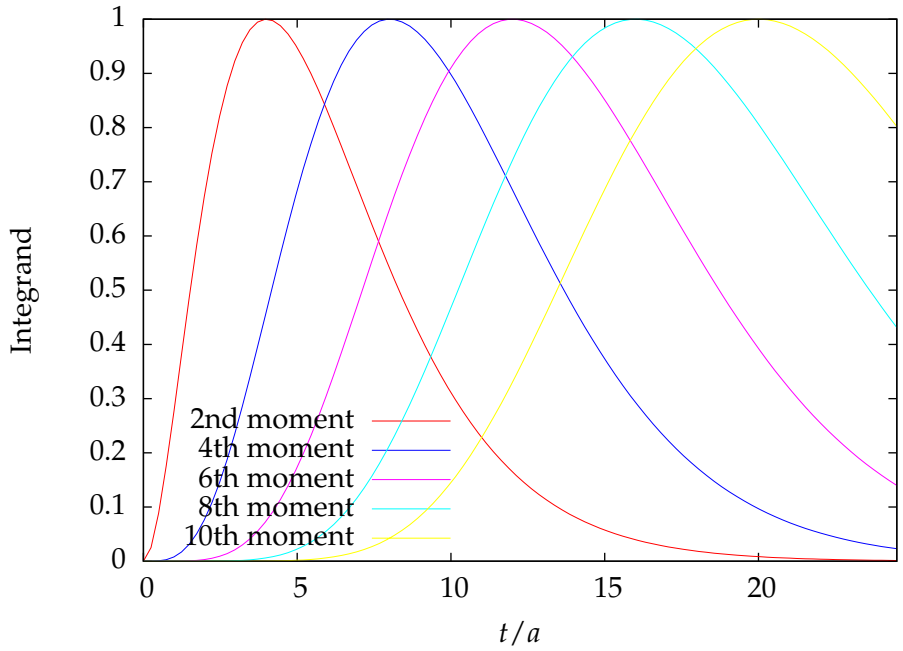

Figure 3.6: Contribution of a single exponential to the integrand in eq. (3.53).

thus consists of terms of the form $t^n \exp(-tE_l)$. The larger the energy of the state $|l\rangle$ related to the exponential and the lower the power n, the better the integral will be saturated in the finite summation. The opposite can happen if the asymptotic behavior of the correlator is dominated by a very light state of if we are interested in higher moments. Note that $t^n \exp(-tE_l)$ has a maximum at n/E_l. Thus for any correlator there will be a maximal n for which a moment can be reasonably defined. These issues are depicted in figure [3.6]. The energy in lattice units is chosen as $aE = 0.5$. The curves are normalized to 1 at their maximum. We see that in this example moments with $n = 8$, 10 are not well defined on this lattice with time extent $T = 24a$. This is usually only a problem in the light quark sector. The energy chosen is in the range of the mass of the lightest vector meson state we measure for our ensembles. On the contrary, in the charm (valence) sector individual moments for n as high as 20 can be estimated reliably from the lattice data.

From the position of the maximum and the general shape of the curves we deduce further that the lower/higher the order of the moment, the more sensitive the moment is to the short/long-distance physics encoded in the correlator. Or the lower the moment, the more perturbative its character. In fact, the lowest 8 moments have been calculated exactly for a heavy valence quark in continuum perturbation theory to 4-loop order.

The expansion around the origin for the charm valence quark reads

$$\Pi_c(q^2) = \frac{3}{16\pi^2} \sum_{n\geq 0} \left(\frac{q^2}{4\bar{m}_c^2}\right)^n C_n \tag{3.56}$$

$$C_n = \sum_{k\geq 0} \left(\frac{\alpha_s}{\pi}\right)^k \sum_{0\leq l\leq k} C_n^{kl}(n_l)\, \log^l(\bar{m}_c^2/\bar{\mu}^2)$$

$$\alpha_s = \alpha_s(\bar{\mu}, n_f)\,.$$

The C_n^{kl} are real numbers that depend on the type of current correlator and the number of massless sea quarks. Typically, one will have one heavy quark and three massless sea quarks (charm + massless up, down and strange) or one massive and four massless quarks in case of a bottom quark as valence quark. The relationship between the lattice moments G_n and coefficients C_n reads

$$G_{2n+2} = \frac{3}{16\pi^2}\,(2n+2)!\,\frac{C_n}{(2a\bar{m}_c)^{2n}} \;+\; \text{lattice artifacts}\,. \tag{3.57}$$

The pQCD community defines their own moments which have a slightly different notation that we want to mention here. The moments M_n are defined as

$$M_n = \frac{12\pi^2}{(n)!}\left(\frac{d}{dq^2}\right)^n \Pi_c\Big|_{q^2=0} = \frac{9}{4}\,\frac{C_n}{(4\bar{m}_c^2)^n}\,. \tag{3.58}$$

$$G_{2n+2} = \frac{1}{12\pi^2}\,(2n+2)!\,a^{-2n}\,M_n\,. \tag{3.59}$$

$$\tag{3.60}$$

Note that factors of couplings, like for instance the electromagnetic charges Q_f^{em} of the quark flavors f building J^{em}, are kept as explicit factors and are not part of the coefficients C_n

In case of the pseudoscalar and scalar moments we can make use of the tmLQCD specific renormalization pattern of the twisted quark mass $\mu_R(\bar{\mu}) = \mu_0/Z_P(\bar{\mu})$ and build

the modified renormalized moments

$$\begin{aligned}\tilde{G}^{p}_{2n+4} &= (2a\mu_0)^2\, 2\, a^6 \sum_{t/a=1}^{T/(2a)-1} (t/a)^{2n+4} \langle P\, P\, (t,\, \vec{q}=0)\rangle^{av} \\ &\to \frac{3}{16\pi^2}\,(2n+4)!\,\frac{C_n}{(4a\bar{m}_c^2)^n} \;+\; \text{lattice artifacts} \qquad (3.61)\\ \tilde{G}^{s}_{2n+4} &= (2a\mu_0)^2 \left(\frac{Z_S}{Z_P}\right)^2 2\, a^6 \sum_{t/a=1}^{T/(2a)-1} (t/a)^{2n+4} \langle S\, S\, (t,\, \vec{q}=0)\rangle^{av} \\ &\to \frac{3}{16\pi^2}\,(2n+4)!\,\frac{C_n}{(4a\bar{m}_c^2)^n} \;+\; \text{lattice artifacts} \qquad (3.62)\end{aligned}$$

In equation (3.61) we use the fact, that the bare operator $\mu_0 P$ is renormalization group invariant, i.e. $\mu_0 P = [m_q P]_R$. The advantage of the combination in equation (3.62) lies in the appearance of the ratio Z_P/Z_S, instead of only Z_S as the renormalization factor of the scalar current. In contrast to $Z_S = Z_S(\bar{\mu})$ the scale dependence cancels in the ratio Z_P/Z_S [32]. With this variation together with the vector and axial vector moments the scalar and pseudoscalar moments remain scale invariant lattice quantities.

We note that with equations (3.61) and (3.62) we potentially mix the non-singlet and singlet renormalization constants. For instance equation (3.61) is only rigorously true if $P = P^{\pm}$ is the charged pseudoscalar field. The non-singlet vector Ward identity in the twisted basis guarantees renormalization group invariance with the identification $Z_\mu = 1/Z_P^{NS}$. However, when studying moments of the charm correlators, we are interested in currents $\bar{c}\,\Gamma\, c$, which are not from the non-singlet sector. We then either rely on the degeneracy of the (spurious) heavy doublet and consider appropriate operators $\bar{\chi}_h^{\pm}\,\Gamma'\,\chi_h^{\mp}$, which renormalize with the non-singlet Z-factors. Or we use operators with flavor structure τ^3 in the heavy quark sector. These differ from the singlet case only by (small) quark-disconnected contributions, but can again be renormalized by the non-singlet factors.

Finally, the scale invariant Z-factors become unity in the continuum limit. So one might ultimately think about leaving them out of the lattice operators, as long as a well-supported continuum limit is taken. However, by this procedure we would lose the suppression of lattice artifacts and the scaling properties of the lattice moments in the continuum limit would become worse.

3.6 Lattice vacuum polarization with continuous external momentum

In the previous section we showed that we can estimate derivatives of a polarization function by temporal moments of the corresponding current correlator. A particularly

useful application arises for the correlator of the conserved vector current

$$\Pi^{\mathrm{em}}(0) = \frac{1}{6}\sum_{i=1}^{3}\sum_{t/a}^{t_{\max}} (t/a)^2 \langle J_i^{\mathrm{em}} J_i^{\mathrm{em}}(t,\vec{q}=0)\rangle\,. \tag{3.63}$$

$$\frac{d\,\Pi^{\mathrm{em}}}{d\,\hat{K}^2}(0) = \frac{1}{72}\sum_{i=1}^{3}\sum_{t/a}^{t_{\max}} (t/a)^2 \left(1-(t/a)^2\right) \langle J_i^{\mathrm{em}} J_i^{\mathrm{em}}(t,\vec{q}=0)\rangle\,. \tag{3.64}$$

$\Pi^{\mathrm{em}}(0)$ is required for the subtraction of the vacuum polarization, whereas the derivative at zero momentum can be shown to be strongly related to the leading order hadronic anomalous magnetic moment of the electron. The definition (3.63) uses a sum with a power of t to define the momentum derivative. This corresponds to derivatives with respect to K. The lattice Π^{em} is a function of $\hat{K} = 2\sin(K/2)$ and we have

$$\begin{aligned}
\xi(\hat{K}) &= \frac{d\,K}{d\,\hat{K}}(\hat{K}) = \frac{1}{\sqrt{1-(\hat{K}/2)^2}} \\
\xi(0) &= 1 \\
\frac{d\,\xi}{d\,\hat{K}}(0) &= 0 \\
\frac{d^2\,\xi}{d\,\hat{K}^2}(0) &= \frac{1}{4} \\
\left(\frac{d}{d\,\hat{K}}\right)^2 &= \left(\frac{d\,\xi}{d\,\hat{K}}\right)\frac{d}{d\,K} + \xi^2\,\frac{d^2}{d\,K^2} \overset{\hat{K}=0}{\to} \frac{d^2}{d\,K^2} \\
\left(\frac{d}{d\,\hat{K}}\right)^4 &= \left(\frac{d^3\xi}{d\hat{K}^3}\right)\frac{d}{d\,K} + 4\left(\frac{d^2\xi}{d\hat{K}^2}\right)\xi\,\frac{d^2}{d\,K^2} + 3\left(\frac{d\xi}{d\hat{K}}\right)^2\,\frac{d^2}{d\,K^2} \\
&\quad + 6\left(\frac{d\xi}{d\hat{K}}\right)\xi^2\,\frac{d}{d\,K^3} + \xi^4\,\frac{d}{d\,K^4} \\
&\overset{\hat{K}=0}{\to} \frac{d^2}{d\,K^2} + \frac{d^4}{d\,K^4}\,.
\end{aligned} \tag{3.66}$$

Note that in the t-sum we differentiate the correlator, not Π itself. Recalling the correspondence $d/dK \leftrightarrow it$ we thus use (up to normalization) t^2 for the second and $t^2(a^2-t^2)$ for the fourth derivative with respect to $\hat{K}^2$, which lead to the first and second derivative with respect to $\hat{K}^2$ of the polarization function.

Having the derivatives of the polarization function at zero spatial momentum we can use the analytic properties of the polarization functions and sum them to all orders. This brings us to view the exponential $\exp(iq_0\,t)$ in the Fourier transform as the derivative operator

$$\int dt \exp(iK\,t) = \exp\left(iK\frac{d}{dq_0}\right), \tag{3.67}$$

which defines the value of a function of q_0 at K, if the series defined by eq. (3.67) converges at K. Since the current correlators we look at are of the form $q^2\,\Pi(q^2)$ we must subtract the first term in the exponential series. Moreover, if we are interested in the renormalized vacuum polarization we must also subtract the second term. We thus write

$$\begin{aligned}\Pi^{\delta,\kappa}(\hat{K}^2) &= \sum_{t/a=-t_{\max}}^{t_{\max}} \frac{e^{iKt}-1}{\hat{K}^2}\,\langle J^{\delta,\kappa}\,J^{\delta,\kappa}(t,\vec{q}=0)\rangle \\ &= \sum_{t/a=1}^{t_{\max}} \frac{4\,\sin^2(Kt/2)}{\hat{K}^2}\,\langle J^{\delta,\kappa}\,J^{\delta,\kappa}(t,\vec{q}=0)\rangle^{av} \qquad (3.68)\\ \Pi_R^{\delta,\kappa}(\hat{K}^2) &= \sum_{t/a=1}^{t_{\max}} \left(\frac{4\,\sin^2(Kt/2)}{\hat{K}^2} - t^2\right)\langle J^{\delta,\kappa}\,J^{\delta,\kappa}(t,\vec{q}=0)\rangle^{av}\,. \qquad (3.69)\\ \hat{K} &= 2\sin(K/2) \qquad (3.70)\end{aligned}$$

Starting with this section we have left open the upper summation limit $t_{\max} \le T/2 - a$. This is required to optimize the definition with respect to the noisy large-time behavior of the actual lattice correlators. As a general rule of thumb we extend the sum up to the point, where the correlation function becomes zero within errors, if such a t-value exists. From this point on the central value will stabilize within errors, but the polarization function will continue to pick up noise reflected in a growing statistical uncertainty.

The kernel function $f_t(\hat{K}^2) = \sin^2(Kt/2)/\sin^2(K/2)$ is depicted in figure [3.7] for several values of t. Note that $0 \le \hat{K} \le 2$ for real $\hat{K}$ and in physical units the squared momentum takes values $0 \le Q^2 = \hat{K}^2/a^2 \le 4/a^2$. In the appendix 4 we remind ourselves in a few steps that for non-negative integer $t/a = l$ the function f_t satisfies

$$f_t(\hat{K}^2) = \hat{K}^2\,P_l(\hat{K}^2) \qquad (3.71)$$

with a polynomial P_l of degree $l-1$. The cases $l = 2,\ldots,6$ shown in figure [3.7] are listed in the appendix (35). The curves are normalized to 1 at the origin. Their first root is at $\hat{K}_0^2 = 4\sin^2(\pi a/t)$ and moves towards the origin with increasing t/a. In a rough characterization, coming from larger momentum they are close to zero up to the first exact root and then rise sharply to their maximal value $(t/a)^2$ at $\hat{K}^2 = 0$. We shall remember this when we perform the integration of Π_R^{em} for the hadronic leading order contribution to the muon anomalous magnetic moment: the large time behavior of the correlator mostly fine-tunes the low-momentum shape of the polarization function which is of significant impact.

The advantage of the definitions in equation (3.69) is that we can define the subtracted polarization function for any momentum value in the mentioned limits without a fit, extrapolation or interpolation. We can also define derivatives the same way. For

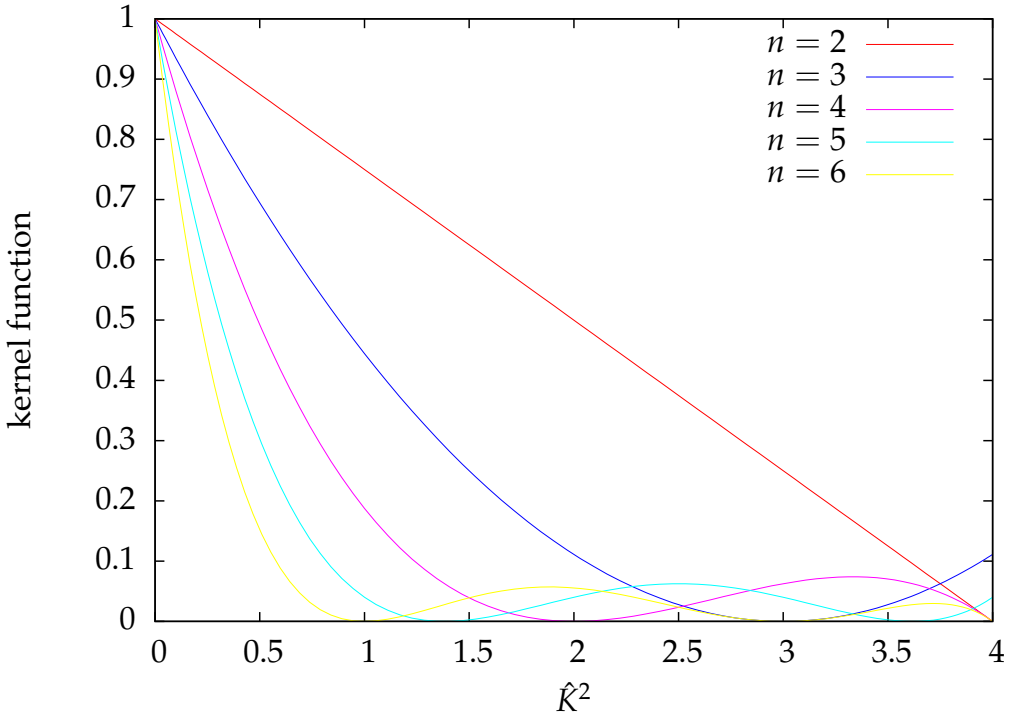

Figure 3.7: Kernel function $f(\hat{K}^2)$ for $t/a = 2, \ldots, 6$.

instance using the electromagnetic current correlator, we can define the Adler function

$$\begin{aligned} D(\hat{K}^2) &= \hat{K}^2 \frac{d}{d\hat{K}^2} \Pi^{\mathrm{em}}(\hat{K}^2) \\ &= \sum_{t/a=1}^{t_{\max}} \frac{4 \sin^2(Kt/2)}{\hat{K}^2} \left(\frac{t \tan(K/2)}{\tan(tK/2)} - 1 \right) \langle J_i^{\mathrm{em}} J_i^{\mathrm{em}}(t, \vec{q} = 0) \rangle^{av} . \end{aligned} \tag{3.72}$$

The kernel functions in equations (3.69) and (3.72) can be continued to imaginary momentum values iK with consequently $\hat{Q}^2 = -\hat{K}^2 \leq 0$.

$$\Pi_R^{\delta,\kappa}(\hat{Q}^2 = -\hat{K}^2) = \sum_{t/a=1}^{t_{\max}} \left(\frac{4 \sinh^2(Kt/2)}{\hat{K}^2} - t^2 \right) \langle J^{\delta,\kappa} J^{\delta,\kappa}(t, \vec{q} = 0) \rangle^{av} . \tag{3.73}$$

$$D(\hat{Q}^2 = -\hat{K}^2) = \sum_{t/a=1}^{t_{\max}} \frac{4 \sinh^2(Kt/2)}{\hat{K}^2} \left(\frac{t \tanh(K/2)}{\tanh(tK/2)} - 1 \right) \langle J_i^{\mathrm{em}} J_i^{\mathrm{em}}(t, \vec{q} = 0) \rangle^{av} \tag{3.74}$$

$$\hat{Q} = i\hat{K} = 2 \sin(iK/2) = i\, 2 \sinh(K/2) .$$

For imaginary momentum squared the kernel function rises exponentially with t/a. Due to the finite upper limit in the t-sum we can apply these definitions for any value

of $\hat{K}$. But in order to be meaningful we must have $|\hat{Q}|$ at least smaller than the ground state energy of the lightest state present in the expansion of the correlator.

In the new definitions we use time dependent correlators at zero spatial momentum. So potentially we do not have to calculate the complete polarization tensor in momentum space. We can use the usual correlators from point sources or even stochastic timeslice sources that have been produced on numerous occasions while studying the meson spectrum.

3.7 Comparison of vacuum polarization definitions

3.7.1 Light quark sector

For a detailed comparison we will again use the vector current correlator as an example. In figure [3.8] we compare the lattice vacuum polarization data with the definition via the t-summation. We find full agreement of both definitions with only a slight deviation at the upper momentum limit, where $K \approx \pi/a$ and we approach a corner of the Brillouin zone. We then must anticipate lattice artifacts to be more visible. Comparing B_2 and C_2 we find that this effect is suppressed for the smaller lattice spacing.

To check the saturation of the t-sum we look at figure [3.9]. In the upper panel we show the value of $\Pi(0)$ depending on the upper summation limit $t_{max}/a \leq T/(2a) - 1$. The formulas for these two cases were stated in equations (3.63) and (3.64) above. The summation seems to be saturated for all ensembles except B_1 and B_7, where the central value is still decreasing at the end of the summation window. But within the statistical accuracy in those two examples we can identify a plateau. From the same plot we deduce that we indeed have to use t-sums for the extension to continuous momenta: the same procedure can be carried out for a component of the spatial momentum. But we would sum only up to $L/(2a) - 1 = T/(4a) - 1$ and the sums are not saturated at this point, which leads to a significantly altered curvature of the polarization function. The situation changes when considering the derivative $d\Pi/d\hat{K}^2(0)$. Ensembles B_1, B_6 and B_7 clearly show finite-T effects. However, for B_1 and B_6 the sums are still saturated within the statistical uncertainty, whereas for B_7 this is no longer the case.

As an example application we show the continuous subtracted polarization function and the Adler function for ensemble B_2 in figure [3.10].

3.7.2 Heavy quark sector

If we consider the charm vector current correlator, we can use the perturbative expansion around $Q^2 = 0$ in a neighborhood of the origin, which is well defined for all spacelike momenta and timelike momenta as long as $-Q^2 < m_{J/\psi}^2 \approx 9\,\mathrm{GeV}^2$ is fulfilled. To compare to the approximation in equation (3.56) we further need to ensure that $|z| \ll 1$ or $|Q^2| \ll 4\bar{m}_c^2$. The charm quark mass is of the order of 1 GeV and therefore we choose a window $-1\,\mathrm{GeV}^2 \leq Q^2 \leq 1\,\mathrm{GeV}^2$ for our comparison. Of course we need to keep in mind that the lattice curve we show is affected by lattice artifacts, which are sizeable in the charm sector due to the large value of the quark mass. Moreover, we approximate

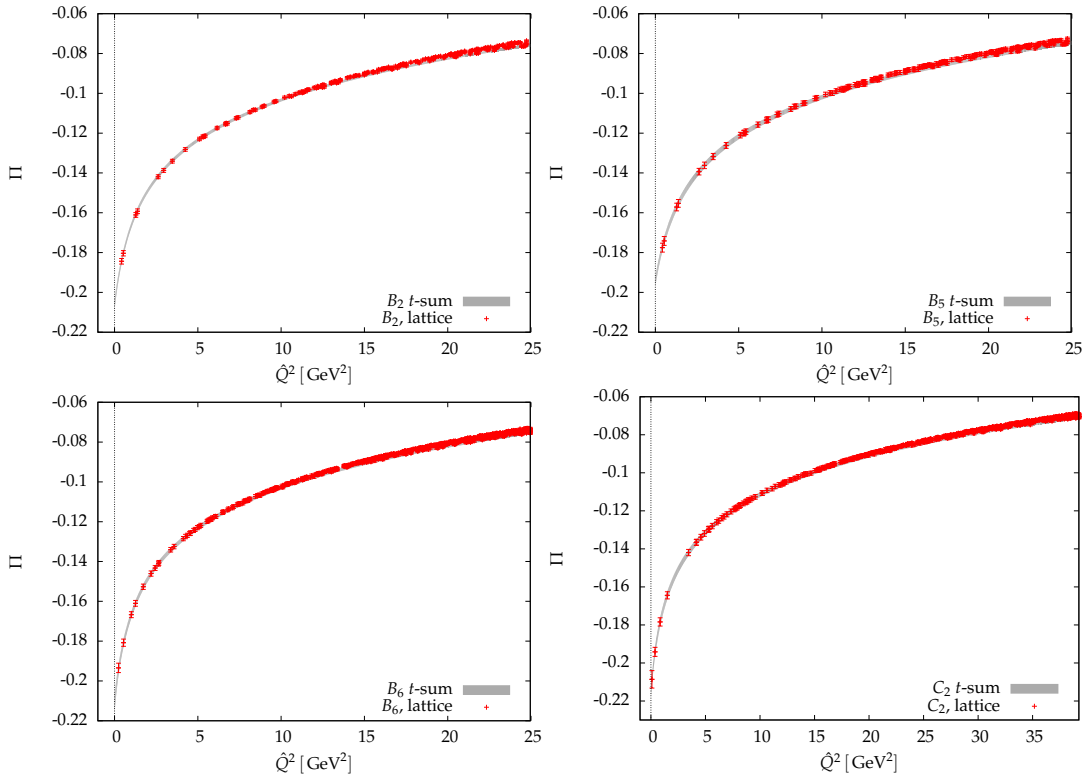

Figure 3.8: Four examples for the comparison of lattice vacuum polarization with t-integration.

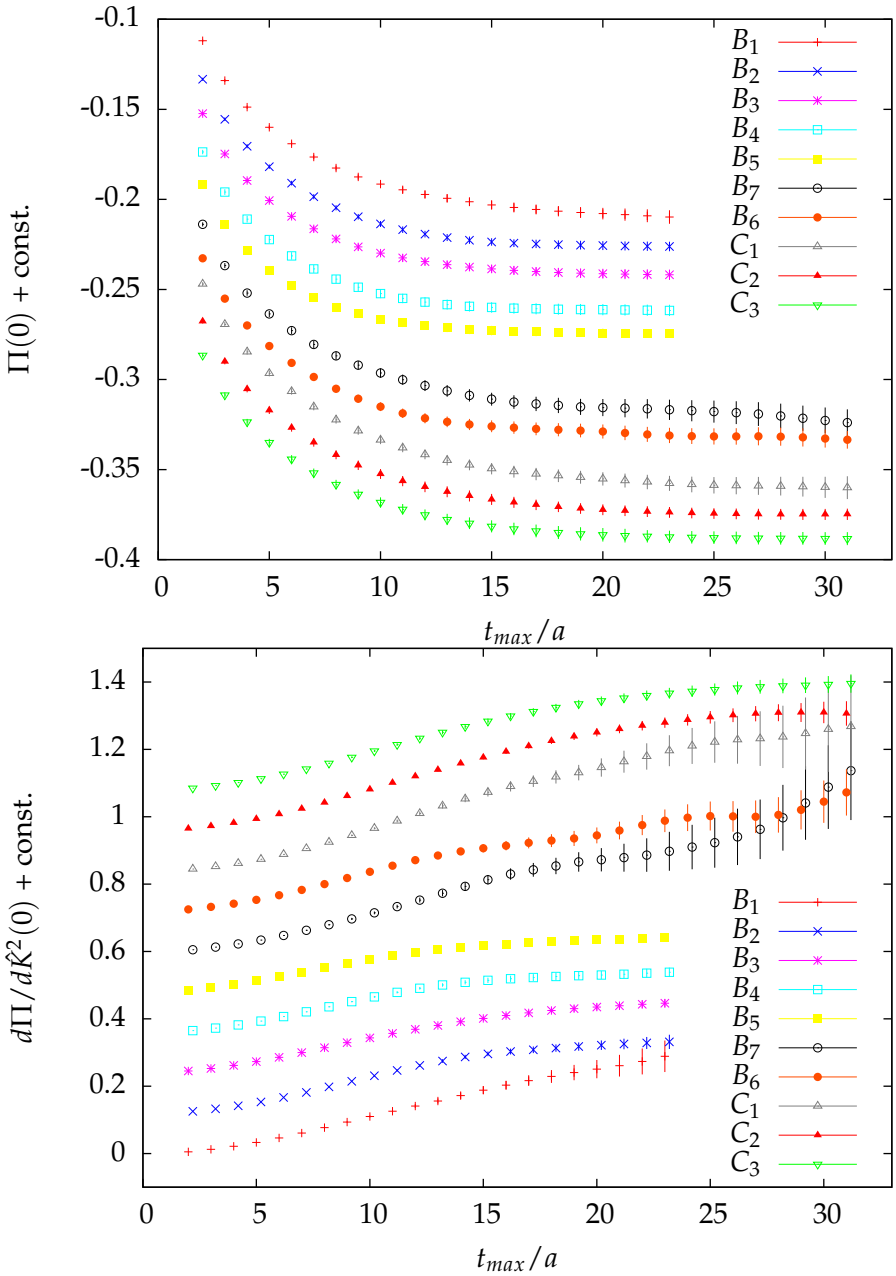

Figure 3.9: Dependence of $\Pi(0)$ (top) and $d\Pi/d\hat{K}^2(0)$ (bottom) on the upper limit $t_{\max}$ of the t-sum. The curves have been shifted by a constant.

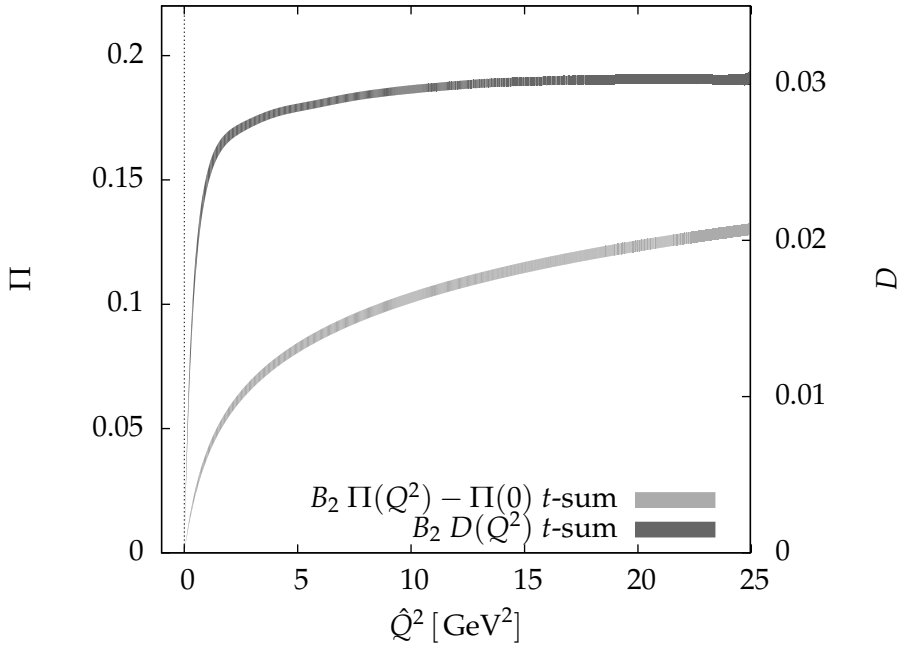

Figure 3.10: Continuous subtracted vacuum polarization (left vertical axis) and Adler function (right vertical axis) for ensemble B_2.

the pQCD curve by the polynomial of order 3 in z. We use the pQCD results from SFB TR9 provided in [96] (and references therein): it lists the perturbative C coefficients in all generality decomposed into contributions from the massless, heavy and mixed sector such that we can best approximate the model we use in our lattice calculation, that includes one charm (heavy) and two light (approximately massless) quarks. [4]

We check for rough agreement for reasonable values of the charm quark mass and strong coupling. In a thorough analysis we would tune the valence charm quark mass and take the continuum limit. Moreover, we would compare derivatives at the origin directly instead of polynomial approximations of finite order. The pQCD curve has two parameters, α_s and $\bar{m}_c$. We fix the strong coupling to $\alpha_s(\bar{\mu} = 2\,\text{GeV}, \Lambda^{(2)}_{\overline{\text{MS}}})$ and tune the quark mass by hand to get good overlap of the curves. We take one ensemble from each lattice spacing, B_2, C_1 and D_1 and the smallest bare valence charm quark mass in each case. The results are shown in figure [3.11]. We find agreement for the pQCD and t-summed polarization function in the chosen interval. From our point of view the simultaneous consistency for both positive and negative values of $\hat{Q}^2$ by adjusting one parameter only is non-trivial. In the t-sum the time dependence in the kernel function changes from sine to hyperbolic sine, while we sum with the same lattice correlator. But these two functions give a very different weight to the different time regions. The first one oscillates with constant amplitude, while the second one grows exponentially with

[4] For the charm quark we use the valence approximation on the lattice. But we keep the charm sea effects in the perturbative formula, since they are a small effect, that we do not resolve here.

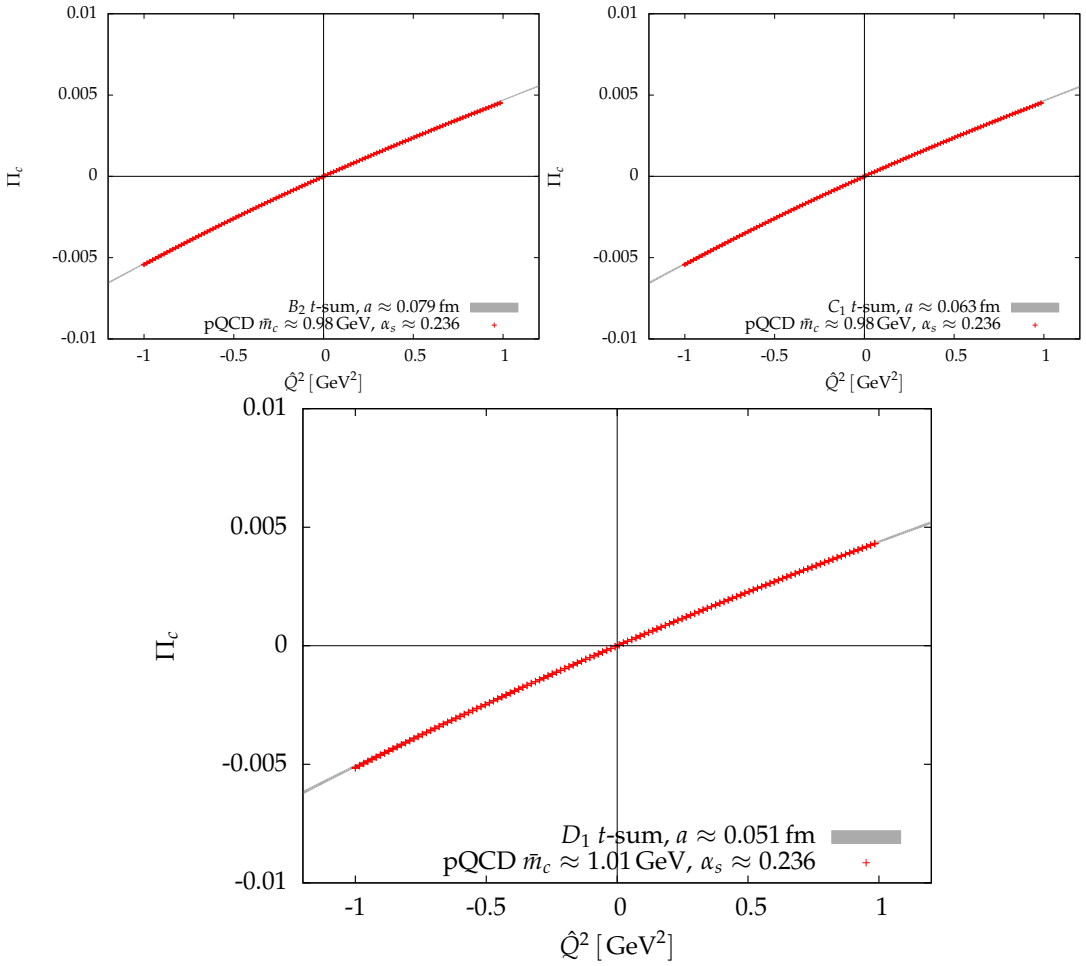

Figure 3.11: Comparison of pQCD and t-summed charm vacuum polarization around the origin.

t. Typically, the signal to noise ratio of lattice correlators decreases towards large times, which makes the estimation for negative $\hat{Q}^2$ more difficult.

3.7.3 Correlators from local current operators

We went from using the complete vacuum polarization tensor in momentum space to the zero momentum time dependent correlators to generate the polarization function. For Π^v we have so far used the 1-point split conserved vector current. There are two other prevalent choices for correlators: local correlators from point sources and from stochastic timeslice sources. Since the local currents are not conserved, they need to be normalized with corresponding renormalization factors. For the time being we use ensemble-wise determined values for Z_V from the ratio conserved (J^c) over local (J^l) vector current correlator. This goes along the lines of the procedure named alternative method in reference [32], where the non-singlet vector Ward identity was exploited and thus a different pair of correlators was used.

$$r_{ll}^{cc}(t) = \left(\frac{\sum_{i=1}^{3} \sum_{\vec{x}} \langle J_i^c(t,\vec{x})\, J_i^c(0,0)\rangle^{av}}{\sum_{i=1}^{3} \sum_{\vec{x}} \langle J_i^l(t,\vec{x})\, J_i^l(0,0)\rangle^{av}} \right)^{\frac{1}{2}} \overset{t \text{ window}}{\sim} Z_V$$

$$Z_V = \frac{1}{t_{\max}/a - t_{\min}/a + 1} \sum_{t=t_{\min}}^{t_{\max}} r_{ll}^{cc}(t)\,. \tag{3.75}$$

We use ensembles B_2 and C_2 as two examples. We find plateaus for $r_{ll}^{cc}(t)$ starting at $t/a = 5$ and choose $t_{\min}/a = 5$, $t_{\max}/a = 8$ and find

$$Z_V(B_2) = 0.5702\,(59) \qquad Z_V(C_2) = 0.6230\,(86)\,. \tag{3.76}$$

There is no significant change when increasing $t_{\min}/a$ or $t_{\max}/a$ by up to 2 or 4 units, respectively. For the moment we ignore the uncertainty of Z_V in order to make our point clear. The left and right panel of figure [3.12] show the subtracted vacuum polarization from the (multiplicatively renormalized) local and conserved vector current correlator for ensembles B_2 and C_2. In both cases we find good agreement up to momenta of order $1/a^2$ ($\sim 6\,\mathrm{GeV}^2$ (B_2), $10\,\mathrm{GeV}^2$ (C_2)). As mentioned earlier we must anticipate a stronger impact of lattice artifacts as we approach momentum values $K \gtrsim 1/a$. We note that this divergence of the curves is again much suppressed when the lattice spacing is decreased from $a(B_2) \approx 0.079\,\mathrm{fm}$ to $a(C_3) \approx 0.063\,\mathrm{fm}$. For the most interesting low-momentum region the curves fall on top of each other.

The propagators building the correlation functions have up to now been point-to-all propagators that are calculated by inverting the twisted mass Dirac operator on a point source. Since we use the time dependent current correlators at zero momentum, we can generalize to any source that allows for the estimation of the former. We add an example for stochastic timeslice sources that shows another application of the definition

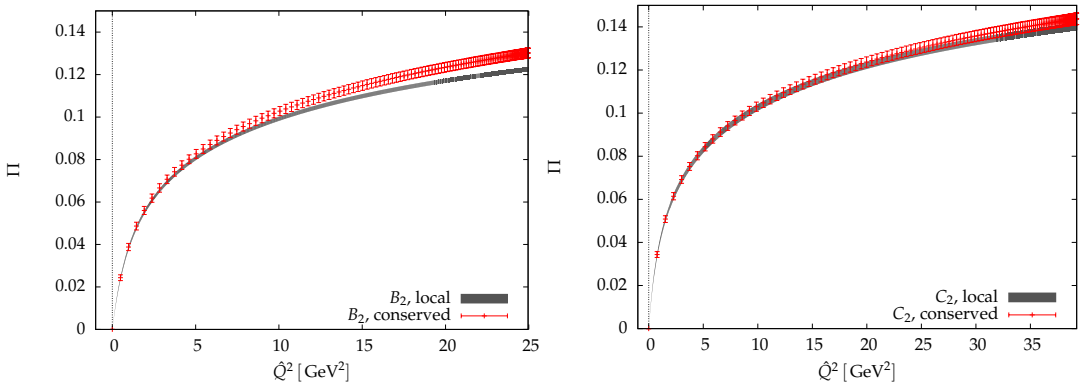

Figure 3.12: Comparison of the renormalized vacuum polarization from a t-sum of the local and conserved current correlator.

of polarization functions using a t-sum. To that end we consider the flavor non-singlet vector Ward identity in the twisted basis.

$$Q^2\,\Pi^v(Q^2) = (4m_q^2)\left(\Pi^p(Q^2) - Q^2\left[\partial\Pi^p\partial Q^2\right]_{Q^2=0}\right). \tag{3.77}$$

On the right-hand side of equation (3.77) appears the twice subtracted polarization function. This can be generated from the lattice current correlator as before if the kernel function is modified accordingly (we assume t to be taken in lattice units)

$$f_t^{(2)}(\hat{K}^2) = \frac{1}{4\,\sin^4(K/2)}\left(\sin^2(Kt/2) - t^2\,\sin^2(K/2) + \frac{1}{3}\,t^2\,(t^2-1)\,\sin^4(K/2)\right). \tag{3.78}$$

The second subtraction term has the form $t^2(t^2-1)$, which ensures the exact evaluation to zero for $t = 0$ and $t = 1$ for any value of K (cf. equation (3.64)). These two timeslices would otherwise have a non-zero contribution even in the limit $\hat{K} \to 0$. For an example using lattice data we take the charm sector again. Note that the vacuum polarization function for the pseudoscalar current correlator is ill defined in the light quark sector on our lattices due to the small mass m_{PS} of the ground state. The lattice time extent is too small to saturate the t-sums. In the charm sector the lightest pseudoscalar $c\bar{c}$ meson is the η_c with a mass of approximately 3 GeV and hence the t-sums are well-defined. Since this example serves to illustrate the method, we want to compare data sets at finite lattice spacing without a detailed continuum extrapolation at this point and must hence again anticipate lattice artifacts. In order to keep the latter as small as possible we take the ensemble D_1, which has the smallest available lattice spacing of approximately 0.05 fm. We tune the renormalization factor to have best overlap of the two curves and find $Z_V(D_1, a\mu_c = 0.1670) \approx 0.714$, which is close to the preliminary result from the correlator ratio 0.7219 (18)[5]. Our main comment is that the calculation

[5]Note that we could use the polarization functions to define a renormalization factor instead, too.

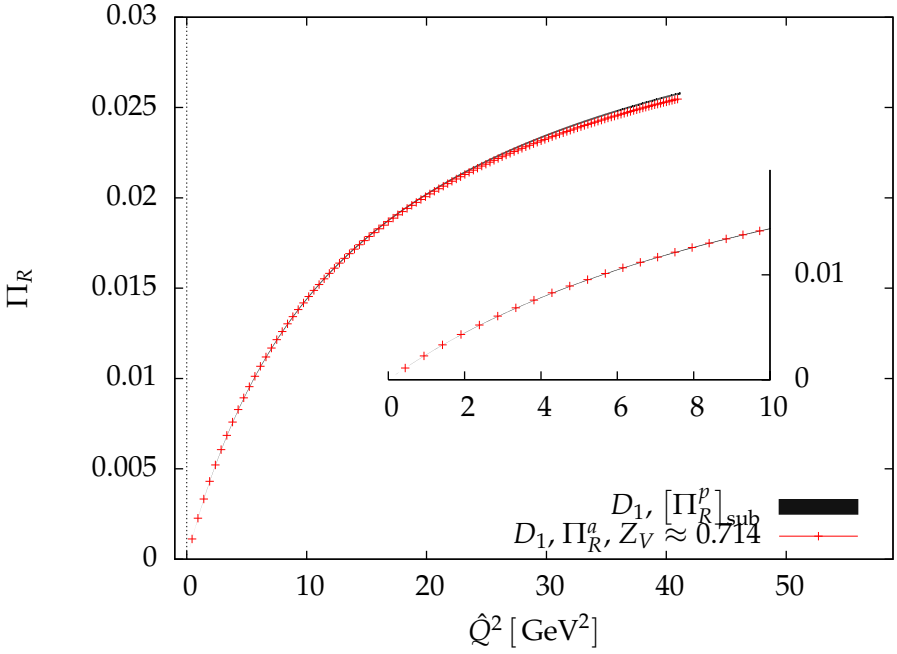

Figure 3.13: Non-singlet vector Ward identity in the charm sector with ensemble D_1 and $a\mu_c = 0.1670$.

of the subtracted Π_R^p can be calculated just like Π_R^p itself from stochastic noise sources without additional fits or extrapolations and that using the t-sum definition we find the lattice Ward identity fulfilled.

3.8 Vacuum polarization fit

We proceed with a discussion of our fits of the vacuum polarization function from the electromagnetic current correlator in the light quark sector. The description of the vacuum polarization in terms of analytic functions is a prerequisite for the calculation of the muon anomalous magnetic moment. We will start with an investigation of the time-dependent current correlator that will give us access to the mass and electromagnetic coupling of the lightest lattice vector meson, which we associate with the ρ in the continuum limit. We describe the fits for the vacuum polarization function arising from up and down quark, but remark that with corresponding changes the same procedure works for different quark sectors. For instance the fit in the charm sector is analogous if we replace $m_\rho \leftrightarrow m_{J/\psi}$.

3.8.1 Extraction of the vector meson mass and electromagnetic coupling

Phenomenology tells us that the ρ as the lightest standard model vector meson is unstable and decays almost exclusively into a pair of pions with a branching ratio of

$\approx 100\%$ [102]. The vector meson and pseudoscalar fields as well as their interactions are, however, effectively included in the lattice calculation by the $N_f = 2$ fermion dynamics. The decay $\rho \to \pi\pi$ can thus in principle happen on the lattice, the lattice ρ and $\pi\pi$ states mix and a rigorous analysis of the situation would require treating the light vector meson as a lattice resonance state (cf. e.g. [53] for a recent lattice calculation with twisted mass fermions). The rigorous treatment of the ρ is computationally demanding (cf. [93, 94] for a methodological discussion) and not the central concern of this work. What comes to our aid is the kinematical region in which the ETMC gauge field ensembles are set. To allow for the decay of the vector meson the kinematical condition $m_V \geq 2\sqrt{m_{PS}^2 + p^2}$ must hold with $p \neq 0$. This follows from considering the decay in the rest frame of the vector meson. Since the vector meson at rest has total angular momentum quantum number $J = 1$, the two pseudoscalar fields have to form a state with orbital angular momentum $l = 1$, which implies that the pions must have non-zero momentum. On the lattice with finite spatial volume L^3 the momenta are quantized, which means $p_i \geq 2\pi/L$. So the condition becomes

$$m_V \geq 2\sqrt{m_{PS}^2 + \left(\frac{2\pi}{L}\right)^2}. \tag{3.79}$$

We will see a posteriori from our analysis that for all the ensembles we use this condition is not fulfilled, that in fact up to one exception there is a significant gap, by which the energy of the 2-pion-state is larger than the vector meson mass [6].

We conclude that given this special kinematical situation we can safely treat the lightest vector meson as a stable asymptotic state and make use of the well-known techniques to extract spectral information from the asymptotic, large time-behavior of the corresponding 2-point correlation function. We need to stay aware, however, that as the physical point is approached within the lattice calculation the techniques to extract the vector meson spectral data will have to be adjusted accordingly.

The asymptotic vector meson state $|V, p, \epsilon\rangle$ with 3-momentum $\vec{p}$ and polarization ϵ shall be characterized in the usual way by its mass m_V and electromagnetic coupling $g_{\mathrm{V,em}}$ defined by the relation

$$\langle\, \Omega \,\big|\, J_\mu^{\mathrm{em}}(0) \,\big|\, V,\, p,\, \epsilon \,\rangle = m_V^2\, g_{\mathrm{V,em}}\, \epsilon_\mu(p)\,. \tag{3.80}$$

The normalization of $g_{\mathrm{V,em}}$ is such that the decay rate for the process $V \to e^+e^-$ (or $V \to \mu^+\mu^-$) reads

$$\Gamma\left(V \to l^+l^-\right) = \frac{4\pi}{3}\,\alpha^2\, g_{\mathrm{V,em}}^2\, m_V \left(1 + \frac{2m_l^2}{m_V^2}\right)\sqrt{1 - \frac{4m_l^2}{m_V^2}}\,, \tag{3.81}$$

where $m_l = m_e$ or m_μ. This quantity is tabulated in the PDG [102] for the light vector meson triplet.

[6] For ensemble B_7 the inequality is still true, but the levels become consistent within errors

V	m_V [MeV]	Γ_{full} [MeV]	$\Gamma(V \to e^+e^-)$ [MeV]	$g_{\text{V,em}}$	f_V [MeV]
ρ	775.49 (34)	149.1 (8)	0.00704 (6)	0.20174 (87)	221.2 (09)
ω	782.65 (12)	8.49 (8)	0.00060 (2)	0.05862 (98)	194.6 (32)
ϕ	1019.46 (02)	4.26 (5)	0.00126 (2)	0.07439 (51)	227.5 (16)

Table 3.3: Compilation of light vector meson decay rates [102], corresponding electromagnetic couplings and dimensionful decay constants.

The recent numbers for the three light vector mesons are collected in the fifth column of {3.3}. For the sake of completeness we give the vector meson masses, full width and decay rate to an electron-positron pair in the columns 2 to 4. Another very useful parametrization of these couplings is in terms of an isospin basis of currents

$$J_\mu^{I=0} = \frac{1}{\sqrt{2}}\left(\bar{u}\gamma_\mu u + \bar{d}\gamma_\mu d\right), \quad J_\mu^{I=1} = \frac{1}{\sqrt{2}}\left(\bar{u}\gamma_\mu u - \bar{d}\gamma_\mu d\right), \quad J_\mu^{s} = \left(\bar{s}\gamma_\mu s\right) \tag{3.82}$$

according to the defining relation

$$\langle\, \Omega \,\big|\, J_\mu^I(0) \,\big|\, V,\, p,\, \epsilon \,\rangle = f_V^I\, m_V^I\, \epsilon_\mu(p)\,. \tag{3.83}$$

This defines the dimensionful coupling f_V for the isospin current J^I. With these basis currents we can decompose the 3-flavor electromagnetic current as follows

$$J_\mu^{\text{em}} = \frac{1}{3\sqrt{2}} J_\mu^{I=0} + \frac{1}{\sqrt{2}} J_\mu^{I=1} - \frac{1}{3} J_\mu^{s} \tag{3.84}$$

and associating the isospin currents with the corresponding mesons $J^{I=0} \Leftrightarrow \omega$, $J^{I=1} \Leftrightarrow \rho$ and $J^s \Leftrightarrow \phi$, we arrive at the couplings as displayed in the last column of table {3.3} again using the input from PDG [102].

Associating the ϕ with a pure $s\bar{s}$ state we find the rough agreement of the decay constants f_ρ, f_ω, f_Φ seen in table {3.3}. This degeneracy is a behavior predicted by chiral perturbation theory.

In a slightly generalized framework we can define m_V and f_V with $g_V = f_V/m_V$ as the generic vector meson mass and couplings and allow for a mixing of the ω and ϕ field parametrized by a mixing angle θ. This leads to the following relation of the electromagnetic couplings to the generic ones

$$g_{\rho,\text{em}} = \frac{1}{\sqrt{2}} g_V\,, \quad g_{\omega,\text{em}} = \frac{\sin(\theta)}{\sqrt{6}} g_V\,, \quad g_{\phi,\text{em}} = \frac{\cos(\theta)}{\sqrt{6}} g_V\,. \tag{3.85}$$

The case of $\tan(\theta) = 1/\sqrt{2}$ corresponds to the special case of ϕ being a pure $s\bar{s}$ state. In that case the couplings follow the $SU(3)$ nonet prediction

$$g_{\rho,\text{em}} \,:\, g_{\omega,\text{em}} \,:\, g_{\phi,\text{em}} = 1 \,:\, 1/3 \,:\, \sqrt{2}/3\,.$$

For a consistent analysis in terms of error propagation we extract these quantities from the same lattice data that we use to estimate the vacuum polarization tensor, albeit in the mixed $(t, \vec{p})$ representation. Our estimation of both the vector meson mass and electromagnetic coupling will follow the analysis described in reference [77]. We use the three spatial, diagonal components of the connected part of the polarization tensor in position space to build the time-dependent vector meson correlator at zero spatial momentum

$$C(t_x - t_y; \vec{p} = 0) = \sum_{\vec{x}} \langle J_i(t_x, \vec{x})\, J_i(t_y,\, \vec{y})\rangle = \sum_{\vec{x}} \sum_{i=1}^{3} \Pi_{ii}^{u}\,(t_x, \vec{x};\, t_y, \vec{y}) \tag{3.86}$$

$$\xrightarrow[\text{finite } L]{t_x - t_y \gg 1/\Delta m} 3\, m_V\, f_V^2\, \mathrm{e}^{-m_\rho \frac{T}{2}}\, \cosh\Big(\big(T/2 - (t_x - t_y)\big)\, m_V\Big)\,. \tag{3.87}$$

By Δm in equation (3.87) we allude to the gap between the mass of the ground state and that of the first excited state, which implies the usual condition of fitting the correlator at times large in units of the splitting. Likewise as usual, the gap is unknown and the specific choices of a t-range to fit the asymptotic behavior is described below. Note that in neglecting quark-disconnected contributions our operator choice is an interpolating field for both the ρ^0 as well as ω. On this level we imply the degeneracy of masses $m_V = m_\rho = m_\omega$ as well as decay constants $f_V = f_\rho = f_\omega$.

In table {3.4} we give an overview of the ensembles used in our calculation. The nomenclature is standard for the ETMC $N_f = 2$ ensembles and is taken from reference [8]. [7] From the same reference we take the values for the lattice spacing, the light pseudoscalar mass m_{PS} and the renormalization factor of the pseudoscalar quark bilinear $Z_P^{\overline{\mathrm{MS}}}(2\,\mathrm{GeV})$, which defines the renormalized light quark mass μ_R in the $\overline{\mathrm{MS}}$ scheme at renormalization scale $\bar{\mu} = 2$ GeV via the relation $\mu_R^{\overline{\mathrm{MS}}}(2\,\mathrm{GeV}) = (a\mu_0)/(a\, Z_P^{\overline{\mathrm{MS}}}(2\,\mathrm{GeV}))$. Since we do not use the quark mass explicitly, we only cite a rounded value for orientation and leave out the uncertainty. The latter can be inferred from fit results for Z_P and the lattice spacing (modulo correlation) in reference [8]. The two uncertainties given for m_{PS} are the statistical error of the fit parameter am_{PS} in lattice units and the uncertainty of the lattice spacing, whose correlation we again ignore. (L and $m_{PS}L$ will carry the corresponding uncertainties of a and am_{PS}, which we leave out at this point.) For the five ensembles whose name has a star superscript we have performed estimates of the quark-disconnected diagram. We see that the ensemble groups $B_1, \ldots, B_5$ and C_1, C_2, C_3 will allow for an investigation of quark mass dependence for fixed lattice spacing and volume. B_0, B_1, B_6 and C_5, C_2 will allow for volume studies at fixed lattice spacing and quark mass (or light pseudoscalar mass). Finally, B_1, C_1 and B_4, C_3 will enable comparisons at approximately fixed lattice volume and renormalized quark mass.

For the fit range of lattice timeslices , $[t_{\min}, t_{\max}]$, we demand the usual conditions: first, the fit interval has to start at a large enough $t_{\min}$, such that the first excited state

[7] The ensemble in the first line does not have an official label. We will refer to it as B_0.

Ens.	β	L/a	$a\mu_0$	$a\,[\mathrm{fm}]$	$L\,[\mathrm{fm}]$	$\mu_R^{\overline{\mathrm{MS}}}$	$m_{PS}\,[\mathrm{MeV}]$	$m_{PS}L$
B_0	3.90	20	0.0040	0.0790 (26)	1.6	23	347.9 (6.2) (11)	2.76
B_1^*	3.90	24	0.0040	0.0790 (26)	1.9	23	340.2 (1.7) (11)	3.27
B_2^*			0.0064			37	423.1 (1.0) (14)	4.04
B_3			0.0085			49	484.6 (1.2) (16)	4.62
B_4			0.0100			58	524.5 (1.2) (17)	5.01
B_5			0.0150			86	645.9 (1.7) (21)	6.26
B_7^*	3.90	32	0.0030	0.0790 (26)	2.5	17	291.5 (1.0) (10)	3.67
B_6			0.0040			23	334.2 (0.5) (11)	4.18
C_5	4.05	24	0.0060	0.0630 (20)	1.5	42	453.5 (3.4) (14)	3.42
C_1^*	4.05	32	0.0030	0.0630 (20)	2.0	21	325.1 (1.9) (10)	3.34
C_2^*			0.0060			42	448.5 (1.9) (14)	4.56
C_3			0.0080			55	517.1 (1.6) (16)	5.27
D_1	4.20	48	0.0020	0.05142 (83)	2.5	16	284.0 (1.2) (5)	3.55

Table 3.4: Parameter values for the ensembles used in this work. We give an approximate value of the renormalized light quark mass in MeV at renormalization scale 2 GeV. The ensemble D_1 is added for later reference.

is sufficiently suppressed. The correlator should be dominated by the overlap with the ground state and should be describable with a single state, which is e.g. indicated by plateaus of the effective masses that have non-empty overlap for all ensembles. Secondly, we intend to use the extracted masses and couplings to model the vacuum polarization function and to extract $a_\mu^{\mathrm{hlo}}(m_{PS}^2)$, which in turn needs to be extrapolated to the physical point. In light of the sensitivity of such an extrapolation we must make sure there is as little as possible artificial dependence of m_V and g_V on the pion mass introduced by potentially different choices of fit intervals for different pion masses. We thus seek a smooth dependence $t_{\mathrm{min/max}}$ on m_{PS}. Thirdly, since we use point sources, we know the relative error of the correlator increases with time. This restriction is particularly severe for the comparatively noisy point-split vector current correlator that incorporates additional noise from the gauge links. So to extract parameters with reasonable precision we must not fit at too large times, where in fact the correlator is lost in noise and statistically consistent with zero.
We thus choose a compromise for the fit interval:

Ensembles	t_{min}/a	t_{max}/a
$B_0 - B_4$, B_6, B_7	8	12
B_5	9	13
$C_1 - C_3$, C_5	12	16

and will refer to fits with these limits and using equation (3.87) as the standard fit. The deviation of the fit interval for B_5 compared to the remaining $B-$ensembles will be explained below.

Ensemble	f_V [GeV]	m_V [GeV]	g_V	χ^2/dof
B_0	0.329 (33) (11)	1.186 (101) (39)	0.2769 (83)	0.11
B_1	0.300 (12) (10)	1.093 (41) (36)	0.2748 (38)	0.83
B_2	0.304 (12) (10)	1.100 (36) (36)	0.2765 (37)	0.89
B_3	0.314 (11) (10)	1.167 (30) (38)	0.2690 (39)	0.98
B_4	0.313 (12) (10)	1.160 (33) (38)	0.2695 (46)	0.42
B_5	0.312 (12) (10)	1.215 (26) (40)	0.2566 (53)	0.94
B_7	0.287 (29) (09)	1.029 (97) (34)	0.2789 (77)	2.48
B_6	0.305 (15) (10)	1.077 (46) (35)	0.2832 (59)	0.85
C_5	0.309 (21) (10)	1.096 (51) (35)	0.2815 (76)	0.10
C_1	0.274 (39) (09)	1.009 (02) (32)	0.2704 (149)	0.65
C_2	0.260 (24) (08)	1.014 (65) (32)	0.2557 (81)	0.56
C_3	0.290 (15) (09)	1.105 (41) (35)	0.2625 (60)	1.86

Table 3.5: Results for the standard fit of the vector current correlator (details given in the text).

We perform a correlated fit to each individual ensemble and use the bootstrap method to estimate the statistical uncertainty of the fit parameters. The results of the standard fit setup are collected in table {3.5} and shown in figures [3.14] for m_V, [3.15] for f_V and [3.16] for g_V. The coupling g_V is not part of the fit, but is actually estimated from the distribution of the ratio f_V/m_V. We further note the strong positive error correlation of f_V and m_V, that leads to significant error cancellations for the coupling g_V. The fit results am_V and af_V are converted to physical units using the lattice spacing. Apart from the statistical error stemming from the fit (first bracket) this induces another systematic error (second bracket). The lattice spacing and our two fit parameters stem from the same set of gauge configurations, so in principle they are correlated quantities. We ignore this correlation and add the uncertainties in quadrature.

We find that our choice of t_{min} and t_{max} lead to statistically good fits with a χ^2/dof around 1 except for ensemble B_7. Moreover, within the statistical uncertainties we find a smooth dependence of all three quantities on the pion mass. Before further interpreting these fit results, we comment on our various cross checks of the integrity of our fits. First, let us consider the effective masses shown in appendix 5 in conjunction with the standard fit results. They are defined for a pair of timeslices $t, t+a$ as the solution of

$$\frac{C(t,\vec{p}=0)}{C(t+a,\vec{p}=0)} = \frac{\cosh\left(m_V^{\mathrm{eff}}(t-T/2)\right)}{\cosh\left(m_V^{\mathrm{eff}}(t+a-T/2)\right)} \tag{3.88}$$

and are determined using the Newton-Raphson-method [109].

Inspecting the figures for the different ensembles we observe immediately, that the statistical quality of the 2-point correlators varies significantly from one ensemble to the next: there are some ensembles, B_2 and B_4 amongst others, which show a clear plateau range that can be associated with a single state. Yet there are others, which do

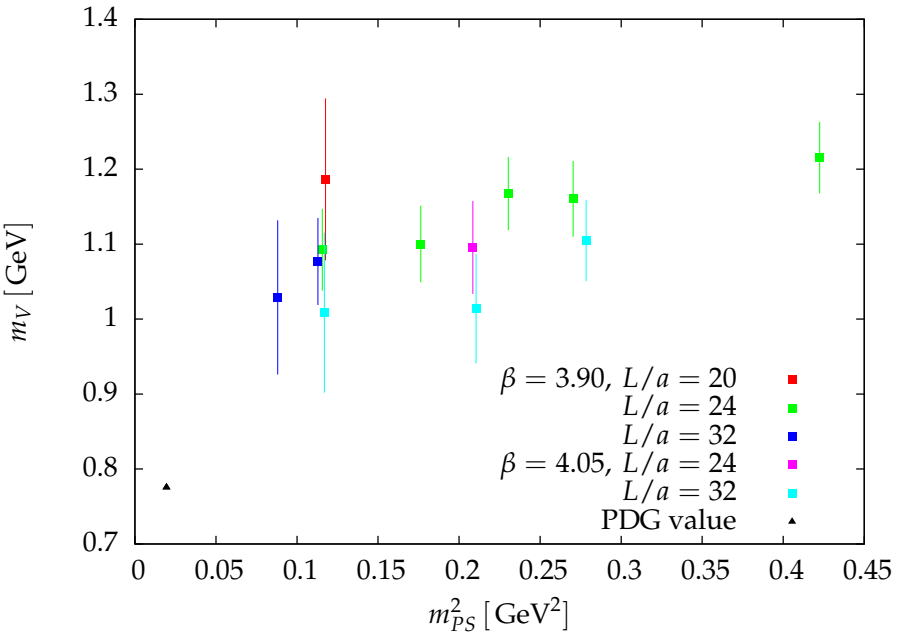

Figure 3.14: Results for the vector meson mass m_V from standard fit.

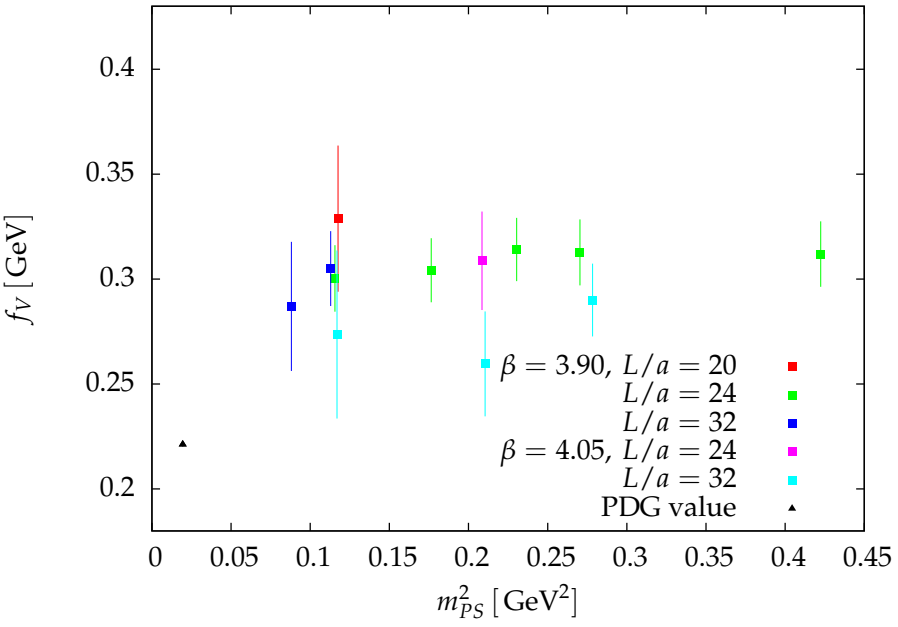

Figure 3.15: Results for the vector meson decay constant f_V from standard fit.

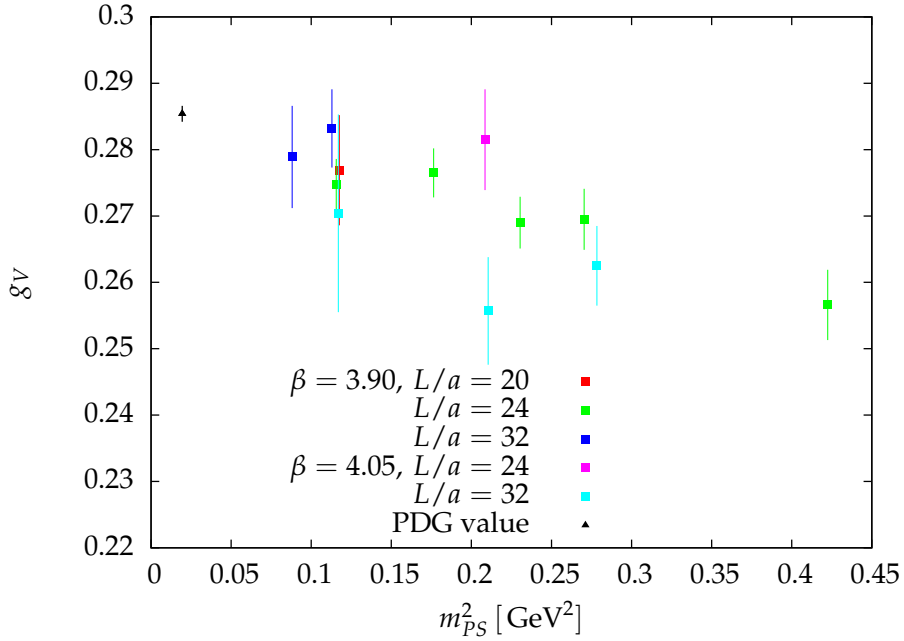

Figure 3.16: Results for the vector meson coupling g_V from standard fit.

not display any plateau before the signal is lost in noise at large times or they show a region that can be interpreted as a plateau, but then with a mass value e.g. far below the one for the next lighter ensemble. On physical and algorithmic grounds we would expect the heavier ensembles to show a better signal quality than the light ones, but such a trend is not obvious. Instead there are both light and heavy ensembles with both poor and strong signal quality. We elaborate on these observations to amplify that we would not improve the physical information in our fit parameters by some intensive fine tuning procedure of the fit ranges. We included the fit results for m_V with its standard deviation as the shaded region in each plot and the fit interval is marked by the dotted lines. Whenever there is a reasonable plateau it shows that our choice provides a good fit. If the definition of a plateau is dubious, we can fall back on the statistical evaluation of our fit in those cases and let us be guided by the reduced χ^2 and by the fact that a posteriori we find a smooth dependence on the pion mass.

For ensemble B_5 an alteration of the fit window was suggested by both the behavior of the effective mass (cf. figure [1] in appendix 5) and the large value of $\chi^2/\mathrm{dof} \approx 5$ we find when using the standard fit window. Shifting by one unit towards larger times is a minimal measure that remedies these issues.

Since the uncertainty of the effective mass or the relative error of the 2-point correlation function itself grows with the time distance from the source timeslice, the fits are far less sensitive to the choice of t_{max} than that of t_{min}. We can include a stepwise reduction of the dependency of our fit results on the choice of t_{min} by including additional states in the fit while simultaneously shifting t_{min} to its lower boundary. We thus amend the

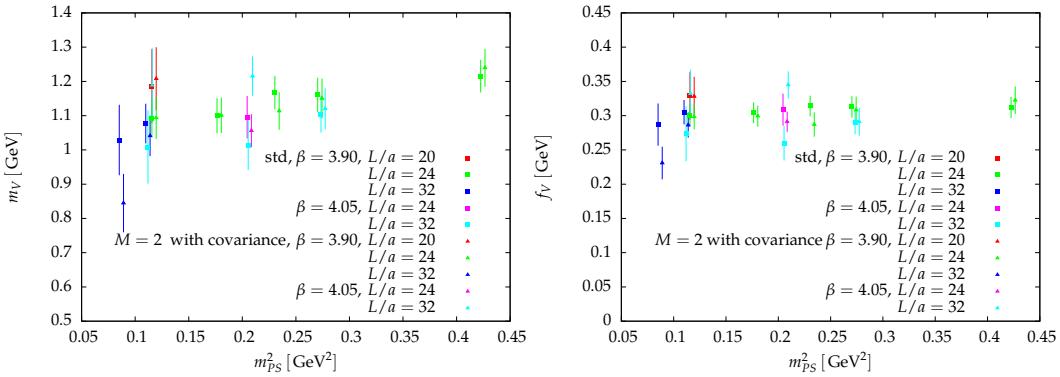

Figure 3.17: Comparison of the vector meson masses and decay constants estimated with $M = 2$ to the standard fit.

fit formula (3.87) to include contributions from excited states

$$C(t; \vec{p} = 0; M) = \sum_{i=1}^{M} 3\, m_i\, f_i^2\, \mathrm{e}^{-m_i \frac{T}{2}}\, \cosh\left((T/2 - t)\, m_i\right) , \tag{3.89}$$

We identify the smallest mass with m_V. Note that the remaining pairs (f_i, m_i) cannot be associated to single states of higher mass but instead represent mixtures of contributions from states lying higher in the energy spectrum. Apart from the pair with lowest mass which has a definite physical meaning we thus interpret this formula in a purely numerical sense as a better description of the correlator data down to smaller values of the source-sink time separation. $M = 1$ is our standard fit described above. The fit range for $M = 2$ is taken in accordance with the proposal in [77]; for $M = 3$ we find that we can fit the complete correlation function on all timeslices. We thus use

M	$[t_{\min}/a,\, t_{\max}/a]$	
	$\beta = 3.90$	$\beta = 4.05$
2	[4, 20]	[5, 25]
3	[1, 20]	[1, 25]

Note that $t_{\max}/a$ scales with the lattice spacing. We further find that $M = 3$ is the maximal number of discriminable exponential terms we can include in the fit: starting with $M = 4$, mass parameters of allegedly different size will converge to a common value on a regular basis, thus giving a lower number of effectively fitted terms. The results for these fits are collected in tables {1} and {2} in the appendix and shown in figures [3.17] and [3.18].

Looking at figures [3.17], [3.18] we conclude that apart from ensemble $C2$ we cannot find any statistically significant differences in the masses or couplings between the three fits. From this observation we conclude that with our choice of $t_{\min}$ and $t_{\max}$ we do neither induce nor hide a systematic dependence on the fit interval. Moreover, the uncertainties of the ground state mass and coupling are mutually consistent between

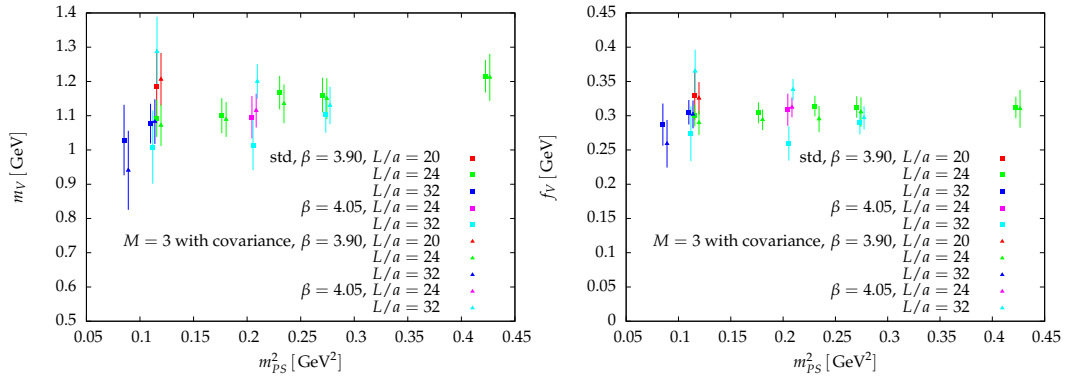

Figure 3.18: Comparison of the vector meson masses and decay constants estimated with $M = 3$ to the standard fit.

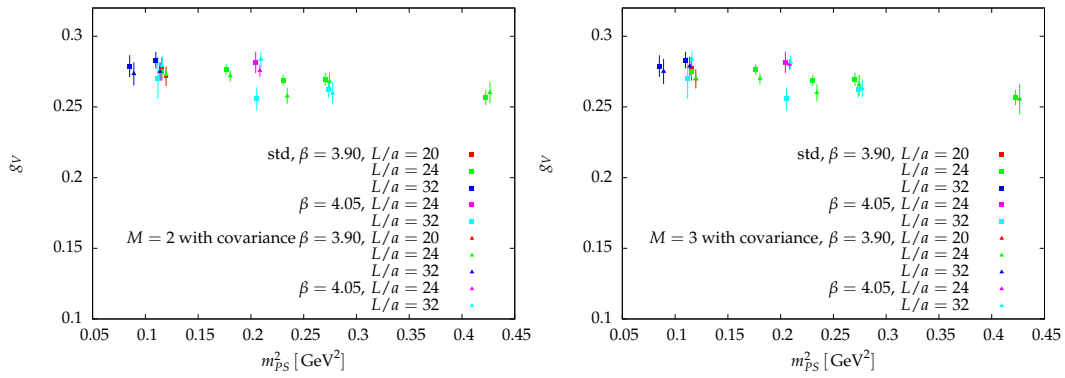

Figure 3.19: Comparison of the electromagnetic coupling from the standard fit with results from $M = 2$ (left) and $M = 3$.

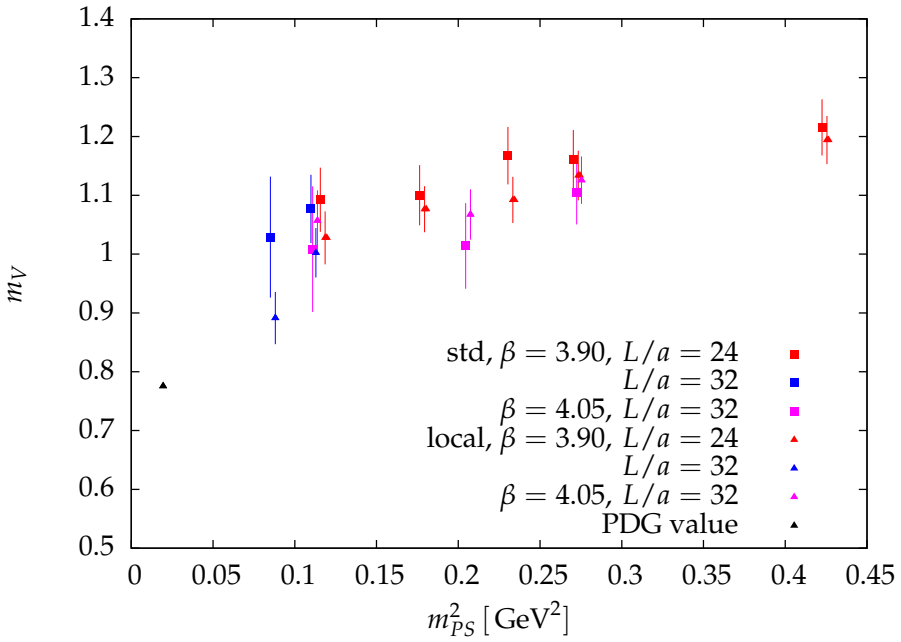

Figure 3.20: Comparison of the vector meson mass fits from conserved and local current.

all the fits, so we do neither significantly under- nor overestimate the errors. Thirdly, fits modeling different degrees of excited state contributions lead to agreement in the fit parameters of the ground state. We thus find that our choice of the standard fit is free from discernible excited state contamination that we can significantly resolve with the data at hand.

A further obvious check is the comparison with fits from the local currents. It is shown in figure [3.20]. The correlator from the local currents is more precise by a factor of 2 compared to the point split one, which manifests itself in the uncertainty of the fit parameters. The (optimized) fit interval for the local correlator was chosen as $[t_{\mathrm{min}}/a, t_{\mathrm{max}}/a] = [10, 18]\,(\beta = 3.90)\,,\ [12 : 22]\,(\beta = 4.05)$. The masses found for the local current are completely consistent with reference [77], which also used local operators. Moreover, they are notably, but statistically insignificantly lower than the values from the point-split current.

As another comparison we use the results of Feng et al. in [53]. Here the aforementioned finite volume method was used to extract the resonance mass of the lightest vector meson. For the overlapping ensembles we show a comparison of the extracted mass values in figure [3.21]. Again we find good agreement of both calculations within statistical errors for all ensembles. Here, too, we notice the trend that the mass values extracted with the volume method are lower than our values.

To sum up, the parameter estimates from our standard fit are consistent with the two other external references using ETMC ensembles. As we stressed on previous occasions, the point-split vector current correlator picks up additional gauge noise. Hence we must

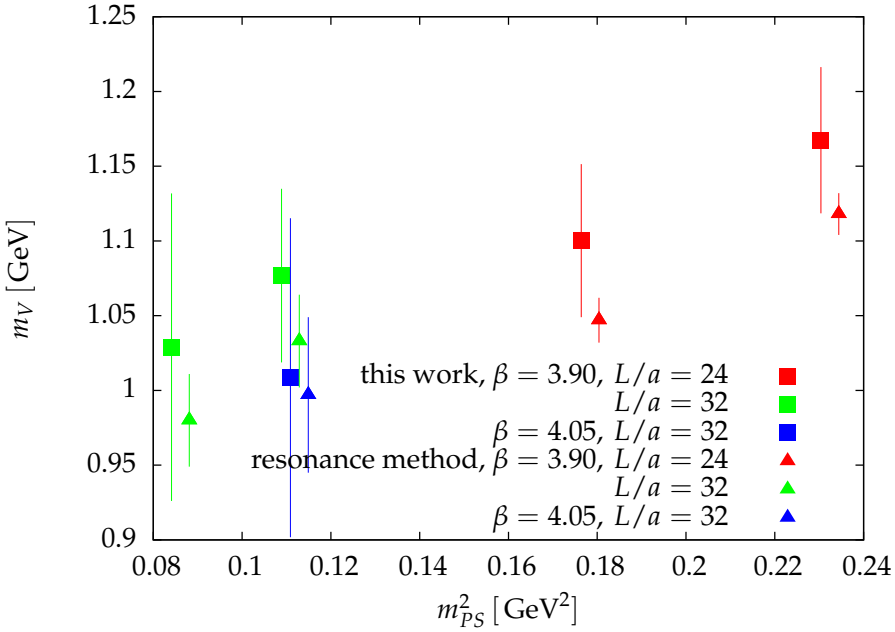

Figure 3.21: Comparison of the vector meson masses calculated in [53] with the standard analysis of this work.

anticipate that for our estimates the uncertainties may come out larger than those of references [77, 53]. Later on we will show that it is still advantageous for us to use our own results. The reasons are a consistent propagation of the uncertainties of f_V and m_V to other derived quantities and the correct normalization of the coupling $g_V = f_V/m_V$ without any further renormalization factors. We will come back to this issue when discussing the fits of the vacuum polarization function itself.

In preparation of the following analysis of the muon anomaly we would like to briefly review our fit results on more general terms. Inspecting table {3.5} and figure [3.14] we find that for all available pion masses the vector meson mass comes out larger than the physical value, slightly descending towards the latter as the pion mass approaches its physical value. But not only is it larger, the data points suggest that to meet the physical value of the ρ mass at the physical point there must be a strong curvature of the function $m_V(m_{PS}^2)$ in the small remaining gap between lattice data and the physical point. This overestimation has been observed in previous studies as well [77, 53]. This is a distinct feature we need to keep in mind for the forthcoming interpretation of the data for a_μ^{hlo}. The problem becomes apparent if we take the mass data and try to extrapolate it to the physical point. To do that we use three different ansätze – fits labeled *lin*, *eft* and *BM* –

fit	m_ρ^0 [GeV]	c_1	c_2	c_3	$m_\rho(m_\pi^2)$ [GeV]	χ^2/dof
lin	1.020 (42)	0.46 (12)			1.029 (40)	4.7/10
eft	1.050 (121)	0.05 (143)	0.5 (19)		1.052 (99)	4.7/9
BM	1.028 (58)	0.31 (52)	0.09 (49)	−0.12 (28)	1.035 (51)	[4.3, 0.01] /8
*lin**	0.729 (360)	3.2 (32)			0.791 (298)	0.8/3

Table 3.6: Results for fit parameters from different extrapolation formulas for $m_V(m_{PS}^2)$. Note that c_i is given in units of GeV^{-i}. For fit *BM* we list in square brackets χ^2 and and χ^2_{aug} from the priors.

as described in reference [77] with the fit models in equation (3.90).

$$\begin{aligned} lin \quad m_\rho(m_{PS}) &= m_\rho^0 + c_1\, m_{PS}^2 \\ eft \quad m_\rho(m_{PS}) &= m_\rho^0 + c_1\, m_{PS}^2 + c_2\, m_{PS}^3 \\ BM \quad m_\rho(m_{PS}) &= m_\rho^0 + c_1\, m_{PS}^2 + c_2\, m_{PS}^3 + c_3\, m_{PS}^4\, \log(m_{PS}^2/m_\rho^2) \end{aligned} \tag{3.90}$$

The first fit, *lin*, is a linear fit in m_{PS}^2 and thus the easiest choice for an extrapolation. The second one, *eft*, comes from the most basic effective field theory approach for light vector mesons [77, 11, 86]. The third one is a chiral extrapolation formula derived by Bruns and Meißner [27]. We show the results for all three fits in the upper two and the lower left panel of figure [3.22] as well as the results for the fit parameters in table {3.6}.

Given the statistical uncertainties of the per-ensemble fit parameters we do not see significant dependencies of the vector meson mass data on lattice spacing or volume. It appears justified to use the data from all twelve ensembles simultaneously and we do so for this trial extrapolation. We note that for the fit *BM* according to Bruns and Meißner we used the same priors as reference [77] to stabilize the fit results, $c_i \cdot (1\,\text{GeV})^i \leq 3$ by augmenting the χ^2 function with a term

$$\chi^2_{\text{aug}} = \sum_i [(c_i - 0)/3]^2$$

(and using m_{PS} in physical units). The augmented χ^2 of the final parameters is added in brackets for that fit. We observe that with the present statistics we can only constrain the coefficient of the m_{PS}^2 term, while the addition of higher powers renders the fit coefficients zero within the statistical uncertainty. Moreover, we find consistent results at the physical point from all three fits with a value that overestimates the ρ mass by $O(10\%)$. The fits *eft* and *BM* have difficulties picking up the right curvature due to the large uncertainty at small pion masses. We elaborate on these extrapolations because they will help us to pin down what to our understanding is the major issue in previous lattice estimates of the hadronic leading order muon anomaly. In all fits the value of the ρ mass at the physical point is overestimated and we shall discuss later on that a_μ^{hlo} is in fact sensitive to the lattice vector meson mass. An overestimation of m_ρ

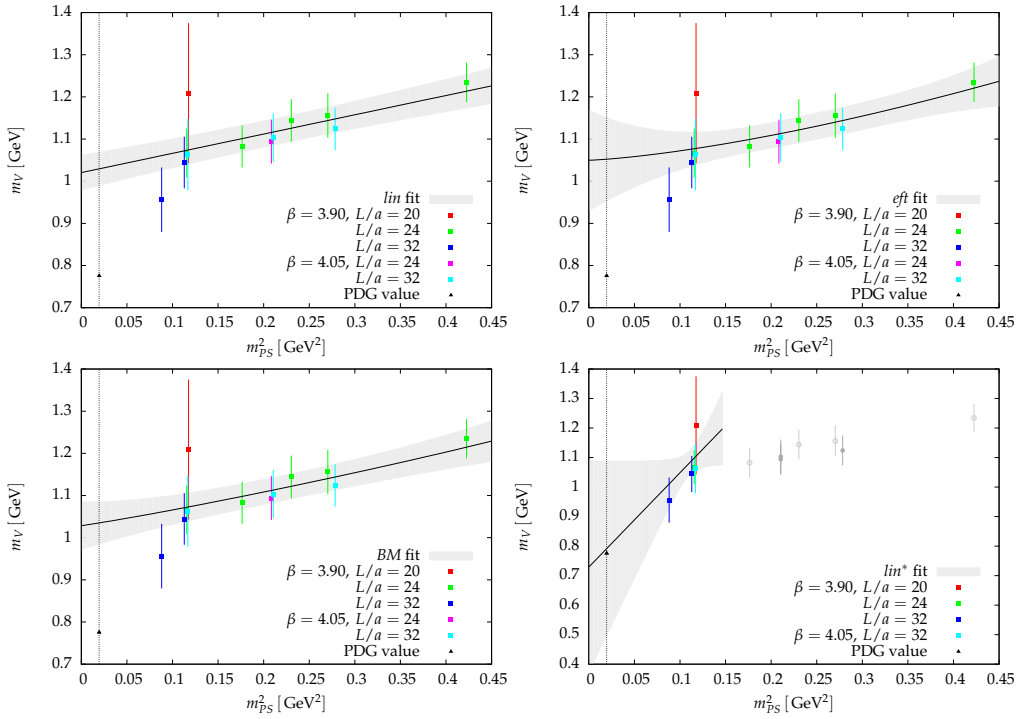

Figure 3.22: Extrapolation of the vector meson mass to the physical point.

must be expected to give an enhanced effect in a_μ^{hlo}. For now we anticipate the need for an extrapolation of the light vector meson mass to the physical point that gives a result consistent with the physical value. For simplicity we use the linear fit and find that restricting it to those data points that fulfill the requirement $m_{PS} \lesssim 0.370\,\mathrm{GeV}$ is a minimal condition for such an extrapolation (indeed, including the data point with the next larger pseudoscalar mass, ensemble B_2, results in $m_V(m_\pi^2) = 1.037\,(86)\,\mathrm{GeV}$ for the extrapolated vector meson mass at the physical point). The result is shown in the lower-right panel of figure [3.22] and the fit parameters listed in the fourth line of table {3.6}.

By visual inspection of figure [3.15] and due to the strong correlation of m_V and f_V we must expect an analogous behavior concerning the required strong curvature at small pseudoscalar masses for $f_V(m_{PS}^2)$ along with the overestimation when extrapolating the vector meson decay constant to the physical point. We will not carry out these fits but instead proceed to the case of the isospin coupling g_V defined by the ratio $g_V = f_V/m_V$ shown in figure [3.16]. Here the data point directly to the experimental value and the quark mass or m_{PS}^2 dependence is much milder than in case of the mass or decay constant. Since both m_V and f_V individually give results larger than the corresponding measured value at the physical point, it seems intuitive that these deviations can be compensated in their ratio. Moreover, observing that m_V and f_V show a similar running with the quark mass, a suppression of this running suggests itself for the ratio as well.

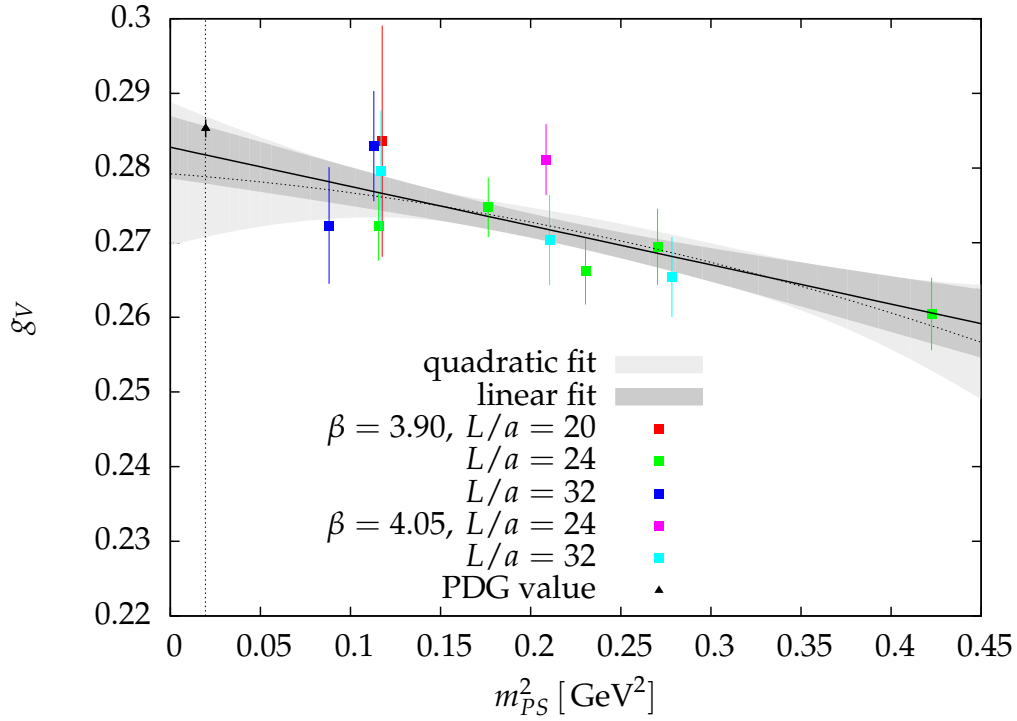

Figure 3.23: Result for the linear and quadratic extrapolation of g_V to the physical point.

fit	g_V^0	$c_1\,[\mathrm{GeV}^{-2}]$	$c_2\,[\mathrm{GeV}^{-4}]$	$g_V(m_\pi^2)$	χ^2/dof
linear	0.2854 (40)	−0.067 (18)		0.2841 (37)	9.18/10
quadratic	0.2833 (91)	−0.047 (84)	−0.045 (173)	0.2824 (76)	9.13/9

Table 3.7: Fit parameters for the linear and quadratic extrapolation of g_V to the physical point.

We perform a fit linear and quadratic in m_{PS}^2 with coefficients

$$g_V(m_{PS}^2) = g_V^0 + c_1\, m_{PS}^2 + c_2\, m_{PS}^4$$

and use all twelve data points. There are again no obvious significant dependencies on lattice spacing or volume, except for the ensembles C_5 and C_2, whose error bars barely overlap. This might hint at a small finite size effect, but with the present statistical uncertainty a definitive statement is not possible. The extrapolations are shown in figure [3.23] and the fit parameters listed in table {3.7}. The quadratic fit is underdetermined by the fit data; its result at the physical point is in very good agreement with that from the linear fit within the statistical uncertainty. Moreover, it does not introduce a significant curvature; in fact, the central value of quadratic fit function (dotted line) remains within the uncertainty band of the linear fit. Hence we quote as

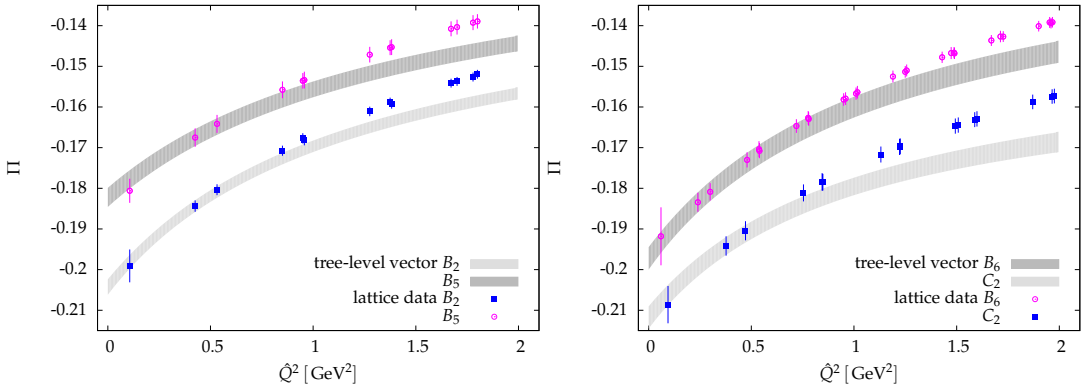

Figure 3.24: Comparison of tree-level vector vacuum polarization and lattice data; left: B_2 and B_5, right: B_6 and C_2 (shifted for better distinguishability)

our continuum estimate of g_V

$$g_V = 0.2841\,(37)\ \text{lattice} \tag{3.91}$$
$$g_V = 0.2853\,(12)\ \text{experiment} \tag{3.92}$$

which fully agrees with the experimental value determined from the relation $g_V = \sqrt{2}\, g_{\text{V,em}}$ and table {3.3}.

In summary, whichever of the three extrapolation ansätze we choose, we significantly overestimate the vector meson mass in the continuum limit. Although not further investigated here, this statement will hold for the decay constant as well. The pion mass dependence of both quantities must pick up a strong curvature in the vicinity of the physical point, a behavior that is not yet reflected in our data. Yet both ensemble B_7, which starts to bend the curve $m_V(m_{PS}^2)$ downward towards m_ρ, and the extrapolation *lin** herald the onset of correct chiral behavior once a higher precision is reached for $m_{PS} < 370\,\text{MeV}$. For later reference we can thus observe here that the extrapolation of the dimensionful m_V and f_V individually and based on our lattice data are not safe. By contrast, the dimensionless coupling g_V has a mild pion mass dependence and extrapolates linearly to consistency with the physical point — without any significantly discernible nor necessary curvature. This property makes the extrapolation to the physical point a safe and reliable procedure.

Finally, from equation (3.68) and figure [3.7] we found that the large time behavior of the time dependent current correlator shapes the polarization function at small momenta. The contribution of a single vector meson state might thus already be a reasonable approximation for Π at lowest momenta, its form in the continuum theory

and the lattice version read

$$\Pi^{\text{cont}}(\hat{K}^2) = \frac{f_V^2}{m_V^2 + \hat{K}^2} = g_V^2 \frac{m_V^2}{m_V^2 + \hat{K}^2} \tag{3.93}$$

$$\begin{aligned}\Pi^{\text{latt}}(\hat{K}^2) = &-\frac{am_V f_V^2}{2} \frac{[P_{t_{\max}+1} - P_{t_{\max}} \, \mathrm{e}^{-am_V}]}{\hat{M}^2 + \hat{K}^2} \, \mathrm{e}^{-m_V t_{\max}} \\ &+ \frac{m_V f_V^2}{2\hat{M}} \frac{2\,\mathrm{e}^{am_V/2} - a\hat{M} - 2\mathrm{e}^{-m_V(t_{\max}+a/2)}}{\hat{M}^2 + \hat{K}^2} \\ \hat{M} = &\frac{2}{a} \sinh(am_V/2)\,,\end{aligned} \tag{3.94}$$

where the polynomials are understood to be evaluated at $\hat{K}^2$.
In the left panel of figure [3.24] we show a comparison of the tree-level vector vacuum contribution in continuum form and the lattice data for ensembles B_2 and B_5 from the lower and higher end of the mass spectrum. For each ensemble the curves are matched at the smallest spatial momentum available, $\hat{Q}^2_{\text{match}} = 4/a^2 \, \sin^2(a\pi/L)$. Although only three lattice momenta are available, the tree-level vector model provides a reasonable description of the lattice vacuum polarization below $1\,\text{GeV}^2$, from this point on, the two curves start to deviate significantly. This is confirmed by the corresponding compilation for ensemble B_6 in the right-hand plot: B_6 has a larger spatial volume, which makes the good overlap more apparent. We add the analogous data for ensemble C_2, which has a smaller lattice spacing and is otherwise roughly comparable to B_2. But the low momentum region is dominated by finite volume instead of effects of non-zero lattice spacing, which is confirmed in this plot as well, where little difference in the quality of the overlap can be found.

3.8.2 Fit and extrapolation of Π

To arrive at a complete description of the vacuum polarization from the lattice data we start with augmenting our model function for $\Pi(\hat{Q}^2)$ in two directions. We already showed that on the one hand we find a rough (and expected) agreement of the lattice vacuum polarization with the tree-level vector meson model in the low-momentum region. On the other hand already at momenta beyond $1\,\text{GeV}^2$ there is a noticeably good overlap with the continuum perturbation theory result, which lasts until the corner of the Brillouin zone is reached and lattice artifacts take over. Based on these two observations, we divide the momentum axis into a low- and high-momentum part. For both regions we define a series of model functions that can increasingly exploit all the available information from the lattice data and will allow us to check systematically for the dependence of fit results and derived quantities on the specific number of terms included in the model. Our model program differs somewhat from the one recently described in [6], which is based on Padé functions.

In the low-momentum region we use the generalized model function

$$\Pi_{\text{low}}(\hat{Q}^2) = -\sum_{r=1}^{M} g_r^2 \frac{m_r^2}{m_r^2 + \hat{Q}^2} - \sum_{s=0}^{N-1} a_s \, \hat{Q}^{2s} \,. \tag{3.95}$$

The motivation for this form comes from the observation, that the polarization function in momentum space can be represented as the Fourier transform in (t, q_0) of the time-dependent vector 2-point correlator. While this relation is exact in the continuum, on the lattice this relation would be distorted by effects from non-zero lattice spacing and the reduced space time symmetry group. (Cf. also the motivation from χPT point of view in appendix 6.) In subsection 3.8.1 it was shown that with an increasing number of exponentials we necessarily come to the point of accurately describing the vector correlator for all times down to $t/a = 1$. Each exponential will give rise to a term in the first sum in equation (3.95) via the Fourier transform. So we know what the values of the parameters should be: they are precisely the parameters fitted in the multiple-state fits of the vector correlation function. Hence we will use these predetermined fit parameters as input to the fit of the vacuum polarization function in momentum space. We can thus interpret the terms for $r \geq 2$ as parametrizing the excited state contributions beyond the tree-level vector meson model.

Since the coupling and mass parameters are fixed beforehand, the first term in the second sum, a_0, parametrizes the value $\Pi(0)$, which is to be subtracted to form the renormalized vacuum polarization,

$$\Pi(0) = \Pi_{\text{low}}(0) = -\sum_{r=1}^{M} g_r^2 - a_0 \,.$$

The remaining terms with $a_1, a_2, \ldots$ account for contributions beyond the tree-level vector meson model. Amongst those are the lattice artifacts, since every power of $\hat{Q}^2$ is accompanied by a power of a^2 in the dimensionless Π.

Note that due to the finite number of momenta in the fit and the limited statistics per momentum value, we have a freedom to decrease M and increase N (and vice versa) while achieving equally good fits. Given the large values of the mass parameters for $r \geq 2$ compared to the momentum values, these terms can be safely Taylor-expanded in the low-momentum region.

For the high-momentum region we let ourselves be inspired by the pQCD form of the vacuum polarization, which, at the low orders we compared to, has the characteristic *log* behavior. We thus define

$$\Pi_{\text{high}}(\hat{Q}^2) = \log(\hat{Q}^2) \sum_{r=0}^{B-1} b_r \, \hat{Q}^{2r} + \sum_{s=0}^{C-1} c_s \, \hat{Q}^{2s} \,. \tag{3.96}$$

Note that a truly pQCD-like fit form would include correction terms with momentum dependence $\propto (\bar{m}^2/\hat{Q}^2)^s$ stemming from the non-zero quark mass. However, due to

lattice artifacts we have to include polynomial terms in any case and the finite precision of our lattice data restricts the number of additional terms we can distinguish to 1 or 2. Moreover, as outlined before, our primary interest lies in a smooth description of the data, and we emphasize that Π_{high} is purely an interpolator in contrast to Π_{low} which defines $\Pi(0)$.

We refer to the gluing together of the two fit functions as "matching". The matching is achieved by weighing both fit functions with a matching function $\zeta(\hat{Q}^2)$ and $1-\zeta(\hat{Q}^2)$, respectively, that increases from close to zero to close to unity in a region δ^2_{match} around $\hat{Q}^2_{\text{match}}$. In practice, we choose

$$\zeta(\hat{Q}^2) = \frac{1}{2}\left(1+\tanh\left(\frac{\hat{Q}^2-\hat{Q}^2_{\text{match}}}{\delta^2_{\text{match}}}\right)\right). \tag{3.97}$$

Note that a value of δ^2_{match} smaller than the gap between lattice momenta renders ζ effectively a discrete step function. This can hamper a smooth transition due to lack of overlap of the low- and high-momentum model function. We place the matching momentum around $\hat{Q}^2_{\text{match}} = 2\,\text{GeV}^2$ with a width of $\delta^2_{\text{match}} = 0.3\,\text{GeV}^2$. This region has the advantage of allowing good descriptions of the lattice data with either Π_{low} or Π_{high} and given the density of lattice momenta the matching region is sufficiently broad to enforce a smooth transition. Moreover, this choice places the overlap in a safe distance from the crucial low momentum region up to around $1\,\text{GeV}^2$. It also leaves a window of $O(4)$ lattice momenta on either side of the matching point to force agreement on low and high momentum fit. This concerns primarily the integral definition of a_μ^{hlo} into which the propagation of any systematic effects arising from the overlap should be avoided.

We note in passing that the logarithmic term in Π_{high} together with a non-zero weight from $1-\zeta(0)$ in principle does not allow for a rigorous evaluation of the complete fit function at zero momentum. We resolve this issue by simply ignoring Π_{high} when evaluating $\Pi(0)$. This poses no problem, since e.g. for $\delta^2_{\text{match}} = 0.3\,\text{GeV}^2$ we have that $1-\zeta(0) < 2\cdot 10^{-6}$. The matching region is illustrated in figure [3.25] for the lattice data from ensemble B_2 using the parameters quoted above.

Another improvement technique that we can readily apply is the tree-level improvement of the vacuum polarization function. The term tree-level is now meant with respect to the strong coupling α_s and is to be distinguished from the effective field theory meaning in the previous subsection. It basically consists of exchanging the lattice tree-level contribution for the continuum one in the high-momentum region. To that end we repeat the calculation of the gauge field dependent $\Pi[U]$ with $U \equiv \mathbb{1}$ and the tree-level value $\kappa_{\text{cr}} = 1/8$ of the critical coupling while keeping the bare twisted quark

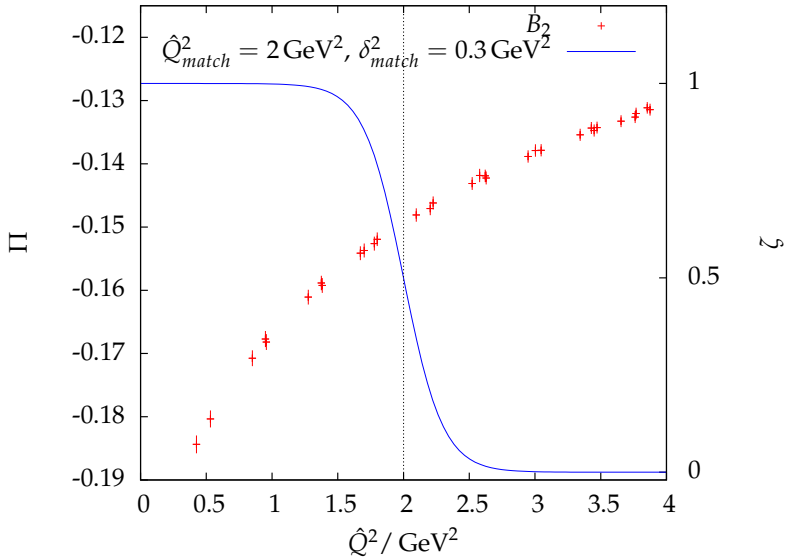

Figure 3.25: Matching region for ensemble B_2.

mass. We then build

$$\Pi(\hat{Q}^2) \to \Pi(\hat{Q}^2) - \Pi_{tl}^{lQCD}(\hat{Q}^2) + \Pi_{tl}^{pQCD}(\hat{Q}^2) \quad \forall\, \hat{Q}^2 \geq \hat{Q}^2_{\text{match}} \tag{3.98}$$

$$\Pi_{tl}^{pQCD}(\hat{Q}^2) = \frac{20}{9} - \frac{4}{3}\log\left(\hat{Q}^2/\mu^2\right) - 2\frac{4\bar{m}^2}{\hat{Q}^2} + \left(\frac{1}{4} + \log\left(\frac{\hat{Q}^2}{\bar{m}^2}\right)\right)\left(\frac{4\bar{m}^2}{\hat{Q}^2}\right)^2 .$$

The pQCD form of Π_{tl} is taken from reference [30] and we exchanged $-q^2 \to \hat{Q}^2$ with $\hat{Q}^2 \geq 0$.

The tree-level improvement subtracts the lowest order lattice artifacts. In the twisted mass formalism the vacuum polarization function has finite lattice spacing artifacts starting at second order. The tree-level improvement changes this to

$$\Pi^{latt} = \Pi^{cont} + O\left(a^2\right) \longrightarrow \Pi^{latt} = \Pi^{cont} + O\left(\alpha_s a^2\right) .$$

Note further, that even for our ensemble B_5 with largest quark mass, at the matching momentum we have $\bar{m}^2/\hat{Q}^2 < 0.02$ and we can thus safely assume the massless case. In figure [3.26] we show four examples for the change the tree-level improvement causes. The visible effect of the improvement is small except for very large momenta. Also the cancellation of anisotropy artifacts is rather limited in the additive improvement. But the overall momentum dependence and even more importantly the normalization is conserved by the additive procedure. We note that the cancellation of anisotropy artifacts could be nicely achieved by a multiplicative improvement using the ratio $\Pi^{lQCD}/\Pi_{tl}^{lQCD}$: the polarisation function then collapses onto a narrow band whose width corresponds to the uncertainty of the data points only. But simultaneously this changes the normalization of the polarization function which is problematic in view of

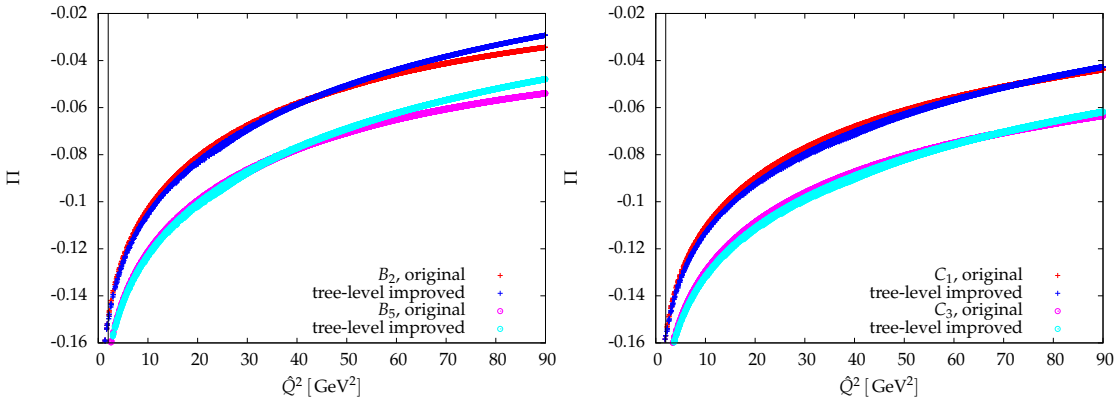

Figure 3.26: Comparison of original and tree-level improved lattice data for vacuum polarization function; left: B_2 and B_5; right: C_1 and C_3.

the applications we aim for. We conclude that the additive version appears as the best choice to take advantage of a small improvement that comes at very little additional cost without complicating the systematic analysis.

With these definitions at hand we can move forward to fitting the (tree-level improved) vacuum polarization function itself to the $(M,N)+(B,C)$ models in our nomenclature. To perform the fit we use the bootstrapping method as before. As was the case for the tree-level vector meson contribution we use the samples of $(f_V,\, m_V)$ consistently as input values for the fit and determine the remaining coefficients a_i, b_j, c_k.

In the model χ^2 function we do not include the full covariance matrix

$$C_{ij} = \mathrm{cov}(\Pi(\hat{Q}_i^2),\, \Pi(\hat{Q}_j^2))\,,$$

but neglect the off-diagonal elements, despite the strong correlation of different momenta; in case of e.g. ensemble B_2, we find that 99% of all correlation coefficients are larger or equal 0.9. The reason for keeping only the diagonal values lies in the limitations of our available statistics: depending on the extension of the fit range in $\hat{Q}^2$ we easily include $N_D \approx O\,(100 \sim 1000)$ data points in the fit. Consequently we would have to estimate the covariance matrix with $O\left(10^4 \sim 10^6\right)$ elements from the $N_G \approx O\,(100 \sim 200)$ gauge configurations for which we have values for Π. The magnitudes here would be in clear violation of the rule of thumb $N_D \approx \sqrt{N_G}$ [99] that needs to be fulfilled in order to have a sufficiently well defined covariance matrix. In such a case instabilities and a distortion of the χ^2 function must be expected. We note that different methods have been devised to tackle this problem, which essentially alter the covariance matrix to restrict the impact of very small eigenvalues. Yet these would introduce further systematic effects that need to be controlled. Moreover, in our tests of these procedures we found that under the present circumstances to arrive at a reasonable fit that is not distorted from the data and has a $\chi^2/\mathrm{dof} \sim O\,(1)$ the reduction of the covariance matrix had to be pushed to extremes that would allow keeping only a small fraction of non-zero

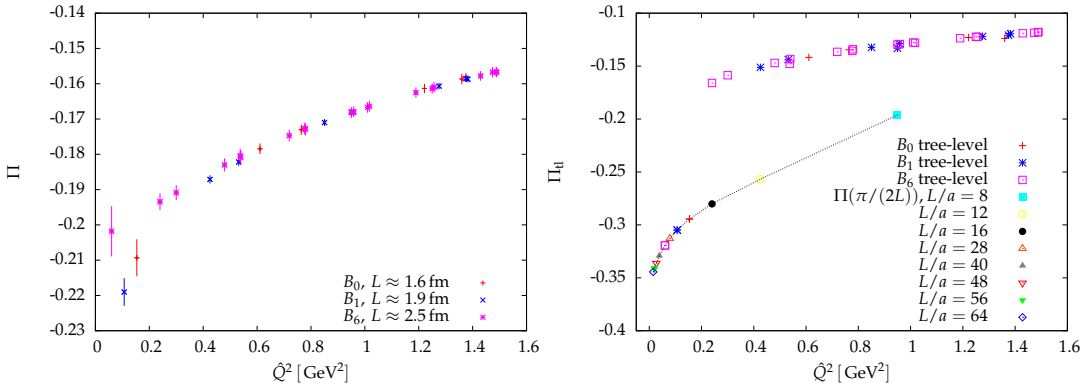

Figure 3.27: Comparison of lattice vacuum polarization for different volume in the low-momentum region.

eigenvalues. In order to avoid such a behavior we use only the diagonal part of the covariance matrix from the beginning. We emphasize that we can still call the so defined fits "correlated", since via the bootstrap sampling we keep track of the correlation of the lattice vacuum polarization function at different momenta in the fit.

Furthermore, we leave the lowest lattice momentum out of the fit, $\hat{Q}^2 = 4\sin^2(\pi/T)$. At first glance this step may seem questionable, given our repeated emphasis of the importance of the low momentum region. But for all ensembles the vacuum polarization at this momentum has a considerably larger error and it is strongly effected by finite size effects. This becomes clearly visible in figure [3.27]. In the left-hand panel we show a comparison of the vacuum polarization lattice data for ensembles B_0, B_1 and B_6, which show the suppression of curvature towards the zero momentum point with increasing volume. We corroborate this impression with the tree-level study in the right-hand panel. With $a\mu_0 = 0.0040$ fixed we find that apart from the lowest momentum the curves fall on top of each other. We added the value of Π_{tl} for a number of values of $L/a = 8, \ldots, 64$, which sketches the development of the momentum dependence at this lowest value of $\hat{Q}^2$. Since we do fits without the covariance matrix in the definition of χ^2, in keeping this said momentum point we would risk that the fitted curve would try to follow this clearly identifiable finite-size effect in the course of adding more parameters to the model function. By leaving it out we automatically take out this effect and the fitted values for $\Pi(0)$ from different volumes will be closer to each other.

Let us start with the fit $M1N2B1C3$. To give an idea of the kind of fit result we are looking at, we show the result of the fit in question for ensemble B_2 in the left-hand panel of figure [3.28]. In this overview comprising the complete fit range from the previously defined $\hat{Q}^2_{\mathrm{min}}$ to $90\,\mathrm{GeV}^2$ we find very good agreement of lattice data and model function throughout all momentum regions. The right-hand plot shows a detail view of the matching region. The matching of the functions from the two realms is a subtle point and we require a smooth transition to exclude systematic artifacts in the numerical integration leading to a_μ^{hlo}. We compare results from three fits $M1N2B1$ using

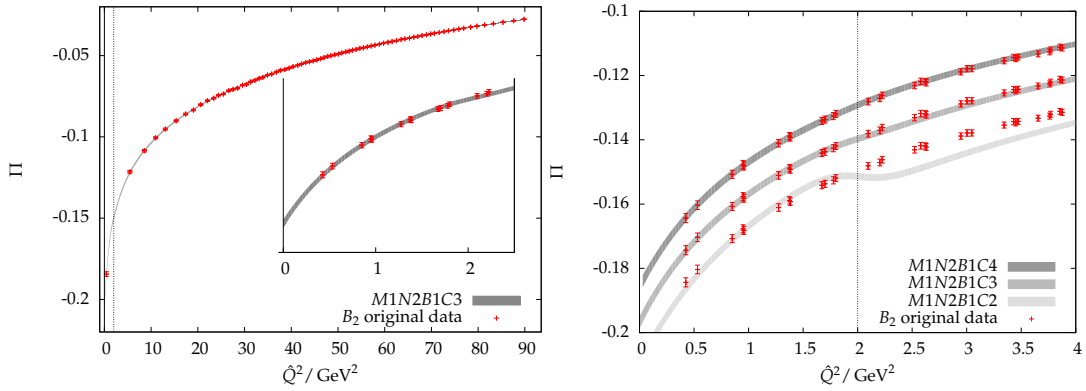

Figure 3.28: Comparison of tree-level improved lattice data and the fit band $(M = 1, N = 2) + (B = 1, C = 4)$; left: global comparison, right: detail around the matching region with comparison of $C = 2, 3, 4$.

$C = 2, 3, 4$. Clearly, the logarithm plus a linear function in $\hat{Q}^2$ is insufficient to describe the lattice data in the high-momentum region. Yet our smoothness demand is already fulfilled for $C = 3$. The fit with $C = 4$ additionally provides a slightly better description of the data for $2\,\mathrm{GeV}^2 \leq \hat{Q}^2 \leq 4\,\mathrm{GeV}^2$ and we shall thus use $M = 1$, $N = 2$, $B = 1$, $C = 4$ as our reference fit. The results for the fit parameters of this standard fit are collected in table {4} in the appendix 8. We repeat that in addition the parameters for the standard ρ fit enter the fit as well, though they are not listed.

In an analogous way we use model functions with $M > 1$. Since with $M = 2, 3$ we can describe the lattice data in a larger window we can expand the small momentum region and move the matching point to larger values. $\hat{Q}^2_{\mathrm{match}} \sim 6 - 8\,\mathrm{GeV}^2$ are typical values for a model function Π_{low} with $M = 2, 3$ and $N = 2$. Furtheron, we explored fits for different values of B and C, as well as trading coefficients N for B, C at fixed original matching conditions and $M = 1$. Since the methodology is similar to what we discussed above, we will not go into detail about these fits, but postpone further comments until we discuss their application in estimating the lepton leading order anomalous magnetic moments. For completeness the parameters for these fits are collected in appendix 8.

In summary, with the standard $M1N2B1C4$ fit model and the temporal moment method we have now two independent methods to describe the polarization function from the point-split vector current correlator. The most interesting quantities to compare here are the value and the derivative of Π at zero momentum. In the light quark sector these have immediate impact on the estimation of the hadronic LO anomalous magnetic moments of the leptons. We show the estimates from both ways in figure [3.29]. As our primary interest lies in a side-by-side comparison of the two methods, we plot the derivative of Π in lattice units.

Note that the uncertainties for the results for both quantities derived from the fit function $M1N2B1C4$ are only statistical and do not contain the systematic error from the choice of a model function. In terms of the $t-$sum method, on the other hand, we

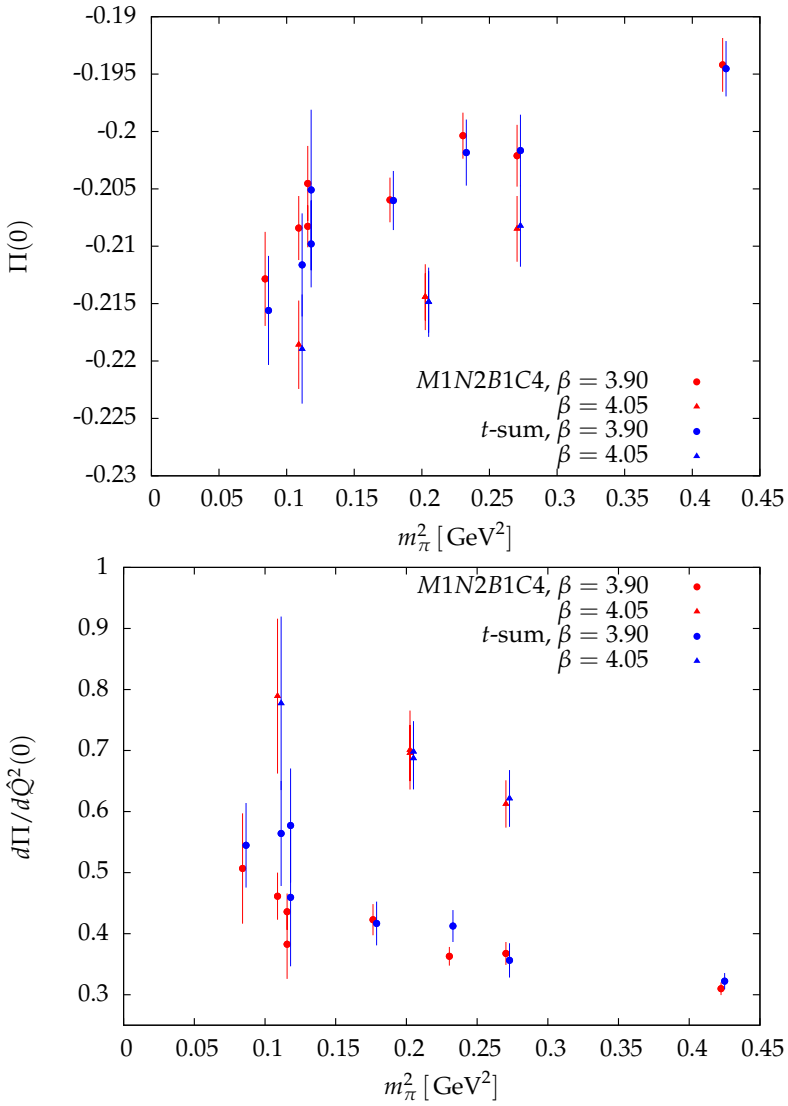

Figure 3.29: Comparison of $\Pi(0)$ and $d\Pi/d\hat{Q}^2(0)$ from $M1N2B1C4$ extrapolation and t-sum for the point-split vector current.

have a model independent formula in finite volume. Moreover, the estimation of the error is different for both ways: we use the bootstrapping method for the fit and the Γ-method for the t-sum [127], which explicitly includes the correlation of the lattice data on different timeslices. We find consistent results from both the fit and the sum with a tendency of larger uncertainties for the t-sum result. The latter have a direct dependence on the correlator data, especially their behavior on the larger timeslices, which is an issue in particular for the lightest ensembles. The mutual agreement for results from the two independent approaches gives reassurance in both procedures.

4 The muon anomalous magnetic moment in theory and experiment

In the following two chapters we will discuss the ETMC project which set out to investigate the muon anomalous magnetic moment in a lattice calculation. Before going into depth about the practical calculations, data acquisition, different fits and extrapolations, we would like to start with a brief overview on the situation of the experimental measurement and theoretical determination in pQCD and lattice QCD. Moreover, some phenomenological considerations will deliver vital arguments for our following discussion and the analysis, so we will prepend the core topic with some recapitulation of the phenomenology of the lepton anomalies. The authors of [83, 85] have compiled a comprehensive description of the muon anomalous magnetic moment including many aspects from the different stages of experimentation over the earliest calculations of leading order QED corrections to the most recent models including extensions of the standard model and their contributions to the muon anomaly. It is a major source for the following discussion.

4.1 Leptonic anomalous magnetic moments in theory and experiment

The magnetic moment of the muon parametrizes the strength of the interaction of a muon with an external magnetic field in the limit of zero momentum transfer with the external field. With the muon spin $\vec{s}$ and electric charge e this interaction gives rise to an energy contribution of size

$$V_\mu = -g_\mu \frac{e\hbar}{2m_\mu c}\vec{s}\cdot\vec{B} = -\vec{\mu}_\mu \cdot \vec{B}\,. \tag{4.1}$$

The classical Dirac theory for point-like charged fermions with spin quantum number $s = 1/2$ predicts a value $g_\mu = 2$ for the magnetic moment of the muon. Beyond the classical theory the magnetic moment receives contributions from radiative corrections, the difference $g_\mu/2 - 1$ thus acquires a non-zero value from the interaction effects of the standard model fields, and the muon anomalous magnetic moment is defined as

$$a_\mu = \frac{g_\mu - 2}{2}\,. \tag{4.2}$$

Experimentally the muon anomaly is determined at muon storage rings. Muons are

produced e.g. by pion decay, polarized and selected to have the so called magic energy $E \approx 3.098\,\mathrm{GeV}$ and are fed into a storage ring. During their dilated lifetime they are in highly relativistic circular motion in a uniform magnetic field and perpendicular to its direction. The difference of the cyclotron frequency ω_c and the frequency ω_s of the precession of the muon spin around the magnetic field then gives the muon anomaly as the solution of the equation

$$\vec{\omega}_s - \vec{\omega}_c = a_\mu \frac{e}{m_\mu c}\vec{B}\,. \tag{4.3}$$

The ability of experimentalists to control the uniformity of the magnetic field and to measure the frequencies with high precision then makes a_μ one of the most precisely determined physical quantities.

The processes involved in the experiments are inclusive with respect to standard model interactions. All interactions allowed for the energy range of the experiment are inseparably woven together in the final result. In the theoretical determination of a_μ we actually come the opposite way. The separation of a_μ into contributions from distinct standard model sectors is natural and we add up the contributions to form the full quantity.

For the theoretical definition in Minkowski and finally Euclidean space we study the muon-photon vertex encoding the interaction of muon and photon field in the electroweak sector of the standard model with perturbative (in the electroweak sense) corrections from QCD. Since the following considerations apply equally to all three leptons e, μ, τ we generalize the language and use the lepton label l instead of the muon. The amplitude for the electromagnetic interaction of a lepton in the presence of an external electromagnetic field is given by the matrix element in momentum space

$$\begin{aligned}
\mathcal{M}(p_1,p_2,q) &= \int d^4x\, \langle l^\pm(p_2,\, r_2)|\, j^{\mathrm{em}}_{l\,\mu}(x)\, |l^\pm(p_1,\, r_1)\rangle\, \mathrm{e}^{-iqx} \\
&= \delta^{(4)}(p_2 - p_1 - q)\; i\Gamma_\mu(p_1,p_2) \\
i\Gamma_\mu(p_1,p_2) &= \langle l^\pm(p_2,\, r_2)\,|\, j^{\mathrm{em}}_{l\,\mu}(0)\,|\, l^\pm(p_1,\, r_1)\rangle \\
&= \bar{u}_{l^\pm}(p_2,\, r_2)\,\Pi_\mu(q)\,u_{l^\pm}(p_1,\, r_1)\,.
\end{aligned} \tag{4.4}$$

Here j^{em}_l denotes the electromagnetic lepton current and $u_{l^\pm}$ the free lepton spinor. Upon scattering with a photon the initial state lepton changes momentum and third spin component from $(p_1,\, r_1)$ to $(p_2,\, r_2)$. With the lepton momenta on the mass shell and based on Lorentz covariance the vertex function has the following decomposition within the standard model

$$\Pi_\mu(q) = F_E(q^2)\,\gamma_\mu + F_M(q^2) i\sigma_{\mu\nu}\frac{q_\nu}{2m_l} + F_D(q^2)\,\sigma_{\mu\nu}q_\nu\gamma_5 + F_A(q^2)\left(\gamma_\mu - \frac{2m_l\,q_\mu}{q^2}\right)\gamma_5\,. \tag{4.5}$$

The form factors appearing in equation (4.5) are the electric charge form factor F_E, the magnetic form factor F_M and the anapole and electric dipole moment form factors F_A

and F_D. The latter two terms are not invariant under time-reversal and combined charge conjugation and parity symmetry, respectively. They can contribute due to the breaking of charge conjugation and parity symmetry by the weak interactions, which also implies the breaking of time reversal invariance according to the CPT invariance of the standard model. Restricting the case to QED+QCD, the action will be invariant under all three transformations individually and the anapole and electric dipole moment terms are forbidden by the enhanced symmetry properties. So for our purposes we can write the vertex function as

$$\Pi_\mu(q) = F_E(q^2)\,\gamma_\mu + F_M(q^2) i\sigma_{\mu\nu}\frac{q_\nu}{2m_l}\,. \tag{4.6}$$

In the classical limit of zero momentum transfer $q^2 = (p_2 - p_1)^2 \to 0$ one has $F_E(0) = 1$ expressing the charge renormalization condition and the lepton anomalous magnetic moment is given by

$$a_l = F_M(0) \tag{4.7}$$

The next step will now be the extraction of the form factor $F_M(q)$ from the amputated vertex function $\Pi_\mu(q)$. Before we continue with this calculation we would like to stay a little longer with the full vertex function and discuss the different types of contributions. This will give us a nice overview of the significance of the contributions from the individual sectors of the standard model and more importantly help us to better assess the relevance of the leading order hadronic part for $g_\mu - 2$. The usual procedure is to label contributions as stemming from QED, hadronic effects and from the weak sector of the standard model, which at the same time mirrors in descending order their magnitude. The by far largest contribution comes from QED corrections alone. In figure [4.1] we show as an example the diagrams for the leading and next-to-leading order QED corrections to the muon-photon vertex entering the lepton anomaly. The universal leading order QED contribution, $a_l^{\mathrm{QED\,lo}} = \alpha/(2\pi)$, is the famous result obtained by Schwinger in 1948 [114]. In case of the muon, the summed pure QED corrections to a_μ up to the 5-loop order alone give approximately 99.994% of the final estimate from standard model physics (cf. [85] and references therein).

The leading and next-to leading order hadronic contributions can be nicely deduced from figure [4.1] by inserting one hadronic vacuum polarization diagram into the leading order and next-to-leading order QED diagrams, respectively. In figure [4.2] we show the leading order (α^2) diagram (1) that we will be concerned with, as well as representatives of the commonly distinguished classes of diagrams of next-to-leading order. The vacuum polarization insertion is depicted by the shaded bubble. The twelve next-to-leading order diagrams of class $(2a)$ comprise those that result from the diagrams (1) to (6) in figure [4.1] upon inserting the hadronic vacuum polarization into one of the two virtual photon lines. Class $(2b)$ consists of two diagrams, the one not shown with exchanged electron loop and vacuum polarization insertion. Finally, class $(2c)$ is marked by two insertions of the hadronic vacuum polarization. The diagrams (1) and $(2a-c)$ share the property of being calculable by a combination of 1- and 2-loop QED

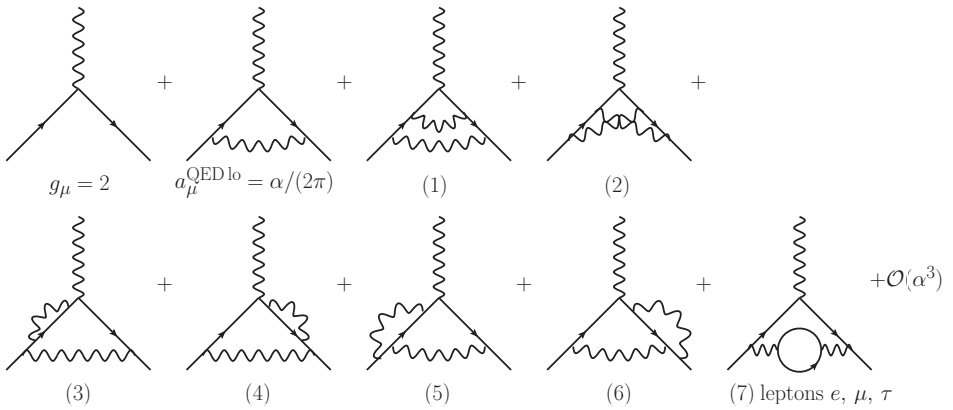

Figure 4.1: Tree-level, leading order and next-to-leading order ((1)-(7)) QED diagrams contributing to the muon anomaly.

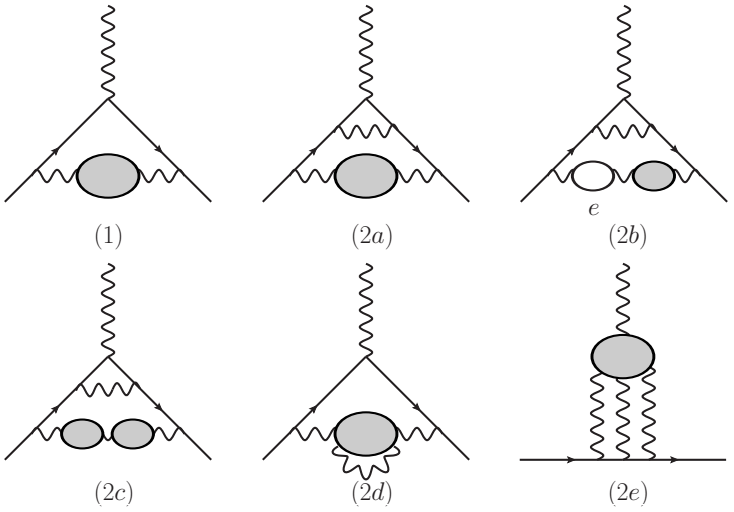

Figure 4.2: Leading order hadronic contribution a_μ^{hlo} to the muon anomaly (1) and representatives of classes $((2a)$-$(2e))$ of next-to-leading order.

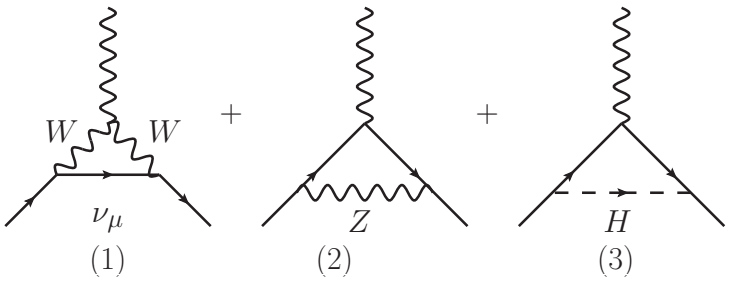

Figure 4.3: Diagrams for the leading order weak contributions.

Contribution X	$a_\mu^X \times 10^{-11}$
QED (incl. 4-loops, LO 5-loops)	116584718.1 (0.2)
LO hadronic vacuum polarization	6903.0 (52.6)
NLO hadronic vacuum polarization	-100.3 (1.1)
Hadronic light-by-light	116.0 (39.0)
Weak (incl. 2-loops)	153.2 (1.8)
Theory	116591790.0 (64.6)
Experiment	116592080.0 (63.0)

Table 4.1: Decomposition of the theoretically predicted a_μ into contributions form different SM sectors and comparison with the experimental measurement.

perturbation theory, respectively, and the data for the hadronic vacuum polarization. The remaining classes $(2d)$ and $(2e)$ are of a different character. They involve hadronic light-by-light scattering diagrams, denoted by the effective four-photon vertex with the shading representing the full QCD interaction. The contributions resulting from the former vacuum-polarization type diagrams can be calculated in Minkowski and Euclidean space [85, 111], once data for the hadronic vacuum polarization is available. By contrast the light-by-light contributions cannot be rigorously represented such that the non-perturbative QCD effects can be accounted for by vacuum polarization insertions. In particular a dispersive ansatz using experimental data is not possible in this case. For these contributions one has to resort to models and effective theories to decompose the effective four-photon vertex [71, 10, 70, 90, 89, 24] or use lattice techniques different from those discussed in this work. Such an investigation has for instance been started by the authors of reference [20]. According to the analysis in [85] the relative contribution of the hadronic leading order a_μ^{hlo} amounts to approximately 6×10^{-3} %. The hadronic light-by-light scattering and higher-order vacuum polarization contributions add about 10^{-4} % and -9×10^{-5} %, respectively.

Finally, in figure [4.3] we exemplarily list the leading order weak corrections to the muon-photon vertex that give a further correction a_μ^{weak}, which is of relative size 1.3×10^{-4} %.

We summarize the situation in table {4.1}. This compilation clearly brings out the

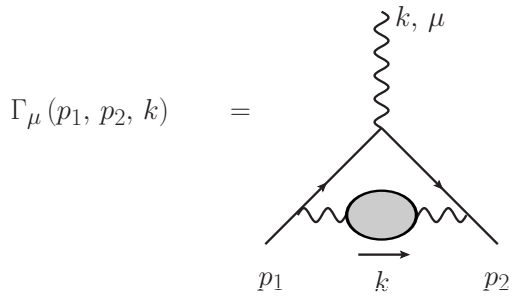

Figure 4.4: Leading order hadronic correction to the electromagnetic vertex with assigned momenta as used in equation (4.9).

conclusions of this brief review: the LO hadronic and the light-by-light contribution give the by far largest contributions to the uncertainty of the final estimate. Thus the first step in improving on the theoretical uncertainty of the anomalous magnetic moment of the muon must be a careful analysis of the leading order hadronic contribution and a reduction of its uncertainty. In terms of diagram (1) in figure [4.2] this means a precise evaluation of the 1-loop hadronic correction to the muon-photon vertex and in particular gaining control over the hadronic vacuum polarization insertion into the photon propagator.

4.1.1 Leading order hadronic contribution

In the previous subsection we discussed the decomposition of the electromagnetic vertex in the standard model and QCD in particular. We now focus on the form factor $F_M(q^2)$ that determines the anomalous magnetic moment $a_l = F_M(q^2 = 0)$. We consider the correction to the lepton-lepton-photon vertex as depicted in figure [4.4].

A commonly used tool for the extraction of the form factors listed in equation (4.5) from the amputated vertex is the projection method: for each form factor F_X, $X = E$, M, it defines a projector $P_X\,(p_1, p_2, m_l)$, such that $F_X = \mathrm{Tr}\left(P_X^\mu\,(p_1,\,p_2,\,m_l)\,\Pi_\mu\,(p_1,\,p_2,\,m_l)\right)$. The details have been given in e.g. reference [83].

The leading order hadronic correction Π_μ^{hlo} to the vertex function follows from the relevant interaction lagrangian of the form

$$\mathcal{L}_{QED}^{int} = e\,J_\mu^{\mathrm{em}\,lep}\,A^\mu + e\,J_\mu^{\mathrm{em}\,had}\,A^\mu\,, \tag{4.8}$$

where we use the notation $J_\mu^{\mathrm{em}\,lep}$ and $J_\mu^{\mathrm{em}\,had}$ for the leptonic and hadronic electromagnetic currents, respectively, and A^μ for the photon field.

The Feynman diagram in figure [4.4] then corresponds to a fourfold insertion of the QED interaction term in the perturbative expansion (at order $e^4 \propto \alpha_{\mathrm{QED}}^2$), while we keep the full QCD interaction term and treat the hadronic electromagnetic current correlator

in an exact, non-perturbative manner.

$$\begin{aligned}\Pi_\mu^{\text{hlo}}(p_1,\, p_2,\, m_l) = \int dx_1\, dx_2\, dx_3\, dx_4\, \langle l^\pm \,|\, (ie)^4\, J_\mu^{\text{em},lep}(x)\, J_\kappa^{\text{em},lep}(x_1)\, A^\kappa(x_1)\, A^\lambda(x_2) \times \\ \left[J_\lambda^{\text{em},had}(x_2)\, J_\rho^{\text{em},had}(x_3)\, \exp\left(-iS_{\text{QCD}}^I\right)\right] \times \\ A^\rho(x_3)\, A^\sigma(x_4)\, J^{\text{em},lep}\,|\, l^\pm\rangle_{\text{QED+QCD}}^{\text{amp,tl}} \\ = \int d\hat{k}\, (ie\gamma_\kappa)\, \frac{i}{\not{p}_2 - \not{k} - m_\mu + i0^+}\, (ie\gamma_\mu)\, \frac{i}{\not{p}_1 - \not{k} - m_\mu + i0^+} (ie\gamma_\sigma) \\ \times \frac{-ig^{\kappa\lambda}}{k^2 + i0^+} \left[\Pi_{\lambda\rho}\right] \frac{-ig^{\rho\sigma}}{k^2 + i0^+}\,. \end{aligned} \tag{4.9}$$

We used the notation $d\hat{k} = d^D k/(2\pi)^D$ for the integration measure in Minkowski-space time, that is finally evaluated for $D = 4$, and $-ig_{\mu\nu}/(k^2 + i0^+)$ for the photon propagator in Feynman gauge.

The corresponding vacuum expectation value of the hadronic current correlator in full QCD is denoted by

$$\Pi_{\lambda\rho}(k) = i \int d^4x\, \mathrm{e}^{i\,x\cdot k}\, \langle J_\lambda^{\text{em},had}(x)\, J_\rho^{\text{em},had}(0)\, \mathrm{e}^{-iS_{\text{QCD}}^I}\rangle_{\text{QCD}}^{\text{tl}} = \left(-g_{\lambda\rho}\, k^2 + k_\lambda k_\rho\right) \Pi\,(k^2) \tag{4.10}$$

The polarization tensor and function have been discussed in detail in the previous chapter. The further evaluation of the integral, including carrying out the projection, Wick rotation, additive renormalization of the hadronic vacuum polarization and angular integrals use standard techniques. The calculation has been laid out previously in the literature and we thus skip the details.

What we are finally left with is an integral over the squared Euclidean virtual photon momentum of the following form

$$a_l^{\text{hvp}} = \int_0^\infty \frac{dk^2}{k^2}\, w(k^2)\, \Pi_R(k^2) \tag{4.11}$$

with the weight function $w(k^2;\, m_l^2)$ given by

$$\begin{aligned} w(k^2;\, m_l^2) &= \frac{m_l^2 k^4\, Z^3\, (1 - k^2 Z)}{(1 + m_l^2 k^2 Z^2)} \\ Z &= \frac{2}{k^2 + \sqrt{k^4 + 4m_l^2 k^2}}\,. \end{aligned} \tag{4.12}$$

This is the definition of the anomalous magnetic moment we will use in our lattice calculation by inserting the lattice vacuum polarization into the integral. It is important

to emphasize that the integral in equation (4.11) is over space-like momenta $k^2 \geq 0$. This is the realm, where we have access to lattice data for the vacuum polarization function for all k^2 up to the lattice cut off.

For our later discussion it will be interesting to look at the shape of the weight function in more detail. For large momenta or small lepton mass, $k^2 \gg m_l^2$, we can look at the asymptotic behavior in the small quantity m_l^2/k^2

$$\begin{aligned} Z &\sim \frac{1}{k^2} - \frac{m_l^2}{k^4} + O\left(\left(\frac{m_l^2}{k^2}\right)^3\right) \\ w(k^2; m_l^2) &\sim \left(\frac{m_l^2}{k^2}\right)^2 + O\left(\left(\frac{m_l^2}{k^2}\right)^3\right). \end{aligned} \tag{4.13}$$

At the lower integration limit where $k^2 \ll m_l^2$ we have the asymptotic expansion

$$\begin{aligned} Z &\sim \frac{1}{m_l^2}\sqrt{\frac{m_l^2}{k^2}} + O(1) \\ w(k^2; m_l^2) &\sim \frac{1}{2}\sqrt{\frac{k^2}{m_l^2}} + O\left(\left(\frac{k^2}{m_l^2}\right)\right). \end{aligned} \tag{4.14}$$

Moreover the weight function has one maximum at $k^2/m_l^2 = \sqrt{5} - 2$. Note that though the weight is divergent at the origin, the integral is well defined. Moreover, the analyticity properties of the subtracted polarization function demand that it is proportional to k^2 close to the origin.

From the behavior given in equations (4.13) and (4.14) it becomes clear that due to the weight function the integral will be highly dominated by the low momentum region. Here we find the mathematical expression of our motivation stated in the introduction that indeed the theoretical tools of lattice QCD are necessary to provide data for the vacuum polarization function in the low-momentum regime. We amplify this point by showing in figure [4.5] the functional dependence of $w(k^2; m_\mu^2)$ in a range of momenta that is of primary interest for the integral, $0 \leq k^2 \leq 2\,\mathrm{GeV}^2$.

Two further limiting cases are the limit of zero and infinitely large lepton mass. In both cases the integral becomes zero, which can be seen from equations (4.13) and (4.14). The massless case can be interpreted in terms of chiral symmetry properties [83]: the lepton anomaly codifies helicity flips of the leptons. The term in the lagrangian that couples left- and right-handed lepton modes is the mass term. The anomalous magnetic moment generates (at non-zero lepton mass) an effective coupling of the form

$$\mathcal{L}_{a_l} = \frac{e a_l}{4 m_l}\,\bar{\psi}\,\sigma_{\mu\nu}\,\psi\,F^{\mu\nu}\,. \tag{4.15}$$

which couples left- and right-handed leptons and reduces to the well known coupling

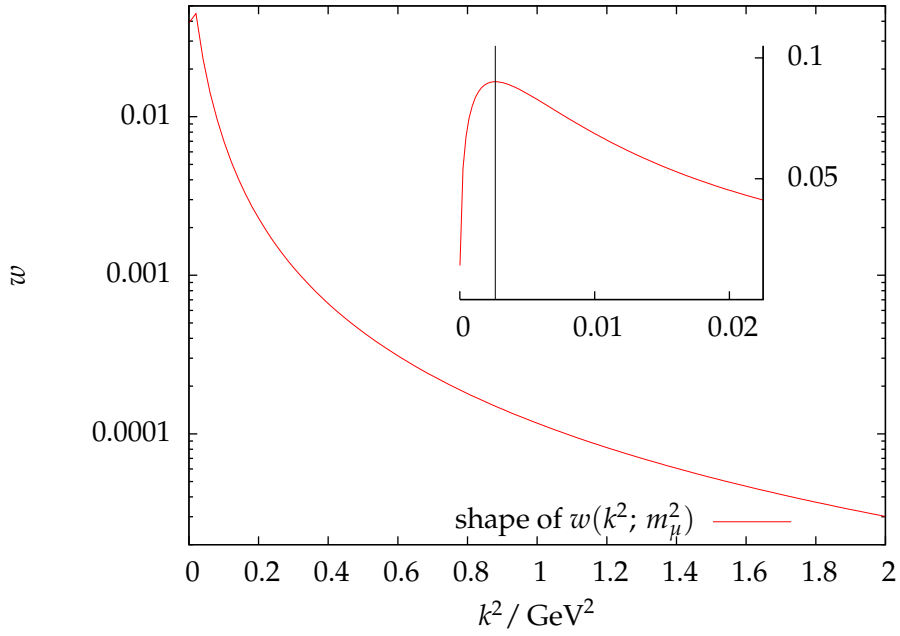

Figure 4.5: Shape of the weight function w. The detail shows the behavior in the small momentum region; the vertical line marks the position of the maximum.

of the spin and magnetic field $\propto \vec{s} \cdot \vec{B}$ in the non-relativistic limit.

If the lepton mass is zero, there is no coupling of left- and right-handed lepton fields in the original lagrangian and the latter is invariant under chiral symmetry transformations. Since chiral symmetry cannot be broken by a perturbatively induced effective coupling and the magnetic anomaly breaks chiral symmetry, the anomalous magnetic moment will not be present in the perturbative approach followed here. As was pointed out in [55] it can however be generated non-perturbatively in a phase where chiral symmetry is broken and a chiral condensate is formed as well as a lepton mass dynamically generated. Such a scenario has been discussed for instance for massless charged leptons in a constant and uniform magnetic field in 2+1 dimensions [65].

4.1.2 Hadronic R-ratio and experimental measurement of the leading order lepton anomaly

In the previous subsection we outlined the definition and origin of the lepton anomaly as a form factor in the structure of the photon-lepton vertex. This version will be directly linked to the lattice calculation to follow. Before that, however, we would like to highlight the relation to the traditional approach of calculating a_μ^{hlo}, which at the same time was the only rigorous treatment of the anomaly before the advancement of lattice methods. To date it still provides the most precise estimate of the leading order hadronic contribution to the muon anomaly and is the standard choice for evaluating the final $g_\mu - 2$.

In the following discussion we will for the moment go back to Minkowski space such that Euclidean momenta have negative square, $k_E^2 \leq 0$. The central ingredient in the defining integral in equation (4.11) is the hadronic vacuum polarization function $\Pi(-k_E^2)$ which must be known over the complete momentum range $-\infty < k_E^2 \leq 0$, but due to the weight function especially in the region of small absolute value of momentum: the major contributions to the integral arise from physics at scales beneath $1\,\mathrm{GeV}^2$.

In this low-momentum region the running strong coupling α_s assumes values of $O(1)$ and the perturbative expansion with presently manageable loop orders becomes unreliable. A similar statement holds for the non-analytic, purely non-perturbative behavior at quark flavor thresholds, when a new channel for the pair production of a quark flavor and the formation of associated hadronic states in the vacuum polarization process opens up [1].
Moreover, there is also no rigorous perturbative treatment in momentum ranges that favor the resonant production of hadronic excitations like the light vector mesons.

Thus data for the integrand must be acquired from a likewise non-perturbative source. In this work we use $\Pi\left(-k_E^2\right)$ as determined in a first-principles lattice calculation to estimate the integral (4.11) over the space-like momentum region. Unitarity of the scattering matrix and causality allow for a transformation of the integral over the space-like momentum region into one over time-like momenta above the two-particle threshold. This is precisely the region of momenta that is accessible in experimental scattering and decay processes.

Copying from chapter 3 we write the once subtracted polarization function as an integral of the imaginary part along the branch cut

$$\Pi(s) - \Pi(0) = \frac{s}{\pi} \int_{s_0}^{\infty} ds' \, \frac{\mathrm{Im}\left(\Pi(s')\right)}{s'(s-s')} \,. \tag{4.16}$$

starting at $s_0 = 4\,m_\pi^2$, which is the center of mass energy for the production of the lowest lying hadronic final state consisting of a pion pair, $e^+e^- \to \gamma^* \to \pi^+\pi^-$. Together with R_h, the cross section for electron-positron annihilation to hadronic final states normalized by the cross section for annihilation to pair production of muons (point cross section)

$$R_h(s) = \frac{\sigma\left(e^+e^- \to \gamma^* \to \{H\}\right)}{\sigma\left(e^+e^- \to \gamma^* \to \mu^+\mu^-\right)} = 12\pi\,\mathrm{Im}\left(\Pi(s)\right) \,,$$

the subtracted polarization function can be represented by a dispersion integral using experimental data for the $R-$ratio.

One thus has the following integral representation of the leading order hadronic contribution a_μ^{hlo}, which is the starting formula for traditional and currently most precise

[1] There are, however, methods to model the energy dependence of the polarization function in the region approaching a flavor threshold from above as demonstrated for example in references [72, 88]

determinations of a_μ^{hlo}

$$a_\mu^{\text{hlo}} = \left(\frac{\alpha m_\mu}{3\pi}\right)^2 \int_{s_0}^{\infty} \frac{ds}{s^2} R_h(s)\, \hat{K}(s) \tag{4.17}$$

where $\alpha = \alpha_{\text{QED}}(s)\big|_{s=0}$ is the fine structure constant and the weight function $\hat{K}(s)$ is given by [26]

$$\hat{K}(s) = \frac{3s}{m_\mu^2} \int_0^1 \frac{x^2\,(1-x)}{x^2 + (1-x)\,s/m_l^2}\,.$$

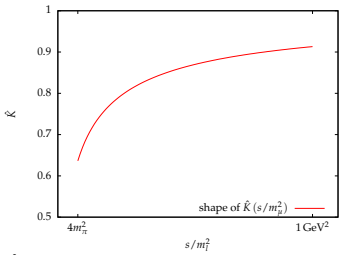

As shown in the figure above, the weight $\hat{K}(s)$ is a bounded and slowly rising function in the integration range. Thus similar to the case of the integral over space-like momenta in equation (4.11) the complete integration weight $\hat{K}(s)/s^2$ is steeply rising towards lower momenta and hence the low-momentum contributions to the hadronic R-ratio will dominate the integral.

At high enough energies (and thus at smaller values of the strong coupling) and sufficiently far from the flavor thresholds the cross section $\sigma(e^+e^- \to q\bar{q})$ can be reliably calculated in perturbation theory. The quark-hadron-duality then allows for the identification of $\sigma(e^+e^- \to q\bar{q})$ and $\sigma(e^+e^- \to \{H\})$ and the experimentally determined cross section ratio, $R_h^{\text{exp}}(s)$, can be safely replaced with its perturbative counterpart, $R_h^{\text{pQCD}}(s)$, if the necessary input values for quark masses and the running strong coupling are given. If s_{pQCD} denotes the value of this threshold energy then the integral formula is modified to

$$a_l^{\text{hlo}}(DR) = \left(\frac{\alpha m_\mu}{3\pi}\right)^2 \left(\int_{s_0}^{s_{\text{pQCD}}} \frac{ds}{s^2} R_h^{\text{exp}}(s)\, \hat{K}(s) + \int_{s_{\text{pQCD}}}^{\infty} \frac{ds}{s^2} R_h^{\text{pQCD}}(s)\, \hat{K}(s) \right). \tag{4.18}$$

The application of equations (4.17) and (4.18) to estimate the hadronic leading order contribution to the muon anomaly requires to gather the experimental data for $R_h(s)$ from the numerous experiments that focus on different regions of center of mass energy and to perform the data analysis. Since different experiments are oftentimes designed with overlapping energy regions and as individual experiments in many cases provide data from several runs separated in time and possibly with a modified setup the analysis requires a specification of strategies for choosing data to be included, combining and modeling it and estimating statistical and systematic errors for the energy dependent R-ratio as well as the final integral. Such strategies, of which there are many, will depend on the group carrying out the analysis and the available data. Two recent examples can be found in references [67, 34]. In table {4.2} we quote an updated version of the corresponding table 4 in [85] of final estimates and uncertainties of the lowest order

No.	$a_\mu^{\mathrm{hlo}}(DR) \times 10^{10}$	reference
(1)	693.5 (5.9)	de Troconiz 2004 [35]
(2)	701.8 (5.8)	de Troconiz 2004 (τ)[35]
(3)	690.8 (4.4)	Davier 2007 [33]
(4)	692.3 (4.2)	Davier et al. 2010 [34]
(5)	701.5 (4.7)	Davier et al. 2010 (τ)[34]
(6)	690.9 (4.4)	Eidelman 2007-2009 [45, 47, 46]
(7)	689.4 (4.6)	Hagiwara 2006 [66]
(8)	694.9 (4.2)	Hagiwara 2011 [67]
(9)	692.1 (5.6)	Jegerlehner 2006 [81]
(10)	690.3 (5.3)	Jegerlehner 2008, 2009 [82, 84]

Table 4.2: Results for $a_\mu^{\mathrm{hlo}}(DR)$ from e^+e^- (and τ decay) data.

hadronic contribution to provide an overview of the magnitude of deviations arising amongst different analysis methods.

The τ symbol at the reference means that the value was obtained using data for the τ decay to pions, the unmarked results are obtained using electron-positron annihilation data only. For the quoted results the values vary in a region $689.4 \leq a_\mu^{\mathrm{hlo}}(DR) \leq 701.8$. All of the (e^+e^-)-data based results are in mutual agreement within one standard deviation, whereas the (e^+e^+, τ)-data based results mutually agree and agree with the former results within two standard deviations (cf. figure [4.6]).

As mentioned earlier the dispersion integral (4.17) is the only alternative non-perturbative treatment of a_μ^{hlo} besides the lattice calculation. It will thus be the basis for an independent comparison of the results of our lattice method. Our determination of a_μ^{hlo} will be for QCD with two light quark flavors, so it will not be possible to compare directly to the numbers in table {4.2}. In fact, in order to enable a meaningful comparison to the dispersion integral method, we will have to specify a way for extracting the flavor dependent value of the leading order hadronic contribution from the data used in reference [82], which we use as a standard reference for the experimental determination using the dispersion integral method. There we can find the decomposition of the integral into contributions from different resonances and energy regions, which will be necessary for a the comparison later on.

4.2 Phenomenological analysis of a_μ^{hlo}

We displayed a survey of the contributions to the muon anomaly from the different sectors of the standard model as presently known in section 4.1. Now we will focus further on the decomposition of the leading order hadronic contribution within QCD and in the spirit of the segmentation of the dispersion integral as done in [82] or [34]. Due to our calculation setup including up and down sea quarks special emphasis will be put on the disentanglement of contributions from different flavors.

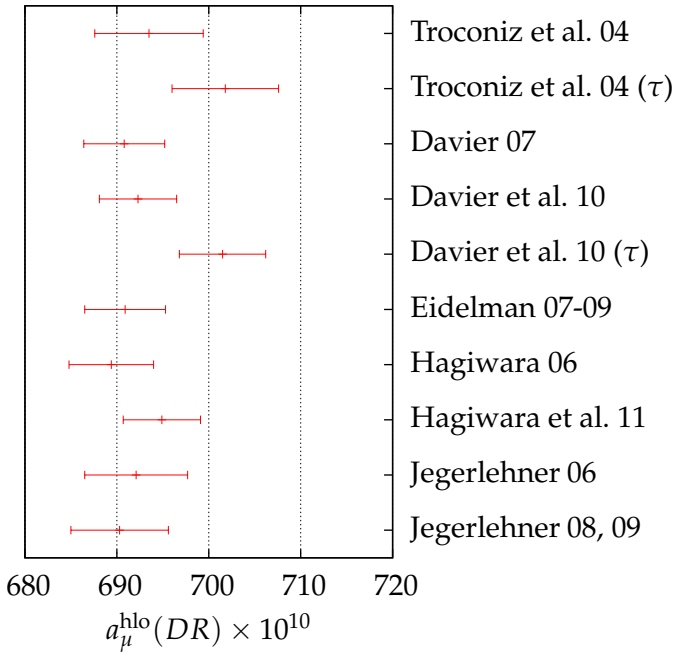

Figure 4.6: Results for $a_\mu^{\rm hlo}$ from different analyses using e^+e^- (and τ decay) data.

flavor	(u,d)	s	c	b
final state	$\pi^0\,\gamma$ / $\pi^+\,\pi^-$	$\eta\,\gamma$ / K_S, K_L	$J/\psi(1S)$ / 2 D	$\Upsilon(1S)$ / 2 B
$E_{\rm threshold}$ [GeV]	0.135 / 0.279	0.548 / 0.995	3.10 / 3.73	9.46 / 10.6

Table 4.3: Quark flavor dependent energy thresholds for the first flavored hadronic final state.

In support of our following discussion we show data for the hadronic cross section ratio in the three panels of figure [4.7] as provided in reference [85].

We will first focus on the region for center of mass energy E ranging from the 2-pion threshold up to and including the ϕ resonance, $2m_{\pi^\pm} \leq E \lesssim 1.020\,\text{GeV}$. This corresponds to the complete range displayed in the top panel of figure [4.7] and the left boundary region of the middle panel. Hadronic physics in this region is largely shaped by the light vector meson resonances, the neutral $\rho\,(770\,\text{MeV})$, the $\omega\,(782\,\text{MeV})$ and the $\phi\,(1020\,\text{MeV})$ meson. The active quark degrees of freedom are up, down and strange.

The preferred decay modes of the light vector meson resonances are given by final states involving multiple pions or multiple pions plus a photon. A very detailed account of the decay channels is given in TABLE II of reference [34]. Moreover, in this energy interval the hadronic R-ratio cannot be represented as an inclusive quantity given the need to discriminate the relevant hadronic final states from the leptonic ones. Thus a channel-by-channel identification of final states and summation of contributions to $a_\mu^{\rm hlo}(DR)$ is mandatory. The 2-pion decay is the dominant channel in the interval

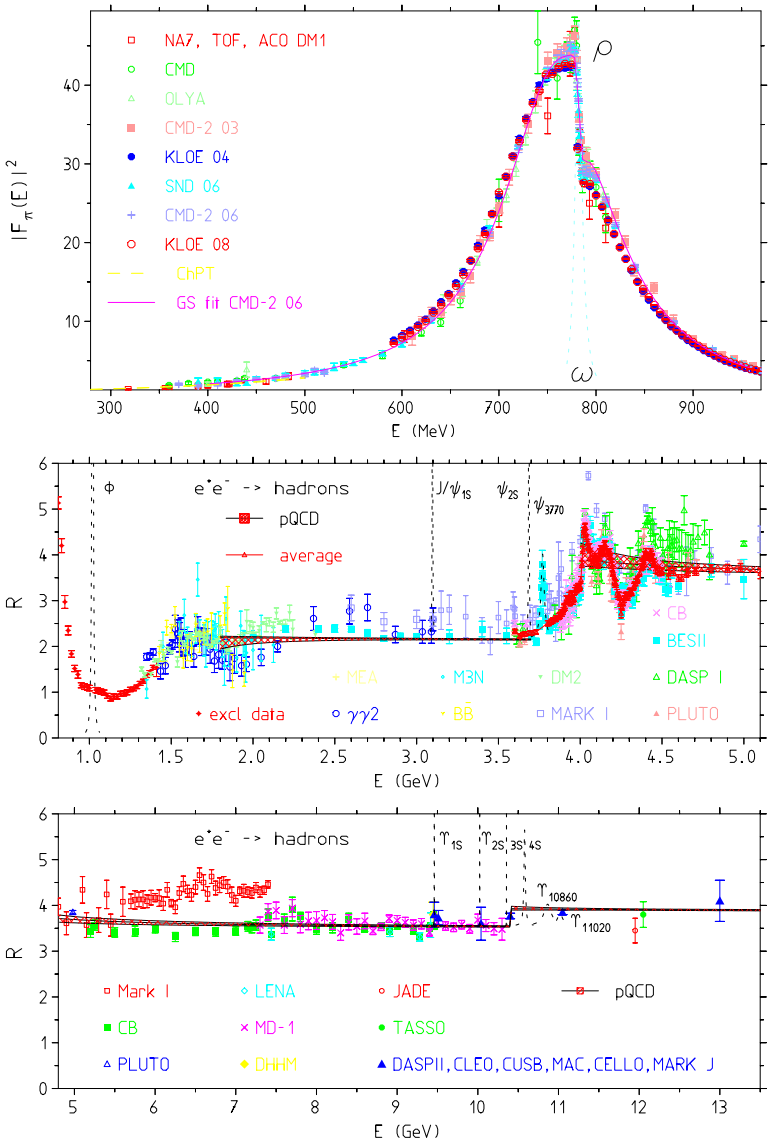

Figure 4.7: Compilation of experimental results for the hadronic R-ratio in different energy regions: ρ resonance region (top), $1\,\text{GeV} \leq E \leq 5\,\text{GeV}$ (middle) and $5\,\text{GeV} \leq E \leq 13\,\text{GeV}$ (bottom). The plots are taken from [85].

$2m_{\pi^\pm} \leq E < 3m_{\pi^\pm}$. The partial R-ratio for this channel is related to the effective coupling of a photon to two oppositely charged pions, which is the electromagnetic pion form factor $eF_\pi(E)$ times a kinematical factor

$$R_h^{\pi\pi}(s) = \frac{1}{4}\left(1 - \frac{4m_\pi^2}{s}\right)^{\frac{3}{2}} \left| F_\pi^{(0)}(E) \right|^2 , \tag{4.19}$$

where $F_\pi^{(0)}$ denotes the undressed electromagnetic pion form factor without vacuum polarization effects. The top panel of figure [4.7] shows the experimentally measured pion form factor data from threshold across the ρ resonance region.

In a decay channel-wise inspection of R_h and the contributions to $a_\mu^{\mathrm{hlo}}(DR)$ of all the multi-pion decay modes the 2-pion channel gives the by far largest portion of the integral [34]. The former amounts to approximately 73% of the final value. It is followed by the channels $e^+e^- \to \pi^+\pi^-\pi^0$ ($\approx 7\%$), $e^+e^- \to \pi^+\pi^- 2\pi^0$ (2.6%) and $e^+e^- \to 2\pi^+2\pi^-$ ($\approx 2\%$).

From these numbers we understand that this momentum interval from threshold to the ϕ resonance contains more than 80% of contributions to the muon anomaly. In our lattice data analysis we will not digress into the details of individual decay channels but stay with the language of the vector meson resonances. In terms of them the contributions read as follows (cf. table {4.4} below):

Meson X	ρ	ω	ϕ
$a_{\mu\ X}^{\mathrm{hlo}}(DR) \cdot 10^8$	5.011 (30)	0.370 (11)	0.344 (09)

The ρ resonance is strongly tied to the 2-pion decay contribution, since the PDG listing tells us that the fraction of ρ decays via two pions is almost 100%; thus the ρ alone accounts for about 73% of the a_μ^{hlo} and the three resonances together amount to 83% of the total number. The observation of the impact of the low-lying vector resonances on a_μ^{hlo} based on R_h brings into focus the conceptual question, to which extent is the lattice model capable of reproducing the contributions from the light vector mesons. We pay particular attention to this issue in our analysis, to optimally carve out the vector meson contribution from the lattice vacuum polarization data. Notwithstanding the importance of this momentum region, to reach the few percent level of precision in determining a_μ^{hlo} the contributions from the adjacent intermediate momentum region shaped by strange and charm physics will have to be properly taken into account as well.

Continuing along the center of mass energy axis in the middle panel of figure [4.7] we pass the threshold for pair production of strange mesons (cf. table {4.3}) and beyond the resonance region the R-ratio rises to the 3-flavor asymptotic value given by perturbative

QCD

$$R_h^{\mathrm{pQCD}}\Big|_{\mathrm{asymptotic}} = 3 \sum_{\text{active flavors } f} (Q_f^{\mathrm{em}})^2$$
$$= \begin{cases} 5/3 & \approx 1.67 \quad N_f = 2 \\ 6/3 & = 2 \quad\;\; N_f = 3 \\ 10/3 & \approx 3.33 \quad N_f = 4 \\ 11/3 & \approx 3.67 \quad N_f = 5 \end{cases}$$

This quasi-plateau in the mid-panel of figure [4.7] persists up to the charmed resonances starting with the J/ψ at $E \approx 3.1\,\mathrm{GeV}$. There the pattern of resonance region followed by meson pair production threshold and asymptotic behavior repeats itself up to the bottom region, where another such sequence starting with the $\Upsilon(1S)$ resonance begins. The contribution from the J/ψ resonance region amounts to $8.51\,(55) \times 10^{-10}$. Recalling the difference $a_\mu^{\mathrm{ex}} - a_\mu^{\mathrm{th}} = 290(90) \times 10^{-11}$ the inclusion or exclusion of this would have an effect of order of one standard deviation in the discrepancy. Thus the charm quark contribution to the muon anomaly is at the moment on the edge of significance. Any potential realistic estimation aiming at an impact on the discrepancy will have to properly take into account both strange and charm degrees of freedom.

The major bottom quark contribution is represented by the Υ resonance region and its size is $O\left(10^{-11}\right)$. It thus does not have a significant effect given the currently achievable precision.

4.2.1 Extraction of $a_\mu^{\mathrm{hlo}}(DR, N_f)$: quark-hadron-duality vs. decay channel decomposition

In the following we would like to arrive at a dispersion integral based estimate of the N_f dependent leading order hadronic contribution to the muon anomaly. Such an estimate will rely on data obtained in actual experiments and in any given energy region all active quark flavors will interrelatedly contribute to R_h. In the end a unique flavor-wise separation of contributions will be impossible and we will have to resort to a choice of prescription that will always be an approximation afflicted with systematic uncertainties.

We contrast two different ways of extracting the leading order hadronic contribution to the muon (or again lepton in general) anomaly depending on the number of sea quark flavors. We consider QCD-like theories that differ by the maximal number of active sea quark flavors. A special case is of course our lattice calculation with $N_f = 2$ light sea quarks that are the only active quark degrees of freedom irrespective of the energy scale.

The first method is motivated by the principle of quark-hadron-duality (QHD) and allows the N_f-dependent extraction even for data from inclusive measurements, where a decomposition into definite final states is not possible. The second one requires precisely that detailed decomposition of R_h into individual final states (decay channel

decomposition DCD), which will allow us to single out those contributions that we attribute to a certain quark flavor. The procedure was brought to our attention by private communication with Michel Davier and his collaborators.

To illustrate our discussion we recite in table {4.4} a combined and compactified version of TABLE II in [34] and Table 1 from [82]; this data will be the basis for our $a_\mu^{\rm hlo}(DR)$ estimates.

We will start with the QHD method and use the data provided in the rightmost three columns of table {4.4}. The principle of quark-hadron-duality states that the averaged non-perturbative cross section of electron-positron annihilation is approximately equal to the perturbative quark cross section at center of mass energy squared s if the averaging includes the energy range $[E_{\rm thr},\ \sqrt{s}]$ [83] .

$$\overline{\sigma\left(e^+e^-\to\{H\}\right)} = \sum_{q\in\,[E_{\rm thr},\ \sqrt{s}]} \sigma_q\left(e^+e^-\to q\bar{q}\right), \tag{4.20}$$

where the notation $q \in [E_{\rm thr},\ \sqrt{s}]$ denotes that the sum extends over all quark flavors whose pair production channel is open in the given energy interval. In the quark loop picture each quark flavor q that is open for pair production adds a contribution $Q_q^2\,\Pi^q(s)$ to the vacuum polarization function, where in Π^q the photon couples to the pair of quarks of flavor q, and Q_q is the electromagnetic charge in units of the positron charge e of the quark flavor. Guided by the asymptotic behavior, that once active each quark flavor gives an equal contribution, we use a reweighing procedure of the form

$$\Pi_{N_f}(s) = \frac{\sum\limits_{q\in[E_{\rm thr},\ \sqrt{s}],\,q\le N_f} Q_q^2}{\sum\limits_{q\in[E_{\rm thr},\ \sqrt{s}]} Q_q}\,\Pi_{\rm data}(s)\,. \tag{4.21}$$

Given the data in the rightmost three columns of table {4.4} this amounts to the energy interval dependent reweighing factors for the case $N_f = 2$

energy interval [GeV]	reweighing factor
(0.28, 3.10)	5/6
(3.10, 9.46)	5/10
(9.46, ∞)	5/11

Strictly speaking this will be a correct approximation at high energy sufficiently far from flavor thresholds, where the cross section is well approximated by the asymptotic perturbative behavior. However, given the ambiguities we must accept in the first place, we feel that this method – even if applied for lower $\sqrt{s}$ – will give a meaningful estimate. To get back to the vacuum polarization in the hadron picture we simply go the opposite way from the right- to the left-hand side in equation (4.20). We thus arrive at the value for the two-flavor contribution

$$a_\mu^{\rm hlo}(DR,\,N_f=2) = 566.0\,(4.4)10^{-10}\,. \tag{4.22}$$

Davier et al. [34]		Jegerlehner [82]		
Channel	$a_\mu^{\rm hlo}(DR)\cdot 10^{10}$	Ch.		$a_\mu^{\rm hlo}(DR)\cdot 10^{10}$
$\pi^0\gamma$	4.42 (0.19)	ρ	(0.28, 0.99)	501.07 (3.02)
$\eta\gamma$	0.64 (0.02)	ω	(0.42, 0.81)	36.96 (1.09)
$\pi^+\pi^-$	507.80 (2.84)	ϕ	(1.00, 1.04)	34.42 (0.93)
$\pi^+\pi^-\pi^0$	46.00 (1.48)	J/ψ		8.51 (0.55)
$2\pi^+2\pi^-$	13.35 (0.53)	Y		0.10 (0.01)
$\pi^+\pi^-2\pi^0$	18.01 (1.24)	$R_{\rm data}$	(0.99, 2.00)	67.12 (3.87)
$2\pi^+2\pi^-\pi^0$ (η excl.)	0.72 (0.09)	$R_{\rm data}$	(2.00, 3.10)	22.13 (1.23)
$\pi^+\pi^-3\pi^0$ (η excl., from isospin)	0.36 (0.04)	$R_{\rm data}$	(3.10, 3.60)	4.02 (0.11)
$3\pi^+3\pi^-$	0.12 (0.01)	$R_{\rm data}$	(3.60, 9.46)	13.89 (0.08)
$2\pi^+2\pi^-2\pi^0$ (η excl.)	0.70 (0.11)	$R_{\rm data}$	(9.46, 13.00)	1.30 (0.09)
$\pi^+\pi^-4\pi^0$ (η excl., from isospin)	0.11 (0.11)	R_{QCD}	(13.0, ∞)	1.53 (0.00)
$\eta\pi^+\pi^-$	1.15 (0.10)			
$\eta\omega$	0.47 (0.06)			
$\eta 2\pi^+2\pi^-$	0.02 (0.01)			
$\eta\pi^+\pi^-2\pi^0$ (estimated)	0.02 (0.01)			
$\omega\pi^0$ ($\omega\to\pi^0\gamma$)	0.89 (0.07)			
$\omega\pi^+\pi^-, \omega 2\pi^0$ ($\omega\to\pi^0\gamma$)	0.08 (0.01)			
ω (non-$3\pi, \pi\gamma, \eta\gamma$)	0.36 (0.01)			
K^+K^-	21.63 (0.73)			
$K_S\,K_L$	12.96 (0.39)			
ϕ (non-$K\bar{K}, 3\pi, \pi\gamma, \eta\gamma$)	0.05 (0.00)			
$K\bar{K}\,\pi$ (partly from isospin)	2.39 (0.16)			
$K\bar{K}\,2\pi$ (partly from isospin)	1.35 (0.39)			
$K\bar{K}\,3\pi$ (partly from isospin)	-0.03 (0.02)			
$\phi\,\eta$	0.36 (0.03)			
$\omega\,K\bar{K}$ ($\omega\to\pi^0\gamma$)	0.00 (0.00)			
J/ψ (Breit-Wigner integral)	6.22 (0.16)			
$\psi(2S)$ (Breit-Wigner integral)	1.57 (0.03)			
$R_{\rm data}$ [3.7 – 5.0 GeV]	7.29 (0.30)			
R_{QCD} [1.8 – 3.7 GeV]$_{uds}$	33.45 (0.28)			
R_{QCD} [5.0 – 9.3 GeV]$_{udsc}$	6.86 (0.04)			
R_{QCD} [9.3 – 12.0 GeV]$_{udscb}$	1.21 (0.01)			
R_{QCD} [12.0 – 40.0 GeV]$_{udscb}$	1.64 (0.01)			
R_{QCD} [> 40.0 GeV]$_{udscb}$	0.16 (0.00)			
R_{QCD} [> 40.0 GeV]$_t$	0.00 (0.00)			
Sum	692.3 (4.2)			691.0 (5.3)

Table 4.4: Integrated data for $a_\mu^{\rm hlo}(DR)$ decomposed into resonance contributions and perturbative regions for individual final states (left, [34]) and inclusively for energy intervals (right, [82]).

N_f	$a_e^{\rm hlo}(DR,\, N_f)\times 10^{14}$	$a_\mu^{\rm hlo}(DR,\, N_f)\times 10^{10}$	$a_\tau^{\rm hlo}(DR,\, N_f)\cdot 10^{8}$
2	155.3 (3.4)	566.0 (4.4)	268.1 (7.6)
3	186.4 (4.1)	679.2 (5.3)	321.7 (9.2)
4	188.4 (4.1)	690.8 (5.3)	337.6 (9.3)
5	188.5 (4.1)	691.1 (5.3)	338.3 (9.3)

Table 4.5: Estimates for the lepton anomalies $a_l^{\rm hlo}(DR, N_f)$, $l = e,\, \mu,\, \tau$, for QCD models with 2 to 5 flavors; the 5-flavor values correspond to the estimates in the original literature for the muon [82] and the electron and τ [80]

N_f	$a_\mu^{\rm hlo}(DR,\, N_f)\cdot 10^{10}$
2	629.2 (3.5)
3	677.5 (3.6)
4	692.1 (3.6)
5	692.3 (3.6)

Table 4.6: Estimates for the muon anomaly $a_\mu^{\rm hlo}(DR, N_f)$, for QCD models with 2 to 5 flavors; the 5-flavor values correspond to the estimates in the original literature [34].

For later use we shall repeat this calculation also for the two other standard model leptons. The corresponding additional values for the electron, muon and τ lepton for the cases $N_f = 2,\, 3,\, 4,\, 5$ are collected in table {4.5}.

For the DCD method we start from the leftmost two columns of table {4.4}. The point of DCD, we follow here, is to attribute each final state to a certain flavor combination according to the following rules

1. final states including only $\pi^\pm$, π^0 or ω and γ contribute to $N_f \geq 2$;
2. final states including η, ϕ or $K^\pm$, K_L^0, K_S^0, K, $\bar{K}$ contribute to $N_f \geq 3$;
3. final states including J/ψ, $\Upsilon(2S)$ contribute to $N_f \geq 4$;
4. non-resonant, intermediate energy intervals are treated as in the QHD case by appropriate rescaling with the charge Q-factor;

For the muon anomaly this strategy results in the numbers given in table {4.6}.

A remark on the error estimates is in order. In our procedure we add all errors from distinct energy regions and/or decay channels in quadrature. The neglect of the existing correlations of the errors, discussed e.g. in [34], makes it clear that we must regard both uncertainties as a crude estimate.

Given the results for $a_\mu^{\rm hlo}(DR,\, N_f = 2)$ from QHD and DCD in tables {4.5} and {4.6}, respectively, we observe that both results are subject to a relative deviation of

$$a_\mu^{\rm hlo}(DCD,\, N_f = 2) - a_\mu^{\rm hlo}(QHD,\, N_f = 2) = 63.2(5.6)\, 10^{-10}\,,$$

which is a discrepancy of order of 10 standard deviations if we again add the errors of both results in quadrature.

To assess these observations let us comment on some of the approximations underlying the estimates. In the intermediate perturbative intervals the rescaling by the Q-factors disregards the decoupling relations for the running strong coupling at flavor thresholds. Moreover, the procedure neglects the influence of quark-disconnected diagrams proportional to $Q_q Q_{q'}$ for $q \neq q'$ that start at $O\left(\alpha_s^3\right)$, an approximation that becomes more accurate at high energies. Additionally, again at high energies $E \gg m_{ud}$, m_s the contributions of up, down and strange to the vacuum polarization function approach each other and the quark-disconnected contributions behave $\propto (Q_u + Q_d + Q_s + \ldots)^2 \, \Pi^{disc}$, where then the first three summands cancel.

A second issue concerns the resonances. There is no unambiguous way to extract the contribution of a particular flavor to a resonance or to an individual final state. We think that the strong interrelation especially of the three lightest flavors becomes apparent for example in case of the ϕ, whose branching ratio for a decay via a ρ is about 15% [102]. Yet in the DCD extraction we adhered to the measure of strictly separating both resonances to different flavors.

In light of the ambiguities just discussed the difference of the two extractions gives us a hint at the order of magnitude of systematic error, that we must associate with the attempts to extract $a_\mu^{\mathrm{hlo}}(DR,\, N_f = 2)$. Note, however, that this is a particular problem of the two-flavor case. Comparing the results for $a_\mu^{\mathrm{hlo}}(DR,\, N_f = 3)$ we find agreement of the results within the estimated uncertainties, confirming the notion that the ambiguities are much more suppressed in the case of three flavors. By construction any discrepancy will disappear once a realistic setup with up, down, strange and charm quark is used in the lattice calculation.

5 Muon anomalous magnetic moment in twisted mass lattice QCD

We will now proceed with the detailed description of the steps followed in our calculation of the leading order hadronic contribution to the muon anomaly in twisted mass lattice QCD. The basic concept is to use the definition of a_μ^{hlo} as a weighted integral of the hadronic vacuum polarization over all space-like momenta as given in equation (4.11) with a weight function, that is known from the 1-loop correction to the muon-photon vertex in leading-order QED perturbation theory (cf. eq. (4.12)).

Lattice QCD will contribute the non-perturbative data for the hadronic vacuum polarization. We laid the groundwork for this analysis with our discussion of the vacuum polarization function in chapter 3. We can thus assume to have a smooth parametrization of $\Pi_R(\hat{Q}^2)$ in analytic form ready for integration. Our focus in this chapter will be on the actual extraction of a_μ^{hlo} and a detailed view on the statistical and systematic uncertainties.

5.1 Contribution of a narrow width resonance to a_μ^{hlo}

We found the vector meson dominance (VMD) ansatz a solid approximation when modeling the polarization function in 3.8.2 and saw this confirmed in the previous chapter on phenomenological grounds. It is now interesting to see whether the VMD concept carries over to the estimation of a_μ^{hlo} in twisted mass lattice QCD. To that end we start by considering the contribution of a narrow width vector meson resonance to a_μ^{hlo}.

We recall the derivation of the corresponding contribution to Π using leading order chiral perturbation theory in the appendix 6, which leads to

$$\Pi_{R,V}(\hat{Q}^2) = g^2_{\text{V,em}} \frac{\hat{Q}^2}{\hat{Q}^2 + m_V^2} \,. \tag{5.1}$$

Formula (5.1) corresponds to a narrow width resonance contribution in the cross section ratio $R_h(s)$ of size [85]

$$R_h^{NW}(s) = \frac{9\pi}{\alpha^2} \, m_V \, \Gamma(V \to e^+e^-) \delta(s - m_V^2) \,,$$

which together with the width in equation (3.81) means

$$R_h^{NW}(s) = 12\,\pi^2\, m_V^2\, g_{\mathrm{V,em}}^2\, \delta(s - m_V^2)\,. \tag{5.2}$$

The conversion to the vacuum polarization function then follows again from the causality relation.

The entailed contribution to the muon anomaly, a_μ^V, can be calculated analytically and we show the calculation in appendix 9. It can be cast in the form

$$a_\mu^V = 4\,\alpha^2\, g_{\mathrm{V,em}}^2\, \frac{m_\mu^2}{m_V^2}\, f_<\left(m_\mu^2/m_V^2\right)\,. \tag{5.3}$$

The explicit functional form of $f_<$ is given in equation (49) in the appendix. If for the moment we go back to the more general case of considering any of the three leptons and potential heavier resonances, then we note that the functional form depends on the ratio of lepton to resonance mass: for $m_V > 2m_l$ the function is given by $f_<$ (eq. (49)). In the alternate case $m_V < 2m_l$ (e.g. tree-level ρ resonance contribution to a_τ^{hlo}) it is $f_>$ as displayed in eq. (50). The full form of the function $f_<$ eludes an understanding of the main features of the tree-level contribution. For that reason we look at the expansion of it for small values of the argument (recall $m_\mu^2/m_V^2 \approx 0.02 \ldots 0.01$ for $V = \rho,\, \omega,\, \phi$).

$$\begin{aligned} f_<(y) = {} & \frac{1}{3} + \frac{25}{12}y + \frac{97}{10}y^2 + \frac{208}{5}y^3 + \frac{3608}{21}y^4 + y\,\log(y)\left(1 + 6y + 28y^2 + 120y^3\right) \\ & + O\left(y^5,\, \log(y)y^5\right)\,. \end{aligned} \tag{5.4}$$

With formula (5.3) at hand we can check the impact of the tree-level vector contribution on the complete vector meson resonance contribution as given in table {4.4}. To that end we use again the data for the vector meson masses and decay constant provided by the PDG [102]. This gives the following results for the three light vector resonances ρ, ω and ϕ:

$$a_{\mu,\rho_{\mathrm{tl}}}^{\mathrm{hlo}} = 4.709\,(41)\cdot 10^{-8}\,; \quad a_{\mu,\omega_{\mathrm{tl}}}^{\mathrm{hlo}} = 0.391\,(13)\cdot 10^{-8}\,; \quad a_{\mu,\phi_{\mathrm{tl}}}^{\mathrm{hlo}} = 0.386\,(5)\cdot 10^{-8} \tag{5.5}$$

We compare these numbers to the resonance contributions derived from the dispersion integral, which we cited in the right-hand columns of table {4.4}. The tree-level formula is a rough but reasonable agreement throughout the three vector mesons. The agreement is closer in case of the ω and ϕ. This is to be expected, since these resonances have a much smaller width compared to the ρ and are hence better modeled by a narrow-width-resonance.

This comparison of tree-level to experimental contribution tells us that indeed the tree-level form of the contribution of a vector meson is a reasonable approximation and will serve as a good starting point for building a model for the vacuum polarization function. Yet keeping in mind the gap between the two values in case of the ρ amendments beyond it are required for a systematic analysis.

Ensemble	m_{PS} GeV	$a_\mu^V \times 10^8$
B_0	0.340	227 (39)
B_1	0.340	258 (25)
B_2	0.420	258 (23)
B_3	0.480	218 (17)
B_4	0.520	221 (18)
B_5	0.650	183 (13)
B_7	0.290	303 (58)
B_6	0.330	282 (31)
C_5	0.450	269 (17)
C_1	0.330	294 (47)
C_2	0.450	258 (22)
C_3	0.520	230 (16)

Table 5.1: Results for the tree-level vector contribution a_μ^V to a_μ^{hlo}.

5.1.1 Tree-level vector contribution to a_μ^{hlo} on the lattice

As a natural continuation we will start with the tree-level vector contribution a_μ^V and then proceed to the full hadronic piece. The tree-level vector meson contribution has been argued to be the dominant part of a_μ^{hlo} and though model dependent a good approximation of the latter. We thus use Π_V as the leading term in an expansion of the vacuum polarization in a basis of functions in the later refined analysis of the full contribution. According to equation (5.3) apart from the lepton mass a_μ^V only depends on the vector meson mass m_V and coupling $g_{\mathrm{V,em}}$. We can evaluate it directly using the approximation in equation (5.4) or use the numerical integration

$$a_\mu^V = 4\alpha^2 \int_0^{\hat{Q}^2_{\mathrm{max}}} \frac{d\hat{Q}^2}{\hat{Q}^2}\, w\left(\hat{Q}^2/m_\mu^2\right)\, \Pi_V(\hat{Q}^2)\,. \tag{5.6}$$

We use both methods and list the results of the latter approach in table {5.1} and depict them in figure [5.1]. As the upper integration limit we choose $\hat{Q}^2_{\mathrm{max}} = 100\,\mathrm{GeV}^2$. This represents a conservative upper limit. In fact, given the uncertainty of the vector meson mass and the steep decline of the weight function (4.12) (cf. equation (4.13) and figure [4.5]), the integral (5.6) is statistically saturated already for $Q^2_{\mathrm{max}} \approx 1\,\mathrm{GeV}^2$: a further increase only leads to an insignificant increase of the central value of the integral. The error budget of the results in table {5.1} contains the uncertainty of the vector meson mass, the electromagnetic coupling and the lattice spacing. The latter is needed in order to convert either the lepton mass to lattice or the vector meson mass to physical units. We neglected the uncertainty of the lepton mass, since the muon mass is known with relative precision of $O\left(10^{-8}\right)$, which is about five orders of magnitude below the uncertainty of the lattice quantities. To convey our statements in a clearer way we do not

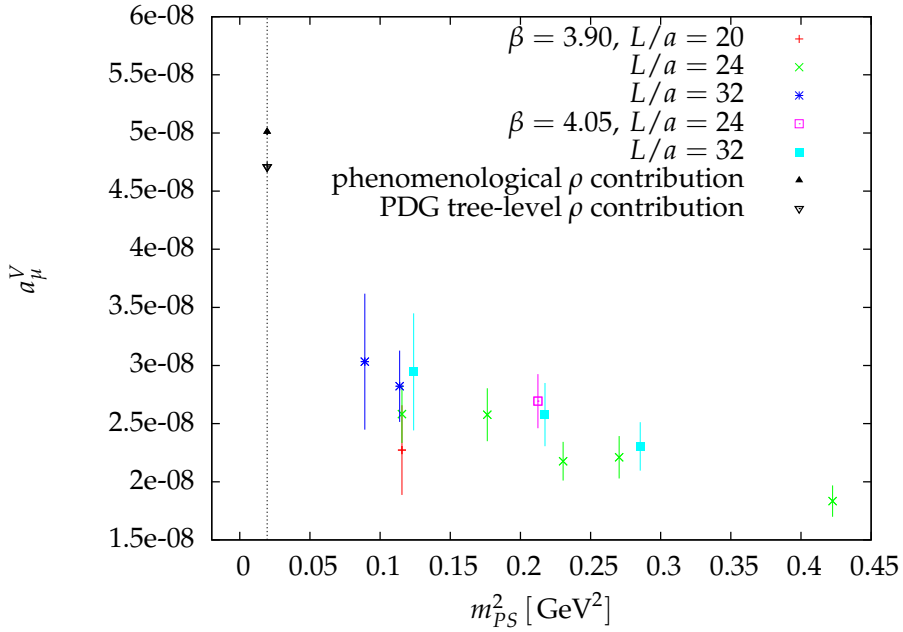

Figure 5.1: Tree-level vector contribution a_μ^V from the ρ meson to a_μ^{hlo}.

display the uncertainty of the pseudoscalar mass on the abscissa axis, since the latter is small with reference to the spread of mass values we show and does not have an impact on the conclusions drawn from the figure. These errors will, however, be taken into account in further treatment of the data, like the extrapolation to the physical point.

As reference points, we show two values in figure [5.1] at the physical pion mass: the larger one is the phenomenological contribution of the ρ (cf. table {4.4}). The lower one is the tree-level vector contribution evaluated at the physical values of the mass and electromagnetic coupling of the ρ (cf. equation (5.5)). As was stated earlier, the difference between these two must be expected, since the ρ resonance is not narrow, which was the assumption underlying the numbers in equation (5.5). Moreover, from equation (5.3) we know that to lowest order in $(m_l/m_V)^2$ we have the dependence $a_\mu^V \propto g^2_{\mathrm{V,em}}/m_V^2$ (and for the vector meson masses in the lattice calculation $(m_\mu/m_V)^2 \sim O(0.01) \ll 1$). The analysis of m_V and g_V in subsection 3.8.1 told us that while the coupling can be safely extrapolated to the physical point even with a linear dependence on m_{PS}^2, the vector meson mass must develop a strong curvature towards the physical point. The same must thus be true for a_μ^V, although as before the onset of such a curved development is not yet reflected in the lattice data.

To round up this discussion, we attempt an extrapolation of these intermediate results to the physical point. We start with the data points for one lattice spacing, $a(\beta = 3.90) = 0.079\,\mathrm{fm}$, only. In order to suppress the influence of finite size effects we will put the restriction $m_{PS}L \geq 4$ in place, which leaves us with the five ensembles B_6, B_2, ..., B_5. We ignore the larger physical volume of B_6 for the time being and regard this set as

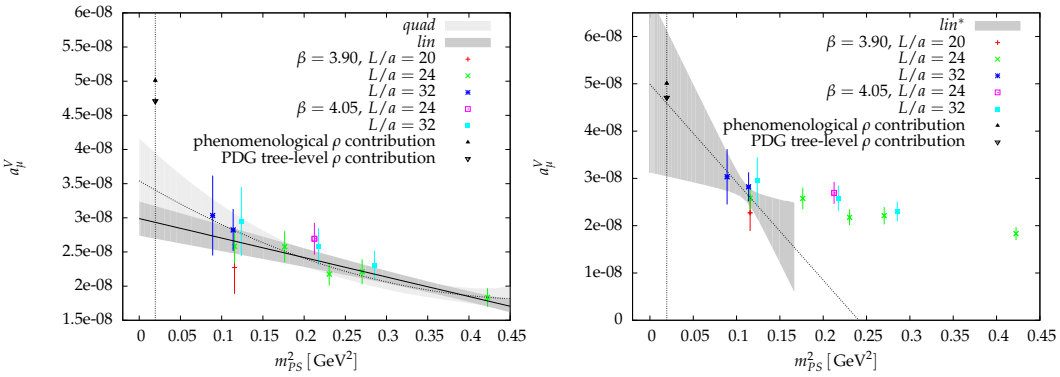

Figure 5.2: Extrapolations of a_μ^V to the physical point. The light/dark shaded regions mark the error band of the *lin*/*quad* fit.

fit	$a_0^{(n)}$	$a_1^{(n)}$ [GeV^{-2}]	$a_2^{(n)}$ [GeV^{-4}]	b_1 [GeV^2]	$a_\mu^V(m_\pi^2)\cdot 10^{10}$	χ^2/dof
lin	299 (25)	−285 (63)			293 (24)	1.1/3
quad	354 (62)	−714 (425)	733 (703)		341 (54)	0.8/2
lin^a	349 (76)	−331 (82)		−0.7 (1.3)	343 (74)	1.6/4
lin*	499 (187)	−21 (17) 10^3			459 (154)	0.80/3

Table 5.2: Fitted parameter values for three different extrapolations of a_μ^V. The parameters $a_1^{(n)}$, $a_2^{(n)}$, $a_3^{(n)}$ are given in units of 10^{-10}.

showing the pure quark mass dependence without volume effects. As a fit ansatz we use the simplest possible linear and quadratic functions (in m_{PS}^2) to model the behavior of a_μ^V. The parameters of the fit functions will be labeled $a_i^{(n)}$, $i = 0, \ldots, n$ for $n = 1$ (*lin* fit) amd $n = 2$ (*quad* fit). Note that we fit the results of calculations on mutually independent ensembles of gauge fields. However, both in the numerical integration and for the physical values of the pion mass on the abscissa we need the lattice spacing to convert from lattice to physical units. Thus via the lattice spacing a correlation of the results of a_μ^V and m_{PS} is necessarily introduced. We keep track of this correlation and at the same time of the uncertainty of the lattice spacing by sampling each lattice spacing subject to a Gaussian distribution once and then using these samples for all ensembles having the same value of β during the extrapolation.

The results for the *lin* and *quad* extrapolation are shown in [5.2], the fitted parameter values are collected in table {5.2}. In the fit *lin*^{a} we try to include lattice artifacts. To that end we use the linear fit as in *lin* but multiply it by an additional factor

$$lin^a = \left[a_0^{(1)} + a_1^{(1)}\, m_{PS}^2\right] \times \left[1 + b_1^{(1)} a^2\right]. \tag{5.7}$$

We find that while the *lin* fit works well with the data at hand, the latter is insufficient to simultaneously constrain the fit parameters $a_i^{(2)}$. The same is true when including

Ensemble	$a_\mu^{\mathrm{hlo}} \cdot 10^{-10}$
B_0	252 (38)
B_1	286 (25)
B_2	277 (23)
B_3	239 (17)
B_4	242 (19)
B_5	205 (14)
B_7	329 (58)
B_6	301 (30)
C_5	290 (25)
C_1	325 (52)
C_2	290 (30)
C_3	256 (21)

Table 5.3: Results for a_μ^{hlo} from the fit $M1N2B1C4$.

Fit	a_0	$a_1\,[\mathrm{GeV}^{-2}]$	$a_2\,[\mathrm{GeV}^{-4}]$	$b_1\,[\mathrm{GeV}^{\pm 2}]$	$a_\mu^{\mathrm{hlo}}(m_\pi^2) \times 10^{10}$	χ^2/dof
lin	319 (25)	−280 (61)			314 (24)	1.2/3
quad	369 (60)	−673 (408)	677 (675)		356 (52)	0.96/2
lin^a	392 (87)	−3.45 (84)		−1.0 (1.2)	385 (85)	1.9/4
log	395 (84)	−233 (90)		252 (297)	391 (85)	1.6/5

Table 5.4: Results for the parameters from different extrapolations of a_μ^{hlo} to the physical point. Note that b_1 assumes units depending on the fit function. Parameters a_0, a_1, a_2 are given in units of 10^{-10}.

one term modeling lattice artifacts in the lin^a fit. As expected from the considerations above all extrapolations are far off the dispersion relation and PDG-derived values at the physical point. More articulately than in case of the vector meson mass and decay constant, however, the extrapolation picks up the correct sign of curvature when adding the term quadratic in m_{PS}^2. Nevertheless the *lin* and *quad* fit show a 7.4σ and 2.4σ discrepancy when compared to the PDG value. In fact, we need to go to a cubic fit (in m_{PS}^2) to find a result, which is compatible with the reference values within one standard deviation, or again restrict the included data set to have $m_{PS} < 370\,\mathrm{MeV}$ (cf. lin^* fit and right panel figure [5.2]). Conclusions from these extrapolations are hampered by the large relative uncertainty at the physical point.

5.2 Lattice QCD estimate of a_μ^{hlo}

In figure [5.3] we show the results for a_μ^{had} from the connected vacuum polarization function for all ensembles introduced above. The integration range was $[0,\, 90\,\mathrm{GeV}^2]$. Note that we could have extended the integration up to the maximal lattice momentum

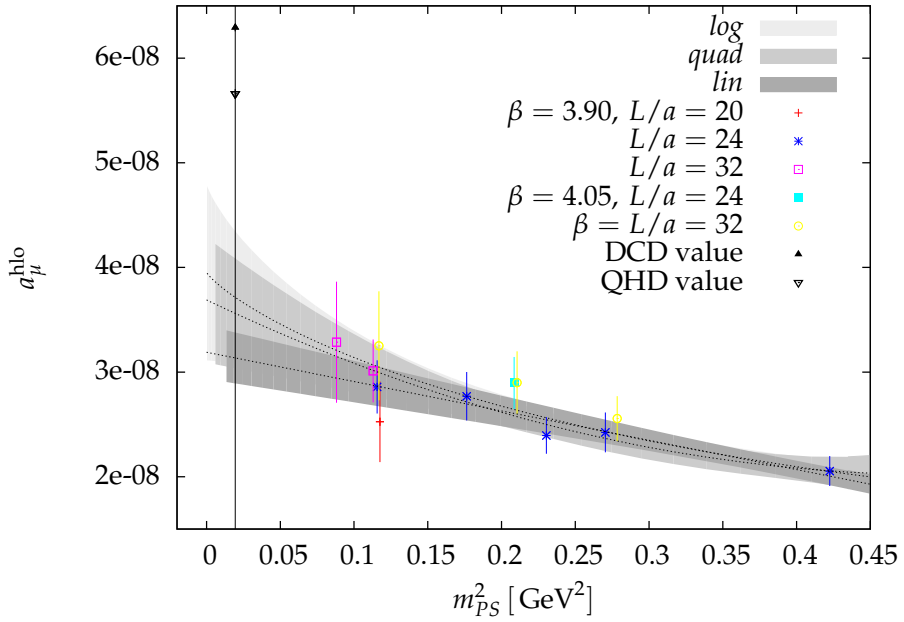

Figure 5.3: Results of the fit *M1N2B1C4* and extrapolation to the physical point. Shown are the *lin*, *quad* and *log* extrapolation in m_{PS}^2.

$16/a^2$, which corresponds approximately to 100 GeV^2 for the $B-$ and 157 GeV^2 for the $C-$ensembles, but this will not alter the integral in any significant way. We notice the absence of any significant differences across all volumes and lattice spacings. The situation here is very similar to what we found, when investigating the tree-level vector meson contribution and its extrapolation to the physical point. We observe again the rather flat behavior of the $a_\mu^{\mathrm{hlo}}(m_{PS}^2)$ within the available range of pion masses. We perform the *lin*, *quad* and *lin*^{a} fit and extrapolation with the constraint $m_\pi L > 4$ analogously to what was done for a_μ^V in the previous subsection. Moreover, we try the fit labeled *log*, which attempts to model a χPT inspired behavior like

$$a_\mu^{\mathrm{hlo}}(m_{PS}^2) = a_0 + a_1 m_{PS}^2 + b_1 m_{PS}^2 \log(m_{PS}^2/\mu_{\mathrm{ren}}^2)\,, \tag{5.8}$$

where we set $\mu_{\mathrm{ren}} = 1$ GeV and relax the constraint on finite volume effects to $m_\pi L \geq 3.5$. The results at the physical point are shown in the last but one column of table {5.4}. Looking at both the absolute of a_μ^{hlo} for each ensemble individually as well as the shape as a function of m_{PS}^2 we find confirmation of the dominance of the tree-level contribution of the lightest vector meson and it thus comes at no surprise that the extrapolations we try fall short of reaching the phenomenological value analogously to the vector meson mass.

We postpone the study of systematic effects until the next chapter, where an alteration of the current analysis will be introduced. We would rather put our results obtained with the standard analysis method into perspective by comparing with results from

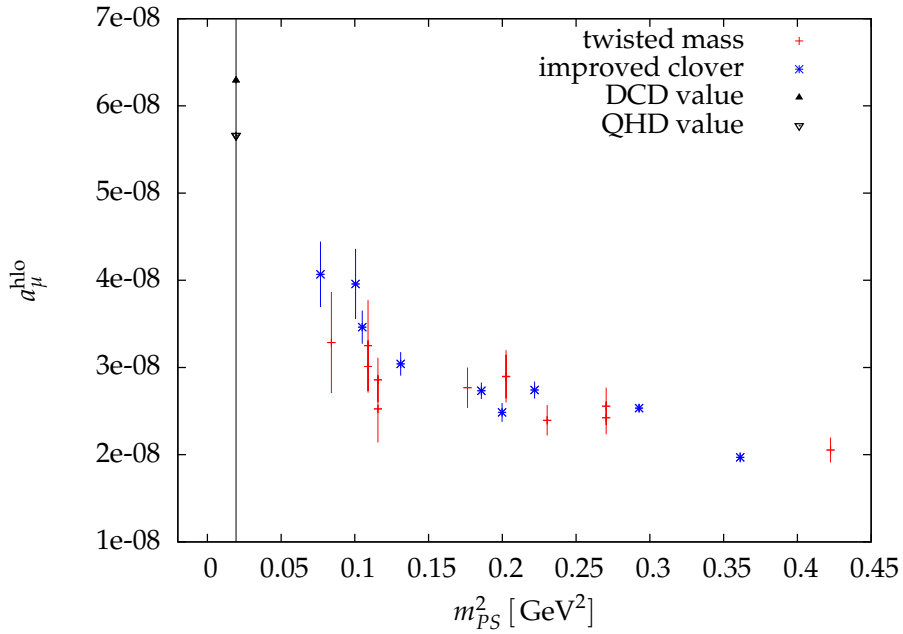

Figure 5.4: Comparison of twisted mass and improved clover results for $a_\mu^{\rm hlo}$. To facilitate the comparison we do not distinguish different volumes and lattice spacings.

other groups.

5.2.1 Comparison with past and recent determinations

As a prominent and challenging quantity to be calculated on the lattice, $a_\mu^{\rm hlo}$ has been investigated by different groups using all common formulations of lattice QCD and flavor combinations ranging from quenchend to $N_f = 2$, $2(+1)$, $2+1$, $2+1+1$ [1]. For the case of two dynamical quark flavors we have comparable results produced with non-perturbatively improved clover fermions [39]. Both the latter and the present calculation have data for several lattice spacings and volumes. As can be inferred from figure [5.4] we find compelling agreement of both calculations. The clover results, which include data at even smaller pion mass than the present calculation, support the notion of a steep rise of $a_\mu^{\rm hlo}(m_{PS}^2)$ close to the physical pion mass.
This agreement gains in depth, since not only were the results obtained with different fermion and different gauge action, but also the fitting procedure in the low momentum region was different from ours: reference [39] uses a Padé ansatz to obtain the data shown in figure [5.4] as well as twisted boundary conditions to populate the gaps between lattice momenta with additional data points.

Let us summarize our observations. We have shown in this chapter how we calculate the leading order hadronic contribution to the muon anomalous magnetic moment in

[1] With the number in brackets we denote a quenched quark flavor.

twisted mass lattice QCD. In this first part we followed the standard analysis and found that with the presently available ensembles concerning lattice volumes and in particular pion masses this standard analysis leads to extrapolated results that are afflicted by large errors and even within these large errors are significantly below the results we would expect from phenomenology. We brought forward arguments that trace back the origin of this discrepancy to the behavior of the lightest vector meson mass as a function of the pseudoscalar mass.

5.3 Extrapolation to the physical point revisited — the modified method

Let us come to the task of extrapolating the ensemble-wise estimated a_μ^{hlo} to the physical point, $a_\mu^{\mathrm{hlo}}(m_{PS}^2) \to a_\mu^{\mathrm{hlo}}(m_\pi^2)$. With the pseudoscalar masses available in our lattice calculation ranging from approximately $m_{PS} \lesssim 650\,\mathrm{MeV}$ down to $m_{PS} \gtrsim 290\,\mathrm{MeV}$ such an extrapolation constitutes a major obstacle. One key observation of the previous section was, that we may indeed be too far from the physical point, i.e. at pion masses too large to see the correct chiral behavior of the quantities of interest, m_V, f_V, a_μ^{hlo}, which must be a sharp rise towards their physical values. Further on, we do not have a guiding extrapolation formula from chiral perturbation theory for $a_\mu^{\mathrm{hlo}}(m_{PS}^2)$ in the first place. So our interest might be to suppress the (analytically unknown) pion mass dependence as far as possible in the course of the extrapolation. The aim of this section is to show, that this is indeed possible in a systematic way. In the following we use the $\hat{}$ -notation to indicate quantities in lattice units.

5.3.1 Running of a_μ^{hlo} with the quark mass

We will first write down the basic formulas for the change of a_μ^{hlo} with the quark mass μ_0. The problematic quark mass dependence was already present when looking at data for a single value of the lattice spacing (or β) and we thus keep the bare lattice coupling fixed in what follows. Recalling that at full twist the quark mass is renormalized multiplicatively, $\mu_R = Z_P\,\mu_0$, we seek to evaluate

$$\mu_0 \frac{\partial}{\partial \mu_0} a_\mu^{\mathrm{hlo}} = \mu_R \frac{\partial}{\partial \mu_R} a_\mu^{\mathrm{hlo}} = \mu_0 \frac{\partial}{\partial \mu_0} \int_0^\infty \frac{dQ^2}{Q^2}\, w(Q^2/m_\mu^2)\, \Pi_R(a^2 Q^2) \tag{5.9}$$

$$\tag{5.10}$$

We write $\Pi(a^2\hat{Q}^2)$ to emphasize that as we calculate Π on the lattice it is naturally given as a function of the lattice momenta.

In twisted mass lattice QCD the lattice spacing is generically a function of the bare quark mass and the coupling, $a = a(\beta, \hat{\mu}_0)$, if for the moment we ignore the size parameters T and L. Then fixing the coupling leaves us with only the quark mass dependence. Hence there are two sources of quark mass dependence in equation (5.9):

an explicit one coming from the appearance of the quark mass in the lattice action, and an implicit one stemming from the quark mass dependence of the lattice spacing. The explicit dependence of the expectation value Π on the quark mass can be cast in the form of a 3-point function by recalling that $\Pi(a^2Q^2)$ is essentially the Fourier transform of

$$\Pi_{\mu\nu}(x;\, y) = \langle J_\mu(x)\, J_\nu(y)\rangle = \int DUD\chi D\bar{\chi}\, J_\mu(x)\, J_\nu(y)\, \mathrm{e}^{-S(\hat{\mu}_0)}$$

and the action is a function of $\hat{\mu}_0$ via the twisted mass term $i\hat{\mu}_0\bar{\chi}\gamma_5\tau^3\chi$. Thus differentiating with respect to $\hat{\mu}_0$ will bring the twisted mass term as a product to the integrand

$$\begin{aligned}
\hat{\mu}_0 \frac{\partial}{\partial\hat{\mu}_0} a_\mu^{\mathrm{hlo}} &= \int_0^\infty \frac{dQ^2}{Q^2}\, w(Q^2/m_\mu^2)\hat{\mu}_0 \frac{\partial}{\partial\hat{\mu}_0}\, \Pi_R(a^2Q^2) \\
\hat{\mu}_0 \left(\frac{\partial\Pi_R(a^2Q^2)}{\partial\hat{\mu}_0}\right)_{\mathrm{expl}} &= \sum_{q\in[q^2]} \frac{i\,\hat{\mu}_0}{P_{\lambda\kappa}(q)P^{\kappa\lambda}(q)}\, P^{\mu\nu}(q) \Big\{ \\
&\qquad \sum_{x,z} \langle \Big(J_\mu(x)\, J_\nu(y) + J^{(2)}(y)\, \delta_{\mu\nu}\Big)\, P^3(z)\rangle\, \mathrm{e}^{iq(x+a\hat{\nu}-y-a\hat{\nu})} \Big\} - \frac{\partial}{\partial\hat{\mu}_0}\, \Pi(0) \\
P^3(z) &= \bar{\chi}(z)\, \gamma_5\tau^3\, \chi(z)\,.
\end{aligned} \tag{5.11}$$

The first part of the derivative can in principle be measured on the lattice using techniques to evaluate 3-point functions. At this point the value of $\Pi(0)$ is determined from a fit, but of course it is still a function of the lattice parameters and we keep the notation general. Here we have used the fact that by definition of the ETM collaboration the pseudo-critical value of the hopping parameter κ_{cr} is not a function of $\hat{\mu}_0$ at fixed coupling for the 2-flavor ensembles (cf. [23] for the ETMC definition of κ_{cr}). Since κ_{cr} appears in the lattice action there would otherwise be another contribution proportional to the scalar density $S = \bar{\chi}\,\chi$ with a coefficient $\partial\,\kappa_{\mathrm{cr}} \,/\, \partial\hat{\mu}_0$.

The second, implicit quark mass dependence arises from the scale dependence of the integral defining a_μ^{hlo}: the muon mass enters the integrand as an external scale, that is not related to any other lattice quantity. In the practical calculation either the muon mass in the weight function or (by a change of the integration variable) the momentum in the vacuum polarization function must be converted from physical to lattice units, which requires the presence of a scale function $H = H(\beta, \hat{\mu}_0)$. The first quantity, that comes to mind to achieve this, is the lattice spacing itself. The second part of the derivative thus gives a contribution

$$\begin{aligned}
\hat{\mu}_0 \left(\frac{\partial\Pi(a^2Q^2)}{\partial\hat{\mu}_0}\right)_{\mathrm{impl}} &= \frac{\hat{\mu}_0}{a^2}\, \frac{\partial a^2}{\partial\hat{\mu}_0}\, a^2\, \frac{\partial}{\partial a^2}\, \Pi(a^2Q^2) \\
&= \frac{\hat{\mu}_0}{a^2}\, \frac{\partial a^2}{\partial\hat{\mu}_0}\, \hat{Q}^2\, \frac{\partial}{\partial\hat{Q}^2}\, \Pi(\hat{Q}^2)\,.
\end{aligned} \tag{5.12}$$

So far we have used the lattice spacings that come from a chiral perturbation theory analysis of ETMC [8] and are the result of a combined fit and extrapolation to the physical pion mass

$$a(\beta) = \frac{1}{f_\pi^{\text{phys}}} \lim_{m_{PS}\to m_\pi} (a f_{PS})^{\text{latt}}(\beta, \hat{\mu}_0)\,. \tag{5.13}$$

Equation (5.13) sketches the general notation we will use in the following: the lattice scale is defined as a ratio of a lattice quantity, which is dimensionless due to an appropriate power of the lattice spacing, and its counterpart at the physical point in physical units. For the example above

$$\begin{aligned}\hat{H} &= \lim_{m_{PS}\to m_\pi} (a f_{PS})^{\text{latt}}(\beta, \hat{\mu}_0)\\ H &= f_\pi\,[\,\text{GeV}]\\ a &= \hat{H}/H\,.\end{aligned}$$

In particular in the standard analysis we have

$$\partial\hat{H}/\partial\hat{\mu}_0 = 0\,, \tag{5.14}$$

the scale does not depend on the quark mass. So, if we look at the problematic quark mass dependence in a plot like [5.3] this is solely the result of the explicit (and numerically undetermined) quark mass dependence given in equation (5.11).

We can now proceed along two directions to further exploit these general properties. First, we can generalize our choice of the scale function $\hat{H}/H$, in particular allow for a bare twisted quark mass dependent $\hat{H}$. Secondly, with our *MNBC* fit model we have smooth parametrizations of the polarization function, with which we can try to evaluate the implicit and explicit quark mass dependence. In short, we now consider

$$\hat{\mu}_0 \frac{\partial a_\mu^{\text{hlo}}}{\partial\hat{\mu}_0} \propto \int \frac{dQ^2}{Q^2}\, w(Q^2/m_l^2) \left[\hat{\mu}_0 \left(\frac{\partial\Pi_R}{\partial\hat{\mu}_0}\right)_{\text{expl}} + \frac{\hat{\mu}_0}{\hat{H}^2}\left(\frac{\partial\hat{H}^2}{\partial\hat{\mu}_0}\right)\hat{Q}^2\,\frac{\partial\Pi_R}{\partial\hat{Q}^2}\right]. \tag{5.15}$$

If we think of a controlled suppression of the quark mass dependence we must find a way to keep the integral as small as possible. We know that the major contribution comes from the lower end of the integration interval. and furthermore that $\partial\Pi_R/\partial\hat{\mu}_0(\hat{Q}^2)$ is negative: with increasing quark mass the curvature of Π becomes smaller and so does Π_R. Moreover, from the general shape of $\Pi_R(\hat{Q}^2)$ we know that its slope is always positive. One ansatz is to find a positive $\hat{H}^2$ such that $\partial\hat{H}^2/\partial\hat{\mu}_0 > 0$ and which keeps the integrand itself as close to zero as possible. Expressed differently, we can view equation (5.15) as a differential equation for the scale function $\hat{H}$. A proper solution must fulfill the additional requirements of the existence of a counter part H in the continuum theory at the physical point and of consistency of the scale setting at the physical point. An

example for the latter would be that given the ETMC lattice spacing we have

$$\lim_{m_{PS}\to m_\pi} \frac{\hat{H}}{a^{d_H} H} = 1\,, \tag{5.16}$$

up to lattice artifacts, where d_H is the mass dimension of H.
Let us illustrate the situation with the example of the tree-level vector meson contribution (fit $M1N1$)

$$\Pi(\hat{Q}^2) = -g_V^2 \frac{\hat{m}_V^2}{\hat{m}_V^2 + \hat{Q}^2} + a_0$$
$$\Pi_R(\hat{Q}^2) = g_V^2 \frac{\hat{Q}^2}{\hat{m}_V^2 + \hat{Q}^2}$$

Given the fixed value of the lattice coupling and our presumed stability of the lightest vector meson state, we have a 1-1 correspondence $\hat{m}_V = \hat{m}_V(\hat{\mu}_0)$ and $g_V = g_V(\hat{\mu}_0)$ for the mass and coupling. If for brevity we use the notation

$$\gamma_A = \frac{\hat{\mu}_0}{A}\frac{\partial A}{\partial \hat{\mu}_0} = \frac{\partial \log(A)}{\partial \log(\hat{\mu}_0)}$$

the differential equation assumes the form

$$0 = \left[\gamma_{g_V^2}\, g_V^2 \frac{\hat{Q}^2}{\hat{m}_V^2 + \hat{Q}^2} - \gamma_{\hat{m}_V^2}\, g_V^2 \frac{\hat{Q}^2}{\left(\hat{m}_V^2 + \hat{Q}^2\right)^2}\right] + \gamma_{\hat{H}^2}\left[g_V^2 \frac{\hat{m}_V^2\,\hat{Q}^2}{\left(\hat{m}_V^2 + \hat{Q}^2\right)^2}\right]$$
$$\gamma_{\hat{H}^2} = -\gamma_{g_V^2} \frac{\hat{m}_V^2}{\hat{m}_V^2 + \hat{Q}^2} + \gamma_{\hat{m}_V^2}\,. \tag{5.17}$$

For the tree-level vector meson contribution we have three quantities that determine the running of a_μ^{hlo} with the quark mass: the scale function $\hat{H}$, g_V, and $\hat{m}_V$. The first one did not play a role so far and the second one has been shown to be controllable in the extrapolations in subsection 3.8.1. The problem arises with $\gamma_{\hat{m}_V^2}$. For $\hat{m}_V$ we have seen that an extrapolation to the physical pion mass is not under control with our lattice data at hand.
At small momentum $\hat{m}_V^2/(\hat{m}_V^2 + \hat{Q}^2)$ is a slowly decreasing function close to one. To first approximation we can take its value unity at $\hat{Q}^2 = 0$. Then the solution to equation (5.17) becomes

$$\hat{H} = \frac{\hat{m}_V}{g_V}\,. \tag{5.18}$$

Hence we find that by an appropriate choice of $\hat{H}$ we can cancel the major quark mass dependence of a_μ^{hlo}. Of course this depends on the parametrization. Had we chosen a

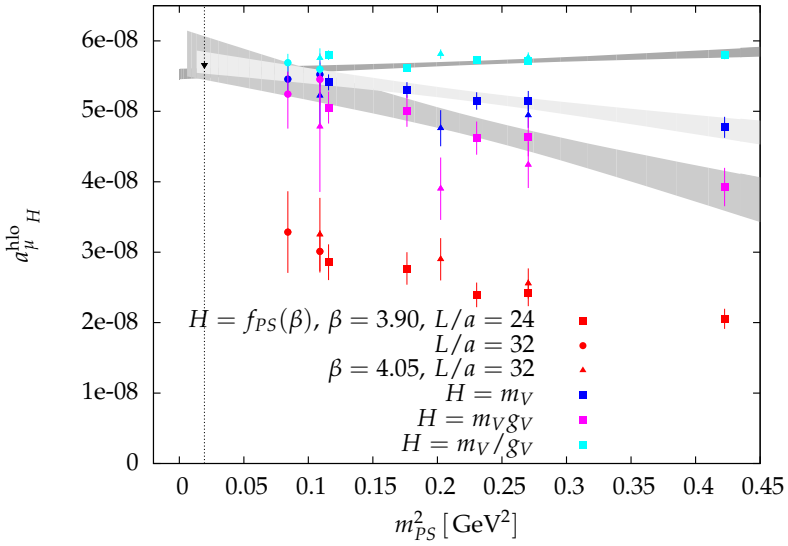

Figure 5.5: Dependence of $a_\mu^{\mathrm{hlo}}{}_H$ on the pseudoscalar mass for different choices of H.

different model for Π_R, we would have found a different functional form for the scale function. We note that we do not have to use the actual solution in equation (5.18), but we can also choose a similar form to achieve a partial cancellation of the quark mass dependence. Moreover, we established already the dominance of the tree-level vector meson contribution in the estimate of the full a_μ^{hlo} from our lattice data and we can expect a potential improvement of the quark mass dependence for the $M1N1$ model to work for the model $M1N2$ as well.

Each choice of $\hat{H}$ defines a different estimator

$$a_\mu^{\mathrm{hlo}}{}_H = 4\,\alpha^2 \int_0^{Q^2_{max}} \frac{dQ^2}{Q^2}\, w(Q^2/m_\mu^2)\, \Pi_R\left(\hat{H}^2\, Q^2/H^2\right). \tag{5.19}$$

All these estimators converge to the same quantity at the physical point due to the consistency condition imposed on $\hat{H}$. Thus any such $a_\mu^{\mathrm{hlo}}{}_H$ is a well defined estimator for a_μ^{hlo}. In figure [5.5] we compare the result for $a_\mu^{\mathrm{hlo}}{}_H$ for several natural choices $\hat{H} = \hat{m}_V$, $af_V = g_V \cdot \hat{m}_V$, $\hat{m}_V/g_V$. Let us first focus on the curve $H = f_{PS}(\beta)$ (lowest set of points) and on the curve $H = m_V$. The first one corresponds to the standard analysis that has been reported in the first part of this chapter. The second one is going to be the choice we focus on for the analysis of systematic errors. Moreover, defining the lattice scale by a hadron mass $a = \hat{m}_V/m_V$ is a natural choice as long as the corresponding state is stable on the lattice and we can measure it in a reliable way.

We find that the curve with $H = m_V$ is lifted compare to the standard curve and the data points have collapsed onto a straight line with a significantly smaller uncertainty and a reduced slope compared to the standard curve. The reduced dependence on

m_{PS}^2 is what we would expect from equation (5.17), since $\gamma_{\hat{H}^2}$ (largely) cancels $\gamma_{\hat{m}_V^2}$ and the leading mass dependence now stems from g_V. But we have seen that g_V can be extrapolated linearly from the lattice data to a value consistent with the experimental one. Due to the dominance of the tree-level vector meson contribution and by choosing $H = m_V$ we thus automatically get a major part with correct size and small uncertainty at the physical point.

This behavior is taken one step further for $H = m_V / g_V$: we largely suppress the mass dependence that enters a_μ^{hlo} via g_V^2 and we find even more error cancellations and an even flatter curve. The choice $H = m_V g_V$ suppresses the dependence on the pion mass as well, albeit to a lesser degree and with a smaller suppression of the uncertainty. We summarize the magic in equation (5.20), where we list the form of the tree-level vector meson term in the vacuum polarization for the displayed choices of H.

$$\begin{aligned} H &= 1 && g_V^2 \, \frac{a^2 Q^2}{\hat{m}_V^2 + a^2 Q^2} \\ H &= m_V && g_V^2 \, \frac{Q^2}{m_\rho^2 + Q^2} \\ H &= m_V \, g_V && g_V^2 \, \frac{Q^2}{m_\rho^2 \, g_\rho^2 / g_V^2 + Q^2} \\ H &= m_V / g_V && g_\rho^2 \, \frac{Q^2}{m_\rho^2 + Q^2 \, g_\rho^2 / g_V^2} \end{aligned} \tag{5.20}$$

With the $M1N_*B_*C_*$ model functions the choice of H allows us to enforce the correct value of the tree-level vector meson contribution at the physical point. All contributions beyond that stem in small part from the high momentum region and predominantly from the polynomial terms in the low momentum region below $\hat{Q}^2_{\text{match}}$. It is equally interesting to study the effects of the choice of H on those (summed) contributions alone. This is done in figure [5.6]. We find that again the curves are lifted for each ensemble due to the larger scale. For the $M1N2$ low-momentum model what is seen in the figure is largely the integral of the term $a_1 \, a^2 Q^2$, which becomes $a_1 \, \hat{H}^2 \, Q^2 / H^2$ for general H. But in contrast to the tree-level vector term, which contains the parameters g_V and $\hat{m}_V$, the polynomial terms are much more decoupled from those parameters, so the error cancellation observed for the tree-level term does not happen in this case. In fact, looking at the relative error of the polynomial low momentum and the high momentum part, the latter is slightly smaller at the lowest two pion masses and then becomes equal and even larger than that of the standard estimators. Nevertheless these contributions to a_μ^{hlo} are small compared to the tree-level part in such a way, that there is an overall gain in precision by altering H appropriately. Moreover, we observe that the modified curves have an increased slope compared to the standard one. We elaborate on these comparisons to emphasize that the improvement we gain by modifying the choice of scale setting is tied to and depends on the model used to describe the vacuum polarization function. By virtue of vector meson dominance we get a large part of a_μ^{hlo}

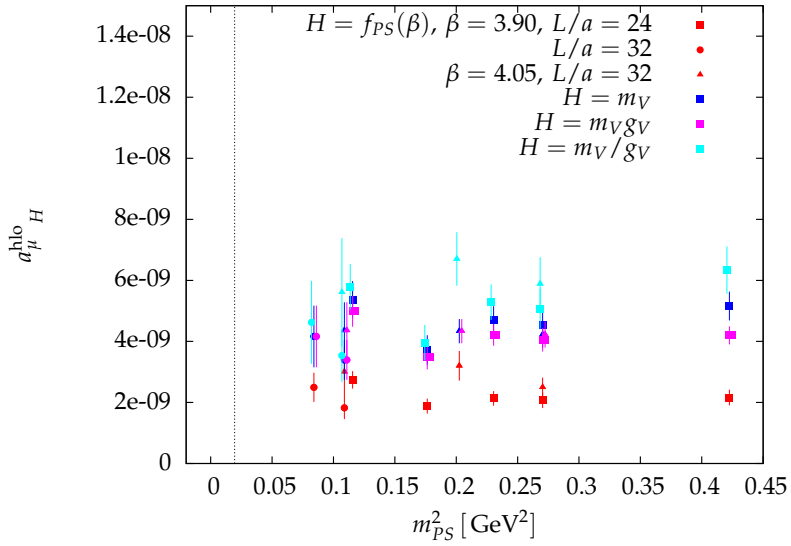

Figure 5.6: Dependence of $a_\mu^{\mathrm{hlo}}{}_H$ without the tree-level vector term on the pseudoscalar mass for different choices of H.

from the tree-level vector term in the vacuum polarization. For the latter we find from equation (5.15) a scale function that entails a far reaching cancellation of uncertainties for the estimator of a_μ^{hlo}.

In summary, we would like to advocate a slightly different point of view here than was stated in [52, 111]. The dependence on an external scale via the muon mass and the implied necessity to introduce a lattice scale to define the dimensionless a_μ^{hlo} on the lattice gives us an additional degree of freedom: we can choose this scale in a way that defines estimators with a milder quark mass dependence and hence an improved extrapolation to the physical point. In a QED+QCD lattice simulation that incorporates the muon as a dynamical fermion field, the muon mass would result from a lattice calculation as well, and the weight function would be a function of a dimensionless ratio $\hat{Q}^2/\hat{m}_\mu^2$. We would then have to rely on $\gamma_{\hat{m}_\mu^2}$ to achieve the cancellations, that we can put in by hand for now.

5.3.2 Modified extrapolation and analysis of systematic errors

We concentrate on the case $H = m_V$ and use the fit $M1N2B1C4$. The extrapolation to the physical point is presented in figure [5.7]. We use extrapolation formulas, which are linear and quadratic in m_{PS}^2. These are shown as the light and dark gray bands in the plot and their parameters are collected in the following table.

fit	a_0	$a_1\,[\mathrm{GeV}^{-2}]$	$a_2\,[\mathrm{GeV}^{-4}]$	$a_\mu^{\mathrm{hlo}}{}_{m_V}(m_\pi^2)\cdot 10^{-10}$	χ^2/dof
lin	574 (17)	−231 (67)		569 (15)	0.95/3
quad	582 (46)	−301 (366)	130 (660)	576 (39)	0.92/2

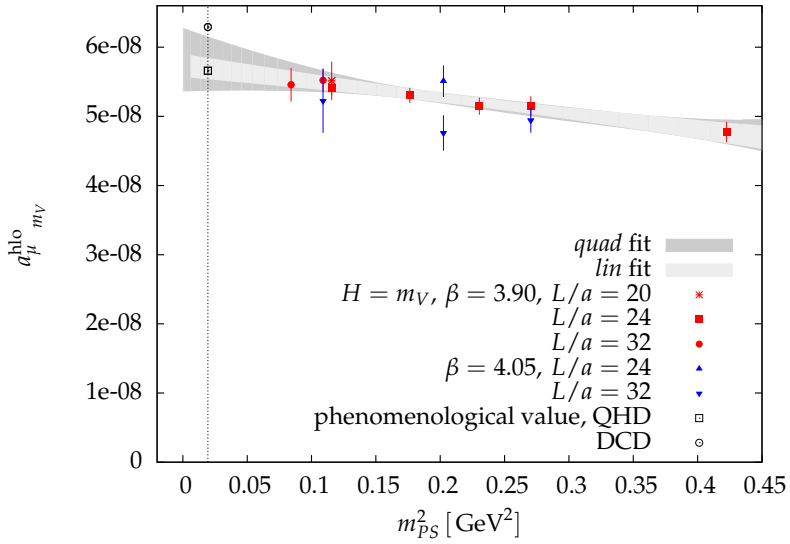

Figure 5.7: Modified extrapolation with $H = m_V$ from $M1N2B1C4$.

The coefficients a_0, a_1, a_2 are given in units of 10^{-10}. The observed pion mass dependence is fully compatible with the linear fit. Adding a quadratic term does not introduce any significant curvature into the fitted dependence on m_{PS}^2 and a_1 and a_2 are individually compatible with zero but highly correlated. With our data we can thus only constrain two parameters.

Model function for $\Pi(\hat{Q}^2)$

Defining a_μ^{hlo} via the integral (4.11) with a fitted and extrapolated vacuum polarization function evokes a systematic uncertainty that stems from the choice of a fit function. Given the strong weight the integrand has in the region without support by lattice data, this systematic error has a potentially large impact. With our generalized *MNBC* fit model we have a set of functions that allow us to investigate the dependence on the choice of a fit function within certain limits. These limits are set by the statistics, which only allows us to constrain a limited number of fit parameters and puts a constraint on reasonable choices of $N + B + C$. We varied $M = 1, 2, 3$, $N = 2, 3$, $B = 1, 2$ and $C = 2, 3, 4$, but not all combinations give a good fit of the data for the complete momentum region $4\sin^2(a\pi/L)^2/a^2 \leq \hat{Q}^2 \leq 90\,\mathrm{GeV}^2$ and a smooth transition at the matching point of Π_{low} and Π_{high}.
For the fits we keep, we collected the results for the corresponding linear extrapolations in table {5.5}. For $M > 1$ we moved the matching point to $\hat{Q}^2_{\mathrm{match}} = 6\,\mathrm{GeV}^2$ and kept the width as before. This reflects the fact that with a larger number of dipole terms we can describe the polarization function in a larger interval in the low momentum region without the need of additional polynomial terms. Moreover, this moves the matching point completely away from the momentum region with significant impact on the value

M	N	B	C	$a_{\mu\ m_V}^{\mathrm{hlo}} \cdot 10^{-10}$
1	2	1	3	577 (16)
1	2	1	4	569 (15)
1	3	1	3	541 (18)
1	2	2	2	569 (15)
2	2	1	3	548 (19)
3	2	1	3	561 (21)

Table 5.5: Results for different choices of model functions for $\Pi(\hat{Q}^2)$.

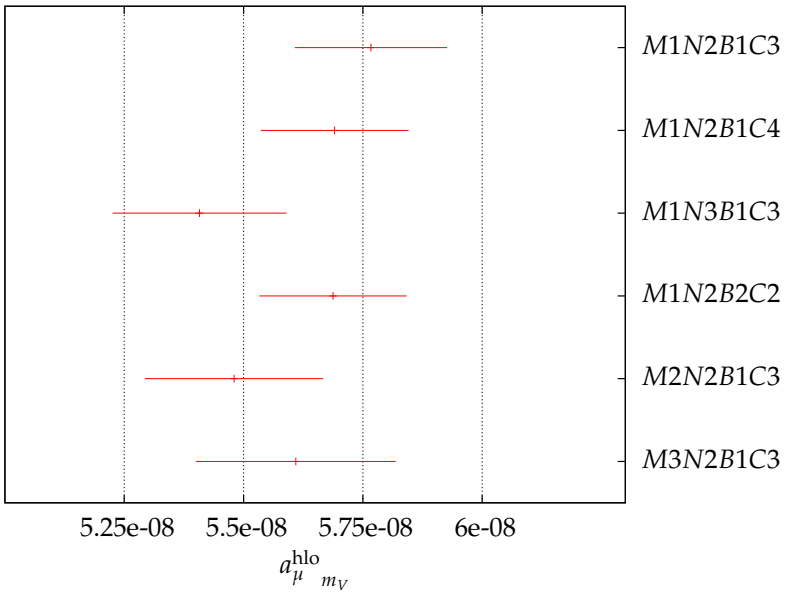

Figure 5.8: Comparison of the fit and extrapolation results in table {5.5}

of the integral (cf. 5.3.2). Comparing the results in table {5.5} with $M1N2$ fixed and $(B, C) = (1,3), (1,4), (2,2)$, we find that changing the model function Π_{high} alone does not significantly impact the value of the integral. This must be expected, since the integral is largely saturated already in $[0, 1\,\mathrm{GeV}^2]$.

The response is different, when changing Π_{low}: the details of the low-momentum model propagate significantly to the extrapolation of the ensemble-wise integrals. Yet all choices for Π_{low} describe the lattice data in the small momentum region well. Still the shape of the model function in the vicinity of the origin, far from the lattice data support will vary and influence the integral.

To estimate the systematic error from the choice of the model function we take the variance of the entries in table {5.5}, $\Delta_m^2 = \mathrm{var}\,(a_{\mu\ m_V}^{\mathrm{hlo}}(MNBC))$, which leads to

$$\Delta_m = 0.14 \cdot 10^{-8}\,. \tag{5.21}$$

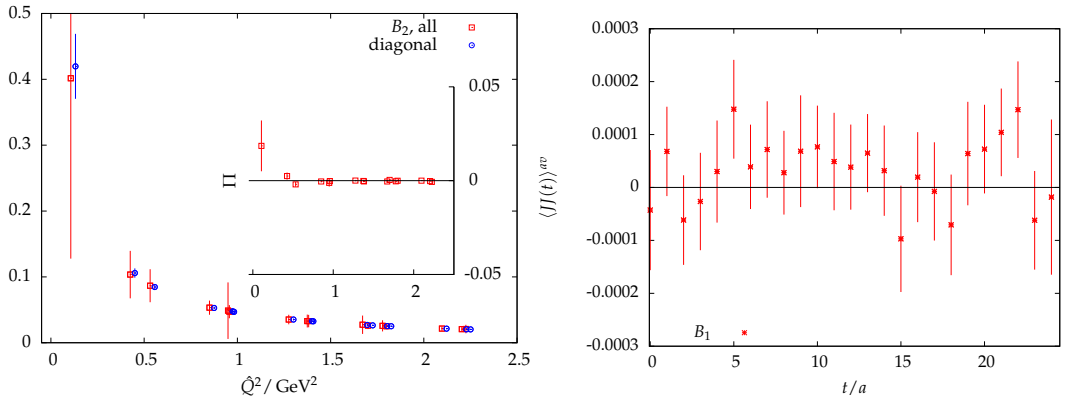

Figure 5.9: Left: disconnected contribution to the vacuum polarization function for ensemble B_2 with uncertainties magnified 20-fold; right: disconnected contribution to ρ correlator for ensemble B_1

Quark-disconnected contribution

The quark-disconnected contributions have been measured for the subset of ensembles marked with a star in table {3.4}. The number of gauge configurations and stochastic volume sources used in the estimation are collected in the following table.

ensemble	B_1	B_2	B_6	C_1	C_2
# sources	24	48	24	29	48
# configurations	237	240	163	54	188

Our philosophy concerning quark-disconnected contributions is to take the estimate of $a_\mu^{\mathrm{hlo}}{}_{m_V}$ from the purely connected data and regard the impact of the disconnected piece as a contribution to the systematic uncertainty. As a motivating example for this ansatz we show the two plots of figure [5.9]. The formula for the quark-disconnected contribution was given in equation (3.45). Skipping notational details it shows that we combine $L^r(q)\,L^s(-q)$ with $r \neq s$. However, it gives an interesting perspective on the quark-disconnected piece to see it as the difference

$$\Pi^{disc} = \Pi^{\mathrm{all}} - \Pi^{\mathrm{diag}} = \left(\sum_r L^r(q)\right)\left(\sum_s L^s(-q)\right) - \sum_r L^r(q)\,L^r(-q)$$

The first term called Π^{all} simply contains all combinations (r,s) and is thus a mixture of connected and disconnected contributions. The second one, Π^{diag}, contains the connected contributions with $r = s$. The left panel of figure [5.9] shows that for these two we have a good signal and that they are equal within errors. So their difference, which leads to Π^{disc} and is shown in the detail view, is consistent with zero.
A second example arisis from observing the time-dependent quark-disconnected piece

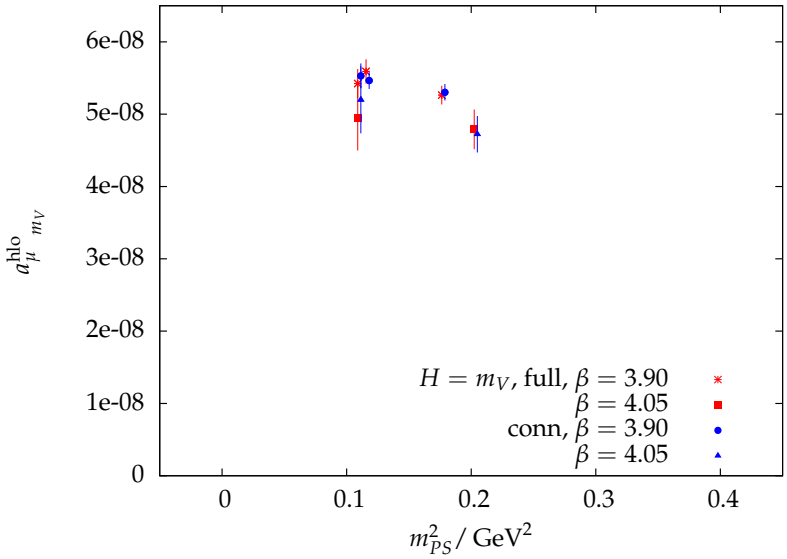

Figure 5.10: Comparison of $a_{\mu}^{\mathrm{hlo}}{}_{m_V}$ from the full vacuum polarization function including disconnected contribution and from the connected part only. The fit used is $M1N2B1C4$.

of the current correlator at zero spatial momentum. It is shown for ensemble B_1 in the right panel of figure [5.9]. Here, too, we find that with the statistics we used there is no signal, the correlator is consistent with zero throughout. These observations are in accordance with the findings in reference [77]: the quark-disconnected contributions to the (local) ρ correlator were found to be negligible. In our case the loops are even more noisy due to the one-point split current. If we cannot find a true signal, the question remains how far we can suppress the gauge and stochastic noise, that may be carried into the full polarization function. We found that the estimator in equation (3.46) leads to the best results. Apart from this choice, we would still find it very interesting to repeat the estimation using the temporal moment method and t-sums with data from the local vector current correlator.

A comparison of $a_{\mu}^{\mathrm{hlo}}{}_{m_V}$ from the full and quark-connected vacuum polarization function is shown in figure [5.10]. We find an increased statistical uncertainty for $a_{\mu}^{\mathrm{hlo}}{}_{m_V}$ from the full polarization function, which was expected. At the same time the estimates for connected and full contribution are consistent within errors for ensembles B_6, B_2, C_1. For C_2 the error bars just touch each other, while for B_1 there is a gap of roughly 2σ. To numerically estimate the systematic error we use a weighted quadratic sum of the

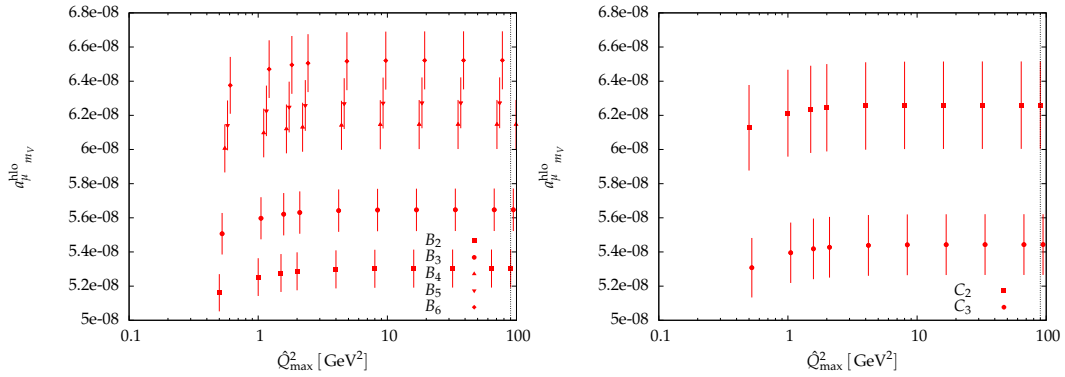

Figure 5.11: Dependence of $a_\mu^{\rm hlo}{}_{m_V}$ on the upper integration limit for $\beta = 3.90$ (left) and $\beta = 4.05$ (right).

deviations of the full and connected $a_\mu^{\rm hlo}{}_{m_V}$

$$\Delta_d^2 = \sum_e \left(a_\mu^{\rm hlo}{}_{m_V}(e, \text{full}) - a_\mu^{\rm hlo}{}_{m_V}(e, \text{conn}) \right) w_e \left(\sum_e w_e \right)^{-1}$$
$$w_e = \frac{1}{\sigma^2_{\rm full}(e) - \sigma^2_{\rm conn}(e)} \,. \tag{5.22}$$

The sum over ensembles e contains those ensembles that fulfill the criteria of the standard fit, that means B_2 and B_6 in the present case. This leads to

$$\Delta_d = 0.07 \cdot 10^{-8} \,. \tag{5.23}$$

The definition (5.22) potentially double counts the uncertainties from full and connected piece. However, using $w_e = 1/\sigma_{\rm full}(e)$ does not change the numerical value in equation (5.23).

Lattice artifacts I: upper integration limit

The first kind of lattice artifacts arise from the upper integration limit: the maximal lattice momentum we can reach for a fixed value a of the lattice spacing is $16/a^2$. For the definition of our standard integral we chose a value $\hat{Q}^2_{\rm max} = 90\,\text{GeV}^2$ as the upper integration limit. This is well below the maximal possible value for both lattice spacings. That such a choice is justified and saturates the integral follows directly from figure [5.11]: we show the dependence of the $B-$ and $C-$ensembles with $m_{PS}L \geq 4$ on the upper integration limit. There is an insignificant rise of the central value, when changing $\hat{Q}^2_{\rm max} = 2\,\text{GeV}^2 \to 4\,\text{GeV}^2$. Beyond that the central value and the uncertainty are stable. Thus any systematic dependence on the upper integration limit is covered by the statistical uncertainty already and $\hat{Q}^2_{\rm max} = 90\,\text{GeV}$ marks a safe choice.

Lattice artifacts II: extrapolation

Another type of lattice artifact arises from the a^2 corrections to a_μ^{hlo} for each individual ensemble that may affect the extrapolation to the physical point. We tried several options to estimate the systematic error.

First we can extrapolate the data for $\beta = 3.90$ and $\beta = 4.05$ individually. To do that we have to relax the constraint $m_{PS}L \geq 4$ for the latter case, since otherwise we would only have two data points. Doing that we perform a linear extrapolation for both sets and measure the difference

$$a_{\mu\ m_V}^{\text{hlo}}(\beta = 3.90) - a_{\mu\ m_V}^{\text{hlo}}(\beta = 4.05) = 0.62\,(62)\,10^{-8}. \tag{5.24}$$

This difference turns out to be statistically insignificant

For the second option we amend the extrapolation function

$$a_\mu^{\text{hlo}}(m_{PS}^2) = \left(a_0 + a_1\, m_{PS}^2\right) \times \left(1 + b_1\, a^2 m_{PS}^2\right) \tag{5.25}$$

and return to the constraint $m_{PS}L \geq 4$ This results in the fit parameters

a_0	$a_1\,[\text{GeV}^{-2}]$	b_1
$5.49\,(24)\,10^{-8}$	$-3.99\,(1.17)\,10^{-8}$	$4.2\,(3.2)$

and the difference to the standard fit is

$$\left[a_{\mu\ m_V}^{\text{hlo}} - a_{\mu\ m_V}^{\text{hlo}}(+a^2)\right]_{m_\pi^2} = 0.28\,(22) \times 10^{-8}. \tag{5.26}$$

This difference, like the b_1, too, is only on the verge of significance.

The third option we try is the amendment of a term

$$a_\mu^{\text{hlo}}(m_{PS}^2) = \left(a_0 + a_1\, m_{PS}^2\right) \times \left(1 + b_1\, a^2\right) \tag{5.27}$$

to the fit function. However, this results in a the following parameters.

a_0	$a_1\,[\text{GeV}^{-2}]$	$b_1\,[\text{GeV}^2]$
$4.80\,(60)\,10^{-8}$	$-1.87\,(62)\,10^{-8}$	$0.06\,(6.89)\,10^4$

This fit does not give a meaningful estimate of b_1, so we neglect this option.

As a systematic error stemming from effects of non-zero lattice spacing we take the result of the second option, i.e. we set

$$\Delta_a = 0.28 \cdot 10^{-8}\,. \tag{5.28}$$

Finite-size effects

We already dealt with one kind of finite size effect, the model dependence of our estimate for a_μ^{hlo}, which results from the gap of lattice momenta near the origin. Another source

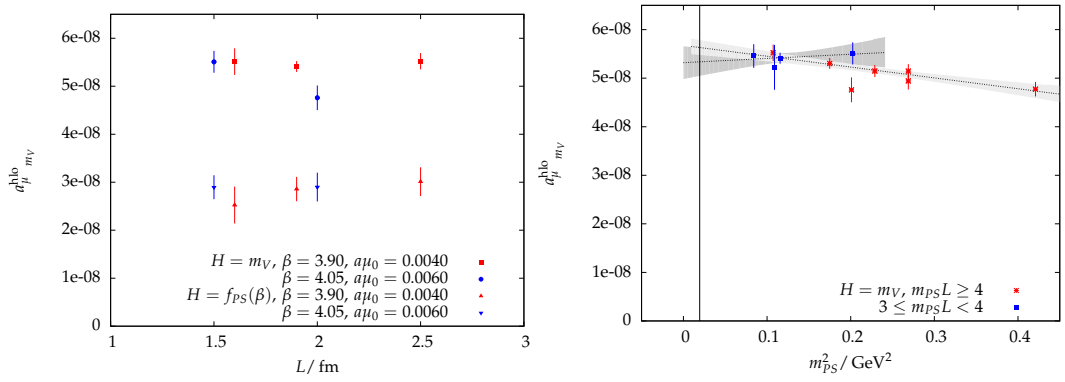

Figure 5.12: Left: ensemble-wise comparison of a_μ^{hlo} for different volumes; right: extrapolations of a_μ^{hlo} with support in two different volume regimes.

of uncertainty are the effects on the spectrum of the theory. These become visible by changing the physical volume of the box we use with all other lattice parameters kept fixed. We can appreciate such a volume change for two examples in the left panel of figure [5.12]: here we compare the value of $a_\mu^{\mathrm{hlo}}{}_{m_V}$ for ensembles (B_0, B_1, B_6) at $m_{PS} \approx 330\,\mathrm{MeV}$ and $a \approx 0.079\,\mathrm{fm}$ and ensembles (C_5, C_2) at $m_{PS} \approx 450\,\mathrm{MeV}$ and $a \approx 0.063\,\mathrm{fm}$. In case of the larger lattice spacing we do not observe any discernible effects of a decreased or increased box length. For the C ensembles the error bars do not overlap. But here the volume dependence becomes slightly obscured by the modified definition using $H = m_V$. The apparent discrepancy is a fluctuation that must be traced back to the estimates of f_V and m_V. This can be seen directly by looking at the corresponding estimates for $H = f_{PS}(\beta)$ in the same plot. With the mass-independent scale function the two points for the C ensembles are perfectly consistent, whereas for the B ensembles one can observe a trend of the estimate to increase with increasing volume, which is, however, statistically not yet significant.

To estimate the systematic uncertainty we use the following procedure: our estimate for central value and statistical error used the condition $m_{PS}L \geq 4$. We thus compare two extrapolations: one using all available ensembles with $m_{PS}L \geq 4$ and another one with all ensembles fulfilling $3 \leq m_{PS}L < 4$. These two extrapolations are shown in the right panel of figure [5.12]. At the phyiscal point this gives a deviation of $\delta a_\mu^{\mathrm{hlo}}{}_{m_V}(m_\pi^2) = 29\,(33)\,10^{-8}$ and this is likely a statistical fluctuation. But we chose the systematic error to account for the deviation at the physical point and quadratically subtract the statistical error of the extrapolated value from $m_{PS}L \geq 4$. We thus set

$$\Delta_L = 0.25 \cdot 10^{-8}\,. \tag{5.29}$$

Summary: modified extrapolation

To sum up we collect the error budget in the following table

Δ_{stat}	Δ_m	Δ_d	Δ_a	Δ_L
$0.15 \cdot 10^{-8}$	$0.18 \cdot 10^{-8}$	$0.07 \cdot 10^{-8}$	$0.28 \cdot 10^{-8}$	$0.25 \cdot 10^{-8}$

We sum the individual errors in quadrature, keeping in mind that the latter three of them are statistically not significant. Moreover, the estimate of Δ_L relies on including amongst others ensembles C_2 and C_3. But these are used to estimate Δ_a as well. As for Δ_m , it stems from varations that are of order of $1 \sim 2\,\sigma$ in terms of the statistical extrapolation error and thus likely statistical fluctuations. The uncertainty of the result at the physical point is thus likely to be covered by the uncertainty of the extrapolation itself already. Taking a conservative approach we quote both uncertainties in our result,

$$a_\mu^{\text{hlo}}(\text{latt}) = 5.69\,(15)\,(42)\,10^{-8}\,. \tag{5.30}$$

5.3.3 Hadronic leading order anomalous magnetic momentum for the electron and tau lepton

The methods to calculate the hadronic LO muon anomalous magnetic moment described so far can be generalized to any of the three standard model leptons: the only reference we make to the specific properties of the muon is in the weight function $w = w(Q^2;\, m_\mu^2)$ as part of the integrand in equation (4.11). Apart from that the treatment for the electron and the tau to define a_e^{hlo} and a_τ^{hlo} is precisely the same from the practical point of view.

Conceptually, however, there is some difference between the three cases, which arises due to the mass hierarchy

$$m_e \approx 0.000511\,\text{GeV} \ll m_\mu \approx 0.105\,\text{GeV} \ll m_\tau \approx 1.78\,\text{GeV}\,.$$

The main support of the weight function can roughly be characterized by the position of its maximum at $(\sqrt{5}-2)\,m_l^2$. Thus the electron weight function essentially probes $\Pi(Q^2)$ in a small neighborhood of the origin, that is, it is essentially a function of the first derivative $d\Pi/dQ^2$ of the polarization function.

The tau weight function on the other hand probes the polarization function on scales of $O\left(1\,\text{GeV}^2\right)$, where the lattice data is already becoming rather dense compared to the muon case. Thus if we model the vacuum polarization function in a fit, then the tau case should be less dependent on the choice of the model function. By contrast in case of the electron a_e^{hlo} will be highly dependent on the model function since after the gap between the origin and the first lattice momentum the weight function has dropped several orders of magnitude leaving the integral virtually void of any direct support by lattice data. We conclude that the estimation of a_e^{hlo} and a_τ^{hlo} are indeed non-trivial tests of our lattice calculation and the modified method in particular.

The analysis of the systematic errors is carried out analogously to the one for a_μ^{hlo} described above with some adaptions and a similar cautious interpretation.

For the case of the electron the integral defining a_e^{hlo} is saturated in a small neighborhood of the origin. The maximum of the weight function occurs at $\hat{Q}^2_{\text{max}} = (\sqrt{5}-2)m_e^2 \approx 6 \cdot 10^{-8}\,\text{GeV}^2$. We can thus lower the upper integration limit to $2\,\text{GeV}^2$, restrict the polarization function to Π_{low} entirely and consider any systematics from the high momentum

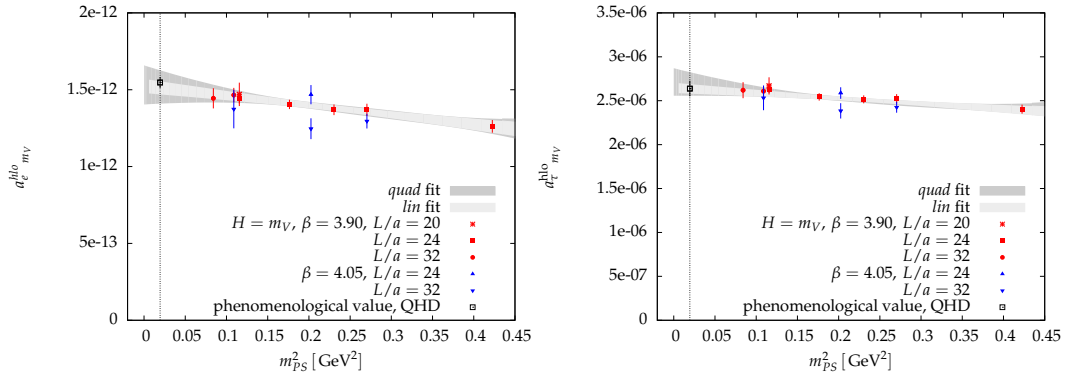

Figure 5.13: Extrapolation of $a_e^{\text{hlo}}{}_{m_V}$ and $a_\tau^{\text{hlo}}{}_{m_V}$ in m_{PS}^2; the data points step from the $M1N2B0C0$ and $M1N2B1C4$ model function, respectively.

region above $2\,\text{GeV}^2$ as negligible. The systematic uncertainty stemming from the choice of a model function is then restricted to varying $M = 1, 2, 3$ and $N = 2, 3$ in the subset of model functions with $B = C = 0$. The systematic errors from the individual sectors are given in the following table.

value	Δ_{stat}	Δ_m	Δ_d	Δ_a	Δ_L
$151.2 \cdot 10^{-14}$	$4.3 \cdot 10^{-14}$	$3.4 \cdot 10^{-14}$	$1.6 \cdot 10^{-14}$	$9.8 \cdot 10^{-14}$	$6.7 \cdot 10^{-14}$

$$\begin{aligned} a_e^{\text{hlo}}(\text{latt}) &= 1.512\,(43)\,(125)\,10^{-12} \\ a_e^{\text{hlo}}(DR,\,QHD) &= 1.553\,(34)\,10^{-12} \end{aligned} \tag{5.31}$$

For the τ lepton the integration region beyond $2\,\text{GeV}^2$ is essential, in fact it gives approximately 50% of the final integral. So this case probes our modeling of the high momentum region. From the right-hand panel of figure [5.14] we deduce that the saturation of the integral occurs still beneath our upper integration limit. The individual systematic uncertainties are listed in the following table.

value	Δ_{stat}	Δ_m	Δ_d	Δ_a	Δ_L
$263.5 \cdot 10^{-8}$	$5.4 \cdot 10^{-8}$	$3.9 \cdot 10^{-8}$	$4.6 \cdot 10^{-8}$	$6.9 \cdot 10^{-8}$	0

In this case we cannot find any discernible effects from comparing extrapolations with $m_{PS}L \geq 4$ and $3 \leq m_{PS}L < 4$. The difference between them turns out to be approximately $1.3 \cdot 10^{-8}$, while at the same time the statistical uncertainties of the individual extrapolations at the physical point are $5.4 \cdot 10^{-8}$ and $9.5 \cdot 10^{-8}$, respectively. So we set this

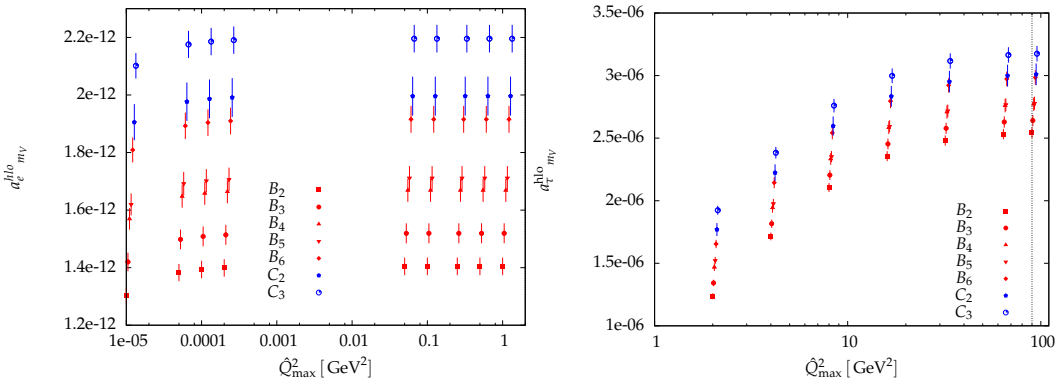

Figure 5.14:

contribution to zero. We thus estimate

$$a_\tau^{\rm hlo}(latt) = 2.635\,(54)\,(92)\,10^{-6} \tag{5.32}$$
$$a_\tau^{\rm hlo}(DR, QHD) = 2.681\,(76)\,10^{-6}\,.$$

The estimates for $a_e^{\rm hlo}$ and $a_\tau^{\rm hlo}$ can be compared to our to our phenomenological estimates in {4.5}, which were obtained from the dispersion relation based on the QHD prescription. We find good agreement for both leptons. We emphasize that the merit of the modified extrapolation is, however, not tied to the agreement with the phenomenological result. The latter has been shown to be disputable and afflicted with systematic errors. The major gain lies in the fact that the modified definitions of $a_{l\ H}^{\rm hlo}$ with appropriate H lead to a much milder mass dependence. This in turn allows for a meaningful extrapolation in the light pseudoscalar mass to the physical point, which would otherwise turn out problematic given presently available lattice data.

5.4 Hadronic leading-order contribution to $g_\mu - 2$ and the temporal moment method

In the previous sections we have followed through the conventional approach to determine the $a_\mu^{\rm hlo}$: it essentially involved (1) a fit to the momentum dependent lattice data for the vacuum polarization function in order to (2) determine $\Pi(0)$ and build the subtracted polarization function and (3) a numerical integration using the model function.

We know that step (1) is the conceptually delicate one as in the absence of infinite lattice volume it necessitates an extrapolation to zero momentum. This always implies a systematic uncertainty that was estimated above by a systematic study of the dependence of the fit results on the specific choice of the model function. Moreover, using a model for Π we need to stay aware of the kinematical setup of our lattice calculation. The box length has a strong impact on the spectrum of the lattice model. As L is varied,

decay channels can open or close, mixing of states can be enhanced or suppressed. Depending on the available precision, a model for Π may have to be changed accordingly to adequately capture the contributions from all states in the theory.

It would be desirable to circumvent steps (1) and (2) and avoid the corresponding issues. This can be achieved by a modification of the procedure in the following sense: we assume we have a function $F_{\mu\nu}$ that allows to write the vacuum polarization function in momentum space as a sum over lattice data contracted with the aforesaid function,

$$\Pi_R(q^2) = \sum_x \sum_{\mu\nu} \overline{\Pi_{\mu\nu}(x,\, y)}\, F_{\mu\nu}(q^2,\, x;\, y)\,. \tag{5.33}$$

The bar over the polarization function indicates that some averaging over directions is involved. The main point is that we have a weight function that carries the full dependence on the squared momentum and the latter is separated from the lattice data. Then we can evaluate the momentum integral independently from the lattice data

$$\begin{aligned} a_\mu^{\text{hlo}} &= \int_0^\infty \frac{dq^2}{q^2}\, w(q^2)\, \Pi_R(q^2) \\ &= \sum_x \overline{\Pi_{\mu\nu}(x,y)} \left[\int_0^\infty \frac{dq^2}{q^2}\, w(q^2)\, F_{\mu\nu}(q,\, x;\, y) \right] \\ &= \sum_x \overline{\Pi_{\mu\nu}(x,y)}\, S_{\mu\nu}(x;\, y)\,. \end{aligned} \tag{5.34}$$

The lattice calculation enters this estimator for a_μ^{hlo} via the position space vacuum polarization tensor $\overline{\Pi_{\mu\nu}(x,y)}$, which is the generic data extracted from the simulation. In particular, this estimator is void of any need to fit, extrapolate or interpolate the lattice polarization function.

With the temporal moment method we have one realization of such a scenario available and as a working example we would like to reconsider a_μ^{hlo} based on the local vector current correlator. This will allow us to further study the scale-function dependent definition of $a_{\mu\ H}^{\text{hlo}}$.

5.4.1 Momentum integration

The few steps in the appendix 10 are a reminder that the momentum integration for the temporal moment method can be done analytically. For the present purpose, however, we use the numerical integration. In the temporal moment method the polarization function is defined as a t-sum

$$\Pi(\hat{K}^2) = \sum_{t=a}^{t_{\max}} f(\hat{K}^2, t)\, \langle JJ(t, \vec{q}=0)\rangle^{av}\,,$$

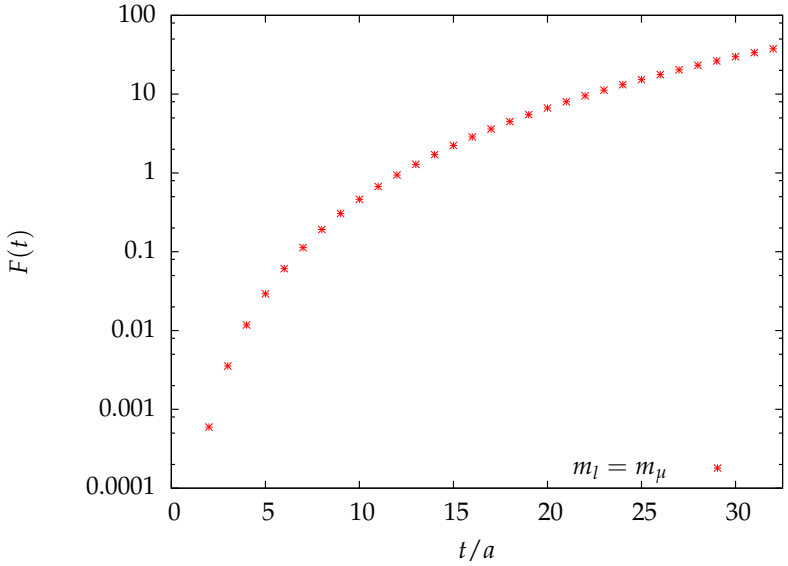

Figure 5.15: Integrated weight function in case of the muon.

which can be evaluated for all $0 \leq \hat{K} \leq 2/a$. The momenum integration then means to determine the coefficients $F(t; m_l)$ given by

$$F(t; m_l) = \int_0^{4/a^2} \frac{d\hat{K}^2}{\hat{K}^2}\, w(\hat{K}^2; m_l^2)\, f(\hat{K}^2, t)\,. \tag{5.35}$$

We show them for the case $m_l = m_\mu$ in figure [5.15].

We fix the integration limits in lattice units to $[0, \hat{K}^2_{\max} = 4]$, which means that in physical units the upper limit will depend on the scale function $Q^2_{\max} = 4\,\hat{H}^2/(H^2\,a^2)$. However, from our previous considerations we know that in this momentum range such a variation of $Q^2_{\max}$ leads to insignificant changes in the value of the integrals.

The local vector correlators are calculated from the same data that has been used for the conserved current. In particular, we then have a factor of five more source locations, which due to autocorrelation leads to an effective increase in statistics by a factor of $2 \sim 2.5$. In practice we block the data with block length 5 and thereby eradicate any residual autocorrelation.

Moreover, we need to set the normalization of the currents. We have found in chapter 3, that within the present setup the vector coupling g_V with its mild mass dependence is a safe quantity for such a purpose. We thus set the normalization of the currents by demanding the correct value of the coupling at the physical point

$$Z_V(\beta) = g_V^{exp} \left(g_V^{lat}(\beta, m_{PS}^2)\big|_{m_{PS}^2 = m_\pi^2} \right)^{-1}. \tag{5.36}$$

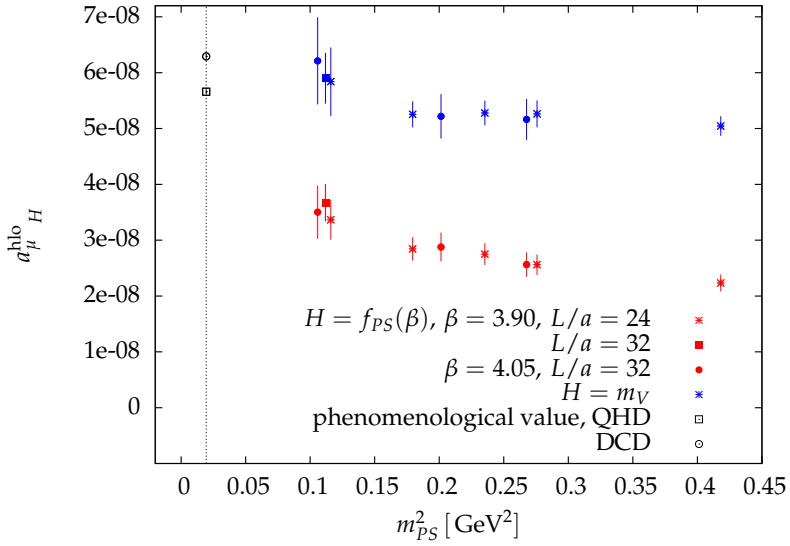

Figure 5.16: Comparison of $a_\mu^{\mathrm{hlo}}{}_H$ from the t-sum definition with $H = f_{PS}(\beta)$ and $H = m_V$.

This results in

$$\begin{aligned} g_V^{lat}(\beta = 3.90) &= 0.4862\,(51)\,, \quad g_V^{lat}(\beta = 4.05) = 0.4562\,(110) \\ Z_V(\beta = 3.90) &= 0.5869\,(66)\,, \quad Z_V(\beta = 4.05) = 0.6253\,(154)\,. \end{aligned} \tag{5.37}$$

The uncertainty of the so defined normalization is propagated consistently to the extrapolation of a_μ^{hlo} and the estimate at the physical point.

In figure [5.16] we gather the ensemble-wise defined values for $a_\mu^{\mathrm{hlo}}{}_H$ from the t-sum definition using $H = f_{PS}(\beta)$ (lower curve) and $H = m_V$. The ensemble B_7 is left out of the plot. In contrast to the other ensembles, the t-summation was not saturated in this case. The vector correlator assumes a constant value for large times $t/a \geq 27$, which is different from zero by approximately 2.5σ. Such a behavior prevents us from applying the t-sum according to our standard definition.

We emphasize that in this case we do not model the polarization function but use the principle of analyticity and lattice data only. We observe that using $H = m_V$ again the curve $a_\mu^{\mathrm{hlo}}{}_{m_V}(m_{PS}^2)$ becomes almost a flat line. We comprehend this as a non-trivial test of the method: even without any model assumptions we find confirmation for the suppression of the quark mass dependence by choosing an appropriate scale function $H = m_V$. Yet, with a word of caution we note that this does not seem to be the case anymore for the ensembles with the smallest pseudoscalar masses in the plot. The onset of the curvature when approaching the physical point seems to be delayed but not altogether eliminated. The statistical significance of this behavior is clearly rather low, but this may indicate, that in the end even when using $H = m_V$ a linear extrapolation in m_{PS}^2 is insufficient. We show the linear and quadratic extrapolation in the left panel

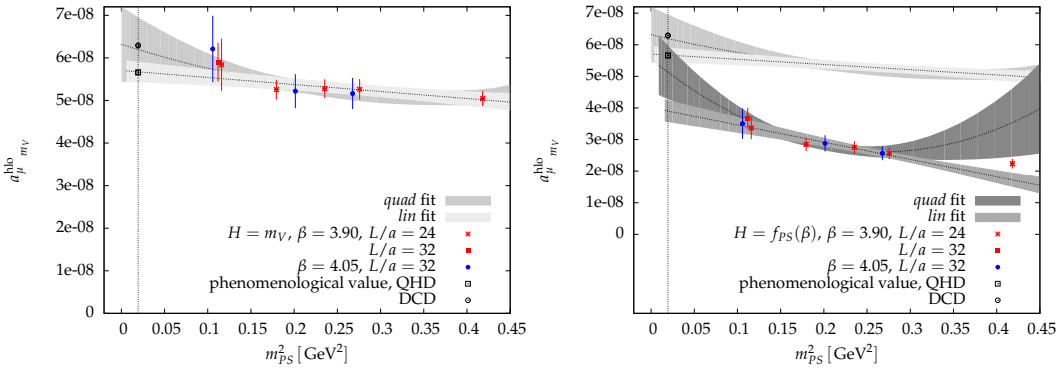

Figure 5.17: Extrapolation of $a_\mu^{\mathrm{hlo}}{}_H$ from the t-sum definition for $H = f_{PS}\beta$, m_V to the physical point.

of figure [5.17]. The result from the linear fit with statistical uncertainty,

$$a_\mu^{\mathrm{hlo}}{}_{m_V}(m_\pi^2)\Big|_{lin} = 567\,(24)10^{-10}$$

is in perfect agreement with our previous analysis based on the conserved current and with the phenomenological value derived using the QHD prescription, albeit with a larger extrapolation error. The quadratic extrapolation is consistent with the linear one due to the large uncertainty at the physical point. Moreover, its 1σ error band includes both the QHD and DCD phenomenological value. The quadratic fit picks up the curvature of the data and brings the central value of the fit very close to the phenomenological value derived with decay channel decomposition.

The ensemble-wise uncertainties for $a_\mu^{\mathrm{hlo}}{}_{m_V}$ are larger in this case, when compared to the $M1N2B1C4$ model. There the error cancellation arising from the change from $H = f_{PS}(\beta)$ to $H = m_V$ was built into the model function and allowed for a small extrapolation error for the linear fit. Due to the model independence of the temporal moment method this cancellation does not happen here.

We note that if for the $M1N2B1C4$ extrapolation we combine our estimate for the systematic error stemming from the choice of a model function with the statistical uncertainty from the linear extrapolation we get $\sqrt{\Delta_m^2 + \Delta_{stat}^2} \approx 23 \cdot 10^{-10}$. This is about the same size as the statistical extrapolation error from the t-sum definition.

Finally, we would like to comment on the right panel in figure [5.17]. We perform an extrapolation with $H = f_{PS}(\beta)$ using ensembles B_2, B_3, B_4, B_6. All ensembles have $m_\pi L \geq 4$ and we leave out the ensemble with the heaviest pseudoscalar mass. Using this setup we find that the extrapolated value from the *quad* fit for $H = f_{PS}(\beta)$ at the physical point overlaps with those from $H = m_V$. The extrapolated value becomes consistent with the QHD and the DCD phenomenological value within approximately 0.5 and 1.5 standard deviations, respectively.

5.5 Leading order charm contribution to a_μ^{hlo} from partially quenched tmLQCD

We would like to apply the methods described in this chapter to the charm sector. The charm quark is not part of the dynamical simulation but introduced in the valence sector as a heavy doublet $\chi_c^\pm$ with twisted charm quark mass $\pm\mu_c$ in the tm Dirac operator. Again we use the polarization function defined by the conserved vector current associated with the charm quark with the positive quark mass. Note that the concept of the conserved vector current is non-trivial in the quenched sector and requires the introduction of the heavy doublet mentioned above as well as the additional dynamics of the ghost fields to regain the Ward identity in terms of the fields $\chi_c^\pm$.

From there on we use the same definitions and extrapolations of a_μ^{hlo} as before with the difference that with the charm valence quark mass we have an additional parameter. The latter is tuned such that at given lattice scale the physical value of a charmed meson, for instance m_{η_c} or $m_{J/\psi}$ is reproduced.

The charm sector offers the advantage that the polarization function, the vector meson mass and the hadronic leading order anomalous magnetic moment can be determined with much higher precision compared to the light sector. Also the decay of the charm vector meson $m_{J/\psi}$ is much less of a problem from the kinematical and dynamical point of view. Finally, we have the possibility to tune the valence quark mass through the physical point (as defined above) and can see the modified extrapolation method at work.
At the same time we must take into account larger artifacts from the lattice spacing, which come in the form $(a\mu_c)^2$.

5.5.1 General remarks and charm vector coupling

The general strategy for the analysis is thus as follows. We determine the value of a_μ^{hlo} in the charm valence sector for several triples $(\beta,\, \mu_0,\, \mu_c)$ of coupling, light quark mass and charm valence quark mass. Likewise we determine the mass and decay constant of the $m_{J/\psi}$ meson. As usual we substitute the lattice parameters $(\beta,\, \mu_0,\, \mu_c) \to (a,\, m_{PS}^2,\, m_{c\bar{c}})$ and consider $a_\mu^{\mathrm{hlo}} = a_\mu^{\mathrm{hlo}}(m_{PS}^2,\, m_V,\, a^2)$.

We show exemplary lattice data for the polarization function and vector coupling in figure [5.18]. In the left panel we observe the influence of heavy quark mass and momentum on the shape of the polarization function in different momentum regions: at large momentum values, such that $\hat{Q}^2 \gg m_c^2$, effects of the charm quark mass are small and the curves for different bare valence quark masses converge. The low momentum region on the other hand is strongly shaped by the size of the quark mass. The latter essentially determines the value and the derivatives at the origin and thus the curves spread out.

As a first test quantity we would like to look at the coupling $g_{\mathrm{V,em}}$ for the charmed electromagnetic current. The right-hand panel of figure [5.18] shows the coupling as a function of the charm vector meson mass. The charm quark has electromagnetic charge

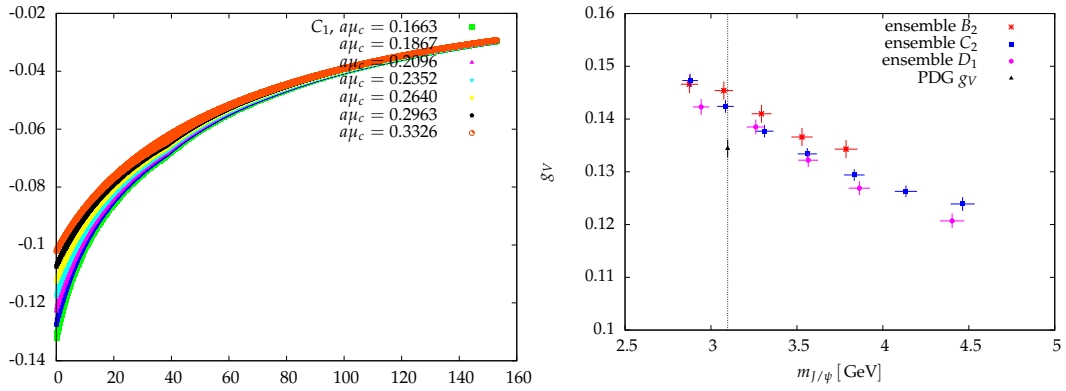

Figure 5.18: Π_c from ensemble C_2 for a range of charm valence quark masses (left) and coupling of the J/ψ for the ensemble with lightest pseudoscalar for each lattice spacing.

$Q_c^{\mathrm{em}} = 2/3$ and its coupling g_V is related to the electromagnetic coupling via

$$\begin{aligned} g_{\mathrm{V,em}} &= \frac{2}{3}\, g_V \\ g_V^{\mathrm{phys}} &= 0.1344\,(17)\,. \end{aligned}$$

We find the lattice data points significantly above the physical value with a trend to decrease with decreasing lattice spacing. These sizeable lattice artifacts were to be expected in the charm sector. Concerning the precision of the charm vector meson mass we mentioned before, we note that the uncertainty of m_V displayed in figure [5.18] stems predominantly from the lattice spacing ($\approx 1.6\%$), while the mass in lattice units has a relative uncertainty in the per mill region (cf. tables {16} and {17} in the appendix 12).

To extrapolate to the physical point in the charm valence sector we perform combined fits with several lattice spacings, pseudoscalar masses and valence quark masses and simultaneously fit the $(m_{PS}^2,\, m_V,\, a^2)$ dependence and likewise simultaneously extrapolate $a \to 0$, $m_{PS}^2 \to m_\pi^2$ and interpolate $m_V \to m_{J/\psi}$. Our model function is polynomial in all three parameters:

$$\begin{aligned} f(m_{PS}^2,\, m_V,\, a^2) &= \mathcal{F}_{\mathrm{cont}}(m_{PS}^2, m_V) \times \mathcal{F}_{\mathrm{latt}}(m_{PS}^2,\, m_V,\, a) \qquad (5.38) \\ \mathcal{F}_{\mathrm{cont}}(m_{PS}^2, m_V) &= \sum_{i=0}^{N_{\mathrm{val}}} \sum_{j=0}^{N_{\mathrm{sea}}} A_{ij}\, m_{PS}^{2j}\, m_V^i \\ \mathcal{F}_{\mathrm{latt}}(m_{PS}^2, m_V, a) &= \sum_{i=0}^{M_{\mathrm{val}}} \sum_{j=0}^{M_{\mathrm{sea}}} \sum_{k=0}^{M_{\mathrm{mi}}} B_{ijk}\, (am_{PS})^{2j}\, (am_V)^{2i}\, a^{2k} \\ B_{000} &= 1\,. \end{aligned}$$

$\mathcal{F}_{\mathrm{cont}}$ accounts for the continuum parametrization of the lattice data. We view this model

as a polynomial parametrization in m_V with coefficients A_k, where each coefficient itself is a function of the light quark mass, which is again modeled by a polynomial dependence $A_k = A_{k0} + A_{k1}\, m_{PS}^2 + \ldots$.
The second factor, $\mathcal{F}_{\text{latt}}$, models lattice artifacts. We distinguish terms with powers of the lattice spacing accompanied by factors of m_V (M_{val}), by m_{PS} (M_{sea}) and those that have neither (explicit) mass dependence (M_{mi}). Since we have data for three lattice spacings, as a rule of thump we keep the total order of corrections arising from the lattice spacing $i + j + k \leq 1$. With this restriction in place we usually fit (a subset of) B_{100}, B_{010}, B_{001}. [2] As in the previous analysis in the light sector, we usually have difficulties in gaining significant estimates for B_{100}, which accounts for $(am_{PS})^2$ artifacts. B_{010} and/or B_{001} on the other hand turn out to be necessary in our fits.

The charm vector meson masses m_V are fit simultaneously with the data: we construct the 2-dimensional grid $(\tilde{m}_V,\ f(\tilde{m}_V;\, m_{PS}, a)$ that best fits our lattice data grid (m_V, g_V). The correlation matrix entering the function χ^2 is constructed in a block-diagonal way, with one block corresponding to one set of valence quark masses for a pair $(\beta,\ \mu_0)$.

To model the dependence on the J/ψ meson mass we include those 3 or 4 valence quark masses for each pair $(\beta,\ \mu_0)$ in the fit, that correspond to a meson mass in the interval $2.8\,\text{GeV} \lesssim m_V \lesssim 3.8\,\text{GeV}$, which encloses the physical value of the $c\bar{c}$ vector meson mass at $m_{J/\psi} = 3.096916\,(11)\,\text{GeV}$. Further on, we put the restriction $m_{PS}L \geq 4$ in place for the $B-$ and $C-$ensemble family. For the smallest lattice spacing we have ensemble D_1 only, which has an $m_\pi L \approx 3.6$. In this case we relax the condition and keep this ensemble as well.

The fit result is given in equation (5.39) together with the result derived from the formula for the decay width $\Gamma(J/\psi \to e^+e^-)$.

$$\begin{aligned} g_V(\text{latt}) &= 0.1372\,(23)\,(15) \\ g_V^{\text{phys}} &= 0.1344\,(17)\,. \end{aligned} \tag{5.39}$$

The first uncertainty in eq. (5.39) is the statistical error from the fit / extrapolation and interpolation to the physical point. For the value itself we use the result from the fit with $N_{\text{sea}} = 2$, $N_{\text{val}} = 3$, $M_{\text{sea}} = 0$, $M_{\text{val}} = 1$ and $M_{\text{mi}} = 0$. The second one is to estimate the systematic dependence on the fit formula. To that end we look at the right panel of figure [5.19], where we show fit results for different choices for the parameters N_X, M_X. We find that though the results are consistent there is a tendency of better agreement with the experimental value if we allow for more terms capturing lattice artifacts. From the variance of these values we derive the systematic error. The extrapolated value agrees with the physical one within one standard deviation. This agreement is encouraging in consideration of the vector meson dominance and the importance of the coupling for the tree-level vector contribution.

[2] In some cases we will also use $i = 2$ with $j = 0 = k$.

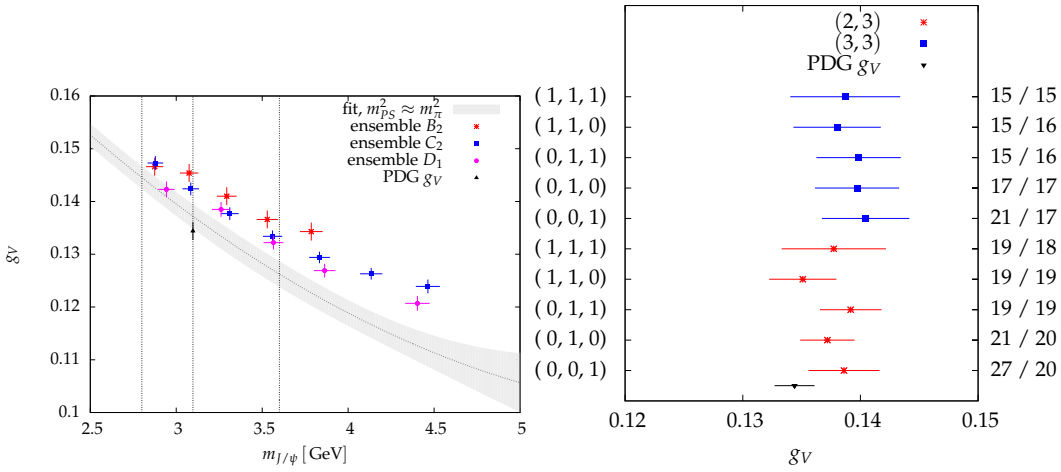

Figure 5.19: Left panel: $\mathcal{F}_{\mathrm{cont}}(m_{PS}^2 \approx m_\pi^2,\, m_V)$ for the fit $(2,3,0,1,0)$; right panel: variance of fit results for different choices for N_{sea}, N_{val}, M_{sea}, M_{val}, M_{mi}. The labels on the left vertical axis show the combination M_{sea}, M_{val}, M_{mi} used in the fit, those on the right vertical axis give the χ^2/dof. The upper five (blue) points correspond to $N_{\mathrm{sea}} = 2$, the lower five (red) to $N_{\mathrm{sea}} = 3$, while $N_{\mathrm{val}} = 3$ throughout.

5.5.2 Calculation of $a_\mu^{\mathrm{hlo}}(\mathrm{charm})$

To compare the charm contribution to the hadronic leading-order anomalous magnetic moment of the muon we again use the QHD and DCD methods to extract a value that can be attributed to the charm quark. Adapting the methods we proceed as follows: for the QHD estimate we add up all contributions to a_μ^{hlo} with $m_{J/\psi} \leq \sqrt{s} < m_\Upsilon$ with weight $4/10$ and all contributions with $m_\Upsilon \leq \sqrt{s} < \infty$ with weight $4/11$.

For the DCD estimate we assign all contributions with final charmed states to the charm piece of a_μ^{hlo} plus all the intermediate pQCD contributions rescaled as for the QHD method. Applying both methods we find

$$a_\mu^{\mathrm{hlo}}(DCD,\, \mathrm{charm}) = 1.454\,(33)\,10^{-9} \tag{5.40}$$

$$a_\mu^{\mathrm{hlo}}(QHD,\, \mathrm{charm}) = 1.163\,(33)\,10^{-9}\,. \tag{5.41}$$

Note that the QHD value is essentially the difference of the value for four and three flavors and that in both cases we disregard the fact, that beyond the valence approximation there is a mismatch of sea quark degrees of freedom that would appear in loops of higher order. As before we work under the hypothesis that sea quark effects are largely covered by the light doublet with the negligence of secondary charm production giving rise to a small systematic effect.

The lattice data for $a_\mu^{\mathrm{hlo}}{}_H$ from the $t-$sum method is shown in figure [5.20] for both choices $H = f_{PS}(\beta)$ and $H = m_V$ and a selection of ensembles (cf. tables {18} and

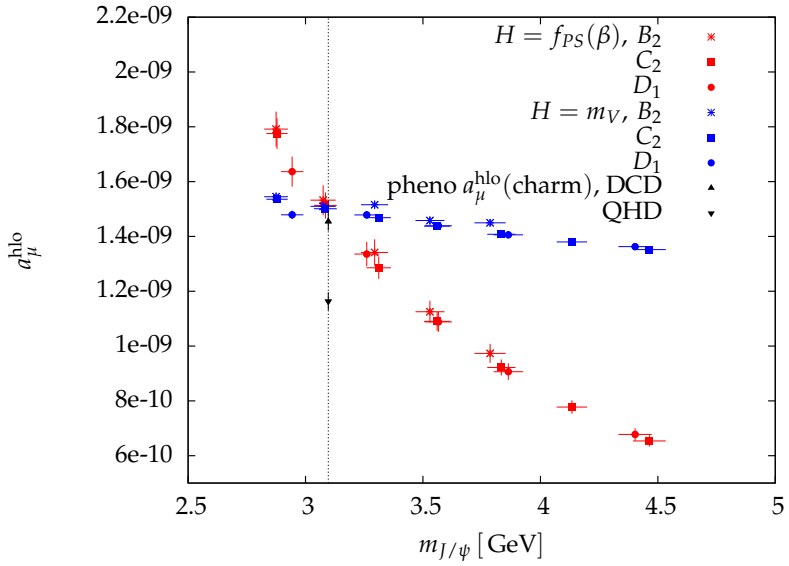

Figure 5.20: Comparison of $a_{\mu\ H}^{\rm hlo}(\text{charm})$ for $H = f_{PS}(\beta)$ and $H = m_V$. The dotted line marks the physical point $m_V = m_{J/\psi}$.

{19} in the appendix 12 for the numerical values). From our point of view this gives a nice visualization of the modified extrapolation method, since in the charm sector and given the quenched charm degree of freedom we can estimate $a_\mu^{\rm hlo}$ across the physical point in $m_V = m_{J/\psi}$. As mentioned before, in contrast to the light sector we can estimate the charm vector meson mass m_V sufficiently precisely, such that we can use it directly to tune the charm quark mass. We include ensembles B_2, C_2 and D_1 as examples. We observe both the suppressed mass dependence and reduced uncertainty of $a_{\mu\ m_V}^{\rm hlo}$ compared to $a_{\mu\ f_{PS}(\beta)}^{\rm hlo}$. The latter effect is, however, due to the fact, that the scale defined from the vector meson mass $(am_V)/m_{J/\psi}$ is per ensemble more precise than the lattice spacing. To extrapolate/interpolate to the physical point we put in place the same restrictions as in case of g_V in the previous subsection. Fortunately, in figure [5.20] we find a weak variation across the available lattice spacings: the data points from ensembles with different values of the latter almost fall on one universal curve. We observe a tendency of the displayed lattice data to decrease with decreasing lattice spacing.

The fits of $a_\mu^{\rm hlo}(m_V)$ turn out to be hampered by an occasionally pathological behavior of the correlation matrix. Interestingly, we can differentiate two scenarios, which are labeled by the choice of scale function H: for $H = f_{PS}(\beta)$ we observe the symptoms of instability of fits when adding further parameters, large values of χ^2/dof and best-fit parameters that leave the fitted curve significantly off the data. This behavior is suppressed when choosing $H = m_V$. In that case we find ourselves able to perform reasonable fits albeit with arguably large values for χ^2/dof, when using our standard $O\,(20 \sim 30)$ lattice data sets.

For the two choices of scale function the correlation behavior can be expected to be quite different, which we would like to illustrate concentrating on one pair (β, μ_0). Using $H = f_{PS}(\beta)$ we necessarily introduce a correlation across all data sets for one value of β. We recall that in the VMD picture the leading term is $a_\mu^{\mathrm{hlo}} \sim g_V^2\, a^2\, m_l^2/(am_V)^2$, which we fit as a function of $(am_V)/a$. The value in brackets indicates the originally obtained value in lattice units. Using $H = m_V$ we have $a_\mu^{\mathrm{hlo}} \sim g_V^2\, m_l^2/m_{J/\psi}^2$ for the leading term, again fitted as a function of $(am_V)/a$. In the first case we must expect an enhanced anticorrelation for the block giving $\mathrm{Cov}(a_\mu^{\mathrm{hlo}}, m_V)$ in the correlation matrix. This is what we find when comparing the normalized correlation matrices for both cases. While in the latter case the correlation coefficients in this block are positive and suppressed by a factor of $O(50)$ compared to the blocks giving $\mathrm{Cov}(a_\mu^{\mathrm{hlo}}, a_\mu^{\mathrm{hlo}})$ and $\mathrm{Cov}(m_V, m_V)$, they remain close to -1 in the former case. We note that due to their definition the correlation of a_μ^{hlo} vs. m_V should be suppressed for the following reason: since we use the $t-$sum to estimate the polarization function and hence a_μ^{hlo}, virtually all contributions to a_μ^{hlo} essentially come from $a \leq t \leq T/2$, whereas the mass fits are almost exclusively performed at times $t \geq T/2$. This decoupling of the support for both quantities adds to a suppression of the cross correlation despite them being derived from the same correlator.

Moreover, when checking the eigenvalues of the covariance matrices for the individual pairs (β, μ_0), we find that even though the matrix dimension does not exceed 8 they span a range, such that the ratio of lowest to largest eigenvalue becomes $\lambda_{\min}/\lambda_{\max} = O\left(10^{-19}\right)$ in some cases, which renders the covariance matrix close to numerically singular. This is, however, true for both choices of scale function.

A noteworthy difference becomes apparent upon an inspection of the eigenvectors of the correlation matrix. The pathological cases are marked by the coincidence of two circumstances: the smallest eigenvalue is two or three orders or magnitude smaller than the next-to-smallest one, giving the associated principal direction a correspondingly larger weight in the fit. Secondly, the eigenvector belonging to the smallest eigenvalue decouples the mass values by having the corresponding vector components again two or three orders of magnitude below the ones projecting on the difference for a_μ^{hlo}. In such a case the fit heavily relies on the one principal direction and the "best fit" can be driven away from the actual lattice data.

In conclusion we will expand our previous fit course of action in two respects. Firstly, instead of only using the standard correlated fits, we will perform additional ones, where we alter the shape of the correlation matrix. Secondly, we use two different fitting strategies for the two choices of the scale function. With these measures we have the opportunity to check for improvements of the fits regarding stability and we have a stronger cross check on the distribution of central values and uncertainties of the fit parameters and evaluation at the physical point.

For $H = m_V$ we will attempt single fits as before with data for multiple lattice spacings, sea quark masses and valence quark masses. In addition to the standard correlated fit we try two methods discussed in [98, 99], which essentially restrict the condition number of the covariance matrix, by lowering the impact of the smallest eigenvalues. For the

first method we start from the largest eigenvalue $\lambda_1 = \lambda_{\max}$ and keep all eigenvalues λ, which fulfill $\lambda/\lambda_{\max} > 10^{-16}$. The inverse of the remaining eigenvalues is set to zero when constructing the square root of the inverse covariance matrix from the singular value decomposition. In practice this modification concerns the lowest eigenvalue for some pairs $(\beta,\, \mu_0)$.

In a second approach we tame the influence of the smallest eigenvalues by averaging them. Using n valence quark masses per pair $(\beta,\, \mu_0)$ we have a $(2n) \times (2n)$ covariance matrix block for this pair and keep the largest $(2n-2)$ original eigenvalues, while we replace $\lambda_{2n-1,2n}$ by $(\lambda_{2n-1} + \lambda_{2n})/2$. With this modification the ability of the smallest eigenpair to solely drive the fit in a certain direction is confined by having the smallest two principal directions in competition on an equal basis.

The specifications of these choices are the result of some empirical studying and to our understanding represent the minimal changes in the respective directions we find necessary to attain a notable change of behavior.

Finally, we complement these two variations by naive uncorrelated fits. Though we cannot fully rely on the error estimates for the fit parameters from such fits, they will still give valuable cross checks on the central values.

We remark that in addition we cross check the fit model in equation (5.38) by replacing the multiplicative addition of lattice artifacts by an additive, but otherwise similar ansatz

$$\begin{aligned} \tilde{f}(m_{PS}^2,\, m_V,\, a^2) &= \mathcal{F}_{\text{cont}}(m_{PS}^2, m_V) + \mathcal{F}_{\text{latt}}(m_{PS}^2,\, m_V,\, a) \\ \mathcal{F}_{\text{latt}}(m_{PS}^2, m_V, a) &= \sum_{i=0}^{M_{\text{val}}} \sum_{j=0}^{M_{\text{sea}}} \sum_{k=0}^{M_{\text{mi}}} B_{ijk}\, (am_{PS})^{2j}\, (am_V)^{2i}\, a^{2k} \\ B_{000} &= 0\,. \end{aligned} \tag{5.42}$$

Since we find agreeing results at the physical point and roughly coinciding values for χ^2/dof from both model functions we only consider results from the multiplicative version explicitly.

For $H = f_{PS}(\beta)$ we pursue an alternative strategy, which we refer to as step-wise fits: first we interpolate the lattice data in the $c\bar{c}$ vector meson mass (or equivalently valence quark mass) and evaluate the interpolation function at the physical value $m_V = m_{J/\psi}$ for each pair $(\beta,\, \mu_0)$ individually. To do that we use a polynomial model function in m_V. For almost all ensembles the available valence $c\bar{c}$ vector meson masses enclose the physical value (at given lattice spacings) $m_{J/\psi}$ (exceptions are the ensembles B_7 and B_6, of which the latter enters the analysis). For each ensemble we use the $n_{\text{val}} = 4$ lowest valence quark masses and fit to a 2nd order polynomial, leaving us with one degree of freedom. To be able to do more rigorous correlated fits we partition the lattice data in n_{val} disjoint subsets of individual measurements and use a different subset for each valence quark mass. We repeat this procedure with all permutations for the mapping of subsets to valence quark masses. Afterward we recombine the samples for the evaluation at the physical value of the vector meson mass from all such fits, taking into account their residual cross-correlation. We can check that the resulting distribution of the combined samples gives a variance that is reduced by a factor of $1/n_{\text{val}}$, not $1/(n_{\text{val}}!)$, compared

(N, M)	full		min ev ratio		max ev no		uncorrel.
2 3 0 0 0	88/22	1.481 (14)	25/22	1.476 (13)	41/22	1.478 (13)	1.476 (13)
2 3 0 0 1	88/21	1.480 (19)	24/21	1.464 (20)	40/21	1.466 (20)	1.466 (21)
2 3 0 1 0	84/21	1.494 (15)	23/21	1.485 (15)	39/21	1.487 (15)	1.470 (20)
2 3 0 1 1	81/20	1.470 (21)	17/20	1.460 (20)	33/20	1.462 (20)	1.458 (21)
2 3 0 2 0	50/20	1.410 (25)	17/20	1.444 (26)	29/20	1.437 (26)	1.428 (26)
2 3 1 1 0	84/20	1.499 (17)	20/20	1.498 (17)	36/20	1.499 (17)	1.473 (28)
2 3 1 1 1	77/19	1.418 (35)	17/19	1.447 (34)	33/19	1.445 (35)	1.441 (32)
2 3 1 2 0	45/18	1.383 (28)	17/18	1.440 (37)	29/18	1.422 (30)	1.453 (52)
2 4 0 0 0	46/20	1.473 (13)	62/20	1.477 (14)	29/20	1.476 (13)	1.490 (16)
2 4 0 0 1	43/19	1.449 (22)	67/19	1.462 (23)	28/19	1.460 (21)	1.478 (23)
2 4 0 1 0	46/19	1.478 (15)	86/19	1.480 (19)	27/19	1.483 (15)	1.481 (21)
2 4 0 1 1	37/18	1.447 (21)	N/18	1.457 (21)	22/18	1.457 (21)	1.469 (23)
2 4 0 2 0	22/18	1.426 (21)	N/18	1.440 (33)	19/18	1.440 (24)	1.449 (30)
2 4 1 1 0	39/18	1.490 (16)	N/18	1.497 (22)	25/18	1.493 (17)	1.476 (28)
2 4 1 1 1	38/17	1.440 (37)	N/17	1.440 (36)	21/17	1.441 (35)	1.451 (33)
2 4 1 2 0	22/16	1.411 (27)	N/16	1.448 (49)	19/16	1.429 (30)	1.486 (63)
3 3 0 0 0	78/19	1.456 (29)	23/19	1.456 (29)	39/19	1.456 (29)	1.462 (29)
3 3 0 0 1	78/18	1.455 (29)	23/18	1.453 (30)	39/18	1.453 (30)	1.455 (28)
3 3 0 1 0	71/18	1.462 (28)	21/18	1.460 (28)	35/18	1.461 (28)	1.456 (28)
3 3 0 1 1	67/17	1.461 (29)	15/17	1.461 (29)	30/17	1.462 (29)	1.458 (27)
3 3 0 2 0	42/17	1.440 (32)	17/17	1.449 (31)	28/17	1.447 (32)	1.429 (29)
3 3 1 1 0	70/17	1.477 (31)	17/17	1.481 (30)	32/17	1.482 (30)	1.454 (32)
3 3 1 1 1	65/16	1.442 (36)	15/16	1.453 (36)	30/16	1.453 (36)	1.441 (33)
3 3 1 2 0	39/15	1.421 (34)	18/15	1.456 (44)	28/15	1.440 (36)	1.464 (55)
weighted	1.447 (24) (30)		1.462 (27) (17)		1.458 (25) (20)		1.454 (29) (17)

Table 5.6: Results for the different types of single fits using $H = m_V$. For each fit type except the uncorrelated we list the value of χ^2/dof and next to it the result for a_μ^{hlo} in units of 10^{-9} with its statistical uncertainty from the fit. For the series of fits, where χ^2 is marked by N, its value turns out rather large; for lack of space they are listed here from top to bottom: $\chi^2 = 488, 503, 249, 1065, 2314$

to the individual fits.

The so obtained values for $a_\mu^{\mathrm{hlo}}(m_{PS}^2; a)$ are then extrapolated to the physical point by a simultaneous fit of the dependence on the light pseudoscalar mass and lattice artifacts using a model function of the type (5.38) with $N_{\mathrm{val}} = 1$ and $M_{\mathrm{val}} = 0$.

This seemingly circuitous procedure allows to perform fully correlated fits without modifications to the correlation matrix, since in the first step we have data sets that are statistically independent. Further on, by recombining the permuted fits we do not lose information.

Let us start with the results for $H = m_V$. We list the fit results in table {5.6}. The left-most column gives the combination of fit parameters for the continuum and lattice part of the fit function, while the remaining four columns show the χ^2/dof and the result at the physical point for each of the fits just discussed. We observe a stable value at the physical point both across variations of $N_{\mathrm{sea}} = 2, 3$, $N_{\mathrm{val}} = 3, 4$ and different choices for

(N, M)	$a-$correlated		full	
2 1 0 0 0	5/5	1.473 (12)	4/5	1.473 (13)
2 1 0 0 1	2/4	1.455 (17)	3/4	1.457 (17)
2 1 1 0 0	4/4	1.475 (12)	4/4	1.473 (13)
2 1 1 0 1	1/3	1.431 (32)	1/3	1.425 (33)
3 1 0 0 0	3/4	1.447 (27)	3/4	1.447 (31)
3 1 0 0 1	2/3	1.445 (27)	3/3	1.453 (32)
3 1 1 0 0	3/3	1.452 (28)	3/3	1.452 (30)
3 1 1 0 1	1/2	1.432 (33)	1/2	1.429 (33)
weighted	1.447 (25) (16)		1.445 (27) (18)	

Table 5.7: Results from various final extrapolations in m_{PS}^2 and a from the step-wise fit procedure. The meaning of the entries is analogous to table {5.6}.

the parametrization of lattice artifacts as well across as across different fitting procedures. We note that for fits using e.g. $N_{\text{sea}} = 2$, $N_{\text{val}} = 4$ we already have a strong correlation of the fit parameters, such that they come out with a broad individual distribution, yet conspiring to give a stable value at the physical point. From that point of view we do not see a benefit in adding more parameters on this side. Moreover, the value at the physical point comes from the evaluation of the continuum parametrization function $\mathcal{F}_{\text{cont}}$ only. Adding lattice artifact terms thus initiates a potential tradeoff between $\mathcal{F}_{\text{cont}}$ and $\mathcal{F}_{\text{latt}}$ that is not under control: contributions can be shifted from the coefficients A_{ij} to B_{klm} and vice versa. We can observe this behavior in our fit results: there is a tendency of decreasing values at the physical point with an increasing number of lattice artifact terms. A remedy for this issue can come from e.g. using Bayesian priors as was advocated in reference [2]. However, we will not use this technique here, but restrict the number of correction terms to a reasonable number. Having data for three lattice spacings we can resolve a linear dependence in a^2 with one degree of freedom, maximally a quadratic dependence without any degree of freedom. We use these figures as restrictions as seen in table {5.6}. In the last row we give the value we derive from the individual fit results by weighting them with the inverse reduced χ^2. The second uncertainty in brackets stems from the variance of the fit results, which represents the spread stemming from the choice of the fit model.

Next, we look at the step-wise fits using $H = f_{PS}(\beta)$. The results for the fits are listed in table {5.7} with again the weighted result and spread in the last row.

We show the results from two variations of treating the correlation: for the column labeled $a-$correlated we keep track of the residual correlation stemming from the lattice spacing by sampling it coherently during the fit. For the column labeled full we use the full correlation matrix across pairs with different light quark mass but the same β (which correspond to one and the same lattice spacing). For the step-wise fits we have an analogous stability of the extrapolated value at the physical point across different choices for the continuum and lattice parametrization. Moreover, these results are in agreement with those from the previous procedure concerning central values and

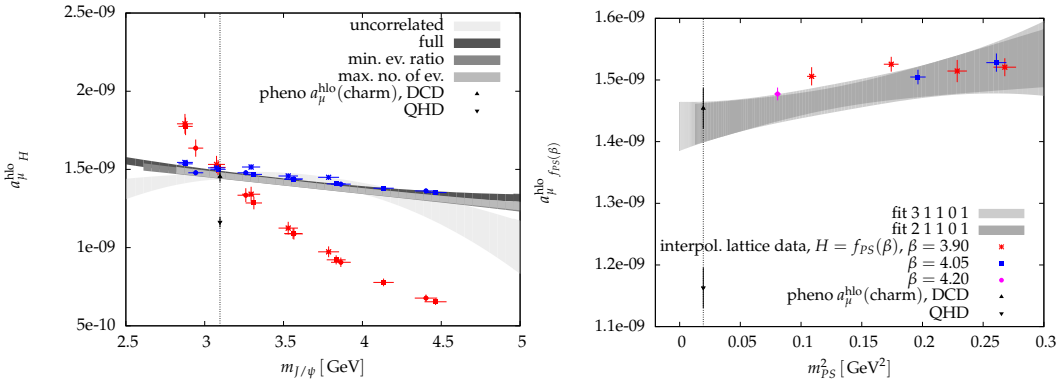

Figure 5.21: Left: extrapolation/interpolation of $a_\mu^{\rm hlo}{}_{m_V}$ for by a single fit (type 2 3 0 1 1) around $m_V = m_{J/\psi}$ at $m_{PS} \approx m_\pi$; right: final extrapolation in the step-wise fit (type 2 1 1 0 1).

uncertainties.

Comparing ensembles B_1 and B_6 at $m_V = m_{J/\psi}$ we can check for finite-size effects. The difference between the two ensembles reads

$$a_\mu^{\rm hlo}{}_{m_V}(B_1) - a_\mu^{\rm hlo}{}_{m_V}(B_6) = 0.24\,(19)\,10^{-9}\,.$$

This number suggests again a lack of statistical significance of the difference. Since furthermore already the statistical uncertainty covers a fluctuation of this size, we do not add an additional error term.

In view of the consistency of results from all fitting prescriptions followed here, we quote as our lattice estimate the result from the full fit using $H = m_V$,

$$a_\mu^{\rm hlo}(\text{latt, charm}) = 1.447\,(24)\,(30)\,10^{-9}\,. \tag{5.43}$$

This value is in full agreement with the DCD result in equation (5.40) and the difference to the QHD estimate is $0.284\,(51)\,10^{-11}$. The disparity is partly driven by the fact, that QHD associates part of the charm resonance contributions from J/ψ and Ψ_2 to the value for 2 and 3 flavors.

In figure [5.21] we exemplarily show two typical extrapolations. The left panel displays the four different interpolations at $m_{PS}^2 \approx m_\pi^2$ for the choice $N_{\rm sea} = 2$, $N_{\rm val} = 3$, $M_{\rm sea} = 0$, $M_{\rm val} = 1$ and $M_{\rm mi} = 1$. Apart from the uncorrelated fit the 1σ bands of the evaluated fit functions overlap. The uncorrelated fit is less constrained in its tend to map out detailed fluctuations of the lattice data and acquires rather strong curvature. Still, at the physical value of the charm vector meson mass it is in agreement with the remaining fits, that keep (a partly modified) version of the correlation.

In the right panel we show the extrapolation in m_{PS}^2 and a for the fit using $N_{\rm sea} = 2$, 3 and $M_{\rm sea} = 0$, $M_{\rm mi} = 1$. Again we find overlapping error bands for the linear and quadratic ansatz in m_{PS}^2 with no discernible curvature in the continuum part of the fit

model.

6 Conclusions and outlook

In this work we were concerned with an investigation of current-current correlation functions in twisted mass lattice QCD. These correlation functions are elementary building blocks of a field theory and they carry a plethora of physical information about the standard model. They can be extracted in lattice field theory by computing 2-point-functions and can be calculated with control over statistical and systematic uncertainties. One major aim of lattice QCD is to provide ab-initio results from non-perturbative calculations of standard model quantities with a precision and reliability that have the potential to challenge experiment. With this work we want to discuss one such observable, namely the hadronic leading order lepton anomaly.

We started by laying out our methods to handle the lattice current correlators. The key questions we addressed were how to describe the inherently discrete lattice vacuum polarization data by a smooth function, that would allow both the evaluation at zero momentum as well as the integration of the subtracted polarization function to form the hadronic leading order anomalous magnetic moment of the muon, a_μ^{hlo}. Based on the notion of vector meson dominance we proposed a family of parametrizations for the lattice vacuum polarization in the complete momentum regime, from the lowest available lattice momentum $2\pi/L$ to the cut-off π/a, that incorporate both the characteristic tree-level vector meson contribution at low momentum as well as the logarithmic behavior at high energy. Beyond these advisedly chosen contributions the parametrizations are sufficiently generalized to systematically cover the complete momentum dependence of the lattice vacuum polarization.

Further on we proposed applying an a priori model independent description derived from the temporal moment method, that we refer to as the t-sum definition of the vacuum polarization function and has its roots in the discrete Chebyshev transform. In the version outlined in this work it has the advantage of requiring only the time dependent current correlation function at zero momentum. We showed that for the available lattice momentum region our fitted parametrizations of the lattice vacuum polarization agree with this new definition. The here developed $t-$sum method provides a formula for the evaluation of the polarization function at the origin without a fit or extrapolation. This in turn provides a substantive cross check of our conventional fits.

The further generalization of the proposed method and its applicability in the time-like momentum region are currently under investigation. An elucidating feature of the $t-$sum method as used here is the nice, direct view it allows on the both qualitative and quantitative impact of individual time regions of the current correlator on the so-described polarization function. One recurring issue we recognize therefrom is the challenge of improving the signal quality in the large time behavior of the correlators, which bears the essential low-momentum spectral information.

We proceeded with the extraction of an estimate of the 2-flavor hadronic leading order muon anomalous magnetic moment. A comparison of $a_\mu^{\mathrm{hlo}}(m_{PS}^2)$ with results from a parallel study using improved clover fermions showed a compelling agreement of both approaches. The independent investigation differs from ours in a number of key aspects regarding the use of twisted boundary conditions and the type of modeling used for the polarization function. This suggests that such lattice artifacts arising from the specific choice of a fermion action discretization seem to be under control with presently achievable statistical uncertainties.

While first using the conventional approach, we encountered the traditional problems when it comes to the extrapolation in the pion mass to the physical point. We elaborated on investigating the origins of this problem and based on the vector meson dominance approach traced it back to the behavior of the lightest lattice vector meson mass and coupling as a function of the pseudoscalar mass, which form a central ingredient for a correct estimate of the bulk contribution to a_μ^{hlo}.

To potentially soften this problem in a systematic way we laid out a new method to extrapolate to the physical point. The otherwise dimensionless hadronic leading order muon anomaly requires the input of a scale function. Provided it fulfills some naturally arising conditions we are free to choose this scale function, H, and can set up a new well-defined estimator $a_{\mu\ H}^{\mathrm{hlo}}$ for a_μ^{hlo} from each such choice. We tried to show that depending on how we parametrize the lattice vacuum polarization function, the choice of H can be optimized to suppress the dependence on m_{PS}^2 when taking the limit $m_{PS}^2 \to m_\pi^2$. Specifically for the VMD inspired family of parametrizations we used, we can show that the natural choices m_V, $g_V \cdot m_V$ and $g_V \,/\, m_V$ built form the vector meson coupling and mass come close to optimal. Focusing on $H = m_V$ we find that the lattice-based $a_{\mu\ m_V}^{\mathrm{hlo}}(m_{PS}^2)$ suggests itself for a linear extrapolation to the physical point, displaying very limited curvature even when allowing for it in the fit. Moreover, for our specific setup of parametrization of the polarization function and the choice of H we observe a far-reaching cancellation of statistical uncertainties, that arise from the fit and extrapolation of the polarization function, in the ensemble-wise determined $a_{\mu\ m_V}^{\mathrm{hlo}}(m_{PS}^2)$. This circumstance and the linear extrapolation result in an unprecedented statistical precision of the extrapolated value at the physical point.

We extended this calculation to estimate the hadronic leading order anomaly for all three standard model leptons and found the modified method to work as expected in all three cases. This provides a non-trivial test due to the mass hierarchy spanned by the leptons, which puts emphasis on different momentum regions when integrating the weighted polarization function. To our knowledge this resulted in the first estimate of a_e^{hlo} and a_τ^{hlo} in a lattice calculation.

What we lack in this work for an independent confirmation of this method is a reliable comparison with experiment. We brought forward a prescription to extract a 2-flavor estimate for the hadronic leading order lepton anomalies from existing experimental data for the hadronic cross section ratio based on the dispersion relation approach. We discussed several assumptions that underlie these estimates and lead to as of yet unresolved systematic uncertainties. In fact, an alternative way to arrive at a 2-flavor

phenomenological estimate for the case of the muon has been brought to our attention. The observation that starting from alternative assumptions but the same experimental input it leads to a result, which differs significantly from ours, prevents us from drawing a final conclusion at this stage.

Nevertheless, it is reassuring for us to see a very good agreement for the lattice estimates of the hadronic leading order anomaly for all three standard model leptons with our phenomenological estimate. The immediate way out of this ambiguity is an estimate based on a simulation that can be directly compared to experiment. Luckily, such an investigation is underway: based on the 2+1+1 simulations of the ETMC, including dynamical strange and charm quark, this project is continued. With its results we can hope to ultimately challenge the usage of the dispersion relation as the standard approach in the estimate of the complete a_μ from standard model physics.

We conduct a further investigation of the new extrapolation method in conjunction with the proposed $t-$sum definition of the polarization function. It shows that we get fully compatible results and thus that in this field of application the $t-$sum definition provides a useful tool. Moreover, results from this study hint at a possible insufficiency of a pure linear extrapolation in m_{PS}^2. It would be interesting to apply the $t-$sum definition in case of the disconnected contribution. So far we could not find a usable signal in the data we have by using the conventional method to extract the polarization function. The alternative definition may open the possibility for a refined analysis.

With present day lattice simulations we consider the new modified extrapolation method as a necessary intermediate step for a reliable calculation of a_μ^{hlo}. As simulations at lower pion masses and in larger spatial volume become feasible, extrapolations to the physical pion mass or to zero momentum become void of systematic uncertainty. At the physical point itself the method will need to be modified and propositions for alternative choices of scale functions have been brought forward already. However, the principle idea will remain unchanged. Further on initial simulations at the physical point are unlikely to be in large volumes and show small statistical fluctuations in observables like a_μ^{hlo}. Thus even in these upcoming scenarios lattice estimates of such quantities will benefit from the modified extrapolation.

Finally, we looked at an estimate of the charm leading order muon anomaly based on a partially quenched calculation. Apart from observables being afflicted with potentially more severe lattice spacing artifacts, the charm sector offers a number of advantages for a methodological study. Amongst those is the much better separability of the generic charm contributions to the vacuum polarization function. As a consequence we have access to a more reliable phenomenological estimate of the charm contribution to a_μ^{hlo} via the dispersion relation. With our analysis we find complete agreement of our partially quenched result for $a_\mu^{\mathrm{hlo}}(\mathrm{charm})$ with the decay-channel-decomposition based estimate from experimental data. For this study we solely used the $t-$sum definition of the polarization function without any fit to estimate the ensemble-wise a_μ^{hlo}.

This is an encouraging result considering further applications of the charm vacuum polarization. We mention in particular the ongoing investigation of the temporal moments or individual derivatives of the polarization function at zero momentum in the very same setup. These derivatives carry information on the charm quark mass and

strong coupling. It will be interesting to see, whether in estimates of the latter we can replace the experimental data for the cross section ratio with charmed final states with the non-perturbative results for the charm vacuum polarization from partially quenched 2-flavor or 4-flavor twisted mass lattice QCD at a compatible level of precision.

The vacuum polarization function has many more applications. The hadronic leading order contribution to the running QED coupling and the $2P/2S$ splitting in the spectrum of muonic hydrogen are two of them. Moreover, from the polarization function in the light sector we have access to the Adler function and can estimate the running strong coupling or the Λ parameter. The weak mixing angle $\theta_W(Q^2)$ in the low-momentum region provides yet another field of application for polarization functions, which is well-suited for a lattice investigation and where the presented methods can have a beneficial impact.

The strive for precise ab-initio estimates of the muon anomaly does not end with a_μ^{hlo}. For the time being it is the contribution to be worked on most urgently. But with growing precision the next-to-leading order terms will become significant for the reduction of the final uncertainty. The focus will move to the vacuum-polarization type and light-by-light contributions of order α^3 and work in both directions is already underway. Moreover, there are electromagnetic and isospin symmetry breaking effects that will have to be included at a certain level of precision. Common to all these uprising working areas is the traditional wish for simulations closer to the physical point in larger volumes with ever growing gauge field ensembles.

These are all demanding challenges, but the progress that has happened in the last years can make us confident that also these difficulties can be overcome and a clean and precise value for a_μ^{had} can be obtained from first principles.

Appendix: Polarization functions

1 Electromagnetic current and lattice Ward identity formulas

We consider an infinitesimal vector flavor transformation generated by Q^{em} which entails a variation of the fermion fields

$$\delta_\alpha^V := \begin{cases} \chi(x) & \to \chi'(x) = \chi(x) + i\alpha(x) Q^{\mathrm{em}} \chi(x) \\ \bar{\chi}(x) & \to \bar{\chi}'(x) = \bar{\chi}(x) - i\alpha(x)\bar{\chi}(x)\, Q^{\mathrm{em}}\,. \end{cases} \tag{1}$$

$$Q^{\mathrm{em}} = \frac{1}{6}\mathbb{1} + \frac{1}{2}\tau^3$$

This variation leads to a corresponding one of the fermionic action at maximal twist ($m_0 = m_{\mathrm{crit}}$)

$$\begin{aligned} \delta_\alpha^V \mathcal{S}_{\mathrm{fermion}}^{tmLQCD} &= ia^3 \sum_{x\in\mathbb{L}} \alpha(x)\bar{\chi}(x) \left[4r\mathbb{1} + am_{\mathrm{crit}}\mathbb{1} + ia\mu_0\gamma_5\tau^3\,,\, Q^{\mathrm{em}}\right] \chi(x) \\ &+ ia^3\frac{1}{2}\sum_{x\in\mathbb{L},\,\mu} \alpha(x)\bar{\chi}(x)\, Q^{\mathrm{em}} \Big((r-\gamma_\mu) U_\mu(x)\, \chi(x+a\hat{\mu}) \\ &\qquad + (r+\gamma_\mu) U_\mu(x-a\hat{\mu})^\dagger \chi(x-a\hat{\mu}) \Big) \\ &- ia^3\frac{1}{2}\sum_{x\in\mathbb{L},\,\mu} \bar{\chi}(x) \Big((r-\gamma_\mu) U_\mu(x)\, \alpha(x+a\hat{\mu})\, Q^{\mathrm{em}}\, \chi(x+a\hat{\mu}) \\ &\qquad + (r+\gamma_\mu) U_\mu(x-a\hat{\mu})^\dagger \alpha(x-a\hat{\mu})\, Q^{\mathrm{em}}\, \chi(x-a\hat{\mu}) \Big) \end{aligned} \tag{2}$$

Upon shifting the summation indices $x - a\hat{\mu} \to x$ in the second summand of the second and third line, respectively, and observing that the commutator in the first line vanishes

due to equation (1), we find

$$\begin{aligned}
\delta_\alpha^V \mathcal{S}_{\text{fermion}}^{tmLQCD} &= ia^3 \sum_{x\in\mathbb{L}} \sum_{\mu} \left(\alpha(x+a\hat{\mu}) - \alpha(x)\right) \times \\
&\qquad \frac{1}{2}\Big(\bar{\chi}(x)\,(\gamma_\mu - r)\, U_\mu(x) Q^{\text{em}}\, \chi(x+a\hat{\mu}) \\
&\qquad + \bar{\chi}(x+a\hat{\mu})\,(\gamma_\mu + r)\, U_\mu(x)^\dagger Q^{\text{em}}\, \chi(x)\Big) \\
&= ia^4 \sum_{x\in\mathbb{L}} \sum_{\mu} \nabla_\mu^f \alpha(x)\, J_\mu^{\text{em}}(x) \\
&= -ia^4 \sum_{x\in\mathbb{L}} \sum_{\mu} \alpha(x)\, \nabla_\mu^b J_\mu^{\text{em}}(x) \qquad (3)
\end{aligned}$$

$$\begin{aligned}
J_\mu^{\text{em}}(x) = \frac{1}{2}\Big(&\bar{\chi}(x)\,(\gamma_\mu - r)\, U_\mu(x) Q^{\text{em}}\, \chi(x+a\hat{\mu}) \\
&+ \bar{\chi}(x+a\hat{\mu})\,(\gamma_\mu + r)\, U_\mu(x)^\dagger Q^{\text{em}}\, \chi(x)\Big). \qquad (4)
\end{aligned}$$

If we use the discretized version of the functional differentiation with respect to $\alpha(y)$ of equation (3) we have

$$\frac{\delta_\alpha^V}{\delta\alpha(y)} \mathcal{S}_{\text{fermion}}^{tmLQCD} = -ia^4 \sum_{\mu} \nabla_\mu^b J_\mu^{\text{em}}(y)\,. \qquad (5)$$

With this result we can derive the Ward-Takahashi-identity we are seeking. We denote by $\mathcal{Z}$ the partition function defined by

$$\mathcal{Z} = \int \mathcal{D}\left[\bar{\chi}\,\chi\right] \mathcal{D}\left[U\right] \exp\left(-\mathcal{S}^{tmLQCD}[\chi\,\bar{\chi}\,U]\right). \qquad (6)$$

The non-anomalous field variations in equation (1) are equivalent to a change of integration variables by a Hermitean generator that leaves the partition function invariant; thus

$$\begin{aligned}
0 = \frac{1}{\mathcal{Z}} \frac{\delta_\alpha^V}{\delta\alpha(y)} \mathcal{Z} &= \frac{1}{\mathcal{Z}} \int \mathcal{D}\left[\bar{\chi}\,\chi\right] \mathcal{D}\left[U\right]\; ia^4 \nabla_\mu^b J_\mu^{\text{em}}(y)\; \exp\left(-\mathcal{S}^{tmLQCD}[\chi\,\bar{\chi}\,U]\right) \\
\Rightarrow 0 &= \langle \nabla_\mu^b J_\mu^{\text{em}}(y) \rangle\,. \qquad (7)
\end{aligned}$$

The divergence of the current J_μ^{em} is zero and the current is conserved. Let now $O(y_1, \ldots, y_n)$ be a multilocal operator composed of fermion field and gauge field el-

ements, then we have

$$0 = \frac{1}{\mathcal{Z}} \frac{\delta_\alpha^V}{\delta\alpha(y)} \int \mathcal{D}[\bar{\chi}\,\chi]\,\mathcal{D}[U]\; O(y_1,\ldots,y_n)\,\exp\left(-\mathcal{S}^{tmLQCD}[\chi\,\bar{\chi}\,U]\right)$$

$$\Rightarrow 0 = ia^4\langle O(y_1,\ldots,y_n)\,\nabla_\mu^b J_\mu^{\mathrm{em}}(y)\rangle + \sum_{i=1}^{n}\delta(y-y_i)\langle\frac{\delta_\alpha^V}{\delta\alpha(y_i)}O(y_1,\ldots,y_n)\rangle\,. \tag{8}$$

Of special interest will be the case $O(y_1,\, y_2 = y_1 + a\hat{\mu}) = J_\nu^{\mathrm{em}}(y_1)$. In that case the derivative of the operator takes the form

$$\begin{aligned}
\delta_\alpha^V J_\nu^{\mathrm{em}}(y) = \frac{1}{2}\Big[&- i\alpha(y)\bar{\chi}(y)Q^{\mathrm{em}}(\gamma_\mu - r)\,U_\nu(y)\,Q^{\mathrm{em}}\chi(y+a\hat{\nu}) \\
&- i\alpha(y+a\hat{\nu})\bar{\chi}(y+a\hat{\nu})Q^{\mathrm{em}}(\gamma_\mu + r)\,U_\nu(y)^\dagger\,Q^{\mathrm{em}}\chi(y)\Big] \\
+ \frac{1}{2}\Big[&\bar{\chi}(y)(\gamma_\mu - r)\,U_\nu(y)\,Q^{\mathrm{em}} i\alpha(y+a\hat{\nu})\,Q^{\mathrm{em}}\,\chi(y+a\hat{\nu}) \\
&+ \bar{\chi}(y+a\hat{\nu})(\gamma_\mu + r)\,U_\nu(y)^\dagger\,Q^{\mathrm{em}} i\alpha(y)\,Q^{\mathrm{em}}\,\chi(y)\Big] \\
= i\,&(\alpha(y+a\hat{\nu}) - \alpha(y))\;S_\nu(y) \\
S_\nu(y) = \frac{1}{2}\Big(&\bar{\chi}(y)\,(\gamma_\nu - r)\,U_\nu(y)\,(Q^{\mathrm{em}})^2\,\chi(y+a\hat{\nu}) \\
&- \bar{\chi}(y+a\hat{\nu})\,(\gamma_\nu + r)\,U_\nu(y)^\dagger\,(Q^{\mathrm{em}})^2\,\chi(y)\Big)
\end{aligned} \tag{9}$$

$$\begin{aligned}
\frac{\delta_\alpha^V}{\delta\alpha(x)}\,J_\nu^{\mathrm{em}}(y) &= i\;(\delta(x-y-a\hat{\nu}) - \delta(x-y))\;S_\nu(y) \\
&= -ia\,\nabla_\mu^b\left(\delta_{\mu\nu}\,\delta(x-y)\,S_\nu(y)\right).
\end{aligned} \tag{10}$$

In the last line the backward derivative is with respect to x and the $\delta(x-y)$ is to be understood as the dimensionless Kronecker-δ $\prod_\mu \delta_{x_\mu/a,\,y_\mu/a}$. The combination of equations (8) and (10) thus gives

$$\langle\nabla_\mu^b J_\mu^{\mathrm{em}}(x)\,J_\nu^{\mathrm{em}}(y)\rangle = a^{-3}\,\nabla_\mu^b\left(\delta_{\mu\nu}\,\delta(x-y)\,\langle S_\nu(y)\rangle\right). \tag{11}$$

2 Gauge field-wise Ward-identities

To see that these identities hold already on the level of individual gauge fields we use the following notation: we denote the decomposition of the twisted mass Dirac operator

by

$$
\begin{aligned}
D_{\mathrm{W}}^{\mathrm{tm}}[U](x,y) &= A(x,y) + H[U](x,y) \\
A(x,y) &= \left(4\frac{r}{a} + m_{\mathrm{crit}} + i\mu_0\gamma_5\tau^3\right)\delta(x-y) \\
H[U](x,y) &= -\frac{1}{2a}\sum_{\mu}\Big((r-\gamma_\mu)U_\mu(x)\delta(x+\hat{\mu}-y) \\
&\qquad + (r+\gamma_\mu)U_\mu(x-a\hat{\mu})^\dagger\delta(x-\hat{\mu}-y)\Big),
\end{aligned}
\tag{12}
$$

where A denotes the spin-color-flavor matrix diagonal in position space and H the usual Wilson-hopping matrix connecting nearest neighbors on the spacetime lattice. Moreover, let $S(x,y) = \langle\chi(x)\bar{\chi}(y)\rangle_f$ be the 2-flavor fermion propagator, which is the inverse of the twisted mass Dirac operator

$$
\sum_{z\in\mathbb{L}} D_{\mathrm{W}}^{\mathrm{tm}}(x,z)\,S(z,y) = a^{-4}\,\delta(x-y) = \sum_{z\in\mathbb{L}} S(x,z)\,D_{\mathrm{W}}^{\mathrm{tm}}(z,y)\,,
$$

such that we also have

$$
\begin{aligned}
\sum_{z\in\mathbb{L}} H(x,z)\,S(z,y) &= a^{-4}\,\delta(x-y) - \sum_{z\in\mathbb{L}} A(x,z)S(z,y) = a^{-4}\,\delta(x-y) - A(x,x)\,S(x,y) \\
\sum_{z\in\mathbb{L}} S(x,z)\,H(z,y) &= a^{-4}\,\delta(x-y) - \sum_{z\in\mathbb{L}} S(x,z)A(z,y) = a^{-4}\,\delta(x-y) - S(x,y)\,A(y,y)\,.
\end{aligned}
\tag{13}
$$

Now we simply perform the fermionic integration part of the path integral for the identity (7):

$$
\begin{aligned}
&\langle \nabla^b_\mu J^{\mathrm{em}}_\mu(x)\rangle_f \\
&= \frac{1}{2}\sum_\mu \langle \bar\chi(x)\,(\gamma_\mu - r) U_\mu(x)\, Q^{\mathrm{em}}\,\chi(x+a\hat\mu) \\
&\qquad\qquad + \bar\chi(x+a\hat\mu)\,(\gamma_\mu + r)\, U_\mu(x)^\dagger\, Q^{\mathrm{em}}\,\chi(x)\rangle_f \\
&\quad - \frac{1}{2}\sum_\mu \langle \bar\chi(x-a\hat\mu)\,(\gamma_\mu - r) U_\mu(x-a\hat\mu)\, Q^{\mathrm{em}}\,\chi(x) \\
&\qquad\qquad + \bar\chi(x)\,(\gamma_\mu + r)\, U_\mu(x-a\hat\mu)^\dagger\, Q^{\mathrm{em}}\,\chi(x-a\hat\mu)\rangle_f \\
&= \frac{1}{2}\sum_\mu \langle \bar\chi(x)\Big((\gamma_\mu - r) U_\mu(x)\, Q^{\mathrm{em}}\,\chi(x+a\hat\mu) \\
&\qquad\qquad - (\gamma_\mu + r)\, U_\mu(x-a\hat\mu)^\dagger\, Q^{\mathrm{em}}\,\chi(x-a\hat\mu)\Big)\rangle_f \\
&\quad + \frac{1}{2}\sum_\mu \langle \Big(\bar\chi(x+a\hat\mu)\,(\gamma_\mu + r)\, U_\mu(x)^\dagger \\
&\qquad\qquad - \bar\chi(x-a\hat\mu)\,(\gamma_\mu - r) U_\mu(x-a\hat\mu)\Big)\, Q^{\mathrm{em}}\,\chi(x)\rangle_f \\
&= \mathrm{Tr}\,(Q^{\mathrm{em}}\ [S\,,\,H])\,(x,x)\,, \qquad (14)
\end{aligned}
$$

The trace is meant in spin-color and flavor space and the commutativity of Q^{em} and H was used. With the equations (13) we thus find for the commutator

$$
\mathrm{Tr}\,(Q^{\mathrm{em}}\ [S\,,\,H])\,(x,x) = \mathrm{Tr}\,([Q^{\mathrm{em}}\,A\,,\,S])\,(x,x) = 0\,, \qquad (15)
$$

since $Q^{\mathrm{em}}\,A$ is diagonal in position space. With an analogous calculation we find the identity for the correlator of two electromagnetic currents. We use the notation introduced in equation (3.27)

$$
\begin{aligned}
D^{\mathrm{tm}}_{\mathrm{W}}(x,y) &= A(x,y) + H(x,y)\,; \quad A(x,y) = A\,\delta(x,y)\,, \\
H &= \sum_\mu \Big(H^-_\mu(x)\,\delta(x+a\hat\mu,y) + H^+_\mu(x)\,\delta(x-a\hat\mu,y)\Big) \\
J^{\mathrm{em}}_\mu(x) &= \bar\chi(x)\,H^-_\mu(x)\,Q^{\mathrm{em}}\,\chi(x+a\hat\mu) - \bar\chi(x+a\hat\mu)\,H^+_\mu(x+a\hat\mu)\,Q^{\mathrm{em}}\,\chi(x) \\
\Big[Q^{\mathrm{em}}\,,\,D^{\mathrm{tm}}_{\mathrm{W}}\Big] &= 0\,. \qquad (16)
\end{aligned}
$$

and consider the correlator of the electromagnetic current with a general multilocal operator $O(y_1, \ldots, y_n)$.

$$
\begin{aligned}
&\nabla_\mu^b \langle J_\mu^{\mathrm{em}}(x)\, O(y_1, \ldots, y_n)\rangle_f = \\
&\sum_\mu \Big(\mathrm{Tr}\left(H_\mu^-(x)\, Q^{\mathrm{em}}\, \langle \chi(x + a\hat{\mu})\, O(y_1, \ldots, y_n)\, \bar{\chi}(x)\rangle_f\right) \\
&\qquad - \mathrm{Tr}\left(H_\mu^+(x + a\hat{\mu})\, Q^{\mathrm{em}}\, \langle \chi(x)\, O(y_1, \ldots, y_n)\, \bar{\chi}(x + a\hat{\mu})\rangle_f\right)\Big) \\
&- \sum_\mu \Big(\mathrm{Tr}\left(H_\mu^-(x - a\hat{\mu})\, Q^{\mathrm{em}}\, \langle \chi(x)\, O(y_1, \ldots, y_n)\, \bar{\chi}(x - a\hat{\mu})\rangle_f\right) \\
&\qquad - \mathrm{Tr}\left(H_\mu^+(x)\, Q^{\mathrm{em}}\, \langle \chi(x - a\hat{\mu})\, O(y_1, \ldots, y_n)\, \bar{\chi}(x)\rangle_f\right)\Big) \\
&= \mathrm{Tr}\left(\, H(x,z)\, Q^{\mathrm{em}}\, K(z, y_1, \ldots, y_n, x) - Q^{\mathrm{em}}\, K(x, y_1, \ldots, y_n, z)\, H(z,x)\right) \\
&= \mathrm{Tr}\left(-A(x,z)\, Q^{\mathrm{em}}\, K(z, y_1, \ldots, y_n, x) + Q^{\mathrm{em}}\, K(x, y_1, \ldots, y_n, z)\, A(z,x)\right) \\
&\quad + \mathrm{Tr}\left(D_{\mathrm{W}}^{\mathrm{tm}}(x,z)\, Q^{\mathrm{em}}\, K(z, y_1, \ldots, y_n, x) - Q^{\mathrm{em}}\, K(x, y_1, \ldots, y_n, z)\, D_{\mathrm{W}}^{\mathrm{tm}}(z,x)\right) \\
&= \mathrm{Tr}\left(-A\, Q^{\mathrm{em}}\, K(z, y_1, \ldots, y_n, x)\, \delta(x - z) + Q^{\mathrm{em}}\, K(x, y_1, \ldots, y_n, z)\, A\, \delta(z - x)\right) \\
&\quad + \mathrm{Tr}\left(D_{\mathrm{W}}^{\mathrm{tm}}(x,z)\, Q^{\mathrm{em}}\, K(z, y_1, \ldots, y_n, x) - Q^{\mathrm{em}}\, K(x, y_1, \ldots, y_n, z)\, D_{\mathrm{W}}^{\mathrm{tm}}(z,x)\right) \\
&= \mathrm{Tr}\left(D_{\mathrm{W}}^{\mathrm{tm}}(x,z)\, Q^{\mathrm{em}}\, K(z, y_1, \ldots, y_n, x) - Q^{\mathrm{em}}\, K(x, y_1, \ldots, y_n, z)\, D_{\mathrm{W}}^{\mathrm{tm}}(z,x)\right) \\
&= \mathrm{Tr}\left(Q^{\mathrm{em}}\, \left[D_{\mathrm{W}}^{\mathrm{tm}}\, ,\, K\right]\right)(x, y_1, \ldots, y_n, x)\,, \qquad (17)
\end{aligned}
$$

where the matrix $K = K[U]$ with

$$K(x, y_1, \ldots, y_n, z) = \langle \chi(x)\, O(y_1, \ldots, y_n)\, \bar{\chi}(z)\rangle_f$$

is a spin-color-flavor matrix for each $(n+2)$-tuple of lattice sites. With the special choice of $O(y) = J_\nu^{\mathrm{em}}(y)$ we recover the contact term $S_\nu(y)$. Equation (17) contains the quark-connected and disconnected contribution. We note that, since the quark-disconnected contribution is proportional to $\langle J_\mu^{\mathrm{em}}(x)\rangle_f \times \langle O(y_1, \ldots, y_n)\rangle_f$, it fulfills the homogeneous Ward identity and the divergence equation for the connected contribution contains the contact term.

3 Contraction formulas for twisted mass current correlators

3.1 Contraction formulas for $C_{\mu\nu}$ using point source propagators

We here give the formulas for the calculation of the connected part of the current-current correlator $\langle J_\mu^{\mathrm{em}}(x)\, J_\nu^{\mathrm{em}}(y)\rangle_f^{conn}$ using the point sources introduced in subsection (3.4.2).

We recall that $\phi_{u/d}(y,\alpha,a)$ is the solution of

$$\begin{aligned} D_{\mathrm{W}}^{\mathrm{tm\,u/d}}\,\phi_{u/d}(y,\alpha,a) &= \eta(y,\alpha,a) \\ \eta(y,\alpha,a)_{z,\beta,b} &= \delta(z-y)\,\delta_{\alpha\beta}\,\delta_{ab} \\ \phi_{u/d}(y,\alpha,a)_{z,\beta,b} &= (D_{\mathrm{W}}^{\mathrm{tm\,u/d}}(z,y))^{ba}_{\beta\alpha}\,. \end{aligned} \tag{18}$$

We thus have for the up-component $C^u_{\mu\nu}$

$$\begin{aligned} C^u_{\mu\nu}(x,y) &= \langle J^u_\mu(x)\,J^u_\nu(y)\rangle_f^{conn} \\ &\quad - \mathrm{Tr}\Big(H^-_\nu(y)\,S_u(y+a\hat{\nu},x)\,H^-_\mu(x)\,S_u(x+a\hat{\mu},y)\Big) \\ &\quad + \mathrm{Tr}\Big(H^+_\nu(y+a\hat{\nu})\,S_u(y,x)\,H^-_\mu(x)\,S_u(x+a\hat{\mu},y+a\hat{\nu})\Big) \\ &\quad + \mathrm{Tr}\Big(H^-_\nu(y)\,S_u(y+a\hat{\nu},x+a\hat{\mu})\,H^+_\mu(x+a\hat{\mu})\,S_u(x,y)\Big) \\ &\quad - \mathrm{Tr}\Big(H^+_\nu(y+a\hat{\nu})\,S_u(y,x+a\hat{\mu})\,H^+_\mu(x+a\hat{\mu})\,S_u(x,y+a\hat{\nu})\Big) \\ &= -\,[H^-_\nu(y)\,\gamma_5]^{ab}_{\alpha\beta}\;\phi_d(y+a\hat{\nu},\beta,b)^\dagger_x\,H^-_\mu(x)\,\gamma_5\,\phi_u(y,\alpha,a)_{x+a\hat{\mu}} \\ &\quad + \Big[H^+_\nu(y+a\hat{\nu})\,\gamma_5\Big]^{ab}_{\alpha\beta}\;\phi_d(y,\beta,b)^\dagger_x\,H^-_\mu(x)\,\gamma_5\,\phi_u(y+a\hat{\mu},\alpha,a)_{x+a\hat{\mu}} \\ &\quad + [H^-_\nu(y)\,\gamma_5]^{ab}_{\alpha\beta}\;\phi_d(y+a\hat{\nu},\beta,b)^\dagger_{x+a\hat{\mu}}\,H^+_\mu(x+a\hat{\mu})\,\gamma_5\,\phi_u(y,\alpha,a)_x \\ &\quad - \Big[H^+_\nu(y+a\hat{\nu})\,\gamma_5\Big]^{ab}_{\alpha\beta}\;\phi_d(y,\beta,b)^\dagger_{x+a\hat{\mu}}\,H^+_\mu(x+a\hat{\mu})\,\gamma_5\,\phi_u(y+a\hat{\mu},\alpha,a)_x\,. \end{aligned} \tag{19}$$

3.2 Contraction formulas for $D_{\mu\nu}$ using stochastic volume sources

We use the notation for Gaussian volume sources η^r and propagators $\phi^r_{u/d}$ as introduced in (3.40).

$$\begin{aligned} L^q_\mu(x) &= \mathrm{Tr}\Big(H^-_\mu(x)\,S_q(x+a\hat{\mu},x) - H^+_\mu(x+a\hat{\mu})\,S_q(x,x+a\hat{\mu})\Big) \\ &= \mathrm{E}\Big[\mathrm{Tr}\Big(H^-_\mu(x)\,\phi^r_q(x+a\hat{\mu})\eta^r(x)^\dagger - H^+_\mu(x+a\hat{\mu})\,\phi^r_q(x)\eta^r(x+a\hat{\mu})^\dagger\Big)\Big] \\ &= \mathrm{E}\Big[\eta^r(x)^\dagger\,H^-_\mu(x)\,\phi^r_q(x+a\hat{\mu}) - \eta^r(x+a\hat{\mu})^\dagger\,H^+_\mu(x+a\hat{\mu})\,\phi^r_q(x)\Big] \\ &= \mathrm{E}\Big[L^{q\,r}_\mu(x)\Big] \\ L^{q_1}_\mu(x)\,L^{q_2}_\nu(y) &= \mathrm{E}\Big[L^{q_1\,r}_\mu(x)\Big]\,\mathrm{E}\Big[L^{q_2\,s}_\nu(y)\Big] \\ &\underset{r\neq s}{=} \mathrm{E}\Big[L^{q_1\,r}_\mu(x)\,L^{q_2\,s}_\nu(y)\Big] \end{aligned}$$

To derive the final estimators (3.46) in terms of L^0 and L^1 we use the two relations

$$\begin{aligned} S_u - S_d &= -2i\mu_0\,S_u\,\gamma_5\,S_d \\ S_u + S_d &= 2\,S_u\,D_W\,S_d\,. \end{aligned} \tag{20}$$

We thus rewrite L^1 as

$$\begin{aligned} L^1_\mu(x) &= \left(L^{u\,-}_\mu(x) - L^{d\,-}_\mu(x)\right) - \left(L^{u\,+}_\mu(x) - L^{d\,+}_\mu(x)\right) \\ &= 2\mathrm{Re}\left(L^{u\,-}_\mu(x) - L^{d\,-}_\mu(x)\right) = 2\,\mathrm{Re}\left(-2i\mu_0\, S_u(x+a\hat{\mu},z)\,\gamma_5\, S_d z, x H^-_\mu(x)\right) \\ &= 4\mu_0\,\mathrm{Im}\left(S_u(x+a\hat{\mu},z)\, S_u(x,z)^\dagger\,\gamma_5\, H^-_\mu(x)\right) \\ &= 4\mu_0\,\mathrm{E}\left[\mathrm{Im}\left(\phi^r_u(x)^\dagger\,\gamma_5\, H^-_\mu(x)\,\phi^r_u(x+a\hat{\mu})\right)\right]. \end{aligned} \tag{21}$$

A similar modification of L^0 reads

$$\begin{aligned} L^0_\mu(x) &= \left(L^{u\,-}_\mu(x) + L^{d\,-}_\mu(x)\right) - \left(L^{u\,+}_\mu(x) + L^{d\,+}_\mu(x)\right) \\ &= 2i\,\mathrm{Im}\left(L^{u\,-}_\mu(x) + L^{d\,-}_\mu(x)\right) = 2i\,\mathrm{Im}\left(2\, S_u(x+a\hat{\mu},z_1)\, D_W(z_1,z_2)\, S_d z_2, x H^-_\mu(x)\right) \\ &= 4i\,\mathrm{Im}\left(S_u(x+a\hat{\mu},z_1)\, D_W(z_1,z_2)\,\gamma_5\, S_u(x,z_2)^\dagger\,\gamma_5\, H^-_\mu(x)\right) \\ &= 4i\,\mathrm{Im}\left(\gamma_5\, D_W(x+a\hat{\mu},z_1)\, S_u(z_1,z_2)\, S_u(x,z_2)^\dagger\,\gamma_5\, H^-_\mu(x)\right) \\ &= 4i\,\mathrm{E}\left[\mathrm{Im}\left(\phi^r(x)^\dagger\,\gamma_5\, H^-_\mu(x)\,\gamma_5\,[D_W\,\phi^r]\,(x+a\hat{\mu})\right)\right]. \end{aligned} \tag{22}$$

3.3 Local current correlator contractions with one-end-trick

To apply the one-end-trick we use a set of four stochastic timeslice sources $\eta(t_s,\alpha)$ with

$$p\left(\eta(t_s,\alpha)_{\beta,c,t,\vec{x}} = \xi\right) = \delta_{t\,t_s}\,\delta_{\alpha\,\beta}\,\frac{1}{\sqrt{2\pi}}\,\mathrm{e}^{-\frac{\xi^2}{2}}, \tag{23}$$

with all components within each field and fields for different α identically and independently distributed. With the corresponding propagators

$$\phi_f(t_s,\,\alpha) = D^{\mathrm{tm}\,-1}_{\mathrm{W}\,f}\,\eta(t_s,\,\alpha)$$

for quark flavor f the quark-connected contractions for the local correlators read

$$\begin{aligned} C^{\Gamma_2\,\Gamma_2}_{f_1\,f_2}(t) &= \langle\,\bar{\chi}_{f_1}(x)\,\Gamma_1\,\chi_{f_2}(x)\,\bar{\chi}_{f_2}(y)\,\Gamma_2\,\chi_{f_1}(y)\,\rangle_f \\ &= (\Gamma_2\,\gamma_5)_{\alpha\beta}\sum_{\vec{x}}\,\phi^\dagger_{f_1}(t_s,\beta)_{t,\vec{x}}\cdot\,(\gamma_5\,\Gamma_1)\,\cdot\,\phi_{f_2}(t_s,\alpha)_{t,\vec{x}} \end{aligned} \tag{24}$$

The dot signifies a scalar product of spinor fields in spin-color space.

3.4 Complex conjugation relation of the quark current-current matrix element

We consider the following change of variables

$$\begin{aligned} \chi(x) &\rightarrow \gamma_5 \gamma_0 \chi \\ \bar{\chi}(x) &\rightarrow \bar{\chi} \gamma_5 \gamma_0 . \end{aligned} \tag{25}$$

Under this transformation the current operators behave as follows:

$$\begin{aligned} \bar{q}(x) H_\mu^-(x) q(x+a\hat{\mu}) &\rightarrow -\bar{q}(x) \gamma_0 \gamma_5 H_\mu^-(x) \gamma_5 \gamma_0 q(x+a\hat{\mu}) \\ &= -q(x)^\dagger \gamma_5 H_\mu^-(x) \gamma_5 \gamma_0 q(x+a\hat{\mu}) \\ &= -q(x)^\dagger H_\mu^+(x+a\hat{\mu})^\dagger \gamma_0 q(x+a\hat{\mu}) \\ &= \left(\bar{q}(x+a\hat{\mu}) H_\mu^+(x+a\hat{\mu}) q(x)\right)^* \\ \bar{q}(x+a\hat{\mu}) H_\mu^+(x+a\hat{\mu}) q(x) &\rightarrow \left(\bar{q}(x) H_\mu^-(x) q(x+a\hat{\mu})\right)^* \\ J_\mu^q(x) &\rightarrow -J_\mu^q(x)^* . \end{aligned} \tag{26}$$

An additional minus sign comes in from the interchange of the two quark fields. The transformation for the fermion action for quark flavor q is worked out using the γ_5-Hermiticity relation for the twisted mass Dirac operator

$$\begin{aligned} D_{\mathrm{W}\,\bar{q}}^{\mathrm{tm}} &= \gamma_5 D_{\mathrm{W}\,q}^{\mathrm{tm}\dagger} \gamma_5 . \\ \bar{q} D_{\mathrm{W}}^{\mathrm{tm}} q \rightarrow -\bar{q} \gamma_0 \gamma_5 D_{\mathrm{W}\,q}^{\mathrm{tm}} \gamma_5 \gamma_0 &= -q^\dagger D_{\mathrm{W}\,\bar{q}}^{\mathrm{tm}\dagger} \gamma_0 q = \left(\bar{q} D_{\mathrm{W}\,\bar{q}}^{\mathrm{tm}} q\right)^* \\ \mathcal{S}^{tmLQCD} &\rightarrow \mathcal{S}^{tmLQCD^*} . \end{aligned} \tag{27}$$

If we additionally use that $\det(\gamma_5) = 1 = \det(\gamma_0)$ we thus arrive at

$$\langle J^{q_1}(x) J^{q_2}(y) \rangle_f = \langle J^{\bar{q}_1}(x) J^{\bar{q}_2}(y) \rangle_f^* , \tag{28}$$

where due to relation (27) the association $\chi_u \leftrightarrow +\mu_0$, $\chi_d \leftrightarrow -\mu_0$ is now interchanged.

Another way to see the connection can be followed on the level of the contracted correlators using the corresponding γ_5-Hermiticity relation for the quark propagators $S_{\bar{q}} = \gamma_5 S_q^\dagger \gamma_5$, which follows directly from the first line of equation (27), and again the relation

$$\gamma_5 H_\mu^-(x) \gamma_5 = H_\mu^+(x+a\hat{\mu})^\dagger .$$

It then follows that

$$\begin{aligned}\langle J^q_\mu(x)\rangle_f &= \mathrm{Tr}\left(H^-_\mu(x)\,S_q(x+a\hat{\mu},x) - H^+_\mu(x+a\hat{\mu})\,S_q(x,x+a\hat{\mu})\right)\\ &= \mathrm{Tr}\left(\gamma_5\,H^-_\mu(x)\,\gamma_5\,S_{\bar{q}}(x,x+a\hat{\mu})^\dagger - \gamma_5\,H^+_\mu(x+a\hat{\mu})\,\gamma_5\,S_{\bar{q}}(x+a\hat{\mu},x)^\dagger\right)\\ &= \mathrm{Tr}\left(H^+_\mu(x+a\hat{\mu})^\dagger\,S_{\bar{q}}(x,x+a\hat{\mu})^\dagger - H^-_\mu(x)^\dagger\,S_{\bar{q}}(x+a\hat{\mu},x)^\dagger\right)\\ &= -\mathrm{Tr}\left(-H^+_\mu(x+a\hat{\mu})\,S_{\bar{q}}(x,x+a\hat{\mu}) + H^-_\mu(x)\,S_{\bar{q}}(x+a\hat{\mu},x)\right)^*\end{aligned}$$

for any quark-disconnected contribution. For the connected contributions the four addends in equation (19) are transformed into each other modulo the change of flavor and complex conjugation

$$\begin{aligned}&-\mathrm{Tr}\left(H^-_\nu(y)\,S_q(y+a\hat{\nu},x)\,H^-_\mu(x)\,S_q(x+a\hat{\mu},y)\right)\\ &= \quad -\mathrm{Tr}\left(H^-_\nu(y)\,\gamma_5\,S_{\bar{q}}(x,y+a\hat{\nu})^\dagger\,\gamma_5\,H^-_\mu(x)\,\gamma_5\,S_{\bar{q}}(y,x+a\hat{\mu})^\dagger\,\gamma_5\right)\\ &= \quad -\mathrm{Tr}\left(H^+_\nu(y+a\hat{\nu})^\dagger\,S_{\bar{q}}(x,y+a\hat{\nu})^\dagger\,H^+_\mu(x+a\hat{\mu})^\dagger\,S_{\bar{q}}(y,x+a\hat{\mu})^\dagger\right)\\ &= \quad -\mathrm{Tr}\left(H^+_\nu(y+a\hat{\nu})\,S_{\bar{q}}(y,x+a\hat{\mu})\,H^+_\mu(x+a\hat{\mu})\,S_{\bar{q}}(x,y+a\hat{\nu})\right)^*\end{aligned}$$

$$\begin{aligned}&\mathrm{Tr}\left(H^+_\nu(y+a\hat{\nu})\,S_q(y,x)\,H^-_\mu(x)\,S_q(x+a\hat{\mu},y+a\hat{\nu})\right)\\ &= \quad \mathrm{Tr}\left(H^+_\nu(y+a\hat{\nu})\,\gamma_5\,S_{\bar{q}}(x,y)^\dagger\,\gamma_5\,H^-_\mu(x)\,\gamma_5\,S_{\bar{q}}(y+a\hat{\nu},x+a\hat{\mu})^\dagger\,\gamma_5\right)\\ &= \quad \mathrm{Tr}\left(H^-_\nu(y)^\dagger\,S_{\bar{q}}(x,y)^\dagger\,H^+_\mu(x+a\hat{\mu})^\dagger\,S_{\bar{q}}(y+a\hat{\nu},x+a\hat{\mu})^\dagger\right)\\ &= \quad \mathrm{Tr}\left(H^-_\nu(y)\,S_{\bar{q}}(y+a\hat{\nu},x+a\hat{\mu})\,H^+_\mu(x+a\hat{\mu})\,S_{\bar{q}}(x,y)\right)^*\,.\end{aligned}$$

The remaining two relations follow from the interchange of the flavor type $q \leftrightarrow \bar{q}$ and complex conjugation of the written ones.

We can use these relations to rewrite the complex conjugate momentum space polarization tensor

$$\begin{aligned}\tilde{\Pi}^{q_1q_2}_{\mu\nu}(q)^* &= \sum_{x\in\mathbb{L}} \mathrm{e}^{-iq(x+a\hat{\mu}/2-y-a\hat{\nu}/2)}\,\langle J^{q_1}(x)\,J^{q_2}(y)\rangle^*_f\\ &= \sum_{x\in\mathbb{L}} \mathrm{e}^{-iq(x+a\hat{\mu}/2-y-a\hat{\nu}/2)}\langle J^{\bar{q}_1}(x)\,J^{\bar{q}_2}(y)\rangle_f = \tilde{\Pi}^{\bar{q}_1\bar{q}_2}_{\mu\nu}(-q)\,.\end{aligned} \tag{29}$$

4 Formulas for t-sum kernel function

The key to the analytic integration is to establish a formula that expresses the integral kernel

$$f_t(K) = \frac{\sin^2(Kt/2)}{\sin^2(K/2)}$$

as a polynomial in $\sin^2(K/2)$. This is possible because t takes integer values on the lattice.

We start by showing that $\sin(2x)\sin(2lx)$ is a polynomial in $\sin^2(kx)$, $k \leq l$ for all $x \in \mathbb{R}$ and $l \in \mathbb{N}$. From

$$\begin{aligned}
&\sin(2x)\sin(2x) = 4\sin^2(x)\,(1-\sin^2(x)) \\
&\sin(2x)\sin(4x) = \sin(2x)\;(2\sin(2x)\cos 2x) = 8\sin^2(x)\,(1-\sin^2(x))\,(1-2\sin^2(x))
\end{aligned} \tag{30}$$

the claim follows for $l = 1, 2$. For the general case let the claim be true up to $l \in \mathbb{N}$. Further on, with

$$\begin{aligned}
\sin(2x)\sin(2(l+1)x) &= \sin(2x)\;(\sin(2lx)\cos(2x) + \sin(2x)\cos(2lx)) \\
&= [\sin(2x)\sin(2lx)]\;(1-2\sin^2(x)) + \sin^2(2x)(1-2\sin^2(lx))
\end{aligned}$$

it follows that the claim is true for $l+1$. It also follows that $\sin(2x)\sin(2lx)$ is proportional to $\sin^2(x)$ for any l.

The next step consists of showing that $\sin^2(lx) = \sin^2(x)\,P_l(\sin^2(x))$, where P_l is a polynomial of degree $l-1$. We use induction again. The claim is true for $l = 1$; moreover,

$$\begin{aligned}
\sin^2(2x) &= 4\sin^2(x)(1-\sin^2(x)) \\
\sin^2(3x) &= (\sin(x)\cos(2x) + \sin(2x)\cos(x))^2 \\
&= \sin^2(x)\,(1-2\sin^2(x))^2 + 4\sin^2(x)(1-\sin^2(x))\,(1-\sin^2(x)) \\
&\quad + 4\sin^2(x)(1-\sin^2(x))\,(1-2\sin^2(x))\,.
\end{aligned} \tag{31}$$

Assuming the claim to be true for all $k < n$, we deduce immediately for even $n = 2m$

$$\sin^2(2mx) = 4\sin^2(mx)\,\left(1-\sin^2(mx)\right).$$

The claim was true in particular for m, so it holds for n. If $n = 2m+1$ then

$$\begin{aligned}
\sin^2((2m+1)x) &= (\sin(2mx)\;\cos(x) + \sin(x)\cos(2mx))^2 \\
&= \sin^2(2mx)\,(1-\sin^2(x)) + \sin^2(x)(1-2\sin^2(mx))^2 \\
&\quad + \sin(2x)\sin(2mx)\,(1-2\sin^2(mx))\,.
\end{aligned} \tag{32}$$

The claim was true for $2m$ and we previously showed that $\sin(2x)\sin(2mx)$ is proportional to $\sin^2(x)$ and a polynomial in $\sin^2(kx)$ for $k \leq m$.

4.1 Relations for polynomials P_l

In the spirit of the above arguments we write down recursion relations for the polynomials P_l, that facilitate their construction. If $l = 2k$ is even we have the recursion

relation

$$\begin{aligned} P_1(x) &= 1 \\ P_{2k}(x) &= 4\,P_k(x)\,(1 - x\,P_k(x))\;\forall\; n \geq 1\,. \end{aligned} \tag{33}$$

If $l = 2k+1$ is odd we write

$$\begin{aligned} \sin^2((2k+1)\alpha) &= [\sin(2k\alpha)\,\cos(\alpha) + \sin(\alpha)\,\cos(2k\alpha)]^2 \\ &= \sin^2(2k\alpha)\,(1 - \sin^2(\alpha)) + \sin^2(\alpha)\,(1 - \sin^2(2k\alpha)) \\ &\quad + (1 - 2\sin^2(k\alpha))\,\sin(2\alpha)\,\sin(2k\alpha) \\ &= x\,(1 - 2x\,P_k(x)) + x\,P_{2k}(x)\,(1-x) + (1 - 2x\,P_k(x))\,I_k(x) \\ I_k &= \sin(2\alpha)\,\sin(2k\alpha) = 4x(1-x)\,(1 - 2x\,P_{k-1}(x))) + (1-2x)\,I_{k-1}\,. \end{aligned} \tag{34}$$

We write down the first six polynomials as examples.

$$\begin{aligned} P_1(\hat{K}^2) &= 1 \\ P_2(\hat{K}^2) &= 4 - \hat{K}^2 \\ P_3(\hat{K}^2) &= \left(3 - \hat{K}^2\right)^2 \\ P_4(\hat{K}^2) &= \left(4 - \hat{K}^2\right)\left(2 - \hat{K}^2\right)^2 \\ P_5(\hat{K}^2) &= 1 + \left(4 - \hat{K}^2\right)\left(1 - \hat{K}^2\right)\left(6 - 5\hat{K}^2 + \hat{K}^4\right) \\ P_6(\hat{K}^2) &= \left(3 - \hat{K}^2\right)^2\left(1 - 9\hat{K}^2 + 6\hat{K}^4 - \hat{K}^6\right) \end{aligned} \tag{35}$$

Note that the P_n can be expressed in terms of the Chebyshev polynomials T_n of the first kind. For odd $n = 2l+1$ we have

$$\begin{aligned} \sin\left(n\arcsin(\hat{K}/2)\right) &= \cos\left(\frac{\pi}{2} - n\,(-\arcsin(\hat{K}/2) + \pi/2)\right) \\ &= (-1)^l\,\cos\left(n\arccos(\hat{K}/2)\right) \\ &= (-1)^l\,T_{2l+1}(\hat{K}/2)\,. \end{aligned} \tag{36}$$

We thus have for the t-sum kernel function

$$\begin{aligned} f_{2l+1}(\hat{K}^2) &= \left(\frac{T_{2l+1}(\hat{K}/2)}{\hat{K}/2}\right)^2 \\ f_{2l}(\hat{K}^2) &= \frac{1 - T_{2l}(\hat{K}/2)^2}{\hat{K}^2/4} \end{aligned} \tag{37}$$

Alternatively, one can write for $n = t/a$

$$f_n(\hat{K}^2) = 2\frac{(-1)^n\, T_{2n}(\hat{K}/2) - 1}{\hat{K}^2} \tag{38}$$

The roots of the P_n can be read off directly from the condition that the argument of the sine on the right-hand side of equation (36) must be an integer multiple of π

$$P_n(\hat{K}_l^2) = 0 \text{ for } \hat{K}_l^2 = 4\sin^2(l\pi/n)\,,\; l = 1, 2, \ldots, n-1\,. \tag{39}$$

If n is odd, the roots for $l = 1, \ldots, (n-1)/2$ are double roots. The same is true for even n, but then there is an additional simple root for $l = n/2$ ($\hat{K}^2 = 4$).

5 Effective masses for the light vector current correlator

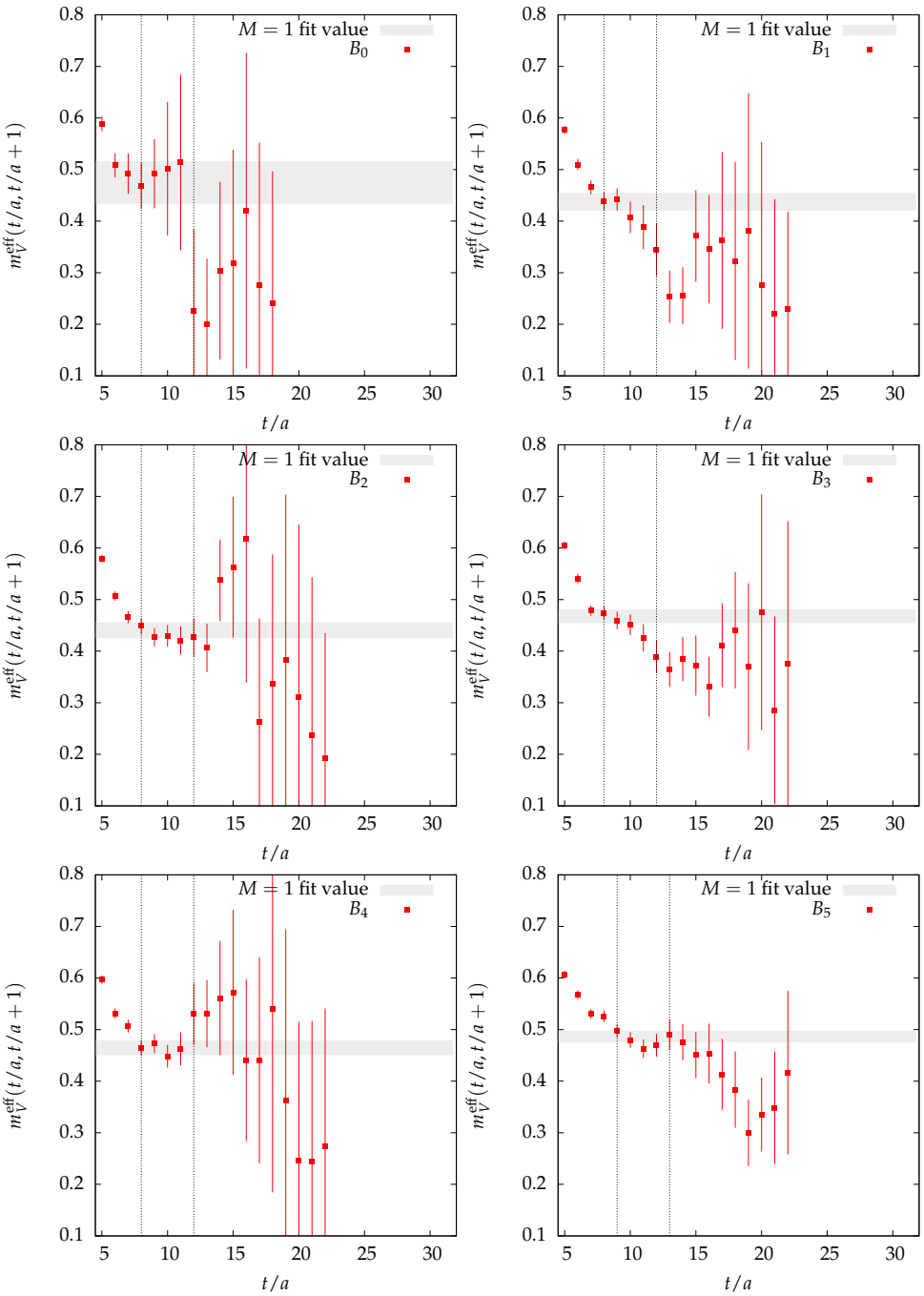

Figure 1: Effective mass plateaus at fit value from the standard fit with $M = 1$ for ensembles B_0 to B_5.

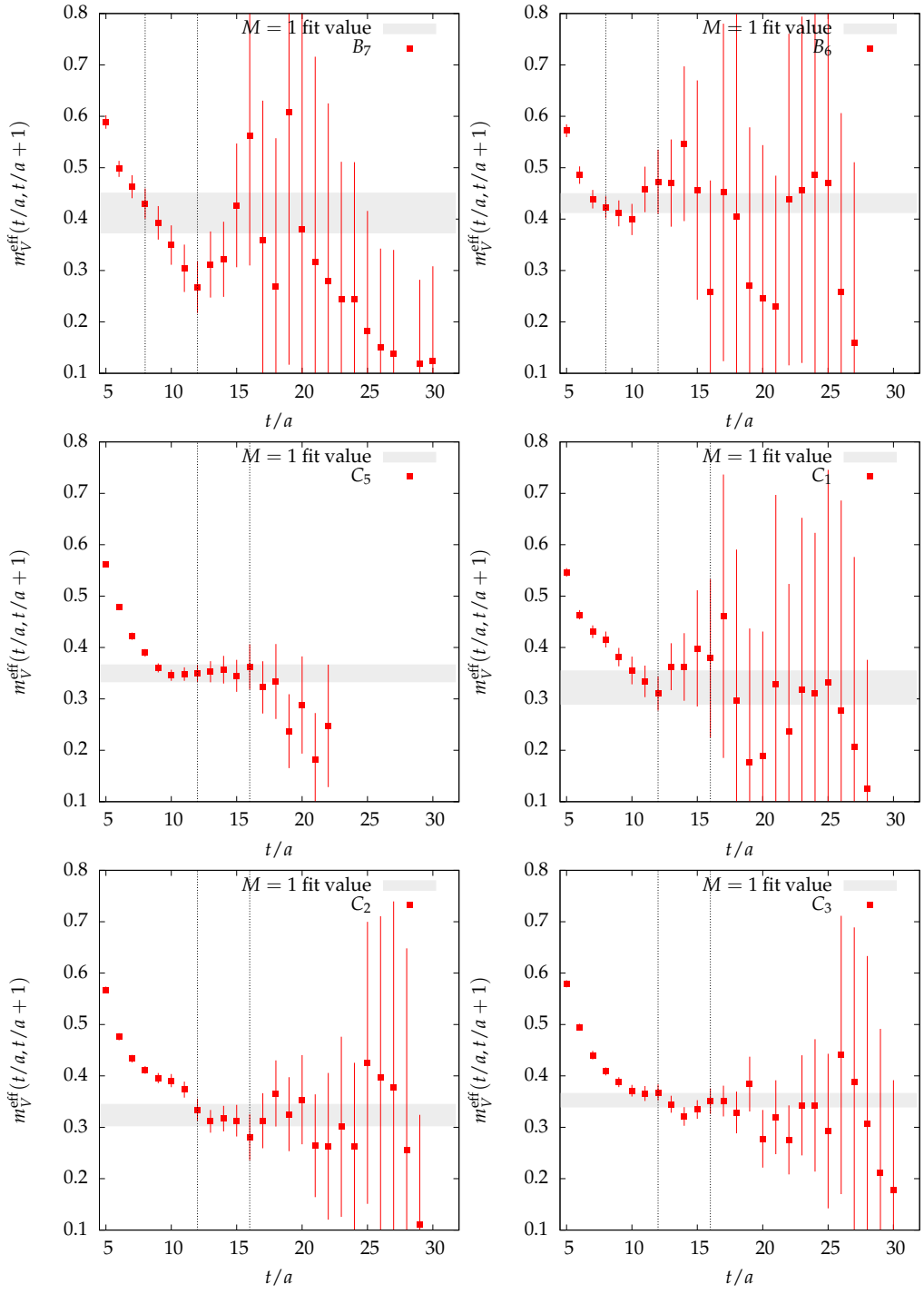

Figure 2: Effective mass plateaus at fit value from the standard fit with $M = 1$ for ensembles B_7, B_6, C_5 and C_1 to C_3.

6 Motivation of the Π fit formula in lowest order $SU(2)$ chiral perturbation theory

To motivate the equation (3.95) from the perspective of chiral perturbation theory we closely follow the reasoning in [44, 5] and adapt it to the present setup. To that end we assume the case that we can decouple the ϕ as a pure $\bar{s}s$ state and are left with the ω and ρ associated to the isospin $I = 0$ and $I = 1$ currents, respectively, as was discussed in section 3.8.1. We will thus leave out the ϕ degrees of freedom out of the following formulas.

As was outlined in equation (3.84) the electromagnetic current in the case of considering up and down quark only is a linear combination of the isospin 0 and 1 currents. We thus need to consider two vector fields, one containing the isospin triplet fields, V, and one for the singlet, V_1. These massive vector fields are antisymmetric spin-1 fields $V_{\mu\nu} = -V_{\nu\mu}$, $V_{1\,\mu\nu} = -V_{1\,\nu\mu}$ with field content

$$V = \begin{pmatrix} \rho^0/\sqrt{2} & \rho^+ \\ \rho^- & -\rho^0/\sqrt{2} \end{pmatrix} = \rho^0/\sqrt{2}\,\tau^3 + \rho^+\tau^+ + \rho^-\tau^- \tag{40}$$

$$V_1 = \omega\,. \tag{41}$$

The kinetic term of the Lagrangian is then given by

$$\begin{aligned}
\mathcal{L}_{kin} &= -\frac{1}{2}\mathrm{Tr}\left(\nabla^\lambda V_{\lambda\mu}\nabla_\nu V^{\nu\mu} - \frac{1}{2}M_V^2 V_{\mu\nu}V^{\mu\nu}\right) - \frac{1}{2}\partial^\lambda V_{1\,\lambda\mu}\partial_\nu V^{1\,\nu\mu} - \frac{1}{2}M_{V_1}^2 V_{1\,\mu\nu}V^{1\,\mu\nu} \\
&= -\frac{1}{2}\left(\partial^\lambda \rho^0_{\lambda\mu}\,\partial_\nu \rho^{0\,\nu\mu} + \partial^\lambda \rho^+_{\lambda\mu}\,\partial_\nu \rho^{+\,\nu\mu\,\dagger} + \partial^\lambda \rho^-_{\lambda\mu}\,\partial_\nu \rho^{-\,\nu\mu\,\dagger}\right) \\
&\quad + \frac{M_V^2}{4}\left(\rho^0_{\mu\nu}\,\rho^{0\,\mu\nu} + \rho^+_{\mu\nu}\,\rho^{+\,\mu\nu\,\dagger} + \rho^-_{\mu\nu}\,\rho^{-\,\mu\nu\,\dagger}\right) + \mathcal{L}_{int}(\rho^+,\,\rho^-,\,A,u) \\
&\quad - \frac{1}{2}\left(\partial^\lambda \omega_{\lambda\mu}\,\partial_\nu \omega^{\nu\mu} - \frac{M_{V_1}}{2}\omega_{\mu\nu}\,\omega^{\mu\nu}\right) \\
\nabla_\mu &= \partial_\mu + \left[\Gamma_\mu,\,\right] \\
\Gamma_\mu &= \frac{1}{2}\left\{u^\dagger\partial_\mu u + u\partial_\mu u^\dagger - ie(u^\dagger Q u + uQu^\dagger)A_\mu\right\},
\end{aligned} \tag{42}$$

where the $SU(2)$ field u contains the pion fields. The electromagnetic field strength terms are defined by

$$F^{\mu\nu}_{R,L} = eQ(\partial^\mu A^\nu - \partial^\nu A^\mu) - ie^2 A^\mu A^\nu\,[Q,Q] = eQ(\partial^\mu A^\nu - \partial^\nu A^\mu) \tag{43}$$

$$f^{\mu\nu}_\pm = uF^{\mu\nu}_L u^\dagger \pm u^\dagger F^{\mu\nu}_R = e(\partial^\mu A^\nu - \partial^\nu A^\mu)(uQu^\dagger + u^\dagger Q u) \tag{44}$$

and the relevant interaction term of order 2 to couple the photon and the vector field

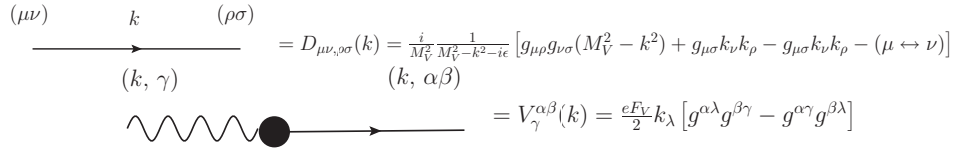

Figure 3: The Feynman rules for the ρ^0 and the interaction with the photon field according to equations (42) and (45). The rules for the ω are analogous.

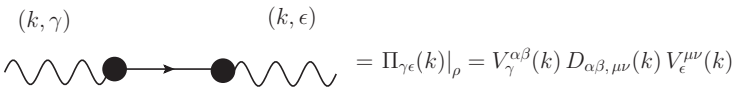

Figure 4: Lowest order contribution of the ρ^0-resonance to the vacuum polarization. There is an analogous diagram for the ω.

reads

$$\mathcal{L}_2 = \frac{F_V}{2\sqrt{2}}\mathrm{Tr}\left(V_{\mu\nu}f_+^{\mu\nu}\right) + \frac{F_{V_1}}{2}V_{1\,\mu\nu}\mathrm{Tr}\left(f_+^{\mu\nu}\right) = \frac{e}{2}\left(F_V\rho^0_{\mu\nu} + \frac{F_{V_1}}{3}\omega_{\mu\nu}\right)\left(\partial^\mu A^\nu - \partial^\nu A^\mu\right)\,, \quad (45)$$

where in the second equation $u = 1$ has been set to get the lowest order term. From equations (42) and (45) one gets the Feynman rules for the ρ propagator and the ρ-photon vertex. Analogous formulas hold for the ω ($M_V \leftrightarrow M_{V_1}$, $F_V \leftrightarrow F_{V_1}/3$). They are depicted in figure [3]. From there we can deduce the lowest order ρ^0-resonance contribution to the vacuum polarization (c.f. figure [4])

$$i\,\Pi_{\gamma\epsilon}(k)\big|_{\rho^0} = ie^2F_V^2(g^{\gamma\epsilon}k^2 - k^\gamma k^\epsilon)\frac{1}{M_V^2 - k^2 - i\epsilon} \quad (46)$$

with an analogous contribution from the ω with the changes $M_V \to M_{V_1}$ and $F_V \to F_{V_1}/3$. If we rotate to Euclidean space and drop the $i\epsilon$ prescription we arrive at

$$\Pi_{\gamma\epsilon}(k)\big|_{\rho^0,\,\omega} = e^2\frac{F_V^2}{M_V^2 + k^2} + e^2\frac{1}{9}\frac{F_{V_1}^2}{M_{V_1}^2 + k^2}\,. \quad (47)$$

The final step consists of the assumption of degeneracy of singlet and triplet, i.e. assuming that $F_V = F_{V_1}$ and $M_V = M_{V_1}$. We see that the ρ decay constant f_ρ entering the vacuum polarization via equation (3.95) is related to the decay constant defined in the interaction Lagrangian in equation (45) by

$$F_V = f_\rho/\sqrt{2}\,. \quad (48)$$

7 Tables for vector meson fits

	state 1			χ^2/dof
Ens.	f_1 [GeV]	m_1 [GeV]	g_1	
B_0	0.3282 (0.0286)	1.2077 (0.0921)	0.2716 (0.0069)	2.07
B_1	0.2982 (0.0182)	1.0935 (0.0617)	0.2727 (0.0040)	1.37
B_2	0.2994 (0.0155)	1.1011 (0.0518)	0.2719 (0.0040)	1.05
B_3	0.2871 (0.0179)	1.1136 (0.0550)	0.2577 (0.0056)	1.22
B_4	0.3083 (0.0196)	1.1503 (0.0581)	0.2678 (0.0060)	0.73
B_5	0.3226 (0.0202)	1.2394 (0.0553)	0.2602 (0.0073)	2.09
B_7	0.2309 (0.0238)	0.8448 (0.0853)	0.2734 (0.0082)	1.62
B_6	0.2863 (0.0183)	1.0410 (0.0590)	0.2750 (0.0065)	0.94
C_5	0.2911 (0.0148)	1.0562 (0.0483)	0.2756 (0.0043)	0.58
C_1	0.3319 (0.0351)	1.1884 (0.1081)	0.2790 (0.0072)	3.25
C_2	0.3449 (0.0198)	1.2155 (0.0574)	0.2837 (0.0057)	1.12
C_3	0.2910 (0.0202)	1.1199 (0.0598)	0.2597 (0.0076)	0.96
	state 2			
Ens.	f_2 [GeV]	m_2 [GeV]	g_2	
B_0	1.0477 (0.3226)	3.7236 (0.4808)	0.2772 (0.0391)	
B_1	0.9085 (0.0947)	3.4084 (0.2430)	0.2660 (0.0097)	
B_2	0.8678 (0.0749)	3.3292 (0.2052)	0.2603 (0.0077)	
B_3	0.7666 (0.0607)	3.0624 (0.2028)	0.2502 (0.0052)	
B_4	0.8102 (0.0929)	3.2199 (0.2577)	0.2511 (0.0097)	
B_5	0.8243 (0.1330)	3.3469 (0.3229)	0.2450 (0.0158)	
B_7	0.7042 (0.0558)	2.7015 (0.2076)	0.2607 (0.0046)	
B_6	0.8191 (0.0847)	3.2054 (0.2396)	0.2551 (0.0088)	
C_5	0.7361 (0.0477)	3.0830 (0.1737)	0.2387 (0.0039)	
C_1	0.9082 (0.6905)	3.4978 (0.6836)	0.2480 (0.0790)	
C_2	1.0194 (0.2249)	3.8235 (0.4164)	0.2639 (0.0279)	
C_3	0.7221 (0.0808)	3.0457 (0.2531)	0.2367 (0.0079)	

Table 1: Results for fit parameters for the 2-state fit ($M = 2$) with covariance matrix.

	state 1			χ^2/dof
Ens.	f_1 [GeV]	m_1 [GeV]	g_1	
B_0	0.3255 (0.0235)	1.2062 (0.0770)	0.2698 (0.0067)	1.35
B_1	0.2896 (0.0178)	1.0719 (0.0606)	0.2701 (0.0041)	1.18
B_2	0.2940 (0.0150)	1.0890 (0.0508)	0.2699 (0.0041)	0.99
B_3	0.2952 (0.0190)	1.1348 (0.0564)	0.2600 (0.0061)	1.37
B_4	0.3054 (0.0214)	1.1496 (0.0598)	0.2655 (0.0075)	0.93
B_5	0.3102 (0.0275)	1.2121 (0.0686)	0.2555 (0.0108)	2.42
B_7	0.2590 (0.0348)	0.9406 (0.1153)	0.2751 (0.0089)	2.54
B_6	0.3019 (0.0204)	1.0829 (0.0653)	0.2788 (0.0067)	1.35
C_5	0.3123 (0.0144)	1.1151 (0.0495)	0.2801 (0.0036)	1.33
C_1	0.3650 (0.0315)	1.2871 (0.1019)	0.2835 (0.0059)	1.45
C_2	0.3380 (0.0155)	1.1999 (0.0508)	0.2817 (0.0047)	0.86
C_3	0.2969 (0.0170)	1.1299 (0.0545)	0.2627 (0.0061)	0.57
	state 2			
Ens.	f_2 [GeV]	m_2 [GeV]	g_2	
B_0	0.8470 (0.1116)	3.4569 (0.3041)	0.2442 (0.0124)	
B_1	0.7599 (0.0630)	3.1399 (0.2051)	0.2418 (0.0059)	
B_2	0.7361 (0.0583)	3.1011 (0.1851)	0.2372 (0.0064)	
B_3	0.7116 (0.0734)	3.0385 (0.2396)	0.2338 (0.0077)	
B_4	0.6962 (0.0889)	3.0342 (0.2762)	0.2288 (0.0104)	
B_5	0.7018 (0.1323)	3.0926 (0.3980)	0.2254 (0.0146)	
B_7	0.7400 (0.1253)	2.9211 (0.3824)	0.2523 (0.0107)	
B_6	0.9125 (0.1340)	3.4789 (0.3117)	0.2611 (0.0162)	
C_5	0.8306 (0.0424)	3.4306 (0.1574)	0.2421 (0.0029)	
C_1	0.9955 (0.1471)	3.9855 (0.4150)	0.2488 (0.0119)	
C_2	0.8398 (0.0591)	3.5432 (0.1924)	0.2369 (0.0058)	
C_3	0.7447 (0.0485)	3.1592 (0.1791)	0.2357 (0.0046)	
	state 3			
Ens.	f_3 [GeV]	m_3 [GeV]	g_3	
B_0	1.8156 (0.0676)	6.6097 (0.3738)	0.2754 (0.0155)	
B_1	1.8237 (0.0616)	6.3653 (0.2587)	0.2867 (0.0082)	
B_2	1.8443 (0.0621)	6.3146 (0.2528)	0.2922 (0.0075)	
B_3	1.8147 (0.0620)	6.1946 (0.2703)	0.2932 (0.0096)	
B_4	1.8633 (0.0648)	6.2450 (0.3096)	0.2988 (0.0117)	
B_5	1.8253 (0.0659)	6.2526 (0.4257)	0.2929 (0.0174)	
B_7	1.8519 (0.0658)	6.3446 (0.4587)	0.2930 (0.0177)	
B_6	1.8128 (0.0719)	6.8223 (0.5795)	0.2671 (0.0193)	
C_5	2.2181 (0.0714)	7.6244 (0.2643)	0.2910 (0.0042)	
C_1	2.1946 (0.0803)	8.1386 (0.6080)	0.2708 (0.0178)	
C_2	2.2069 (0.0724)	7.5982 (0.2983)	0.2906 (0.0065)	
C_3	2.1951 (0.0720)	7.3239 (0.2713)	0.2998 (0.0052)	

Table 2: Results for fit parameters for the 3-state fit ($M = 3$) with covariance matrix.

Ens.	f_V^{loc} [GeV]	m_V^{loc} [GeV]	g_V^{loc}	χ^2/dof
B_1	0.4932 (0.0197) (0.0162)	1.0340 (0.0290) (0.0340)	0.4769 (0.0072)	1.43
B_2	0.5110 (0.0115) (0.0168)	1.0762 (0.0167) (0.0354)	0.4748 (0.0046)	0.61
B_3	0.4979 (0.0112) (0.0164)	1.0921 (0.0159) (0.0359)	0.4559 (0.0048)	1.87
B_4	0.5166 (0.0157) (0.0170)	1.1336 (0.0198) (0.0373)	0.4556 (0.0070)	0.95
B_5	0.5329 (0.0086) (0.0175)	1.1940 (0.0115) (0.0393)	0.4463 (0.0040)	0.71
B_7	0.4123 (0.0190) (0.0136)	0.8913 (0.0334) (0.0293)	0.4625 (0.0073)	1.18
B_6	0.4786 (0.0175) (0.0158)	1.0023 (0.0259) (0.0330)	0.4774 (0.0073)	1.36
C_1	0.4737 (0.0235) (0.0150)	1.0567 (0.0394) (0.0335)	0.4481 (0.0073)	0.76
C_2	0.4545 (0.0159) (0.0144)	1.0674 (0.0268) (0.0339)	0.4257 (0.0054)	1.55
C_3	0.4782 (0.0118) (0.0152)	1.1254 (0.0188) (0.0357)	0.4249 (0.0056)	1.52

Table 3: Results for parameters for fit to the local vector current correlator.

8 Tables for fits of the vacuum polarization function

	Π_{low}		Π_{high}					$\frac{\chi^2}{\text{dof}}$
Ens.	a_0	$a^2\,a_1$	c_0	$a^2\,c_1$	$a^4\,c_2$	$a^6\,c_3$	b_0	
B_0	0.1278 (55)	−0.0356 (57)	0.11946 (95)	−0.003310 (74)	0.0001589 (48)	−0.00000310 (13)	−0.02557 (31)	0.254
B_1	0.1327 (23)	−0.0398 (32)	0.11979 (66)	−0.003326 (62)	0.0001629 (39)	−0.00000327 (10)	−0.02570 (22)	0.332
B_2	0.1295 (23)	−0.0276 (30)	0.12105 (82)	−0.003553 (75)	0.0001769 (46)	−0.00000362 (12)	−0.02552 (26)	0.225
B_3	0.1280 (24)	−0.0312 (28)	0.11965 (104)	−0.003526 (88)	0.0001772 (55)	−0.00000369 (14)	−0.02529 (31)	0.159
B_4	0.1294 (27)	−0.0304 (31)	0.12086 (129)	−0.003641 (119)	0.0001807 (73)	−0.00000365 (19)	−0.02529 (44)	0.137
B_5	0.1284 (27)	−0.0316 (31)	0.11918 (129)	−0.003637 (108)	0.0001814 (66)	−0.00000373 (17)	−0.02480 (39)	0.087
B_7	0.1350 (49)	−0.0363 (63)	0.12082 (112)	−0.003285 (99)	0.0001656 (60)	−0.00000340 (15)	−0.02638 (39)	0.168
B_6	0.1281 (32)	−0.0268 (49)	0.12008 (125)	−0.003430 (104)	0.0001698 (64)	−0.00000347 (16)	−0.02560 (39)	0.165
C_5	0.1351 (49)	−0.0466 (89)	0.11318 (70)	−0.001644 (92)	−0.0000003 (99)	0.00000380 (45)	−0.02721 (27)	0.328
C_1	0.1452 (88)	−0.0685 (177)	0.11360 (108)	−0.001739 (142)	0.0000230 (144)	0.00000230 (62)	−0.02726 (42)	0.179
C_2	0.1489 (52)	−0.0728 (99)	0.11473 (108)	−0.002056 (123)	0.0000563 (117)	0.00000098 (49)	−0.02714 (41)	0.175
C_3	0.1396 (33)	−0.0572 (62)	0.11280 (118)	−0.001976 (144)	0.0000534 (134)	0.00000101 (55)	−0.02684 (42)	0.148

Table 4: Results for the parameters of the $M1N2B1C4$ fit of the vacuum polarization function. The last column shows the uncorrelated reduced χ^2.

	Π_{low}			Π_{high}				$\frac{\chi^2}{\text{dof}}$
Ens.	a_0	$a^2\,a_1$	$a^4\,a_2$	c_0	$a^2\,c_1$	$a^4\,c_2$	b_0	
B_0	0.1284 (54)	−0.0357 (172)	−0.018 (33)	0.11864 (93)	−0.002107 (44)	0.0000604 (14)	−0.02752 (32)	0.286
B_1	0.1340 (24)	−0.0509 (105)	0.015 (21)	0.11890 (65)	−0.002072 (35)	0.0000594 (11)	−0.02769 (23)	0.395
B_2	0.1277 (24)	0.0003 (101)	−0.087 (20)	0.12006 (81)	−0.002161 (43)	0.0000620 (13)	−0.02773 (27)	0.268
B_3	0.1263 (25)	−0.0052 (86)	−0.083 (18)	0.11865 (102)	−0.002099 (48)	0.0000599 (16)	−0.02757 (32)	0.195
B_4	0.1277 (29)	−0.0043 (100)	−0.083 (21)	0.11987 (127)	−0.002239 (69)	0.0000650 (22)	−0.02753 (44)	0.157
B_5	0.1264 (29)	−0.0030 (81)	−0.090 (17)	0.11816 (127)	−0.002200 (63)	0.0000630 (20)	−0.02709 (40)	0.108
B_7	0.1343 (48)	−0.0212 (211)	−0.060 (44)	0.11998 (111)	−0.001944 (55)	0.0000571 (17)	−0.02861 (39)	0.187
B_6	0.1266 (35)	−0.0002 (146)	−0.091 (29)	0.11922 (123)	−0.002057 (60)	0.0000590 (19)	−0.02790 (40)	0.188
C_5	0.1347 (51)	−0.0444 (162)	0.009 (38)	0.11375 (70)	−0.002265 (52)	0.0000783 (20)	−0.02657 (26)	0.331
C_1	0.1467 (91)	−0.1000 (355)	0.138 (97)	0.11396 (108)	−0.002137 (74)	0.0000717 (27)	−0.02683 (40)	0.180
C_2	0.1491 (54)	−0.0772 (186)	0.022 (47)	0.11489 (108)	−0.002228 (67)	0.0000772 (26)	−0.02695 (39)	0.175
C_3	0.1394 (34)	−0.0535 (158)	−0.012 (49)	0.11296 (117)	−0.002152 (82)	0.0000749 (32)	−0.02665 (41)	0.148

Table 5: Results for the parameters of the $M1N3B1C3$ fit of the vacuum polarization function. The last column shows the uncorrelated reduced χ^2.

	Π_{low}		Π_{high}				$\frac{\chi^2}{\text{dof}}$
Ens.	a_0	$a^2 a_1$	c_0	$a^2 c_1$	$a^4 c_2$	b_0	
B_0	0.1291 (55)	−0.0431 (57)	0.11864 (93)	−0.002108 (44)	0.0000604 (14)	−0.02752 (32)	0.286
B_1	0.1335 (23)	−0.0451 (32)	0.11890 (65)	−0.002071 (35)	0.0000594 (11)	−0.02770 (23)	0.395
B_2	0.1309 (23)	−0.0363 (37)	0.11879 (81)	−0.001203 (36)	0.0000581 (10)	−0.02957 (27)	0.462
B_3	0.1295 (25)	−0.0396 (37)	0.11864 (102)	−0.002103 (48)	0.0000600 (16)	−0.02756 (32)	0.195
B_4	0.1307 (28)	−0.0377 (43)	0.11986 (127)	−0.002242 (70)	0.0000651 (22)	−0.02751 (44)	0.158
B_5	0.1294 (28)	−0.0378 (40)	0.11816 (127)	−0.002205 (63)	0.0000631 (20)	−0.02707 (40)	0.108
B_7	0.1361 (49)	−0.0439 (63)	0.11997 (111)	−0.001947 (55)	0.0000572 (17)	−0.02860 (39)	0.187
B_6	0.1293 (33)	−0.0344 (50)	0.11922 (123)	−0.002061 (60)	0.0000591 (19)	−0.02788 (40)	0.188
C_5	0.1346 (49)	−0.0421 (89)	0.11375 (70)	−0.002264 (52)	0.0000783 (21)	−0.02657 (26)	0.331
C_1	0.1450 (88)	−0.0664 (177)	0.11396 (108)	−0.002133 (74)	0.0000715 (27)	−0.02684 (40)	0.180
C_2	0.1488 (52)	−0.0719 (98)	0.11489 (108)	−0.002227 (67)	0.0000771 (26)	−0.02695 (39)	0.175
C_3	0.1395 (33)	−0.0563 (61)	0.11296 (117)	−0.002152 (82)	0.0000749 (32)	−0.02665 (41)	0.148

Table 6: Results for the parameters of the *M*1*N*2*B*1C3 fit of the vacuum polarization function. The last column shows the uncorrelated reduced χ^2.

	Π_{low}		Π_{high}				$\frac{\chi^2}{\text{dof}}$
Ens.	a_0	$a^2\,a_1$	c_0	$a^2\,c_1$	b_0	$a^2\,b_1$	
B_0	0.1276 (55)	−0.0343 (57)	0.12253 (97)	−0.00614 (13)	−0.02388 (33)	0.001483 (34)	0.261
B_1	0.1326 (23)	−0.0393 (32)	0.12273 (68)	−0.00602 (10)	−0.02417 (24)	0.001454 (26)	0.348
B_2	0.1295 (23)	−0.0273 (30)	0.12408 (85)	−0.00631 (13)	−0.02402 (28)	0.001524 (32)	0.235
B_3	0.1280 (24)	−0.0311 (28)	0.12255 (108)	−0.00613 (15)	−0.02394 (32)	0.001480 (38)	0.168
B_4	0.1294 (27)	−0.0298 (31)	0.12407 (132)	−0.00657 (21)	−0.02365 (47)	0.001594 (53)	0.142
B_5	0.1283 (27)	−0.0313 (31)	0.12225 (134)	−0.00642 (19)	−0.02330 (41)	0.001550 (49)	0.092
B_7	0.1350 (49)	−0.0361 (63)	0.12367 (115)	−0.00585 (16)	−0.02499 (41)	0.001425 (41)	0.172
B_6	0.1281 (32)	−0.0265 (50)	0.12305 (130)	−0.00611 (18)	−0.02414 (42)	0.001476 (45)	0.170
C_5	0.1339 (49)	−0.0355 (89)	0.11652 (72)	−0.00487 (12)	−0.02487 (28)	0.001177 (33)	0.343
C_1	0.1445 (88)	−0.0615 (177)	0.11663 (112)	−0.00466 (18)	−0.02513 (43)	0.001118 (46)	0.183
C_2	0.1483 (52)	−0.0667 (98)	0.11784 (112)	−0.00503 (17)	−0.02502 (40)	0.001229 (43)	0.177
C_3	0.1390 (33)	−0.0514 (61)	0.11582 (123)	−0.00486 (20)	−0.02479 (42)	0.001189 (52)	0.150

Table 7: Results for the parameters of the $M1N2B2C2$ fit of the vacuum polarization function. The last column shows the uncorrelated reduced χ^2.

	Π_{low}		Π_{high}				$\frac{\chi^2}{\text{dof}}$
Ens.	a_0	$a^2\,a_1$	c_0	$a^2\,c_1$	$a^4\,c_2$	b_0	
B_0	0.0493 (408)	−0.0026 (49)	0.11839 (93)	−0.001989 (46)	0.0000567 (14)	−0.02795 (34)	0.288
B_1	0.0618 (75)	−0.0041 (13)	0.11850 (65)	−0.001955 (35)	0.0000558 (11)	−0.02812 (24)	0.398
B_2	0.0650 (58)	−0.0032 (11)	0.11970 (81)	−0.002024 (44)	0.0000579 (13)	−0.02823 (28)	0.271
B_3	0.0722 (46)	−0.0050 (10)	0.11832 (103)	−0.001953 (48)	0.0000555 (16)	−0.02810 (33)	0.197
B_4	0.0685 (73)	−0.0035 (15)	0.11951 (128)	−0.002118 (71)	0.0000613 (22)	−0.02796 (46)	0.158
B_5	0.0669 (107)	−0.0038 (22)	0.11789 (127)	−0.002056 (63)	0.0000585 (20)	−0.02761 (41)	0.109
B_7	0.0793 (47)	−0.0062 (13)	0.11968 (111)	−0.001816 (53)	0.0000532 (16)	−0.02908 (39)	0.188
B_6	0.0690 (67)	−0.0044 (15)	0.11894 (124)	−0.001923 (58)	0.0000549 (18)	−0.02839 (42)	0.189
C_5	0.0830 (33)	−0.0074 (13)	0.11334 (70)	−0.002330 (53)	0.0000813 (20)	−0.02641 (27)	0.333
C_1	0.0664 (1185)	−0.0067 (162)	0.11346 (108)	−0.002179 (72)	0.0000735 (25)	−0.02673 (40)	0.181
C_2	0.0611 (188)	−0.0015 (46)	0.11419 (108)	−0.002233 (64)	0.0000774 (23)	−0.02694 (39)	0.175
C_3	0.0844 (65)	−0.0094 (26)	0.11249 (117)	−0.002156 (77)	0.0000750 (29)	−0.02664 (41)	0.148

Table 8: Results for the parameters of the *M2N2B1C3* fit of the vacuum polarization function. The last column shows the uncorrelated reduced χ^2.

	Π_{low}		Π_{high}				$\frac{\chi^2}{\text{dof}}$
Ens.	a_0	$a^2\,a_1$	c_0	$a^2\,c_1$	$a^4\,c_2$	b_0	
B_0	−0.00707 (135)	0.00311 (95)	0.11839 (93)	−0.001989 (46)	0.0000568 (14)	−0.02795 (34)	0.288
B_1	−0.00591 (72)	0.00344 (55)	0.11850 (65)	−0.001956 (35)	0.0000559 (11)	−0.02811 (24)	0.397
B_2	−0.00741 (80)	0.00514 (56)	0.11970 (81)	−0.002025 (44)	0.0000579 (13)	−0.02823 (28)	0.271
B_3	−0.00729 (107)	0.00500 (60)	0.11832 (103)	−0.001955 (48)	0.0000555 (16)	−0.02810 (33)	0.197
B_4	−0.00899 (189)	0.00551 (93)	0.11950 (128)	−0.002119 (71)	0.0000614 (22)	−0.02796 (46)	0.158
B_5	−0.00700 (214)	0.00499 (101)	0.11790 (127)	−0.002057 (63)	0.0000586 (20)	−0.02761 (41)	0.109
B_7	−0.00794 (200)	0.00482 (114)	0.11970 (111)	−0.001818 (53)	0.0000532 (16)	−0.02908 (39)	0.188
B_6	−0.00895 (203)	0.00492 (91)	0.11895 (124)	−0.001924 (58)	0.0000549 (18)	−0.02839 (42)	0.189
C_5	−0.00753 (94)	0.00626 (97)	0.11335 (70)	−0.002331 (53)	0.0000813 (20)	−0.02641 (27)	0.333
C_1	−0.00654 (177)	0.00325 (204)	0.11347 (108)	−0.002178 (72)	0.0000735 (25)	−0.02673 (40)	0.181
C_2	−0.00761 (179)	0.00675 (156)	0.11422 (108)	−0.002234 (64)	0.0000775 (23)	−0.02694 (39)	0.176
C_3	−0.00631 (218)	0.00509 (179)	0.11250 (117)	−0.002156 (77)	0.0000751 (29)	−0.02664 (41)	0.148

Table 9: Results for the parameters of the $M3N2B1C3$ fit of the vacuum polarization function. The last column shows the uncorrelated reduced χ^2.

Appendix: Lattice calculation of $a_l^{\rm hlo}$

9 Formulas for the tree-level vector meson contribution to $a_\mu^{\rm hlo}$

We start from the general integral for $a_\mu^{\rm hlo}$ in equation (4.11). In order to facilitate the calculation it is useful to make a change of the integration variable according to

$$r = \hat{Q}^2/m_l^2 = \frac{x^2}{1-x}$$
$$r \in [0,\infty)\,; \quad x \in [0,1)$$

Expressing the integral measure and weight function through x the integral can be rewritten as follows

$$\begin{aligned} Z &= -\frac{1}{2m_l^2}\,\frac{\hat{Q}^2/m_l^2 - \sqrt{(\hat{Q}^2/m_l^2)^2 + 4\hat{Q}^2/m_l^2}}{\hat{Q}^2/m_l^2} \\ &= \frac{1-x}{x\,m_l^2} \\ w(\hat{Q}^2) &= \frac{m_l^{10}(\hat{Q}^2/m_l^2)^3\,Z^5}{1+m_l^4(\hat{Q}^2/m_l^2)\,Z^2} \\ &= \frac{x(1-x)^2}{2-x} \\ a_\mu^{\rm hlo} &= \int_0^1 dx\,(1-x)\,\Pi_R(x^2/(1-x))\,. \end{aligned}$$

With the special choice $\Pi_R(\hat{Q}^2) = g_V^2\,\hat{Q}^2\,/\,(\hat{Q}^2 - m_V^2)$ this leads to

$$a_\mu^V = \frac{f_V^2}{m_V^2}\int_0^1 dx\,\frac{(1-x)x^2}{x^2+\xi(1-x)}\,,$$

where $\xi = m_V^2/m_l^2 > 0$. Note that the denominator does not have poles in the interval $[0\,,\,1]$ for any choice of positive ξ. We first focus on the case $\xi \geq 4$, i.e. $m_V \geq 2m_l$. In that

case the denominator has two poles at

$$\zeta_\pm = \frac{1}{2}\left(\xi \pm \sqrt{\xi^2 - 4\xi}\right)$$

and we can use partial fraction decomposition and define $z = x - \zeta_\pm$ in the two emerging integrals.

$$\begin{aligned}
&\int_0^1 \frac{x^2(1-x)}{(1-x)\xi + x^2}\,dx = \frac{1}{\zeta_+ - \zeta_-}\int_0^1 x^2\,(1-x)\left(\frac{1}{x-\zeta_+} - \frac{1}{x-\zeta_-}\right)dx \\
=&\frac{1}{\zeta_+ - \zeta_-}\Bigg(\int_{-\zeta_+}^{1-\zeta_+} dz\left(-z^2 + (1-3\zeta_+)z + \zeta_+(2-3\zeta_+) + \frac{\zeta_+^2(1-\zeta_+)}{z}\right) \\
&\quad - \int_{-\zeta_-}^{1-\zeta_-} dz\left(-z^2 + (1-3\zeta_-)z + \zeta_-(2-3\zeta_-) + \frac{\zeta_-^2(1-\zeta_-)}{z}\right)\Bigg) \\
=&\frac{1}{\zeta_+ - \zeta_-}\Big[-\frac{1}{3}z^3 + \frac{1-3\zeta_+}{2}z^2 + \zeta_+(2-3\zeta_+)z + \zeta_+^2(1-\zeta_+)\log(|z|)\Big]_{-\zeta_+}^{1-\zeta_+} \\
&\quad - \frac{1}{\zeta_+ - \zeta_-}\Big[-\frac{1}{3}z^3 + \frac{1-3\zeta_-}{2}z^2 + \zeta_-(2-3\zeta_-)z + \zeta_-^2(1-\zeta_-)\log(|z|)\Big]_{-\zeta_-}^{1-\zeta_-} \\
=&\frac{1}{\sqrt{\xi^2-4\xi}}\Big(-\frac{1}{3}(1-3\zeta_+ + 3\zeta_+^2) + \frac{1-3\zeta_+}{2}(1-2\zeta_+) + \zeta_+(2-3\zeta_+) \\
&\quad + \zeta_+^2(1-\zeta_+)\log((\zeta_+-1)/\zeta_+)\Big) \\
&\quad - \frac{1}{\sqrt{\xi^2-4\xi}}\Big(-\frac{1}{3}(1-3\zeta_- + 3\zeta_-^2) + \frac{1-3\zeta_-}{2}(1-2\zeta_-) + \zeta_-(2-3\zeta_-) \\
&\quad + \zeta_-^2(1-\zeta_-)\log((1-\zeta_-)/\zeta_-)\Big).
\end{aligned}$$

Using the relations

$$\begin{aligned}
\log\left((\zeta_+ - 1)/\zeta_+\right) &= \log\left(\left(1 + \sqrt{1-4/\xi}\right)/2\right) \\
\log\left((\zeta_- - 1)/\zeta_-\right) &= -\log(\xi) - \log\left(1 + \sqrt{1-4/\xi}\right)/2 \\
\zeta_+ - \zeta_- &= \sqrt{\xi^2-4\xi} \\
\zeta_+^2 + \zeta_-^2 &= \xi^2 - 2\xi \\
\zeta_+^2 - \zeta_-^2 &= \xi\sqrt{\xi^2-4\xi} \\
\zeta_+^3 + \zeta_-^3 &= \xi^2(\xi-3) \\
\zeta_+^3 - \zeta_-^3 &= \xi(1-\xi)\sqrt{\xi^2-4\xi}
\end{aligned}$$

we can simplify the above terms as follows:

$$\int_0^1 \frac{x^2(1-x)}{(1-x)\xi + x^2}\,dx = \left(\frac{1}{2} - \xi\right) + \log(\xi)\left(\left(\xi - \frac{\xi^2}{2}\right) + \frac{1}{\sqrt{\xi^2 - 4\xi}}\left(\xi - 2\xi^2 + \frac{\xi^3}{2}\right)\right) + \log\left((1 + \sqrt{1 - 4/\xi})/2\right)\frac{1}{\sqrt{\xi^2 - 4\xi}}\left(-2\xi + 4\xi^2 - \xi^3\right).$$

We set $y = 1/\xi = m_l^2/m_V^2$ and taking out one factor of y we get

$$\begin{aligned} f_<(y) &= \frac{1}{y}\int_0^1 \frac{x^2(1-x)}{(1-x)/y + x^2}\,dx \\ &= \frac{1}{2y} - \frac{1}{y^2} + \log(y)\left(\left(\frac{1}{y^2} - \frac{1}{2y^3}\right) + \frac{1}{\sqrt{1-4y}}\left(\frac{1}{y} - 2\frac{1}{y^2} + \frac{1}{2y^3}\right)\right) \\ &\quad + \log\left((1 + \sqrt{1-4y})/2\right)\frac{1}{\sqrt{1-4y}}\left(-\frac{2}{y} + \frac{4}{y^2} - \frac{1}{y^3}\right). \end{aligned} \tag{49}$$

The case $\xi < 4$ will correspond to the τ lepton, since its mass $m_\tau \approx 1780\,\mathrm{MeV}$ exceeds that of the ρ meson. There are no real valued poles and the integral can be transformed as follows: using $a = \xi/2$, $b^2 = \xi - \xi^2/4$ and $z = x - a$ we get a sequence of standard integrals

$$\begin{aligned} &\int_0^1 \frac{x^2(1-x)}{(1-x)\xi + x^2}\,dx = \int_0^1 \frac{x^2(1-x)}{(x-a)^2 + b^2}\,dx \\ &= \int_{-a}^{1-a}\left\{-\frac{z^3}{z^2+b^2} + (1-3a)\frac{z^2}{z^2+b^2} + a(2-3a)\frac{z}{z^2+b^2} + a^2(1-a)\frac{1}{z^2+b^2}\right\}dz \\ &= -\left\{\frac{1-2a}{2} - \frac{b^2}{2}\log\left(\frac{(1-a)^2+b^2}{a^2+b^2}\right)\right\} \\ &\quad + (1-3a)\left\{1 - b\arctan\left(\frac{1-a}{b}\right) - b\arctan\left(\frac{a}{b}\right)\right\} \\ &\quad + a(2-3a)\frac{1}{2}\log\left(\frac{(1-a)^2+b^2}{a^2+b^2}\right) \\ &\quad + \frac{a^2(1-a)}{b}\left(\arctan\left(\frac{1-a}{b}\right) - \arctan\left(\frac{a}{b}\right)\right) \end{aligned}$$

Setting again $y = 1/\xi$, resubstituting for a and b and taking out one factor y this can be

simplified to read

$$f_>(y) = \frac{1}{y}\int_0^1 \frac{x^2(1-x)}{(1-x)/y + x^2}\,dx = \frac{1}{2y} - \frac{1}{y^2} + \left(\frac{1}{y^2} - \frac{1}{2y^3}\right)\log(y) + \frac{1}{\sqrt{4y-1}}\left(-\frac{2}{y} + \frac{8}{y^2} - \frac{2}{y^3}\right)\left(\arctan\left(\frac{1}{\sqrt{4y-1}}\right) + \arctan\left(\frac{2y-1}{\sqrt{4y-1}}\right)\right). \quad (50)$$

10 Momentum integration with the temporal moment method

In the temporal moment method the polarization function is defined as a t-sum

$$\Pi(\hat{K}^2) = \sum_{t=a}^{t_{\rm max}} f_t(\hat{K}^2)\,\langle JJ(t,\vec{q}=0)\rangle^{av}\,,$$

which can be evaluated for all $0 \le \hat{K} \le 2/a$. The momentum integration then means to determine the coefficients $F(t)$ given by

$$F(t) = \int_0^{4/a^2} \frac{d\hat{K}^2}{\hat{K}^2}\, w(\hat{K}^2/m_l^2)\, f_t(\hat{K}^2)\,. \quad (51)$$

We had shown previously that $f_t(\hat{K}^2)$ is a polynomial in $\hat{K}^2$ for every value of $t/a \in \mathbb{N}$ and the latter can be constructed in various ways. For a polynomial all the integrations can be performed analytically. We thus seek to integrate

$$F(t) = \sum_{l=0}^{t/a} \int_0^{\hat{K}^2_{\rm max}} \frac{d\hat{K}^2}{\hat{K}^2}\, f_t^{(l)}\, \hat{K}^{2l}\, w(\hat{K}^2/m_l^2)\,.$$

We again make use of the change of variables $r = \hat{K}^2/m_l^2$ and $r = x^2/(1-x)$ such that

$$\frac{d\hat{K}^2}{\hat{K}^2}\, w(\hat{K}^2/m_l^2) = dx\,(1-x)$$

$$\begin{aligned}\omega_l &= \int \frac{d\hat{K}^2}{\hat{K}^2}\, w(\hat{K}^2/m_l^2)\, \hat{K}^{2l} = m_l^{2l} \int dx\, \frac{x^{2l}}{(1-x)^{l-1}} \\ &= m_l^{2l} \sum_{k=0}^{l} \int dx\, (-1)^k \binom{2l}{k} (1-x)^{k-l+1} \\ &= m_l^{2l} \Big(\sum_{k\neq l-2} \frac{(-1)^k}{k-l+2}\, (1-x)^{k-l+2} \binom{2l}{k} + (-1)^{l-1}\, \frac{(2l)!}{(l+2)!(l-2)!}\, \log(1-x) \Big).\end{aligned}$$

We can thus use the t-sum definition of Π_R in the defining integral for a_μ^{hlo} and exchange the analytic integration over momentum and the summation in lattice position space.

11 a_l^{hlo} integration results for different *MNBC* fits and scale functions

	$a_{\mu\ H}^{\mathrm{hlo}} \cdot 10^{10}$				
Ens.	$H = f_{PS}(\beta)$	$H = m_V$	$H = m_V g_V$	$H = g_V/m_V$	$H = m_V$, full
B_0	252(38)	551 (28)	523 (54)	583 (14)	
B_1	286(25)	541 (11)	505 (23)	580 (7)	551 (14)
B_2	277(23)	530 (11)	500 (22)	562 (5)	450 (10)
B_3	239(17)	515 (12)	462 (24)	574 (5)	
B_4	242(19)	515 (14)	464 (27)	571 (6)	
B_5	205(14)	477 (15)	392 (27)	580 (6)	
B_7	329(58)	546 (24)	525 (49)	569 (13)	
B_6	301(30)	552 (17)	545 (37)	560 (8)	472 (18)
C_5	290(25)	551 (23)	539 (49)	565 (6)	
C_1	325(52)	522 (46)	478 (93)	576 (14)	440 (37)
C_2	290(30)	476 (26)	390 (44)	581 (7)	412 (20)
C_3	256(21)	494 (18)	424 (33)	576 (7)	

Table 10: a_μ^{hlo} integration results for fit $M1N2B1C4$ using different scale functions H.

	$a_{\mu\ m_V}^{\mathrm{hlo}} \cdot 10^{10}$				
Ens.	*M*1*N*3*B*1*C*3	*M*1*N*2*B*1*C*3	*M*1*N*2*B*2*C*2	*M*2*N*2*B*1*C*3	*M*3*N*2*B*1*C*3
B_0	554 (39)	563 (29)	549 (28)	536 (21)	533 (19)
B_1	556 (17)	548 (12)	540 (11)	536 (12)	530 (12)
B_2	495 (14)	542 (12)	530 (11)	533 (12)	529 (12)
B_3	478 (15)	535 (13)	515 (12)	493 (16)	503 (17)
B_4	479 (17)	534 (15)	514 (14)	524 (18)	521 (21)
B_5	434 (16)	499 (15)	477 (15)	501 (20)	492 (27)
B_7	531 (31)	555 (25)	545 (24)	534 (26)	543 (28)
B_6	521 (20)	562 (17)	552 (17)	541 (20)	554 (21)
C_5	549 (22)	547 (23)	541 (22)	542 (13)	556 (12)
C_1	545 (51)	521 (46)	517 (45)	558 (23)	573 (19)
C_2	479 (25)	475 (26)	471 (25)	569 (18)	564 (15)
C_3	492 (20)	494 (18)	489 (18)	496 (22)	505 (18)

Table 11: a_μ^{hlo} integration results for different fits using scale function $H = m_V$.

	$a_{e\ m_V}^{\mathrm{hlo}} \cdot 10^{15}$		
Ens.	*N*2	*N*3	*N*2, full
B_0	1470 (76)	1720 (174)	
B_1	1442 (31)	1660 (67)	1472 (42)
B_2	1405 (31)	1406 (59)	1395 (34)
B_3	1369 (35)	1485 (73)	
B_4	1369 (40)	1430 (80)	
B_5	1262 (41)	1309 (70)	
B_7	1444 (66)	1503 (95)	
B_6	1466 (47)	1462 (56)	1441 (53)
C_5	1468 (62)	1718 (160)	
C_1	1374 (125)	1417 (138)	1314 (121)
C_2	1246 (68)	1273 (72)	1262 (73)
C_3	1296 (48)	1321 (69)	

Table 12: a_e^{hlo} integration results for different fits using $M = 1$, $B = 0$, $C = 0$ and scale function $H = m_V$.

	$a_\tau^{\mathrm{hlo}}{}_{m_V} \cdot 10^9$				
Ens.	*M*1*N*2*B*1*C*4	*M*1*N*3*B*1*C*3	*M*1*N*2*B*1*C*3	*M*1*N*2*B*2*C*2	*M*1*N*2*B*1*C*4, full
B_0	2669 (98)	2678 (130)	2704 (97)	2660 (96)	
B_1	2628 (41)	2669 (58)	2649 (41)	2624 (41)	2677 (73)
B_2	2543 (42)	2455 (56)	2578 (45)	2540 (42)	2524 (54)
B_3	2516 (46)	2432 (55)	2558 (50)	2513 (45)	
B_4	2522 (54)	2438 (63)	2557 (58)	2517 (54)	
B_5	2404 (51)	2310 (56)	2430 (54)	2400 (51)	
B_7	2620 (91)	2581 (122)	2650 (91)	2617 (91)	
B_6	2609 (59)	2532 (76)	2640 (59)	2607 (58)	2532 (83)
C_5	2587 (66)	2578 (68)	2573 (65)	2550 (65)	
C_1	2532 (141)	2596 (156)	2527 (141)	2513 (140)	2402 (161)
C_2	2385 (87)	2393 (88)	2383 (87)	2369 (87)	2463 (107)
C_3	2425 (62)	2417 (71)	2423 (62)	2409 (61)	

Table 13: a_τ^{hlo} integration results for different fits using $M = 1$ and scale function $H = m_V$.

	$a_\tau^{\mathrm{hlo}}{}_{m_V} \cdot 10^9$	
Ens.	*M*2*N*2*B*1*C*3	*M*3*N*2*B*1*C*3
B_0	2609 (68)	2604 (59)
B_1	2594 (41)	2578 (41)
B_2	2573 (41)	2566 (40)
B_3	2452 (54)	2488 (55)
B_4	2556 (62)	2552 (70)
B_5	2475 (63)	2450 (83)
B_7	2555 (88)	2606 (98)
B_6	2592 (66)	2638 (67)
C_5	2572 (43)	2619 (38)
C_1	2652 (77)	2707 (64)
C_2	2672 (59)	2659 (50)
C_3	2437 (72)	2465 (60)

Table 14: a_τ^{hlo} integration results for fits using $M = 2$, 3 and scale function $H = m_V$.

	$a_{\mu\ H}^{\mathrm{hlo}} \cdot 10^{10}$	
Ens.	$H = f_{PS}(\beta)$	$H = m_V$
B_1	976 (101)	1695 (180)
B_2	825 (58)	1524 (65)
B_3	798 (54)	1531 (59)
B_4	743 (50)	1527 (64)
B_5	648 (42)	1464 (36)
B_7	1706 (222)	2328 (328)
B_6	1065 (94)	1712 (133)
C_1	894 (116)	1588 (212)
C_2	734 (55)	1332 (86)
C_3	654 (46)	1317 (63)

Table 15: Unnormalized a_μ^{hlo} integration results for the local vector current correlator from the t-sum method.

12 Tables for the analysis in the charm valence sector

Ens.	$a\mu_c$	f_V [GeV]	m_V [GeV]	g_V	χ^2/dof
B_1	0.2049	0.4325 (47) (76)	2.8754 (29) (503)	0.1504 (15)	1.14
B_1	0.2300	0.4345 (52) (76)	3.0674 (33) (536)	0.1416 (16)	2.39
B_1	0.2582	0.4504 (54) (79)	3.2845 (33) (574)	0.1371 (15)	2.51
B_1	0.2898	0.4684 (58) (82)	3.5208 (34) (615)	0.1330 (15)	2.57
B_1	0.3253	0.4914 (68) (86)	3.7793 (39) (661)	0.1300 (17)	3.00
B_1	0.3651	0.5183 (85) (91)	4.0573 (46) (709)	0.1278 (20)	2.15
B_1	0.4098	0.5318 (105) (93)	4.3438 (56) (759)	0.1224 (23)	1.96
B_1	0.4600	0.5389 (149) (94)	4.6427 (81) (811)	0.1161 (30)	2.14
B_2	0.2049	0.4214 (52) (74)	2.8745 (33) (502)	0.1466 (17)	1.41
B_2	0.2300	0.4471 (56) (78)	3.0747 (33) (537)	0.1454 (17)	0.37
B_2	0.2582	0.4646 (60) (81)	3.2940 (33) (576)	0.1410 (17)	0.63
B_2	0.2898	0.4821 (64) (84)	3.5297 (34) (617)	0.1366 (17)	1.31
B_2	0.3253	0.5084 (69) (89)	3.7856 (40) (662)	0.1343 (17)	1.44
B_3	0.2049	0.4374 (72) (76)	2.8826 (47) (504)	0.1517 (23)	1.22
B_3	0.2300	0.4374 (70) (76)	3.0751 (41) (537)	0.1422 (21)	0.85
B_3	0.2582	0.4548 (72) (79)	3.2879 (43) (575)	0.1383 (21)	0.65
B_3	0.2898	0.4746 (81) (83)	3.5248 (43) (616)	0.1346 (22)	1.06
B_3	0.3253	0.5068 (100) (89)	3.7880 (55) (662)	0.1338 (25)	2.03
B_3	0.3651	0.5306 (112) (93)	4.0640 (58) (710)	0.1306 (26)	2.75
B_3	0.4098	0.5525 (140) (97)	4.3550 (74) (761)	0.1269 (30)	1.63
B_4	0.2049	0.4417 (62) (77)	2.8821 (39) (504)	0.1533 (20)	2.12
B_4	0.2300	0.4378 (62) (77)	3.0743 (37) (537)	0.1424 (19)	0.78
B_4	0.2582	0.4552 (63) (80)	3.2908 (37) (575)	0.1383 (18)	0.81
B_4	0.2898	0.4754 (66) (83)	3.5268 (38) (616)	0.1348 (18)	0.94
B_4	0.3253	0.4974 (70) (87)	3.7843 (41) (661)	0.1314 (17)	0.96
B_4	0.3651	0.5258 (91) (92)	4.0613 (52) (710)	0.1295 (21)	0.73
B_4	0.4098	0.5484 (120) (96)	4.3527 (67) (761)	0.1260 (26)	1.40
B_4	0.4600	0.5626 (176) (98)	4.6544 (97) (814)	0.1209 (36)	1.64
B_7	0.2300	0.4448 (50) (78)	3.0725 (33) (537)	0.1448 (15)	0.79
B_7	0.2582	0.4631 (53) (81)	3.2907 (33) (575)	0.1407 (15)	0.83
B_7	0.2898	0.4824 (59) (84)	3.5273 (33) (616)	0.1368 (16)	1.40
B_7	0.3253	0.5055 (68) (88)	3.7846 (37) (661)	0.1336 (17)	0.91
B_7	0.3651	0.5288 (89) (92)	4.0602 (45) (710)	0.1302 (21)	1.63
B_7	0.4098	0.5450 (126) (95)	4.3493 (64) (760)	0.1253 (27)	1.72
B_7	0.4600	0.5765 (210) (101)	4.6627 (109) (815)	0.1236 (42)	2.58
B_6	0.2300	0.4409 (56) (77)	3.0714 (34) (537)	0.1435 (17)	1.57
B_6	0.2582	0.4581 (58) (80)	3.2887 (34) (575)	0.1393 (17)	1.70
B_6	0.2898	0.4772 (63) (83)	3.5252 (34) (616)	0.1354 (17)	1.79
B_6	0.3253	0.5003 (72) (87)	3.7833 (37) (661)	0.1322 (18)	1.88
B_6	0.3651	0.5256 (90) (92)	4.0598 (47) (710)	0.1295 (21)	1.33
B_6	0.4098	0.5543 (122) (97)	4.3556 (62) (761)	0.1273 (26)	1.23
B_6	0.4600	0.5643 (187) (99)	4.6538 (100) (813)	0.1212 (38)	0.95

Table 16: Results from fits of charm vector current correlator for the $B-$ensembles. For f_V and m_V the errors are statistical and from the lattice spacing.

Ens.	$a\mu_c$	f_V [GeV]	m_V [GeV]	g_V	χ^2/dof
C_1	0.1663	0.4232 (57) (66)	2.8761 (38) (451)	0.1472 (18)	0.60
C_1	0.1867	0.4377 (58) (69)	3.0821 (37) (483)	0.1420 (18)	0.64
C_1	0.2096	0.4538 (60) (71)	3.3089 (36) (519)	0.1371 (17)	0.67
C_1	0.2352	0.4720 (62) (74)	3.5577 (36) (558)	0.1327 (17)	0.67
C_1	0.2640	0.4956 (70) (78)	3.8328 (39) (601)	0.1293 (17)	1.17
C_1	0.2963	0.5196 (76) (81)	4.1317 (42) (648)	0.1258 (18)	1.23
C_1	0.3326	0.5474 (96) (86)	4.4591 (53) (699)	0.1227 (20)	2.31
C_2	0.1663	0.4239 (40) (66)	2.8785 (27) (451)	0.1473 (13)	1.55
C_2	0.1867	0.4392 (40) (69)	3.0846 (26) (483)	0.1424 (12)	1.48
C_2	0.2096	0.4561 (41) (71)	3.3116 (24) (519)	0.1377 (12)	1.35
C_2	0.2352	0.4750 (42) (74)	3.5603 (24) (558)	0.1334 (11)	1.21
C_2	0.2640	0.4959 (45) (78)	3.8336 (25) (601)	0.1294 (11)	1.02
C_2	0.2963	0.5223 (49) (82)	4.1343 (27) (648)	0.1263 (11)	0.94
C_2	0.3326	0.5532 (59) (87)	4.4638 (32) (700)	0.1239 (13)	1.30
C_3	0.1663	0.4322 (49) (68)	2.8807 (33) (452)	0.1500 (16)	3.11
C_3	0.1867	0.4464 (50) (70)	3.0853 (33) (484)	0.1447 (15)	2.95
C_3	0.2096	0.4619 (52) (72)	3.3106 (32) (519)	0.1395 (15)	2.67
C_3	0.2352	0.4795 (54) (75)	3.5580 (32) (558)	0.1348 (14)	2.10
C_3	0.2640	0.4996 (58) (78)	3.8304 (33) (600)	0.1304 (14)	1.84
C_3	0.2963	0.5257 (60) (82)	4.1314 (34) (648)	0.1273 (14)	1.70
C_3	0.3326	0.5557 (71) (87)	4.4597 (41) (699)	0.1246 (15)	2.16
D_1	0.1420	0.4189 (47) (68)	2.9430 (33) (475)	0.1423 (15)	0.90
D_1	0.1670	0.4517 (48) (73)	3.2606 (35) (526)	0.1385 (14)	0.83
D_1	0.1920	0.4712 (50) (76)	3.5656 (34) (576)	0.1322 (13)	0.95
D_1	0.2170	0.4902 (56) (79)	3.8634 (38) (624)	0.1269 (13)	1.71
D_1	0.2630	0.5313 (63) (86)	4.4030 (40) (711)	0.1207 (14)	1.93

Table 17: Results from fits of charm vector current correlator for $C-$ and $D-$ensembles.

Ens.	$a\mu_c$	$a_{\mu}^{\text{hlo}}{}_{H} \cdot 10^{10}$	
		$H = f_{PS}(\beta)$	$H = m_V$
B_1	0.2049	18.19 (64)	15.69 (15)
B_1	0.2300	15.57 (55)	15.27 (13)
B_1	0.2582	13.30 (47)	14.94 (13)
B_1	0.2898	11.34 (40)	14.62 (13)
B_1	0.3253	9.64 (34)	14.30 (13)
B_1	0.3651	8.16 (29)	13.95 (13)
B_1	0.4098	6.89 (25)	13.49 (12)
B_1	0.4600	5.79 (21)	12.94 (13)
B_2	0.2049	17.91 (63)	15.45 (16)
B_2	0.2300	15.32 (55)	15.10 (16)
B_2	0.2582	13.41 (48)	15.16 (16)
B_2	0.2898	11.25 (40)	14.58 (16)
B_2	0.3253	9.73 (35)	14.50 (14)
B_3	0.2049	18.25 (66)	15.82 (19)
B_3	0.2300	15.39 (56)	15.17 (18)
B_3	0.2582	13.08 (48)	14.72 (19)
B_3	0.2898	11.09 (41)	14.34 (21)
B_3	0.3253	9.41 (34)	14.04 (17)
B_3	0.3651	7.97 (29)	13.67 (17)
B_3	0.4098	6.91 (25)	13.59 (18)
B_4	0.2049	18.21 (65)	15.79 (16)
B_4	0.2300	15.35 (55)	15.12 (17)
B_4	0.2582	13.11 (47)	14.79 (16)
B_4	0.2898	11.17 (40)	14.46 (16)
B_4	0.3253	9.49 (34)	14.13 (16)
B_4	0.3651	8.03 (29)	13.75 (15)
B_4	0.4098	6.77 (24)	13.30 (15)
B_4	0.4600	5.68 (21)	12.75 (15)
B_7	0.2300	15.75 (56)	15.50 (15)
B_7	0.2582	13.45 (48)	15.17 (14)
B_7	0.2898	11.46 (41)	14.83 (14)
B_7	0.3253	9.72 (35)	14.47 (14)
B_7	0.3651	8.22 (29)	14.08 (14)
B_7	0.4098	6.93 (25)	13.60 (14)
B_7	0.4600	5.81 (21)	13.10 (15)
B_6	0.2300	15.35 (55)	15.09 (15)
B_6	0.2582	13.11 (47)	14.77 (14)
B_6	0.2898	11.16 (40)	14.43 (14)
B_6	0.3253	9.48 (34)	14.10 (14)
B_6	0.3651	8.02 (29)	13.73 (14)
B_6	0.4098	6.76 (24)	13.30 (14)
B_6	0.4600	5.67 (20)	12.72 (15)

Table 18: $a_{\mu}^{\text{hlo}}(\text{charm})$ integration results for $B-$ensembles using $H = f_{PS}(\beta)$, m_V

Ens.	$a\mu_c$	$a_{\mu\ H}^{\rm hlo} \cdot 10^{10}$	
		$H = f_{PS}(\beta)$	$H = m_V$
C_1	0.1663	17.81 (59)	15.38 (18)
C_1	0.1867	15.18 (50)	15.04 (17)
C_1	0.2096	12.91 (42)	14.71 (17)
C_1	0.2352	10.95 (36)	14.41 (16)
C_1	0.2640	9.24 (31)	14.11 (16)
C_1	0.2963	7.81 (26)	13.85 (16)
C_1	0.3326	6.57 (22)	13.56 (16)
C_2	0.1663	17.75 (56)	15.35 (12)
C_2	0.1867	15.13 (48)	15.01 (12)
C_2	0.2096	12.86 (41)	14.68 (12)
C_2	0.2352	10.90 (34)	14.38 (11)
C_2	0.2640	9.22 (29)	14.08 (11)
C_2	0.2963	7.77 (25)	13.80 (11)
C_2	0.3326	6.54 (21)	13.52 (11)
C_3	0.1663	18.04 (58)	15.63 (13)
C_3	0.1867	15.37 (49)	15.25 (13)
C_3	0.2096	13.06 (42)	14.91 (13)
C_3	0.2352	11.07 (35)	14.58 (12)
C_3	0.2640	9.36 (30)	14.28 (12)
C_3	0.2963	7.90 (25)	14.00 (12)
C_3	0.3326	6.64 (21)	13.71 (12)
D_1	0.1420	16.36 (55)	14.79 (15)
D_1	0.1670	13.35 (44)	14.79 (14)
D_1	0.1920	10.88 (36)	14.39 (13)
D_1	0.2170	9.06 (30)	14.06 (13)
D_1	0.2630	6.77 (23)	13.63 (12)

Table 19: $a_\mu^{\rm hlo}$(charm) integration results for $C-$ and $D-$ensembles using $H = f_{PS}(\beta)$, m_V

Bibliography

[1] G. Aad et al. Observation of a new particle in the search for the Standard Model Higgs boson with the ATLAS detector at the LHC. *Phys.Lett.*, B716:1–29, 2012. doi: 10.1016/j.physletb.2012.08.020.

[2] I. Allison et al. High-precision charm-quark mass from current-current correlators in lattice and continuum QCD. *Phys.Rev.*, D78:054513, 2008. doi: 10.1103/PhysRevD.78.054513.

[3] M. Antonelli, D. M. Asner, D. A. Bauer, T. G. Becher, M. Beneke, et al. Flavor physics in the quark sector. *Phys.Rept.*, 494:197–414, 2010. doi: 10.1016/j.physrep.2010.05.003.

[4] S. Aoki and O. Bar. Automatic O(a) improvement for twisted-mass QCD in the presence of spontaneous symmetry breaking. *Phys.Rev.*, D74:034511, 2006. doi: 10.1103/PhysRevD.74.034511.

[5] C. Aubin and T. Blum. Calculating the hadronic vacuum polarization and leading hadronic contribution to the muon anomalous magnetic moment with improved staggered quarks. *Phys.Rev.*, D75:114502, 2007. doi: 10.1103/PhysRevD.75.114502.

[6] C. Aubin, T. Blum, M. Golterman, and S. Peris. Model-independent parametrization of the hadronic vacuum polarization and g-2 for the muon on the lattice. *Phys.Rev.*, D86:054509, 2012. doi: 10.1103/PhysRevD.86.054509.

[7] P.A. Baikov, K.G. Chetyrkin, J.H. Kuhn, and J. Rittinger. Vector correlator in massless QCD at order $O(\alpha_s^4)$ and the QED beta-function at five loop. *JHEP*, 1207: 017, 2012. doi: 10.1007/JHEP07(2012)017.

[8] R. Baron et al. Light meson physics from maximally twisted mass lattice QCD. *JHEP*, 1008:097, 2010. doi: 10.1007/JHEP08(2010)097.

[9] G.W. Bennett et al. Final report of the muon E821 anomalous magnetic moment measurement at BNL. *Phys.Rev.*, D73:072003, 2006. doi: 10.1103/PhysRevD.73.072003. Summary of E821 Collaboration measurements of the muon anomalous magnetic moment, each reported earlier in Letters or Brief Reports. Revised version submitted to Phys.Rev.D.

[10] J. Bijnens, E. Pallante, and J. Prades. Hadronic light by light contributions to the muon g-2 in the large N(c) limit. *Phys.Rev.Lett.*, 75:1447–1450, 1995. doi: 10.1103/PhysRevLett.75.1447,10.1103/PhysRevLett.75.1447.

[11] J. Bijnens, P. Gosdzinsky, and P. Talavera. Vector meson masses in chiral perturbation theory. *Nucl.Phys.*, B501:495–517, 1997. doi: 10.1016/S0550-3213(97)00391-X.

[12] B. Blossier, G. Herdoiza, and S. Simula. Twisted mass QCD in the charm sector. *PoS*, LAT2007:346, 2007.

[13] B. Blossier et al. Light quark masses and pseudoscalar decay constants from $N_f = 2$ Lattice QCD with twisted mass fermions. *JHEP*, 0804:020, 2008. doi: 10.1088/1126-6708/2008/04/020.

[14] B. Blossier et al. Pseudoscalar decay constants of kaon and D-mesons from $N_f = 2$ twisted mass Lattice QCD. *JHEP*, 0907:043, 2009. doi: 10.1088/1126-6708/2009/07/043.

[15] B. Blossier et al. f(B) and f(B)(s) with maximally twisted Wilson fermions. *PoS*, LAT2009:151, 2009.

[16] B. Blossier et al. A Proposal for B-physics on current lattices. *JHEP*, 1004:049, 2010. doi: 10.1007/JHEP04(2010)049.

[17] B. Blossier et al. Average up/down, strange and charm quark masses with Nf=2 twisted mass lattice QCD. *Phys.Rev.*, D82:114513, 2010. doi: 10.1103/PhysRevD.82.114513.

[18] B. Blossier et al. Ghost-gluon coupling, power corrections and $\Lambda_{\bar{MS}}$ from twisted-mass lattice QCD at $N_f = 2$. *PoS*, LATTICE2010:227, 2010.

[19] T. Blum. Lattice calculation of the lowest order hadronic contribution to the muon anomalous magnetic moment. *Phys.Rev.Lett.*, 91:052001, 2003. doi: 10.1103/PhysRevLett.91.052001.

[20] T. Blum and S. Chowdhury. Hadronic contributions to g-2 from the lattice. *Nucl.Phys.Proc.Suppl.*, 189:251–256, 2009. doi: 10.1016/j.nuclphysbps.2009.03.042.

[21] T. Blum, E. de Rafael, D. Hertzog, F. Jegerlehner, L. Roberts, A. Vainshtein, et al. INT workshop on the hadronic light-by-light contribution to the muon anomaly. *http://www.int.washington.edu/PROGRAMS/11-47w/*, 2011.

[22] M. Bochicchio, L. Maiani, G. Martinelli, G. C. Rossi, and M. Testa. Chiral symmetry on the lattice with Wilson fermions. *Nucl.Phys.*, B262:331, 1985. doi: 10.1016/0550-3213(85)90290-1.

[23] P. Boucaud et al. Dynamical twisted mass fermions with light quarks: simulation and analysis details. *Comput.Phys.Commun.*, 179:695–715, 2008. doi: 10.1016/j.cpc.2008.06.013.

[24] R. Boughezal and K. Melnikov. Hadronic light-by-light scattering contribution to the muon magnetic anomaly: constituent quark loops and QCD effects. *Phys.Lett.*, B704:193–196, 2011. doi: 10.1016/j.physletb.2011.09.001.

[25] P. Boyle, L. Del Debbio, E. Kerrane, and J. Zanotti. Lattice Determination of the Hadronic Contribution to the Muon $g-2$ using Dynamical Domain Wall Fermions. *Phys.Rev.*, D85:074504, 2012. doi: 10.1103/PhysRevD.85.074504.

[26] S. J. Brodsky and E. De Rafael. Suggested boson - lepton pair couplings and the anomalous magnetic moment of the muon. *Phys.Rev.*, 168:1620–1622, 1968. doi: 10.1103/PhysRev.168.1620.

[27] P. C. Bruns and U.-G. Meissner. Infrared regularization for spin-1 fields. *Eur.Phys.J.*, C40:97–119, 2005. doi: 10.1140/epjc/s2005-02118-0.

[28] R.M. Carey, K.R. Lynch, J.P. Miller, B.L. Roberts, W.M. Morse, et al. The new (g-2) experiment: a proposal to measure the muon anomalous magnetic moment to ±0.14 ppm precision. *Fermilab-proposal-0989*, 2009. Spokespersons: David W. Hertzog, B. Lee Roberts.

[29] S. Chatrchyan et al. Observation of a new boson at a mass of 125 GeV with the CMS experiment at the LHC. *Phys.Lett.*, B716:30–61, 2012. doi: 10.1016/j.physletb.2012.08.021.

[30] K.G. Chetyrkin, J. H. Kuhn, and M. Steinhauser. Three loop polarization function and O (alpha-s**2) corrections to the production of heavy quarks. *Nucl.Phys.*, B482:213–240, 1996. doi: 10.1016/S0550-3213(96)00534-2.

[31] K.G. Chetyrkin, J. H. Kuhn, and M. Steinhauser. RunDec: a Mathematica package for running and decoupling of the strong coupling and quark masses. *Comput.Phys.Commun.*, 133:43–65, 2000. doi: 10.1016/S0010-4655(00)00155-7.

[32] M. Constantinou et al. Non-perturbative renormalization of quark bilinear operators with $N_f = 2$ (tmQCD) Wilson fermions and the tree-level improved gauge action. *JHEP*, 1008:068, 2010. doi: 10.1007/JHEP08(2010)068.

[33] M. Davier. The hadronic contribution to (g-2)(mu). *Nucl.Phys.Proc.Suppl.*, 169: 288–296, 2007. doi: 10.1016/j.nuclphysbps.2007.03.023.

[34] M. Davier, A. Hoecker, B. Malaescu, and Z. Zhang. Reevaluation of the hadronic contributions to the muon g-2 and to alpha(MZ). *Eur.Phys.J.*, C71:1515, 2011. doi: 10.1140/epjc/s10052-010-1515-z.

[35] J.F. de Troconiz and F.J. Yndurain. The hadronic contributions to the anomalous magnetic moment of the muon. *Phys.Rev.*, D71:073008, 2005. doi: 10.1103/PhysRevD.71.073008.

[36] B. Dehnadi, A. H. Hoang, V. Mateu, and S. M. Zebarjad. Charm mass determination from QCD charmonium sum rules at order α_s^3. 2011.

[37] M. Della Morte and A. Juttner. Quark disconnected diagrams in chiral perturbation theory. *JHEP*, 1011:154, 2010. doi: 10.1007/JHEP11(2010)154.

[38] M. Della Morte, B. Jager, A. Juttner, and H. Wittig. The leading hadronic vacuum polarisation on the lattice. *AIP Conf.Proc.*, 1343:337–339, 2011. doi: 10.1063/1.3575022.

[39] M. Della Morte, B. Jager, A. Juttner, and H. Wittig. Towards a precise lattice determination of the leading hadronic contribution to (g-2)_mu. *JHEP*, 1203:055, 2012. doi: 10.1007/JHEP03(2012)055.

[40] M. Della Morte et al. Computation of the strong coupling in QCD with two dynamical flavors. *Nucl.Phys.*, B713:378–406, 2005. doi: 10.1016/j.nuclphysb.2005.02.013.

[41] P. Dimopoulos, R. Frezzotti, C. Michael, G.C. Rossi, and C. Urbach. O(a**2) cutoff effects in lattice Wilson fermion simulations. *Phys.Rev.*, D81:034509, 2010. doi: 10.1103/PhysRevD.81.034509.

[42] P. Dimopoulos et al. Lattice QCD determination of m_b, f_B and f_{B_s} with twisted mass Wilson fermions. *JHEP*, 1201:046, 2012. doi: 10.1007/JHEP01(2012)046.

[43] S. Duane, A.D. Kennedy, B.J. Pendleton, and D. Roweth. Hybrid Monte Carlo. *Phys.Lett.*, B195:216–222, 1987. doi: 10.1016/0370-2693(87)91197-X.

[44] G. Ecker, J. Gasser, A. Pich, and E. de Rafael. The role of resonances in chiral perturbation theory. *Nucl.Phys.*, B321:311, 1989. doi: 10.1016/0550-3213(89)90346-5.

[45] S. Eidelman. Status of (g(mu) - 2)/2 in standard model. *Acta Phys.Polon.*, B38:3015–3020, 2007.

[46] S. Eidelman. Status of the muon g-2. *PoS*, EPS-HEP2009:371, 2009.

[47] S.I. Eidelman. Standard model predictions for the muon (g-2)/2. 2009.

[48] Mike B. et al. (Award Panel). Ken Wilson Lattice Award 2011. *https://kwla.llnl.gov/awards/2011.html*, 2011.

[49] L.D. Faddeev and V.N. Popov. Feynman diagrams for the Yang-Mills field. *Phys.Lett.*, B25:29–30, 1967. doi: 10.1016/0370-2693(67)90067-6.

[50] F. Farchioni, R. Frezzotti, K. Jansen, I. Montvay, G.C. Rossi, et al. Twisted mass quarks and the phase structure of lattice QCD. *Eur.Phys.J.*, C39:421–433, 2005. doi: 10.1140/epjc/s2004-02078-9.

[51] F. Farchioni, K. Jansen, I. Montvay, E. Scholz, L. Scorzato, et al. The phase structure of lattice QCD with Wilson quarks and renormalization group improved gluons. *Eur.Phys.J.*, C42:73–87, 2005. doi: 10.1140/epjc/s2005-02262-5.

[52] X. Feng, K. Jansen, M. Petschlies, and D. B. Renner. Two-flavor QCD correction to lepton magnetic moments at leading-order in the electromagnetic coupling. *Phys.Rev.Lett.*, 107:081802, 2011. doi: 10.1103/PhysRevLett.107.081802.

[53] X. Feng, K. Jansen, and D. B. Renner. Resonance parameters of the rho-meson from lattice QCD. *Phys.Rev.*, D83:094505, 2011. doi: 10.1103/PhysRevD.83.094505.

[54] X. Feng, G. Hotzel, K. Jansen, M. Petschlies, and D. B. Renner. Leading-order hadronic contributions to a_μ and α_{QED} from $N_f = 2+1+1$ twisted mass fermions. *PoS*, 2012.

[55] E. J. Ferrer and V. de la Incera. Dynamically generated anomalous magnetic moment in massless QED. *Nucl.Phys.*, B824:217–238, 2010. doi: 10.1016/j.nuclphysb.2009.08.024.

[56] R. Frezzotti and G. Rossi. O(a**2) cutoff effects in Wilson fermion simulations. *PoS*, LAT2007:277, 2007.

[57] R. Frezzotti and G.C. Rossi. Chirally improving Wilson fermions. 1. O(a) improvement. *JHEP*, 0408:007, 2004. doi: 10.1088/1126-6708/2004/08/007.

[58] R. Frezzotti and G.C. Rossi. Chirally improving Wilson fermions. II. Four-quark operators. *JHEP*, 0410:070, 2004. doi: 10.1088/1126-6708/2004/10/070.

[59] R. Frezzotti, P. A. Grassi, S. Sint, and P. Weisz. Lattice QCD with a chirally twisted mass term. *JHEP*, 0108:058, 2001.

[60] R. Frezzotti, S. Sint, and P. Weisz. O(a) improved twisted mass lattice QCD. *JHEP*, 0107:048, 2001.

[61] P. Fritzsch, F. Knechtli, B. Leder, M. Marinkovic, S. Schaefer, et al. The strange quark mass and Lambda parameter of two flavor QCD. *Nucl.Phys.*, B865:397–429, 2012. doi: 10.1016/j.nuclphysb.2012.07.026.

[62] W.H. Furry. A symmetry theorem in the positron theory. *Phys.Rev.*, 51:125–129, 1937. doi: 10.1103/PhysRev.51.125.

[63] M. Gockeler et al. Vacuum polarization and hadronic contribution to muon g-2 from lattice QCD. *Nucl.Phys.*, B688:135–164, 2004. doi: 10.1016/j.nuclphysb.2004.03.026.

[64] T. Goecke, C. S. Fischer, and R. Williams. Hadronic light-by-light scattering in the muon g-2: a Dyson-Schwinger equation approach. *Phys.Rev.*, D83:094006, 2011. doi: 10.1103/PhysRevD.83.094006.

[65] V.P. Gusynin, V.A. Miransky, and I.A. Shovkovy. Catalysis of dynamical flavor symmetry breaking by a magnetic field in (2+1)-dimensions. *Phys.Rev.Lett.*, 73: 3499–3502, 1994. doi: 10.1103/PhysRevLett.73.3499,10.1103/PhysRevLett.73.3499.

[66] K. Hagiwara, A.D. Martin, D. Nomura, and T. Teubner. Improved predictions for g-2 of the muon and alpha(QED) (M**2(Z)). *Phys.Lett.*, B649:173–179, 2007. doi: 10.1016/j.physletb.2007.04.012.

[67] K. Hagiwara, R. Liao, A. D. Martin, D. Nomura, and T. Teubner. $(g-2)_\mu$ and $\alpha(MZ^2)$ re-evaluated using new precise data. *J.Phys.G*, G38:085003, 2011. doi: 10.1088/0954-3899/38/8/085003. * Temporary entry *.

[68] D. Hanneke, S. Fogwell, and G. Gabrielse. New measurement of the electron magnetic moment and the fine structure constant. *Phys.Rev.Lett.*, 100:120801, 2008. doi: 10.1103/PhysRevLett.100.120801.

[69] M. Hasenbusch. Speeding up the hybrid Monte Carlo algorithm for dynamical fermions. *Phys. Lett.*, B519:177–182, 2001. doi: 10.1016/S0370-2693(01)01102-9.

[70] M. Hayakawa and T. Kinoshita. Pseudoscalar pole terms in the hadronic light by light scattering contribution to muon g - 2. *Phys.Rev.*, D57:465–477, 1998. doi: 10.1103/PhysRevD.57.465,10.1103/PhysRevD.66.019902.

[71] M. Hayakawa, T. Kinoshita, and A.I. Sanda. Hadronic light by light scattering effect on muon g-2. *Phys.Rev.Lett.*, 75:790–793, 1995. doi: 10.1103/PhysRevLett.75.790.

[72] A.H. Hoang, M. Beneke, K. Melnikov, T. Nagano, A. Ota, et al. Top - anti-top pair production close to threshold: synopsis of recent NNLO results. *Eur.Phys.J.direct*, C2:1, 2000.

[73] H. Iinuma. New approach to the muon g-2 and EDM experiment at J-PARC. *J.Phys.Conf.Ser.*, 295:012032, 2011. doi: 10.1088/1742-6596/295/1/012032.

[74] K. Jansen and C. Urbach. tmLQCD: a program suite to simulate Wilson twisted mass lattice QCD. *Comput.Phys.Commun.*, 180:2717–2738, 2009. doi: 10.1016/j.cpc.2009.05.016.

[75] K. Jansen, M. Papinutto, A. Shindler, C. Urbach, and I. Wetzorke. Quenched scaling of Wilson twisted mass fermions. *JHEP*, 0509:071, 2005. doi: 10.1088/1126-6708/2005/09/071.

[76] K. Jansen, C. Michael, and C. Urbach. The eta-prime meson from lattice QCD. *Eur.Phys.J.*, C58:261–269, 2008. doi: 10.1140/epjc/s10052-008-0764-6.

[77] K. Jansen, C. McNeile, C. Michael, C. Urbach, and for the ETM Collaboration. Meson masses and decay constants from unquenched lattice QCD. *Phys.Rev.*, D80:054510, 2009. doi: 10.1103/PhysRevD.80.054510.

[78] K. Jansen, M. Petschlies, and C. Urbach. Charm current-current correlators in twisted mass lattice QCD. *PoS*, LATTICE2011:234, 2011.

[79] K. Jansen, F. Karbstein, A. Nagy, and M. Wagner. $\Lambda_{\bar{M}S}$ from the static potential for QCD with $n_f = 2$ dynamical quark flavors. *JHEP*, 1201:025, 2012. doi: 10.1007/JHEP01(2012)025.

[80] F. Jegerlehner. Hadronic vacuum polarization contribution to g-2 of the leptons and alpha (M(Z)). *Nucl.Phys.Proc.Suppl.*, 51C:131–141, 1996.

[81] F. Jegerlehner. Precision measurements of sigma(hadronic) for alpha(eff)(E) at ILC energies and (g-2)(mu). *Nucl.Phys.Proc.Suppl.*, 162:22–32, 2006. doi: 10.1016/j.nuclphysbps.2006.09.060.

[82] F. Jegerlehner. Muon g - 2 update. *Nucl.Phys.Proc.Suppl.*, 181-182:26–31, 2008. doi: 10.1016/j.nuclphysbps.2008.09.002.

[83] F. Jegerlehner. *The anomalous magnetic moment of the muon*. Springer, 2008. Berlin, Germany: Springer (2008) 426 p.

[84] F. Jegerlehner. Progress in the prediction of g-2 of the muon. *Acta Phys.Polon.*, B40:3097–3109, 2009.

[85] F. Jegerlehner and A. Nyffeler. The muon g-2. *Phys. Rept.*, 477:1–110, 2009. doi: 10.1016/j.physrep.2009.04.003.

[86] E. E. Jenkins, A. V. Manohar, and M. B. Wise. Chiral perturbation theory for vector mesons. *Phys.Rev.Lett.*, 75:2272–2275, 1995. doi: 10.1103/PhysRevLett.75.2272.

[87] A. Juttner and M. Della Morte. New ideas for g-2 on the lattice. *PoS*, LAT2009:143, 2009.

[88] Y. Kiyo, A. Maier, P. Maierhofer, and P. Marquard. Reconstruction of heavy quark current correlators at O(alpha(s)**3). *Nucl.Phys.*, B823:269–287, 2009. doi: 10.1016/j.nuclphysb.2009.08.010.

[89] M. Knecht and A. Nyffeler. Hadronic light by light corrections to the muon g-2: the pion pole contribution. *Phys.Rev.*, D65:073034, 2002. doi: 10.1103/PhysRevD.65.073034.

[90] M. Knecht, A. Nyffeler, M. Perrottet, and E. de Rafael. Hadronic light by light scattering contribution to the muon g-2: An effective field theory approach. *Phys.Rev.Lett.*, 88:071802, 2002. doi: 10.1103/PhysRevLett.88.071802.

[91] J. Koponen et al. Heavy-light current-current correlators. *PoS*, LATTICE2010:231, 2010.

[92] M. Luscher. Construction of a selfadjoint, strictly positive transfer matrix for Euclidean lattice gauge theories. *Commun.Math.Phys.*, 54:283, 1977. doi: 10.1007/BF01614090.

[93] M. Luscher. Volume dependence of the energy spectrum in massive quantum field theories. 1. Stable particle states. *Commun.Math.Phys.*, 104:177, 1986. doi: 10.1007/BF01211589.

[94] M. Luscher. Volume dependence of the energy spectrum in massive quantum field theories. 2. Scattering states. *Commun.Math.Phys.*, 105:153–188, 1986. doi: 10.1007/BF01211097.

[95] M. Luscher and P. Weisz. On-shell improved lattice gauge theories. *Commun.Math.Phys.*, 97:59, 1985. doi: 10.1007/BF01206178,10.1007/BF01206178.

[96] A. Maier, P. Maierhofer, P. Marquard, and A.V. Smirnov. Low energy moments of heavy quark current correlators at four loops. *Nucl.Phys.*, B824:1–18, 2010. doi: 10.1016/j.nuclphysb.2009.08.011.

[97] C. McNeile, C.T.H. Davies, E. Follana, K. Hornbostel, and G.P. Lepage. High-precision c and b masses, and QCD coupling from current-current correlators in lattice and continuum QCD. *Phys.Rev.*, D82:034512, 2010. doi: 10.1103/PhysRevD.82.034512.

[98] C. Michael. Fitting correlated data. *Phys.Rev.*, D49:2616–2619, 1994. doi: 10.1103/PhysRevD.49.2616.

[99] C. Michael and A. McKerrell. Fitting correlated hadron mass spectrum data. *Phys.Rev.*, D51:3745–3750, 1995. doi: 10.1103/PhysRevD.51.3745.

[100] A. Morel. Chiral logarithms in quenched QCD. *J.Phys.(France)*, 48:1111–1119, 1987.

[101] G. Munster, C. Schmidt, and E. E. Scholz. Chiral perturbation theory for partially quenched twisted mass lattice QCD. *Europhys.Lett.*, 86:639–644, 2004. doi: 10.1209/epl/i2004-10255-9.

[102] K. Nakamura et al. Review of particle physics. *J.Phys.G*, G37:075021, 2010. doi: 10.1088/0954-3899/37/7A/075021.

[103] A. Nyffeler. Hadronic light-by-light scattering contribution to the muon g-2. *Chin.Phys.*, C34:705–711, 2010. doi: 10.1088/1674-1137/34/6/016. * Temporary entry *.

[104] K. Osterwalder and R. Schrader. Axioms for Euclidean Green's functions. *Commun. Math. Phys.*, 31:83–112, 1973. doi: 10.1007/BF01645738.

[105] K. Osterwalder and E. Seiler. Gauge field theories on the lattice. *Ann. Phys.*, 110: 440, 1978. doi: 10.1016/0003-4916(78)90039-8.

[106] M. E. Peskin and D. V. Schroeder. *An Introduction to quantum field theory*. ABP, 1995.

[107] M Petschlies. Charm current-current correlators in twisted mass lattice QCD. *PoS*, LATTICE2010:238, 2010.

[108] J. Prades. Theory of the hadronic light-by-light contribution to muon g-2. *PoS*, CD09:079, 2009.

[109] William H. Press, Saul A. Teukolsky, William T. Vetterling, and Brian P. Flannery. Numerical Recipes in FORTRAN: The Art of Scientific Computing. 1992.

[110] for QCDSF Rakow, P. Prospects of the lattice determination of the light-by-light contributions. *Topical Workshop on the Muon g-2, Glasgow, UK*, 2007.

[111] D. B. Renner. Nonpertubative QCD corrections to electroweak observables. *PoS*, LATTICE2011, 2011.

[112] D. B. Renner and X. Feng. Hadronic contribution to g-2 from twisted mass fermions. *PoS*, LATTICE2008:129, 2008.

[113] D B. Renner, X. Feng, K. Jansen, and M. Petschlies. Leading order hadronic contribution to g-2 from twisted mass QCD. *PoS*, LATTICE2010:155, 2010.

[114] J. S. Schwinger. On quantum electrodynamics and the magnetic moment of the electron. *Phys.Rev.*, 73:416–417, 1948. doi: 10.1103/PhysRev.73.416.

[115] J.C. Sexton and D.H. Weingarten. Hamiltonian evolution for the hybrid Monte Carlo algorithm. *Nucl.Phys.*, B380:665–678, 1992. doi: 10.1016/0550-3213(92)90263-B.

[116] S. R. Sharpe and N. Shoresh. Physical results from unphysical simulations. *Phys.Rev.*, D62:094503, 2000. doi: 10.1103/PhysRevD.62.094503.

[117] A. Shindler. Twisted mass lattice QCD. *Phys.Rept.*, 461:37–110, 2008. doi: 10.1016/j.physrep.2008.03.001. * Temporary entry *.

[118] K. Symanzik. Continuum limit and improved action in lattice theories. 1. Principles and phi**4 theory. *Nucl.Phys.*, B226:187, 1983. doi: 10.1016/0550-3213(83)90468-6.

[119] K. Symanzik. Continuum limit and improved action in lattice theories. 2. O(N) nonlinear sigma model in perturbation theory. *Nucl.Phys.*, B226:205, 1983. doi: 10.1016/0550-3213(83)90469-8.

[120] C. Urbach. Lattice QCD with two light Wilson quarks and maximally twisted mass. *PoS*, LAT2007:022, 2007.

[121] C. Urbach, K. Jansen, A. Shindler, and U. Wenger. HMC algorithm with multiple time scale integration and mass preconditioning. *Comput.Phys.Commun.*, 174:87–98, 2006. doi: 10.1016/j.cpc.2005.08.006.

[122] T. van Ritbergen, J.A.M. Vermaseren, and S.A. Larin. The Four loop beta function in quantum chromodynamics. *Phys.Lett.*, B400:379–384, 1997. doi: 10.1016/S0370-2693(97)00370-5.

[123] V. Vrba et al. Letter of intent: new measurement of muon anomalous magnetic moment $g-2$ and electric dipole moment at J-PARC. 2009.

[124] P. Weisz. Continuum limit improved lattice action for pure Yang-Mills theory. 1. *Nucl.Phys.*, B212:1, 1983. doi: 10.1016/0550-3213(83)90595-3.

[125] P. Weisz and R. Wohlert. Continuum limit improved lattice action for pure Yang-Mills theory. 2. *Nucl.Phys.*, B236:397, 1984. doi: 10.1016/0550-3213(84)90543-1,10.1016/0550-3213(84)90543-1.

[126] K. G. Wilson. Confinement of quarks. *Phys.Rev.*, D10:2445–2459, 1974. doi: 10.1103/PhysRevD.10.2445.

[127] U. Wolff. Monte Carlo errors with less errors. *Comput.Phys.Commun.*, 156:143–153, 2004. doi: 10.1016/S0010-4655(03)00467-3,10.1016/j.cpc.2006.12.001.

Acknowledgments

At this point I would like to take a moment and express my gratitude to all the people who in numerous and at times maybe even unrecognized ways enabled and supported my work during the past years. It was their continuous efforts in fore- and background that gave me the freedom to pursue this PhD project and focus on the answers to the day-to-day questions. Let me single out those persons I found closest to me during this time.
I would like to thank Dr. habil. Karl Jansen for initiating this PhD project and supervising my work. Based on my experience I recognize in him every quality I could wish for in an advisor.
In deep gratitude I will not stop remembering the moral and mental support I received from Prof. Dr. Müller-Preußker and Dr. Karl Jansen, especially in mid 2012. The persuasive power of their continuous encouragement was vital for me to finish this thesis.
Moreover, I am indebted to Prof. Dr. Müller-Preussker for his persistent interest in the status of my work and his admirable organization of his research group. His initiation of my stay in Berlin from July to October 2012 is an act I gratefully comprehend as far beyond insightful mentoring.
I would like to express my gratitude to Dr. Carsten Urbach, who coauthored the proposal for this PhD project. Whenever asked for, he generously provided helpful practical advice and insight from his extensive experience.
I am thankful for being able to work with Dr. Xu Feng and Dr. Dru B. Renner. Not only did they introduce me to the $g-2$ project, but also created — and continue to do so — an open-minded and highly educational atmosphere. In particular I want to thank Dr. Renner for sharing his expertise and deep insight in lattice field theory as well as his inspiring way of thinking ahead.
Prof. Dr. Constantia Alexandrou deserves my thanks for her sustained patience and trust during the additional months I worked on finishing this thesis. Likewise I appreciate the supportive attitude of Prof. Dr. Leonard Barrie, vice president of research of The Cyprus Institute, as well as the administrative staff of the latter.
I gratefully acknowledge the financial support of my PhD position and for travel expenses from the Sonderforschungsbereich TR9 ”Computational Particle Physics” of the Deutsche Forschungsgemeinschaft.
With a warm thank-you I think about my fellow students at Humboldt-University and DESY/Zeuthen, especially my office mates Grit Hotzel and Florian Burger, and the numerous joyful conversations and interesting discussions we had together.
I would like to thank the Humboldt Graduate School 1504 "Mass, Spectrum, Symmetry" for accepting me as an associated member. In particular I am thankful for the organi-

zation of the semiannual block courses, which created an intense and fruitful learning environment, and for the generous financial support for the participation in conferences, especially the International Symposium on Lattice Field Theory in 2010 and 2011.

Großer Dank gilt meiner Familie, besonders meinen Eltern Elvira und Frank Petschlies, die mich jeder auf seine Weise jederzeit bedingungslos unterstützt haben. Ihr Zutun gab und gibt mir den Rückhalt, die Ruhe und Kraft, ohne die ich mein Promotionsstudium nicht hätte vollenden können.

Own publications

[1] X. Feng, G. Hotzel, K. Jansen, M. Petschlies and D. B. Renner, "Leading-order hadronic contributions to a_μ and $\alpha_{\rm QED}$ from $N_f = 2+1+1$ twisted mass fermions," arXiv:1211.0828 [hep-lat].

[2] D. B. Renner, X. Feng, K. Jansen and M. Petschlies, "Nonperturbative QCD corrections to electroweak observables," arXiv:1206.3113 [hep-lat].

[3] X. Feng, K. Jansen, M. Petschlies and D. Renner, "Hadronic vacuum polarization contribution to $g-2$ from the lattice," arXiv:1112.4946 [hep-lat].

[4] K. Jansen, M. Petschlies and C. Urbach, "Charm current-current correlators in twisted mass lattice QCD," PoS LATTICE **2011** (2011) 234 [arXiv:1111.5252 [hep-lat]].

[5] X. Feng, K. Jansen, M. Petschlies and D. B. Renner, "Two-flavor QCD correction to lepton magnetic moments at leading-order in the electromagnetic coupling," Phys. Rev. Lett. **107** (2011) 081802 [arXiv:1103.4818 [hep-lat]].

[6] D. B. Renner, X. Feng, K. Jansen and M. Petschlies, "Leading-order hadronic contribution to $g-2$ from lattice QCD," PoS ICHEP **2010** (2010) 371 [arXiv:1103.1392 [hep-lat]].

[7] F. Farchioni, G. Herdoiza, K. Jansen, A. Nube, M. Petschlies and C. Urbach, "Pseudoscalar decay constants from $N_f = 2+1+1$ twisted mass lattice QCD," PoS LATTICE **2010** (2010) 128 [arXiv:1012.0200 [hep-lat]].

[8] D. B. Renner *et al.* [ETM Collaboration], "Leading order hadronic contribution to $g-2$ from twisted mass QCD," PoS LATTICE **2010** (2010) 155 [arXiv:1011.4231 [hep-lat]].

[9] B. Blossier *et al.* [ETM Collaboration], "Quark masses with $N_f = 2$ twisted mass lattice QCD," PoS LATTICE **2010** (2010) 239 [arXiv:1011.1862 [hep-lat]].

[10] M. Petschlies *et al.*, "Charm current-current correlators in twisted mass lattice QCD," PoS LATTICE **2010** (2010) 238

[11] B. Blossier *et al.* [ETM Collaboration], "Average up/down, strange and charm quark masses with $N_f = 2$ twisted mass lattice QCD," Phys. Rev. D **82** (2010) 114513 [arXiv:1010.3659 [hep-lat]].

[12] M. Müller-Preußker, E. -M. Ilgenfritz, K. Jansen, M. P. Lombardo, O. Philipsen, L. Zeidlewicz, M. Kirchner and M. Petschlies *et al.*, "On the phase structure of lattice QCD with twisted-mass Wilson fermions at non-zero temperature," PoS LAT **2009** (2009) 266 [arXiv:0912.0919 [hep-lat]].

[13] E. -M. Ilgenfritz, K. Jansen, M. P. Lombardo, M. Müller-Preußker, M. Petschlies, O. Philipsen and L. Zeidlewicz, "Phase structure of thermal lattice QCD with $N_f = 2$ twisted mass Wilson fermions," Phys. Rev. D **80** (2009) 094502 [arXiv:0905.3112 [hep-lat]].

[14] E. -M. Ilgenfritz, K. Jansen, M. P. Lombardo, M. Müller-Preußker, M. Petschlies, O. Philipsen and L. Zeidlewicz, "The finite-temperature phase structure of lattice QCD with twisted-mass Wilson fermions," PoS LATTICE **2008** (2008) 206 [arXiv:0809.5228 [hep-lat]].

[15] E. -M. Ilgenfritz, M. Müller-Preußker, M. Petschlies, K. Jansen, M. P. Lombardo, O. Philipsen, L. Zeidlewicz and A. Sternbeck, "Twisted mass QCD at finite temperature," PoS LAT **2007** (2007) 238 [arXiv:0710.0569 [hep-lat]].

Berlin, 28 December 2012 Marcus Petschlies

List of Figures

List of Tables

Selbständigkeitserklärung

Ich erkläre, dass ich die vorliegende Arbeit selbständig und nur unter Verwendung der angegebenen Literatur und Hilfsmittel angefertigt habe.

Berlin, den 28.12.2012 Marcus Petschlies